Author:
Gonzalez-Fernandez, Daniel

Title:
Wind-induced dynamic behaviour of slender structures

tall buildings and electricity transmission lines

WIND-INDUCED DYNAMIC BEHAVIOUR OF SLENDER STRUCTURES: TALL BUILDINGS AND ELECTRICITY TRANSMISSION LINES

BY

DANIEL GONZALEZ-FERNANDEZ

SCHOOL OF CIVIL, AEROSPACE AND MECHANICAL ENGINEERING

UNIVERSITY OF BRISTOL

A dissertation submitted to the University of Bristol in accordance with the requirements for award of the Degree of Doctor of Philosophy in the Faculty of Engineering

April 2023

65526 words

ABSTRACT

The design of more slender buildings and the elongation of the spans for cable structures increase the concerns of wind-induced vibrations and aerodynamics and aeroelastic phenomena. Despite nowadays greater awareness and better knowledge of such problems, there are still several uncertainties on the wind-structure interaction, modelling omissions and weakness in understanding the exact mechanism of the underlying phenomena. These are related to the lack of long-term full-scale data for the validation of the methods of analysis and universally accepted principles to predict the structural responses. This research presents results from simple full-scale monitoring approaches for two types of slender structures, two tall buildings and a cable bundle within an electricity transmission line, which was also studied at wind tunnel-scale.

Full-scale measurements were taken of accelerations measured on the two tall buildings and the associated wind conditions to quantify the dynamic behaviour and the effect of the relative orientations of the wind and motion on the modal parameters, i.e., natural frequencies and damping ratios. These parameters have been investigated in relation to a series of variables and supported by a simplified finite element model of one of the structures to assess the long-term variation of the observations. A new empirical amplitude-dependent damping prediction model has been also developed to quantify this relationship in comparison with a series of previous studies.

In order to increase the understanding on the interaction between wind and slender structures, this research has been extended to transmission lines by means of a full-scale analysis founded on a preliminary groundwork study, based on experimental wind tunnel test-data, to investigate the analytical solutions to assess the galloping stability from two existing aeroelastic formulations in literature. In particular, a new study based on the eigenvalue analysis has been presented, for which the calculated stability regions and steady-state responses have been assessed and compared with the published model and wind tunnel tests.

The full-scale investigation in transmission lines has identified trends in the ambient vibrations from tension meters in a range of atmospheric conditions to analyse their effects on the typical measured natural frequencies in operation conditions. A long-term analysis of the non-galloping events has been first presented followed by a detailed shorter-term study of some particular galloping events. It has been complemented by a finite element model of the cable bundle used as a tool that enables the interpretation of the dynamic behaviour of the system from the full-scale observations.

In summary, whilst the presented results are contextual and specific to these structures or structural configurations, this research has demonstrated that minimalistic monitoring systems allow for establishing the vibration characteristics and interpreting the root causes of their variation. Also, it has demonstrated that this approach can be adopted as a tool in the through-life analysis and monitoring of the structural condition and health to assess the performance criterion for serviceability.

ACKNOWLEDGEMENTS

First and most I would like to express my gratitude to my supervisors, Dr. John H. G. Macdonald (†) and Dr. Branislav Titurus, Dr. Djamel Rezgui and Dr. Raffaele De Risi for their constant support, advise and encouragement, their recommendations and thoughtful comments during my research and while writing this thesis.

This research significantly benefited from collaboration arrangements originated by the work of late Professor John H. G. Macdonald between the University of Bristol and external partners. My deepest appreciation should be addressed to him, who introduced me first in the world of research at the Faculty of Engineering of the University of Bristol and who sadly passed away before this PhD study could be completed.

Regarding the work on tall buildings presented in Chapter 1, I am specially indebted to AKT II Ltd. and Dr. Alessandro Margnelli for facilitating and allowing the use of the data monitoring of two tall buildings in London for this research. I would like to thank AKT II Ltd. and Tyréns AB for the monitoring and preliminary analysis and the Institution of Structural Engineers for a Research Award for further analysis of the data.

The investigation on electricity transmission lines presented in Chapters 2 and 3 were carried out in a collaborative research between the University of Bristol and the Central Research Institute of Electric Power Industry (CRIEPI) in Japan. Therefore, I would like to express my gratitude to CRIEPI, Dr. Hisato Matsumiya and Dr. Saki Taruishi for the monitoring, preliminary analysis and support for further analysis of the data.

Finally, I must thank the BritishSpanish Society Scholarship Programme for the sponsorship of this research and my parents for their love and support along all these years I’ve been abroad from Spain, first in London while completing High School, then in Edinburgh during my Degree and Master Degree in Civil Engineering, and now in Bristol for my Doctorate.

AUTHOR'S DECLARATION

I declare that the work in this dissertation was carried out in accordance with the requirements of the University's *Regulations and Code of Practice for Research Degree Programmes* and that it has not been submitted for any other academic award. Except where indicated by specific reference in the text, the work is the candidate's own work. Work done in collaboration with, or with the assistance of, others, is indicated as such. Any views expressed in the dissertation are those of the author.

SIGNED:  DATE: 22/04/2023

TABLE OF CONTENTS

page

LIST OF FIGURES

page

LIST OF TABLES

page

NOMENCLATURE. LIST OF SYMBOLS

The following list summarizes the notation and abbreviations used along this Thesis.

Notation

A	Area projected on a plane normal to the direction of flow
$A(\omega)$	Denominator matrix polynomial
$A_{pk\text{-}pk}$	Peak-to-peak Amplitude
A_q	Amplitude for each direction, $(q = y, z, \theta)$ [Matsumiya *et al*. (2018)]
B	Width of the structure
B	Centre interval of the conductor [Matsumiya *et al*. (2018)]
$B(\omega)$	Numerator matrix polynomial
C	Total damping matrix
c	Distance between leading and trailing edges in the direction of flow
C_a	Full aerodynamic damping matrix for the 3DOF model
C_D	Drag coefficient
C_{Df}	Drag coefficient of the bundle [Matsumiya *et al*. (2018)]
C'_{Df}	Rate of change of the drag coefficient C_{Df} of the bundle [Matsumiya *et al*. (2018)]
C_{Di}	Drag coefficient for each subconductor (i = 1, …, 4) [Matsumiya *et al*. (2018)]
C_L	Lift coefficient
C_{Lf}	Lift coefficient of the bundle [Matsumiya *et al*. (2018)]
C'_{Lf}	Rate of change of the lift coefficient C_{Lf} of the bundle [Matsumiya *et al*. (2018)]
C_{Li}	Lift coefficient for each subconductor (i = 1, …, 4) [Matsumiya *et al*. (2018)]
C_M	Moment coefficient
C_{Mf}	Moment coefficient of the bundle [Matsumiya *et al*. (2018)]
C'_{Mf}	Rate of change of the moment coefficient C_{Mf} of the bundle [Matsumiya *et al*. (2018)]
C_{Mi}	Moment coefficient for each subconductor (i = 1, …, 4) [Matsumiya *et al*. (2018)]
CoF	Change of frequency
C_q	Structural damping coefficient for each direction, $(q = y, z, \theta)$ [Matsumiya *et al*. (2018)]
C_{q0}	Structural damping coefficient at zero-amplitude, $(q = y, z, \theta)$ [Matsumiya *et al*. (2018)]

C_{q1}	Slope coefficient, $(q = y, z, \theta)$
C_s	Structural damping matrix
D	Diameter of the conductor [Matsumiya *et al*. (2018)]
D	A reference dimension of the body [He and Macdonald (2016)]
d	Cable diameter
d/H	Drift ratio
dA	Differential area of the body
D_s	Drag quasi-steady aerodynamic force of the bundle [Matsumiya *et al*. (2018)]
D_{si}	Drag quasi-steady aerodynamic force for each subconductor, (i = 1, …, 4) [Matsumiya *et al*. (2018)]
f	Frequency
F_D	Drag force
F_L	Lift force
f_n	Undamped natural frequency
F_q	Aerodynamic force for each direction, $(q = y, z, \theta)$ [Matsumiya *et al*. (2018)]
fs	Sampling frequency
F_x, F_y, F_θ	Aerodynamic forces for each direction [He and Macdonald (2016)]
f_{y0}	Frequency of the vertical motion
f_{z0}	Frequency of the horizontal motion
$f_{\theta 0}$	Frequency of the torsional motion
G	Mass centre
H	Sag (depth) of the section model from the support point in the stationary condition
^{H}	complex conjugate transpose of a matrix
$H(f)$	Frequency Response Function (FRF) of the system
$H_i(f)$	FRF of mode i
I	Polar second moment of mass of the structure per unit length [Davenport (1962)]
I	Mass moment of inertia of the section model [Matsumiya *et al*. (2018)]
I	Identity matrix [He and Macdonald (2016)]
I_u	Longitudinal mean turbulence intensity
I_v	Full-scale across-wind mean turbulence intensity
K	Stiffness matrix
$< k_i^T >$	Operational reference vector $(i = 1 \ldots n)$
k_x, k_y, k_θ	Structural stiffnesses

L	Horizontal length of the elastic cords
l	Length of the section model
L_a	Aerodynamic centre radius
L_f	Lift quasi-steady aerodynamic force
L_g	Length of the elastic cord
L_i	Length of the elastic cords at each instant, (i = 1, …,4) [Matsumiya *et al*. (2018)]
L_i	Excitation factor ($i = 1 \ldots n$) [Williams (2016)]
$< l_i^T >$	Modal participation factors ($i = 1 \ldots n$)
L_{i0}	Static length of the elastic cord
L_{ig}	Length of the elastic cord in the stationary condition without wind
L_s	Lift quasi-steady aerodynamic force of the bundle
L_{si}	Lift quasi-steady aerodynamic force for each subconductor, (i = 1, …, 4)
m	Mass of the structure [Davenport (1962)]
m	Cable mass per unit length [Post-Tensioning Institute (2006)]
M	Generalised mass [Maia *et al*. (1997)]
M	Mass matrix [He and Macdonald (2016)]
M_f	Moment quasi-steady aerodynamic force
M_i	Generalised mass ($i = 1 \ldots n$)
$M_{p,i}$	Modal participation mass for mode i ($i = 1 \ldots n$) in each degree of freedom p
M_s	Moment quasi-steady aerodynamic force of the bundle
M_{si}	Moment quasi-steady aerodynamic force for each subconductor, (i = 1, …, 4)
N	Length of the Fast Fourier Transform
n	Number of modes
O	Elastic centre
o	Number of measurement channel ($o = 1 \ldots l$)
P	Pressure acting on the surface of the body
p	Polynomial order
p_{y0}	Static wind force
r	Radius of gyration of the section model
R^2	Coefficient of determination
R_m	Radius of the elastic chord support on the section model side
R_s	Radius of the elastic cord support on the holding stay side
$S(\omega)$	PSD matrix

$S_{wind}(f)$	Spectrum for wind loading
$S_{xx}(f)$	Power Spectral Density of the input
$S_{xixi}(f)$	Power Spectral Density of the generalised load of mode *i*
$S_{yy}(f)$	Power Spectral Density of the output
${}_iS_{yy}(f)$	Contribution to the response PSD of mode *i*
T	Tension in the elastic cords in the stationary condition
T_i	Tension in the elastic cords due to the static weight of the model, (i = 1, …,4)
T1	1st Torsional mode
Δt	Sampling time
U	Mean longitudinal wind speed
U_i	Unitary matrix containing the singular vectors u_{ij}
U_{rel}	Relative velocity
U_{ri}	Relative wind speed for each subconductor, (i = 1, …, 4)
U_{rot}	Velocity of the aerodynamic centre
V_{crit}	Critical wind velocity
$\{v_i\}$	Mode shapes ($i = 1 \ldots n$)
X1	1st mode in the *x* direction
$Y_i,\ Z_i,\ R_i$	Functions of the displacements related to the geometry of the wires, (i = 1, …,4)
Y1	1st mode in the y direction
α	Angle of attack
α_0	Angle between wind direction and *x* axis
α_m	Inclined angle of the elastic cord support on the section model side
α_r, β_{or}	Polynomial coefficients
α_{rel}	Angle between relative velocity and reference line
α_{ri}	Relative angle of attack for each subconductor, (i = 1, …, 4)
α_s	Inclined angle of the elastic cord support on the holding stay side
γ_r	Aerodynamic centre angle from the body reference line
δ_q	Logarithmic decrement, $(q = y, z, \theta)$
δ_{st}	Static horizontal deflection
ζ	Damping ratio
ζ_{aero}	Aerodynamic damping
ζ_q	Structural damping ratios for each degree of freedom, $(q = y, z, \theta)$
ζ_{struct}	Structural damping

θ	Rotation of the cross-section measured between the *x* axis and a reference line [He and Macdonald (2016)]
θ	Torsional displacement (corresponds to the angle of attack in the wind direction) [Matsumiya *et al.* (2018)]
θ_0	Static rotation of the shape due to the weight of ice or the mean wind load
λ_i	Poles ($i = 1 \ldots n$)
ξ_i	Eigenfrequencies
ρ	Air density
σ	RMS acceleration amplitude
ϕ_{ri}	Relative angle of attack for each subconductor, (i = 1, …, 4)
ω_i	Damping ratios ($i = 1 \ldots n$)
ω_q	Angular natural frequencies for each degree of freedom, $(q = y, z, \theta)$
$\Omega_r(\omega)$	Polynomial basis function

Abbreviations

AC	Aerodynamic centre
ACSR	Aluminium Conductor Steel Reinforced
CPSD	Cross Power Spectral Density
CRIEPI	Central Research Institute of Electric Power Industry
DOF	Degree of Freedom
EA	Axial rigidity of the elastic cords
EMA	Experimental Modal Analysis
ESDU	Engineering Sciences Data Unit
FDD	Frequency Domain Decomposition
FDM	Finite Difference Method
FEM	Finite Element Method
FFT	Fast Fourier Transform
FPS	Frames per second
FRF	Frequency Response Function
GPS	Global Positioning System
HOT	Higher Order Term
ITV	Industrial Television
IWCM	Iterative Windowed Curve-fitting Method

KPSS	Kwiatkowski-Phillips-Schmidt-Shin test
LED	Light Emitting Diode
LSCE	Least-Squares Complex Exponential
LSCF	Least-Squares Complex Frequency-Domain
LTI	Linear Time-Invariant
MDOF	Multiple-Degree-Of-Freedom
NS	Northside Support
ODE	Ordinary Differential Equation
OMA	Operational Modal Analysis
pLSCF	Poly-reference Least-Squares Complex Frequency-Domain
PSD	Power Spectral Density
RMS	Root Mean Square
SDOF	Single-Degree-Of-Freedom
SISO	Single Input Single Output
SS	Southside Support
SSI	Stochastic Subspace Identification
STFT	Short-Time Fourier Transform

LIST OF PUBLICATIONS

The author's list of publications related to the present Thesis is:

Journal Papers

- Gonzalez-Fernandez, D., De Risi, R., Rezgui, D., Titurus, B., and Margnelli, A. (2023), "Identification of varying modal parameters of a tall building from the full-scale wind-induced responses". *Structures*, **56**, 104770.

Conference Proceedings

- Gonzalez-Fernandez, D., Macdonald, J.H.G., Titurus, B., Margnelli, A., Greco, L., Gkoktsi, K., Leeks, M., Janssen, J. and Zanchetta, M. (2019), "Full-scale identification of aeroelastic effects on a tall building", *Proceedings of the 15th International Conf. on Wind Engineering*, pp. 129-130, Beijing (China).
- Gonzalez-Fernandez, D., Macdonald, J.H.G., Titurus, B., and Margnelli, A. (2021), "Long-term monitoring of wind-induced vibrations of two tall buildings in London", *Proceedings of the 10th International Conference on Structural Health Monitoring of Intelligent Infrastructure*, Porto (Portugal).
- Gonzalez-Fernandez, D., Macdonald, J.H.G., Titurus, B., and Matsumiya, H. (20 22), "Analytical solution for the galloping instability on transmission lines", *8th European-African Conference on Wind Engineering*, Bucharest (Romania).

CHAPTER 1. INTRODUCTION

1.1. BACKGROUND AND MOTIVATIONS

Taller, thinner and more slender structures are landmarks in 21st century engineering. However, the construction of one-kilometre-long bridges, the design of more slender buildings and the elongation of the spans for cable structures increase the relevance of issues related to wind-induced vibrations. Nowadays, a greater awareness of such problems exists thanks to the better knowledge of aerodynamics and aeroelastic phenomena.

Such improved knowledge is built on a few seminal studies and the empirical evidence associated with catastrophic failures. During the 1930s, Den Hartog studied the vibration in overhead electricity transmission lines. In 1940, the Tacoma Narrows bridge failure demonstrated the importance of the wind-induced vibrations of slender structures. Subsequent studies on suspension and cable-stayed bridges assessed the effect of wind on the deck and the cables. Davenport (1961) extended the knowledge on bridges to tall structures in his PhD Thesis at the University of Bristol, "The treatment of wind loads on tall towers and long span bridges in turbulent wind".

With time it has also emerged the importance of full-scale monitoring. Notwithstanding the relevance of experimental tests and the development of computational power, neither wind tunnel tests nor computational fluid dynamics (CFD) simulations can accurately account simultaneously for all parameters (e.g., damping, environmental variables) reproducing critical phenomena such as flutter, galloping, wind buffeting and vortex shedding. A detailed understanding of wind-induced vibrations and the associated aerodynamic effects can only be acquired from full-scale monitoring under real wind conditions. This issue was addressed by John H.G. Macdonald (2000) in his PhD Thesis at the University of Bristol, "Identification of the dynamic behaviour of a cable-stayed bridge from full-scale testing during and after construction". In fact, as will be discussed later, monitoring systems are now standard practice for bridges and tall buildings; most recently, other structures and installations have been considered, e.g., new simple monitoring techniques have been adopted for electricity transmission lines and wind turbines.

Despite great knowledge has been developed through several studies, hybrid phenomena play a major role in the wind-structure interaction, particularly for slender structures where bluff cross-sections are concerned. Thus, there are still remaining gaps in understanding the

exact mechanisms that drive the dynamic response of these structures. This is strongly linked to the difficulties in quantifying the responses under operational conditions and disentangling accurately the influence of each individual parameter in these responses. The dynamic responses of the structures can be quantified on the basis of modal parameters (i.e., damping, natural frequencies and mode shapes) estimated from OMA (Operational Modal Analysis), also known as output-only modal analysis. This technique is commonly adopted in design, because the dissipation of energy of a structure expressed as damping is directly related to the mechanical resonance represented by frequency. However, damping is still harder to calculate and predict confidently than frequency, as observed for tall buildings by Brownjohn *et al*. (2000) and, consequently, it has been often estimated for cable structures based on empirical values without any theoretical background according to Yamaguchi and Jayawardena (1992).

With respect to tall buildings, wind actions, which are the most significant forces apart from seismic, remain a significant epistemic uncertainty. Since occupant comfort is directly related to wind-induced sway, understanding the resulting dynamic responses in this type of structures is now paramount from both ultimate and serviceability points of view. However, there are still uncertainties around these parameters and their long-term variations under operational variable conditions. Smith *et al*. (2010) found that damping ratios for tall buildings are usually overestimated in design in comparison with full-scale measurements, which might lead to an increase in the lateral accelerations ultimately resulting in higher risk of structural damage and occupant discomfort.

Also, despite the increase of damping ratios with amplitude in tall buildings has been described since the early 1980s by Davenport and Hill-Carroll (1986) and Jeary (1986), there is still an open discussion on the amplitude-dependent behaviour of damping ratios because of the discrepancies with other studies supporting opposite trends, such as Tamura (2006) and Kijewski-Correa and Pirnia (2007). Furthermore, the dynamic responses of this type of structures to wind become even more complicated when aeroelastic effects are generated. These effects occur when structures experience aerodynamic forces generated by self-excited structural motions. Although it is globally accepted that aeroelastic effects are significant for long-span bridges or other types of slender structures, they are often neglected or oversimplified for tall buildings. As buildings become taller and more slender, these effects are likely to become more critical; hence quantifying is necessary. With the help of new simple monitoring

techniques in the context of OMA, this analysis has been subsequently extended to several structural systems, such as wind turbines and cable structures.

Cable structures are particularly prone to galloping, which is a low frequency, large-amplitude aeroelastic vibration of slender structures subjected to crosswind motion. It is closely related to the lift force acting on an asymmetrical body section (e.g., due to ice or snow accretion) that commonly results in large amplitudes in a vertical plane. Galloping instability is the most significant type of wind-induced motion in overhead electricity transmission lines and it has also been observed in bridge cables, particularly during construction. Interphase short circuits, conductor broken stocks, conductor strand burns or even support tower collapse are some observed damages in transmission lines, as described by EPRI (2009).

Furthermore, Havard (2003) noted that forced outages caused by galloping might have a more negative effect than direct damage to lines. Solutions might include designing structures capable of withstanding large vibrations or methods that reduce galloping behaviour, avoiding the formation of ice accretion or preventing attaining high amplitudes. To better design such mitigation solutions and improve inspection and maintenance, it is essential to predict the dynamic behaviour of such slender system accurately.

However, inspection and maintenance are very complicated, because of the wind-induced excitations, the high-voltage electricity, and the large ground clearance, therefore, monitoring systems for such infrastructure are now paramount. Full-scale measurements have been recently installed worldwide to understand the dynamic response of transmission lines, particularly under extreme events such as galloping. Thus, this field of research is less developed compared with the analysis of wind actions in tall buildings because of the difficulties to assess complex nonlinear systems and identify the main factors that induce galloping (i.e., shape and distribution of ice accretion and wind speed and direction along the cable span).

CIGRE (2007) stated that the galloping technology remains deficient relating the aerodynamic characteristics of the ice shapes with an actual galloping event. To overcome this problem, full-scale studies on electricity lines have been conducted using comprehensive monitoring equipment including accelerometers and video cameras, as presented by Van Dyke and Laneville (2008) and Matsumiya *et al.* (2012). However, although most results were properly determined using video images, they could only be obtained over a limited period of time because of the poor visibility during night-time, blinding blizzards or thick fog conditions.

1.2. RESEARCH AIM AND OBJECTIVES

1.2.1. Research aim

Within the framework of the aforementioned uncertainties in the study of wind-induced vibrations in slender structures, and inspired by the former research conducted by Macdonald (2000) in bridges, full-scale monitoring is used in this research for two different types of slender structures, two tall buildings in London and a cable bundle within a transmission line in Japan, which has been also studied at wind tunnel scale. Hence, the final aim of this research is to use full-scale data from simple monitoring systems to assess the effect of the wind on their responses in the context of minimal OMA. The purpose of this minimalistic approach is to provide reliable results simply by installing and leaving the monitoring equipment in place for extended periods, and has potential transferability to industrial settings due to its ease of maintenance and low cost to assess the performance criterion for serviceability. Although this research was based on testing the aforementioned selected structures, it seeks to provide insights into the dynamic behaviour that can be applied more generally to other similar structural systems.

1.2.2. Objectives

The main objectives of this research are listed as follows:

- Provide an overview of the dynamic response and corresponding wind conditions for two types of slender structures, two tall buildings and a cable bundle within a transmission line, to enable the validation of minimalistic methods of analysis and the quantification of wind-induced vibrations and aerodynamics and aeroelastic phenomena.
- Quantify and contrast the effect of the wind on the responses of the different structural systems, given their distinct structural characteristics subjected to varying environmental conditions in order to assess the serviceability limit state criterion.
- Identify the most influential modal parameters that govern the wind-induced dynamic behaviour of the selected slender structures including an overview of the typical values in operation from long-term trends and particular events, such as the addition of mass on the structures and short-term galloping phenomenon.
- Compare the full-scale measurements with auxiliary tools, such as simple finite element

models to allow confirmation and empirical interpretation of particular issues.

- Assess existing aeroelastic models for transmission lines in literature to predict the onset of the galloping instability and validate the accuracy of the methods of modelling by comparing the analytical results with the measured full-scale response.

Further remarks of interest for this research might be made to complement and interrelate the main objectives. Thus, seeking to gain understanding of wind-induced vibrations for the monitored structures and facilitate insight into their dynamic behaviour, the empirical data provided by AKT II Ltd. engineering consultancy on tall buildings and the Central Research Institute of Electric Power Industry (Japan) on electricity transmission lines are analysed. This research intents to apply these insights in future to improve the design and mitigate the negative effects of the vibrations on the structures to enhance their performances, increase their lifespans and reduce failure risk. Since the two types of structures have distinctly different characteristics (e.g., dimensions, stiffness properties, flat urban vs. mountainous rural environment), they are selected to explore the adoption of well-established OMA methodology for bridges and buildings in more complex nonlinear systems, such as cables.

Secondly, this investigation seeks to assess the use of simple monitoring systems in tall buildings by evaluating the structural performance and the dynamic properties of the structures from full-scale vibrations measured using only three accelerometers on top of the towers. Thus, with the aim to identify the most influential modal parameters that govern the dynamic response of tall buildings including an overview of the typical values in operation, trends in the estimated modal parameters, natural frequencies and damping ratios are studied in a range of wind conditions. Although numerous authors have comprehensively covered the analysis of modal parameters and the associated wind conditions in tall buildings, this research goes into more detail considering a series of factors, including time, amplitude, wind speed, wind direction and potential aeroelastic effects. In addition, this research also attempts to clarify some uncertainties related to the amplitude-dependency of damping at high amplitudes, for which there is still an open discussion within the community.

With the objective to offer a useful and computationally efficient first point of analysis for identification and assessment of the galloping instability, the full-scale investigation in overhead electricity transmission lines is complemented by a preliminary analytical study. Moreover, with the purpose of assessing the extent to which the minimalistic methodology is sufficient to analyse this phenomena, this study intents to find the analytical solutions from two

existing aeroelastic formulations, developed to predict the emergence of galloping. It has made use of observed aerodynamic characteristics in wind-tunnel tests conducted by Matsumiya *et al.* (2011) on the same full-scale cable bundle geometry. This environment enables the observation of the emergence of galloping in order to prepare the groundwork for a full-scale environment, where similar phenomena are expected.

This research also aims to investigate how well complex and relevant issues on cable structures, which are difficult to simulate in the wind tunnel, can be addressed by using simple monitoring in the full-scale context, which is only comprised of two tension meters attached to the insulators at one span end. Pursuing the identification of the limits of their applicability, assess usefulness and, ideally, propose further refinements and improvements, the tools and elements of methodology from tall buildings are translated to a more challenging setting in transmission lines. As a novelty, this research seeks to identify the conditions under which galloping occurs, based on tension data only, providing an alternative to recent studies on the same monitored transmission line which were usually based on displacements obtained from sophisticated equipment (e.g., video cameras or GPS sensors). Since access to this type of structures is complicated, tension meter installation, calibration and maintenance are cheaper and less demanding than more sophisticated equipment. Furthermore, with a focus on the effects of the atmospheric conditions, trends in the estimated natural frequencies in operation conditions are identified from tension meters. They are firstly obtained from a long-term analysis of the non-galloping events followed by a detailed shorter-term study of some particular galloping events.

Finally, with the objective to support the observations from the minimalistic monitoring systems, analysis of full-scale data is complemented by the use of low fidelity finite element models. Given the extended monitoring period in one of the two studied buildings, to simulate the long-term change of modal parameters with time, an analysis of the temporal changes of modal parameters is conducted with the help of a simplified model of the structure. This type of analysis has received little attention for buildings after the construction completion. Similarly, a geometric nonlinear finite element model is used with the aim of enabling the interpretation of the dynamic behaviour of the cable within a transmission line from the full-scale observations. In both cases, they are not high-precision models that intends to match precisely the structural response; instead, they allow collecting simple insights for the empirical interpretation.

1.3. THESIS STRUCTURE

In order to address the previously detailed aims and objectives of the research, this Thesis is divided as follows.

Chapter 2 – Literature review

This chapter provides an overview of the state of the art on the identification of modal parameters in tall buildings and transmission lines, with a particular focus on wind-induced effects. More detailed descriptions are also provided on the gap research and uncertainties related to the estimation of some modal parameters and its variation under operational conditions, such as the amplitude-dependent behaviour of damping. Secondly, it presents a description of the main relevant findings of galloping in overhead electricity transmission lines from OMA and the role of the atmospheric conditions concluding with a summary of the identified issues that have been addressed and the remaining gaps from this review. Finally, it highlights the key points relating to tall buildings and transmission lines reflecting on similarities and differences in their dynamic behaviour.

Chapter 3 – Effects of wind-induced vibrations on two tall buildings

This chapter is devoted to the full-scale monitoring of two tall buildings. The structural arrangements, the monitoring system and the long-term wind characteristics are firstly described before the system identification process is addressed. Next, relationships between the modal parameters (i.e., natural frequencies and damping ratios) and a series of parameters are presented to identify the dominant factors, including a simplified finite element model to support the interpretation of the empirical data. Possible aeroelastic effects have been studied by looking at the influence of the wind direction on the behaviour and vibrations in the translational directions. Also, an updated empirical model is proposed and compared against previous studies to assess the damping amplitude-dependency of the buildings. This study on tall buildings is used as a first step for gaining better understanding of the wind-induced vibrations in slender structures, such as cables.

Chapter 4 – Preliminary analysis of model scale galloping problem

This chapter addresses the analytical study on electricity transmission lines based on data from a wind tunnel test. It starts in the form of literature review by describing the two existing quasi-steady aeroelastic formulations, developed to assess the galloping stability on transmission lines that are taken as a reference for the analysis published in this research, including their main similarities and differences. This is followed by the estimation process of the position of an aerodynamic centre parameter, which is adopted by one of the two theoretical models, with the objective to implement the results in the analytical study. This chapter ends by comparing the results obtained from the two aeroelastic formulations using two different methods of analysis to predict and understand the emergence of galloping: the amplitudes obtained from the time-history responses and the proposed new study based on the eigenvalue analysis. These analytical results, based on wind-tunnel measurements, are used as a baseline for the full-scale results on the same cable bundle geometry described in Chapter 3.

Chapter 5 – Analysis of full-scale measurements on electricity transmission lines

This chapter presents the full-scale investigation of electricity transmission lines. It firstly describes the studied transmission line span and the monitoring equipment. A summary of the results from a finite element model, which includes a parametric analysis, is compared to the system identification output to provide a first insight into the full-scale results. The limitations of the system identification method used in tall buildings are also highlighted here. Next, it presents an overview of the observations, starting with the description of the atmospheric conditions followed by an analysis of long-term trends of the natural frequencies from records in which galloping was not observed, in relation to a series of parameters to find the dominant effects. Finally, a detailed assessment of some selected galloping events, including the associated wind conditions is made in this chapter.

Chapter 6 – Discussion and conclusions

Finally, this chapter critically reviews the work providing answers to the research aims and objectives, summarises the principal conclusions of the investigation, and provides recommendations for further research.

CHAPTER 2. LITERATURE REVIEW

This chapter is divided into three main sections. Section 2.1 provides an overview of the state of the art on the identification of modal parameters in tall buildings, with a particular focus on damping estimation and wind-induced effects, which have been found to be the sources of more discrepancies between different studies. There is also a detailed review of selected relevant amplitude-dependent damping models and the long-term variation of natural frequencies in tall buildings. Next, Section 2.2 presents a general overview of galloping phenomenon, with a description of the main relevant findings in overhead electricity transmission lines from OMA and some of the formulation developed to describe the mechanisms, including some remarks on the role of the atmospheric conditions. The two existing investigations presented by He and Macdonald (2016) and Matsumiya *et al*. (2018) to assess the galloping stability on transmission lines that are taken as a reference for the analysis in Chapter 4 and play an essential role in this research are also introduced. The issues that have been addressed and the remaining gaps from the review on the galloping phenomena are summarised at the end of Section 2.2. Finally, Section 2.3 highlights the key points relating to tall buildings and transmission lines reflecting on similarities and differences in their dynamic behaviour.

2.1. TALL BUILDINGS

2.1.1. Modal parameter identification in tall buildings

Apart from the specific studies conducted on tall buildings, where trends and relationships previously documented in literature have been confirmed, a series of studies carried out a deeper analysis of the modal parameters in this type of structures. Authors considered the correspondence between damping and amplitude to be the most meaningful issue. One of the first studies was made by Haviland (1976), who presented that the log-normal and gamma distributions give the best fit to the damping variations, after assessing diverse levels of response amplitudes, for different types of structural systems and building heights. Davenport and Hill-Carroll (1986), Jeary (1986) and Tamura *et al*. (2000) described the amplitude-dependent behaviour of damping ratio, while Lagomarsino (1993), Fritz *et al*. (2009) and Bernal *et al*. (2015) only predicted the initial ($d/H = 0$) or constant amplitude-dependent value of the

damping ratio. Davenport and Hill-Carroll (1986) stated that on average, a small increase in damping with increasing amplitude was found for tall buildings while, oppositely, Tamura (2006) and Kijewski-Correa and Pirnia (2007) observed that in some cases damping decreases at greater amplitudes. Moreover, Davenport and Hill-Carroll (1986) observed monotonical and small increase in damping with amplitude while Jeary (1986) and Tamura *et al*. (2000) suggested that the increase of damping ratio may eventually reach a plateau at a certain amplitude.

It should be mentioned that data used in these researches have a significant overlap since they have evaluated common buildings. After Tamura *et al*. (2000) asserted that the damping ratio even decreases after the amplitude reaches the plateau, a 'critical tip deflection' concept was developed by Tamura (2006) in order to quantify this phenomenon. This concept, based on Davenport and Hill-Carroll (1986) study, explained such decrease in damping illustrated by the amplitude at the top of the building at which damping is maximum until structural yielding occurs at much higher amplitudes. Damping ratios maximizes at relatively low tip deflections (e.g. 10^{-5} to 10^{-4} of building height) until structural yielding occurs at a much higher amplitude. The trend can be explained by reference to the next fact. The slipping contact surfaces increases as the amplitude increases, and the damping ratio also increases with amplitude. Nevertheless, Tamura (2013, p. 354), considered that *"after reaching an amplitude where all contact surfaces slip, the total friction force at the slipping contact surfaces causing friction damping does not increase any more amplitude, i.e., the total friction force remains constant with increasing amplitude"*.

These relationships can be illustrated by the amplitude dependency of dynamic properties for a 100-metres high building obtained from Tamura and Suganuma (1996). There, it has been assured that the fundamental natural frequency decreases with acceleration amplitude while the damping ratio increases in the low-amplitude region until it begins to decrease at the high-amplitude plateau. The tip drift ratio is the point where the damping starts to decrease. However, even after the tip drift ratio is reached, the natural frequency still decreases. In fact, as Tamura (2013, p. 353) remarks, *"The damping ratio can decrease even when the number of slipping contact surfaces increases, thus reducing the stiffness, if the increasing rate of amplitude is more significant than that of the number of slipping contact surfaces"*.

However, it should be mentioned that most of the previous studies took place in buildings with less than 29 stories under moderate and low wind speeds, resulting in a lack of data for

structures where higher amplitudes are produced. In addition, for higher buildings Kareem and Gurley (1996) considered that the wind excited resonant part of the structural response, which is influenced by damping, begins to dominate the background (i.e. the non-resonant part).

2.1.2. Case studies: damping evaluation in tall buildings

Few papers have presented results of full-scale measurements on tall buildings. Li *et al*. (2004) presented the amplitude-dependent characteristics of damping at the Guangdong International Building obtained by the Random Decrement Technique (RDT). In parallel with the field measurements in this 63-floor and 200m-high reinforced concrete tower, wind tunnel tests determined the spectral model of across-wind force on rectangular tall buildings characterised by different sides and aspects ratios. In that research, the wind-induced responses of the building in along-wind and across-wind directions were evaluated using the random vibration method. It was found that the measured natural frequencies were larger than those calculated with the exception of one of the directions considered for the third mode of vibration. Plausible reasons could be that the effective mass of the building is less than the designed mass and/or the effective stiffness is higher than the designed stiffness. In addition, Li *et al* (2004) found that lower values of amplitude-dependent damping in the second modes were also observed when compared with the first modes in both directions.

Bashor *et al*. (2005) studied the wind-induced response affecting the occupant comfort of various tall buildings in Chicago. Amplitude-dependence and uncertainty in damping were considered in this paper as well as comparisons to full-scale data to establish agreed criteria defining acceptable motions. It was demonstrated that many of the damping models in the literature are inappropriate because of the lack of datasets on tall buildings. A probabilistic framework using Monte-Carlo simulation assessed the reliability of the monitored buildings and found that a typical tall building can have a 30-40% probability of failure in the habitability limit state.

Fu *et al*. (2012) evaluated the dynamic characteristics and wind effects during a typhoon event on the Guangzhou West Tower, which is 432 m high. The random decrement technique was used to find the damping ratio, which exhibited amplitude-dependent behaviour. Also, the serviceability performance level was estimated for different return period. Moreover, in order to evaluate the characteristics of the measured wind pressure, the wind-induced pressure at the top of the building surface was investigated. Finally, in order to assess the accuracy of the model

test results, the wind-induced acceleration and wind pressure measured for the building were further compared with those obtained from wind tunnel test. However, the damping ratio was not evaluated in terms of the wind speed or wind direction.

Moreover, Huang *et al*. (2013) tested six aeroelastic models of tall buildings with typical cross sections in wind tunnel. The along- and across-wind aerodynamic damping ratios were identified by using the Random Decrement Technique and the Eigensystem Realization Algorithm method jointly. It was found that, in most cases, the along-wind aerodynamic damping was positive and gradually increased with an increase of reduced velocity (i.e. dimensionless parameter given by U/f_nD where U is the wind speed, f_n is the is the natural frequency of the mode of vibration and D is the characteristic linear dimension of the body). The across-wind aerodynamic damping was positive at low reduced velocity in most cases, but suddenly became negative when reduced velocity was greater than 10.5 for the square cross-section building. For a small corner-chamfered square cross section, the along-wind aerodynamic damping ratio showed some small negative and small absolute values at a low wind speed while for the across-wind aerodynamic damping ratio was always small and positive.

Furthermore, Kim *et al*. (2018) investigated the aerodynamic damping and aeroelastic instability of a 180° helical supertall building using an aeroelastic model test (rocking vibration model test). Both 180° helical and square models were considered to evaluate the aerodynamic damping ratio using the random decrement technique. It was found that the displacement responses of the 180° helical model in the along- and across-wind direction exhibited better aerodynamic behaviour than those of the square model. While the aerodynamic damping ratios in the along-wind direction of the 180° helical model showed similar trends to those of the square model, the trends in the across-wind direction of the two models were significantly different. In addition, no effect was found for the wind direction on the aerodynamic damping of the 180° helical model.

In addition, detailed analysis of damping of a high-rise building subjected to wind was presented by Gomez and Metrikine (2019). A new method based on an energy flow analysis was developed for damping identification. Damping operators based on the identified energy dissipation were used to compute the modal damping ratios in a model test before they were compared to those identified in full-scale measurements. In order to enable identification of the damping contribution in each part of the structure to the overall damping, the analysis was broken down into two different parts of the building, the superstructure and the soil-foundation

system. The identification of the source of damping is the main contribution of this paper, where there is evidence that the energy dissipated in the soil-structure interaction was significantly larger than the energy dissipated in the first floors of the superstructure from the ground level.

Finally, Li and Li (2019) presented a damping prediction model for super-tall buildings after evaluating the structural performance and dynamic properties of eight super-tall buildings. The damping ratios of the monitored skyscrapers have been estimated by the random decrement technique and plotted against a dimensionless parameter, d/H, known as "drift ratio". Despite the notable differences in building heights (384 to 600 meters) and structural systems, the damping ratios varied within a limited range from approximately 0.3 to 0.8%. This small increase in positive damping ratio with vibration amplitude has been found in other similar studies conducted on tall buildings [Li *et al*. (2002), Li *et al*. (2004), Au *et al*. (2012), Fu *et al*. (2012), Yi *et al*. (2013)]. However, the plateau of damping ratio with amplitude documented in literature, was not observed in this study. Existing prediction models have been then validated by the field measurements obtained during tropical cyclone events occurred between 1996 and 2017, and a new empirical model for super-tall buildings has been proposed.

The lack of universally accepted formulas to calculate and predict the damping of tall buildings has led to calculations being based on empirical models. Numerous studies have presented results of modal analysis and the associated wind conditions from full-scale measurements on tall buildings [Kijewski-Correa and Kareem (1999), Li *et al*. (2002), Li *et al*. (2004), Li *et al*. (2005), Kijewski-Correa and Pirnia (2007), Li *et al*. (2007), Park *et al*. (2008), Au *et al*. (2012), Fu *et al*. (2012), Shi *et al*. (2012), Yi *et al*. (2013), Krajewski *et al*. (2018), Li and Li (2018), Gomez and Metrikine (2019), Li and Li (2019)]. All of these previous studies have identified the natural frequencies of the structures and evaluated the wind velocities recorded at the building. Most of them also included an extensive analysis of the acceleration, amplitude and damping ratio estimates in relation to a series of parameters.

One of the main findings of the full-scale data analysis is the variation of the damping ratio, and its amplitude-dependent behaviour, which has been noted in most of the above papers. Detailed discussion on the particular case of the amplitude-damping relationship is described in Chapter 3, where a series of studies providing a thorough analysis and prediction models of the relationship between both variables are included. Some other researchers (Tamura, 2005; Smith and Willford, 2007; Tamura and Yoshida, 2008) have also noted a decrease of natural frequency with amplitude, although without providing any theory giving a physical reason to

describe this process. A concept-based data-driven probabilistic model was developed by Spence and Kareem (2014), addressing both phenomena at the same time, considering slip forces and friction surfaces as the sources behind them.

2.1.3. Aerodynamic damping

The dynamic response of slender structures to wind is also affected by aeroelastic influences, which may be more challenging to assess. Whereas aeroelastic effects are very important for long-span bridges, they are often neglected, or at best estimated by simplistic assumptions, for tall buildings. As buildings become taller or more slender, these effects are likely to become more important, hence there is a need to quantify them. Aeroelastic effects in tall buildings can be identified through the study of aerodynamic damping with respect to wind speed and direction. Aerodynamic damping is caused by the interaction between the oscillating structure and the air flow that induces changes in the resulting aerodynamic forces which, under certain assumptions, can be modelled as being proportional to the structure's velocity. At low speeds or under calm air conditions, the forces will result mainly from the viscosity of the air and they are considerably smaller compared with mechanical damping. In strong wind, the main aerodynamic forces are drag and lift, which are the component of the forces parallel and perpendicular to the wind flow direction respectively. Several authors have studied aerodynamic damping and its effect on tall buildings response to wind because it appears to have negative values under some circumstances, particularly across-wind. Since it is difficult to identify the aerodynamic influence on the overall damping for full-scale structures, it has been generally identified through wind tunnel tests.

Based on quasi-steady theory, Davenport (1962) proposed a few methods to calculate the aerodynamic damping of high-rise structures. Other studies (Saunders and Melbourne, 1975; Kareem, 1978) have discussed the magnitude of the reduced velocity at which aeroelastic effects have an impact on different cross-section models. Kareem (1982) found a better match of predictions with measured responses at higher reduced velocity after including the negative aerodynamic damping obtained. Steckley (1989) presented an extensive analysis of the effects of the tip amplitude, aspect ratio, cross-sectional geometry and turbulence intensity on the aerodynamic damping of tall buildings and prisms in wind tunnel tests, and Watanabe *et al*. (1995) proposed an empirical function for different geometries based on Steckley's (1989) analysis. Holmes (1996, 2001) and Gabbai and Simiu (2010) also developed different methods

to obtain the aerodynamic damping based on the quasi-steady assumption. Boggs (1992) focused on the validation of an aerodynamic model and illustrated the implications of neglecting aeroelastic feedback on a slender square building. Huang *et al*. (2013) identified variations in the aerodynamic damping of various aeroelastic models for different wind angles in order to explore the effects of small changes in wind direction. The amplitude-dependent behaviour of damping has also been demonstrated in many of the previous papers.

In most cases, the aerodynamic damping of a structure is quite small compared to the mechanical damping and it is positive in low reduced wind velocities, but at certain wind speeds negative aerodynamic damping can occur. Nevertheless, according to Kareem and Gurtley (1996), the evaluation of the aerodynamic damping has eventually become a relevant issue with the development of the aerodynamic models or those using high-frequency base balances. Since quasi-steady theory can be only applied for high reduced velocities, which are not found in typical studies of tall buildings, unsteady aerodynamics are used for aerodynamic damping evaluation. Kareem and Gurtley (1996) found that it can be identified experimentally by a free vibration test, where it was observed the change of frequency and damping of the oscillating models, or a forced vibration test.

The first research, conducted by Davenport (1967), based on wind tunnel tests for a typical tall building shape (square tower of height to width ratio of 6.5:1), found that the aerodynamic damping is positive for almost all angles of attack except for a small range of wind angles in the normal directions where negative and large damping was measured. This was attributed to the transverse motion inducing forces that reinforce the motion, alternatively to the longitudinal oscillations which induces forces opposing the motion. Saunders and Melbourne (1975), concluded that the aeroelastic effects, or aerodynamic damping could be neglected for reduced velocities below 10 after considering force spectra acting on a wide range of building cross-sections. Aiming to cross-check this data, Kareem (1978) found divergence between the predicted and the measured values for reduced velocities greater than 6 when studying the crosswind spectra derived from integration of surface pressures. It was assumed that ascribing all motion-induced effects to aerodynamic damping was too simplistic since a better comparison of the predictions with the tests at higher reduced velocities was reported in Kareem (1982) after including the negative aerodynamic damping obtained. In fact, for Kareem and Gurtley (1996), the motion of the structure also influences the flow field around leading to an increase in the pressure correlation, which can result in an increased forcing when compared

with that measured by a force balance.

Based on Saunders and Melbourne (1975), Kwok and Melbourne (1981) found that near to the critical reduced velocity and particularly at low structural damping values, displacement dependent lock-in excitation was notable leading to large increases in crosswind responses, particularly when the top displacement/ building width ratio was greater than 0.025. Therefore, it was proposed to consider a sinusoidal lock-in excitation model along with a random excitation model (Kareem and Gurtley, 1996).

Boggs (1992) focused on the validation of the aerodynamic model and illustrated the implications of neglecting aeroelastic feedback on a slender square building. Opposite to the normalized tip deflection criteria, it was evidenced that the reduced velocity and the mass damping provided a more accurate baseline while they were worth consideration at lower reduced velocities (e.g. 6). The tip deflection criteria were found to not be an accurate measure of aeroelastic magnification and the concept of the critical limit was not validated. These findings showed a good agreement with Kareem (1982).

Kareem and Gurtley (1996) observed that some studies used forced vibration tests to measure the experimental aerodynamic forces. For example, a base pivoted model was used by Steckley (1989) to evaluate the variation of motion-induced forces with amplitude for prisms of different cross-section. Using the same data, Watanabe *et al*. (1995) fitted empirical aerodynamic damping functions for operational conditions by considering real and imaginary parts of the modified complex transfer function of a SDOF oscillator. Huilan *et al*. (2012) examined the along-wind aerodynamic damping in 46 aeroelastic models where the increase in aerodynamic damping with reduced wind velocity was found. No clear effect of generalized stiffness on aerodynamic damping ratio was observed.

The response of a structure subjected to dynamic loading is strongly affected by damping, so its estimation is important too. Besides, it might be used as a measure to quantify the effect of wind-induced vibrations and the dissipation of energy of the structure. However, there are several difficulties in estimating damping ratios accurately and coherently. Mathematical damping models, used for convenience, do not and cannot describe accurately the physical process behind them. In addition, there is considerable diversity in the modal parameter estimates obtained from full-scale measurements of tall buildings in different research studies due to factors including: varying structural heights, different structural arrangements (outrigger belt wall systems, concrete core, exterior columns, shear walls), location and types of

monitoring systems (GPS, accelerometers), diverse methods used to extract modal parameters (spectral techniques, time-series methods, random decrement technique), wide range of wind conditions (from low velocities to typhoons), unequal length of records (from minutes to months).

2.1.4. Long-term variation of modal parameters on tall buildings

Limited literature has been published on the long-term variation of the natural frequencies of tall buildings in relation to environmental conditions or changes in the physical parameters of the system. Arakawa and Yamamoto (2004) evaluated the natural frequencies and damping ratios of a rectangular 120 m-high building in Tokyo, estimated from microtremor data, in a similar way as in this research considering motion in the two horizontal directions and in the torsional direction. The building, which houses laboratories, classrooms and offices, was structurally completed in October 1998 and measurements were collected as yet since January 1999. In that work, the natural frequencies of the first 4 modes in each direction decreased gradually with the passage of time with an overall change around 2.7-3.4 % in each mode over 60 months. No explicit reason of this change was provided. Similarly, Kijewski and Kareem (1999) found a similar trend on a 244 m-high building under extreme wind conditions, where a decrease of approximately 7% in the natural frequency values was observed for records from one year to the next. It was addressed that such decrease was probably due to the state of occupancy and design during the measurements. Bashor *et al*. (2012) also observed a slight decrease of the natural frequency over a 5-year period of observations of a tall building standing 60 floors. Although it was aimed to determine if this change in the natural frequencies was due to concrete cracking, a definitive conclusion on the permanent softening of the structure could not be reached. Hence, it seems that reductions in natural frequencies of tall buildings with time are common, but the equivalent pattern has not been published for damping ratios.

2.2. GALLOPING IN TRANSMISSION LINES

Galloping is a low frequency, large-amplitude aeroelastic vibration of slender structures, such as cables, subjected to crosswind motion. It is closely driven by to the lift force acting on an asymmetrical body section that commonly results in large amplitudes in a vertical plane.

Although visually this plane is the prevailing direction of vibration, twisting, lateral and longitudinal motion might be also present. Galloping describes a self-excited oscillation, which might occur indistinctly during turbulent or smooth wind. The galloping motion in cables is reflected in standing and travelling waves that tend to occur with small number of loops in a span. Amplitudes might reach larger values than the sag of the cable, particularly for those with short spans. However, such large amplitudes have been observed for low number of loops in the spans. For some body geometries, upwards velocity increases the vertical force while downwards velocity decreases the vertical force.

In the case of perfectly cylindrical section, the drag force is the dominant force, acting in the wind direction. When the section is asymmetrical, lift forces and torsional moments induce vertical and rotation on the body. The interaction between the gravitational moment due to the eccentric weight stiffness and the aerodynamic moment of the cable section affects the torsional stiffness and consequently, the torsional frequency. This interaction between vertical, torsional and horizontal vibrations often leads to vertical and torsional coupling leading to an elliptical motion when they are out of phase. Torsional motion induces large rotations with the same frequency as the vertical movement, although they are usually out of phase. The torsional motion of the structure may occur with significant amplitudes.

The combination of aerodynamic forces on the slender structure might produce an aerodynamic instability when the resultant aerodynamic damping is negative. This phenomenon occurs when the lines extract energy from the wind inducing growth of the vibration amplitude, which generally increases with the increase in wind velocity. Compared to aerodynamic instability, aeroelastic instability involves more than one degree of freedom motion and it takes place in transmission lines when the aerodynamic forces, as functions of angle of attack, interact with structural properties of the lines. Aeroelastic instability is commonly observed in this type of structure because their natural frequencies in vertical, horizontal and torsional motion tend to be close to each other for any number of loops. Vertical and torsional coupling is generally the most predominant. Given bundled conductor structures tend to behave as a coupled three-degree-of-freedom system, a slight change in the effective angle of attack leads to changes in all three aerodynamic forces.

Galloping instability has a major impact on the design of slender structures with small cross-sections, particularly transmission lines and bridge cables. Report on the Aratsu and Katsushika Bridge presented by Wardlaw (1991) found that pylons are susceptible to galloping.

This is one of the few studies that noted galloping aside from transmission lines. Interphase short circuits, conductor broken stocks, conductor strand burns, or even failure of elements and tower collapse are some observed damages caused by galloping in transmission lines, as described by CIGRE (2007) and EPRI (2009). On top of this, Havard (2003) stated that forced outages caused by galloping might have a more negative effect than direct damage to lines. In the majority of the galloping cases, ice and snow accretion has been found on the subconductor [Den Hartog (1932), Edwards and Madeyski (1956), Richardson *et al.* (1963), Nakamura (1980), Nigol and Buchan (1981), Koutselos and Tunstall (1988), Lilien and Dubois (1988), Lilien and Ponthot (1988), Rawlins and Pohlman (1988), Tunstall and Koutselos (1988), Blevins (1990), Havard (1996)].

The atmospheric conditions that favour the occurrence of ice accretion have been detailed by CIGRE (2001), CIGRE (2006) and Nygaard *et al*. (2011). In-cloud icing occurs when a structure is exposed to liquid cloud droplets at temperatures below 0°C. This phenomenon that usually occurs at high-altitude might lead to ice accretions, for which the attached mass makes the section to be asymmetrical and, in some cases can be larger than the one of the cable. Therefore, it is important to provide solutions to prevent galloping in transmission lines. Methods include avoiding formation of ice accretion, designing methods to reduce galloping behaviour or prevent attaining high amplitudes and designing structures capable of withstand galloping vibrations. The dynamic characteristics of electricity lines, mainly those prone to galloping, are strongly influenced by ambient excitations. Because of these excitations, the high-voltage electricity transmitted through the cables and the large ground clearance, it is not easy to access such infrastructures for maintenance operations.

The effects of ice or snow accretion in cable structures are ambiguous in terms of dynamic response since it differs from the addition of mass to ordinary structures. The ice or snow accretion in cables is responsible for changes in its mass distribution which reduce the natural frequencies. However, it also increases tension which leads to an increase in temperature. An investigation on ice accreted bridge cables in climatic wind tunnel test performed by Demartino *et al*. (2015) found that the aerodynamic coefficients were sensitive to the dimensions and density of the ice accretion.

Although Den Hartog (1932) criterion predicts galloping behaviour, it is limited to single-degree-of-freedom (1-DOF) oscillator normal to the wind direction. Therefore, common effects such as along-wind galloping or aerodynamic coupling between degrees of freedom are not

taken into account. Later on, several papers have dealt with formulation to describe galloping mechanisms [Richardson *et al*. (1963), Hunt and Richard (1969), Parkinson (1974), Nigol and Clarke (1974), Rawlins (1979), Nakamura (1980), Nigol and Buchan (1981), Lilien and Dubois (1988), Lilien and Ponthot (1988), Lilien *et al*. (1989), Yu *et al.* (1993), Wang and Lilien (1994), Lilien and Chabart (1995), Desai *et al.* (1996), Wang (1996), Wang and Lilien (1998), Keutgen (1999), Ohkuma *et al.* (2000), Matsumiya *et al*. (2013), He and Macdonald (2016), Matsumiya *et al*. (2018)]. Usually, aerodynamic forces are considered as quasi-steady forces after estimating steady-state aerodynamic coefficients from wind tunnel tests [Shimizu *et al*. (2004), Propplewell (2005), Matsumiya *et al*. (2011)], although this assumption has not been found valid for large-amplitude oscillations [Kimura *et al.* (1999), CIGRE (2007)]. Despite these efforts, it has been difficult to extract a reliable theory of common usage given the differences in the structural arrangements considered and the high variability of atmospheric conditions, such as the shape and distribution of the ice accretion, wind speed and direction, and the structural arrangement.

To overcome this problem, full-scale studies on electricity lines have been conducted using accelerometers and video cameras, as presented by Dyke and Laneville (2008) and Matsumiya *et al*. (2012), or accelerometers and gyro sensors [Huang *et al*. (2016)]. Moreover, several authors have aimed to establish the critical wind velocity that causes galloping [Ziller and Ruscheweyh (1997), Post-Tensioning Institute (2006)]. Unlike vortex-induced vibrations, galloping is not limited to a specific range of wind velocity. The amplitude of motion above a certain wind velocity increases indefinitely with the wind velocity.

One of the main difficulties when using quasi-steady theory has been the implementation of the rotational velocity. Hence, the aerodynamic centre parameter was first introduced by Slater (1969) and Blevins and Iwan (1974) on the basis of the three-quarter chord point in flutter instability analysis in airfoils conducted by Theodorsen (1935). Several researches have then considered an aerodynamic centre in the analysis of galloping stability [Nakamura and Mizota (1975), Blevins (1994), Robertson *et al.* (2003), Luongo *et al*. (2007), Gjelstrup and Georgakis (2011), He and Macdonald (2016), He and Macdonald (2017), Lou *et al.* (2020)].

An aerodynamic centre is a point for which the relative velocity between the wind and that point, combined with the static force coefficients, gives the force on the body in the presence of that motion. Therefore, the forces on the aerodynamic centre in the presence of translational and rotational motion are the same to the forces on the body if stationary with the

same relative velocity of the wind. However, there is not a theoretical basis to identify the position of an aerodynamic centre, because there is very little experimental data to compare the assumption of its existence with empirical evidence. Thus, different authors have considered different definitions of its position. For example, following Gjelstrup and Georgakis (2011) adoption of the leading edge of the shape, a recent definition was introduced by He and Macdonald (2017, p. 323) when they stated that "*the aerodynamic centre is basically the leading edge of the shape at 0-angle of attack and remains unchanged throughout the analysis*".

Analytical solutions for galloping stability of different models from previous studies have been determined through eigenvalue analysis. With the aim to find the solutions of a theory of galloping for 1-DOF systems with vertical and torsional motion developed by Nigol and Buchan (1981, Part II), an expression to define the variation of the real part of torsional eigenvalue in terms of the wind speed was proposed. Jones (1992) determined analytically the eigenvalues of the linearized coupled translational (along and across-wind) equations of a 2-DOF perfectly tuned system. As Chen and Wu (2021) remark, "*It is more computationally efficient to derive the governing equations using bifurcation theory and approximate perturbation technique and to seek explicit stable solutions for the periodic and quasiperiodic dynamic motion of galloping [e.g., Yu et al. (1993a and b)]*". Luongo and Piccardo (2005) presented an analytical approximated solution of stability criterion of a 2-DOF translational system employing a perturbation approach. In order to provide a deeper understanding of galloping on 2-DOF translational systems, Macdonald and Larose (2008a) conducted an analytical study of the eigenvalue problem where the vibrations of an arbitrary cylinder section were considered, leading to an explicit expression for the minimum structural damping required to prevent galloping. Later, Nikitas and Macdonald (2014) performed an eigenvalue analysis to find an analytical solution for a generalized tuned translational 2-DOF system. Similarly, He and Macdonald (2017) found excellent agreement between the approximated solution of the galloping stability of 3-DOF perfectly tuned systems and the results of the numerical eigenvalue analysis using result from wind tunnel tests. The perturbation method has been also recently used to derive an analytical galloping stability criterion for a 3-DOF system of an ice-accreted conductor [Lou *et al*. (2020), Chen and Wu (2021), Wen and Lou (2022)].

Amongst all of the previous investigations, two of them play an essential role in this research. Although several papers have dealt with formulation to describe galloping mechanisms, two existing 3-DOF quasi-steady formulations, developed to assess the galloping

stability on transmission lines have been taken as a reference for the analysis published in Chapter 4. Matsumiya *et al*. (2018) developed a formulation for each subconductor within squared four-bundled conductors (denoted as Model 1 in this research), for which steady aerodynamic coefficients were measured in static wind tunnel test. These results showed that motion in the individual subconductors from wind tunnel tests agreed well with the prediction of the dynamic response of the theoretical model. He and Macdonald (2016) presented a model of arbitrary rigid cross-section (denoted as Model 2 in this research) that directly takes into account the effect of the aerodynamic centre parameter. Therefore, regarding future application to full-scale level, Model 2 was adopted in this study because it seems a promising approach with potential transferability to different geometric bundle arrangements (e.g., one, two, three, five, six, etc. conductors within a bundle).

It is noted that the biggest concern in overhead electricity transmission lines aerodynamic performance is galloping. There are yet several studies reflecting development and progress in understanding and control of galloping, and fortunately many of them have reached an elaborate state of treatment. However, many disruptive phenomena occur beyond the reach of classical theories and, subsequently they would be unaccounted in any typical design. Not having as yet hard evidence on the quantification and prediction of such instabilities, the only true solution for engineering practice is to recur to experiments. This serves both current and future design, since an empirical basis could subsequently lead to the development of analytical tools. Observations and key results from previous full-scale tests and analytical tools have been reported, but the need for further tests has been demonstrated. OMA over long periods under different environmental conditions would be of particular value in order to address the main needs for full-scale testing in transmission lines:

- Identifying any aerodynamic or aeroelastic instabilities and the conditions causing them.
- Determining the amplitude of vibrations in relation to ice and snow accretions and wind conditions.
- Measuring the response in different conditions to reveal variations in structural modal parameters.
- Identifying cable vibration mechanisms, and measuring the response during operation.

2.3. CONCLUDING REMARKS

In general, the response of a slender structure subjected to wind-induced dynamic loading is strongly affected by its modal parameters, natural frequency and damping. Unfortunately, it has been noted by several authors that there are several difficulties in estimating damping accurately in slender structures, particularly under this type of loading conditions. Some mathematical damping models have been developed and used for convenience in literature, though they cannot accurately describe the physical process behind them. In fact, the lack of universally accepted principles to predict the damping factors in complex systems has led to the use of predominantly empirical models which cannot be generalised accurately to all types of slender structures.

Nowadays, it is paramount to mitigate the impact of wind actions in tall buildings in order to meet the performance criterion for serviceability regarding human comfort. Strong wind gusts can cause oscillation in tall buildings. However, compared to cable structures, these vibrations do not usually lead to structural safety issues because of their generally low amplitudes. However, they can interfere with building occupant's daily activities and general well-being. In summary, important questions as to which variables and mechanisms are significant have been commonly addressed in literature, while validation of theories to predict, quantify and elucidate the sources of the observed variations in the vibration characteristics is still not satisfactory.

On the other hand, wind-induced vibrations in transmission lines sometimes result in structural systems that might not meet strength and serviceability requirements. This fact illustrates that progress in analytical attack on the galloping problem and in development of countermeasures has been slower compared to the understanding of the dynamic behaviour of tall buildings. This is because the structural analysis for cable structures with long-spans (e.g., greater than 100 m), which has been typically conducted by means of wind tunnel testing, is far more complex than for tall buildings due to the geometric and material nonlinearities. Although aeroelastic effects have been often neglected or oversimplified for tall buildings, they play a major role in the design of cable structures. Moreover, the relationship between the atmospheric parameters, such as the wind conditions, temperature, humidity, the amount, distribution of ice accretion and its aerodynamic characteristics is difficult to quantify simultaneously from full-

scale measurements.

The principal issues and methods of analysis of wind-induced dynamic behaviour of slender structures have been reviewed, with a particular emphasis on the variation of structural parameters and interpreting the root causes of their variation. It can be stated that no practical prediction method has been developed that is recognized as fully reliable. For this reason, and in the absence of a clear and consistent common theoretical framework for ensuring quantification and prediction by accounting for the various uncertainties inherent in the analysis, long-term OMA monitoring is particularly valuable. Monitoring during operation allows a number of variations of the structures to be monitored, allowing changes in the response to be measured, and giving greater opportunity for different effects to be observed.

CHAPTER 3. EFFECTS OF WIND INDUCED VIBRATIONS ON TWO TALL BUILDINGS

3.1. INTRODUCTION AND THEORETICAL BACKGROUND

3.1.1. Introduction

With the objective of investigating the wind-induced vibrations on slender structures, this independent research has made use of full-scale measurements obtained by AKT II Ltd. in two tall buildings in London (UK), Tower 1 (150 m) and Tower 2 (205 m). This analysis therefore aims to assess the structural performance and the dynamic properties of the two monitored tall buildings based on the estimated modal properties of the structures under wind loading from OMA (Operational Modal Analysis). This technique is commonly adopted in design, because the dissipation of energy of a structure expressed as damping is directly related to the mechanical resonance represented by frequency. The acceleration measurements and the corresponding wind conditions are analysed to identify the most influential parameters that govern the wind-induced response of this type of systems and the reasons for variations in the structural modal parameters. A set of accelerometers and an ultrasonic anemometer were installed on Tower 1 to monitor the effects of the wind on the structure from October 2017 for a period of about a year, giving a wide range of wind conditions. The same accelerometer equipment was later installed at Tower 2, and it provided a set of measurements during a week at the end of January 2020. It should be noted that due to the significantly shorter length of the measurements on Tower 2, the analysis of the results obtained from this building clearly plays a minor role and they have been used to confirm the results from Tower 1.

Therefore, several environmental parameters are investigated, including the magnitude and the relative directions of the wind with respect to the building motion. Given the long duration of the monitoring period for Tower 1, a finite element model of the structure has been employed to support the experimental observations and provide a detailed analysis of the long-term change of natural frequency with time. The structural response of a tall building might vary notably during the construction phases, under the varying degree of occupation, loading patterns, wind conditions, and aeroelastic phenomena. Although numerous authors have covered the analysis of modal parameters and the associated wind conditions comprehensively, as detailed in Section “Literature Review”, this research goes into more detail considering additional potential aeroelastic effects. Thus, the identified trends between the estimated natural

frequencies, the measured total damping and wind speed for different relative wind directions were assessed and compared with each other and in relation to the equivalent trends in the terms of the amplitude of acceleration. This trends are based on the natural frequencies and damping ratios of the first three vibration modes because such modes presented a higher correlation in the trends with the parameters of interest than the higher modes, and they have been complemented by an investigation of the amplitude-dependent behaviour. Based only on the operational observations, an updated empirical model is proposed and compared against previous results from the literature. Some preliminary results on the two monitored buildings were presented by Margnelli *et al*. (2018), Gonzalez-Fernandez *et al*. (2019) and Gonzalez-Fernandez *et al*. (2020).

3.1.2. Theoretical background of frequency-domain system identifications methods

As detailed by Reynders (2012), the estimation of modal properties from full-scale ambient measurements is generally conducted assuming stochastic stationary processes where a flat spectrum is observed around each natural frequency. The identification of the structural properties from the processed structural responses with unknown initial or artificial excitation (i.e., output only) has been commonly referred in the literature as OMA [Peeters and De Roeck (2001), Cauberghe (2004), Reynders (2012), Brincker and Ventura (2015)]. However, random or stochastic non-stationary process require compatible system identification methods. Therefore, a significant handicap of the use of these previous system identification methods in the context of slender structures subjected to wind loading, such as in this research, is the lack of stationarity. According to Brincker and Ventura (2015), although accurate estimation of natural frequencies can be performed for short records for non-white noise spectrum, biased damping estimates are susceptible to the loading assumption. Accurate damping estimates require consideration of the average characteristics of the response of longer measurement periods.

Although there are numerous techniques available for system identification in OMA, this section describes the theoretical baseline of the two frequency domain system identification methods used in this research: the Iterative Windowed Curve-fitting Method (IWCM) and Frequency Domain Decomposition (FDD). However, it is noted that FDD was only used for intermediate steps in the system identification process and estimation of the modal parameters of the system was entirely conducted using the IWCM.

The frequency domain methods are based on estimates of the Power Spectral Density (PSD, or simply 'spectrum') of the measured responses, which are usually calculated from the measured time histories using the Fast Fourier Transform (FFT). The Peak Picking and Half Power Bandwidth Method developed by Bishop & Gladwell (1963) is the simplest frequency domain method for estimation of modal parameters. An improved method was used by Brownjohn (1988) for OMA in bridges by fitting a curve to the measured PSD around each resonant peak. The FDD introduced by Brincker *et al*. (2000), detailed in Section 3.1.2.2, provided the separated spectral response into a set of Single degree of freedom (SDOF) systems for each individual mode. According to Macdonald (2000), since the frequency domain methods based on the FFT tend to overestimate the damping ratios due to spectral bias errors, the results sensitivity depends on the frequency resolution of the PSD. Alternative to these methods, the Maximum Entropy Method detailed by Campbell & Vandiver (1982) reduced bias errors by improving the resolution of the spectral estimates and provided accurate damping estimates for very short periods.

3.1.2.1. *Iterative Windowed Curve-fitting Method (IWCM)*

This method was developed for estimating modal parameters from ambient vibration measurements by Macdonald (2000) on the Second Severn Crossing (UK) bridge, and it was successfully applied to other structures later by Macdonald and Daniell (2005) and Macdonald (2008).

Before the introduction of the new developments of the IWCM, conventional curve-fitting followed the procedure detailed below. The PSD of the output of a Single Input Single Output (SISO) system subject to random excitation, assuming a Linear Time Invariant (LTI) system, provides the relationship between the unknown inputs and the measured responses as given by Bendat & Piersol (2010):

$$S_{\mathrm{yy}}(f) = |H(f)|^2 S_{\mathrm{xx}}(f) \tag{3.1}$$

where: $S_{yy}(f)$ is the PSD of the output structural acceleration response signal at a given location
f is the frequency
$S_{xx}(f)$ is the PSD of the input structural acceleration response signal at a given location
$H(f)$ is the Frequency Response Function (FRF) of the system

For a given mode, the FRF of the system, $H(f)$, around a resonant frequency, f_n, was expressed by Maia *et al*. (1997) as:

$$H(f) = \frac{-(f/f_n)^2}{M\{1-(f/f_n)^2+2\zeta(f/f_n)i\}} \tag{3.2}$$

where: f_n is the undamped natural frequency

ζ is the damping ratio

M is the generalised mass

i is $\sqrt{-1}$

According to Macdonald (2000), the combination of these two equations gives the following expression for the PSD of the output structural acceleration response signal:

$$S_{yy}(f) = \frac{S_{xx}(f)}{M^2} \frac{(f/f_n)^4}{[\{1-(f/f_n)^2\}^2+(2\zeta f/f_n)^2]} \tag{3.3}$$

When it is assumed that around a given mode the contribution of other close modes is negligible and the value of $S_{xx}(f)$ is constant, by assuming white noise loading as an input, the previous expression for $S_{yy}(f)$ can be fitted to the measured PSD of acceleration in the desired finite frequency range. As detailed by Macdonald (2000), this process results in estimates of the natural frequency, f_n, damping ratio, ζ, and amplitude, $\sqrt{S_{xx}/M^2}$. Therefore, Macdonald (2000) developed the IWCM to provide a more accurate estimation of the parameters for multiple modes affected by bias errors at peaks from previous techniques.

Since Macdonald (2000) observed a rapid decay of magnitude of the loading spectrum with increasing frequency, a more realistic spectrum for wind loading was estimated in order to attenuate the contribution of the lower modes to the response at higher frequencies. It is given by:

$$S_{wind}(f) = R_r S_w f^{-8/3} \chi^2(f, U, \theta) \tag{3.4}$$

where: R_r is a function of the mode shape

S_w is a function of the wind parameters, but constant for a given record

$\chi^2(f, U, \theta)$ is the aerodynamic admittance, modified for wind direction, θ

Macdonald (2000) noted that the total fitted spectrum resulting from the addition of the individual SDOF fitted curves overestimated the measure spectrum, even with the loading spectrum taken into account. This fact, which was attributed to the contributions from other modes around each peak in the measured PSD, resulted in overestimation of damping.

Consequently, in order to take into account the effect of other modes and provide a more accurate estimation of the parameters of individual modes, the IWCM was developed by Macdonald (2000). While maintaining the assumption of linear superposition of modal responses, the total PSD of the response is given by Macdonald (2000) as:

$$S_{yy}(f) = \sum_i S_{yy}(f) = \sum |H_i(f)|^2 S_{x_i x_i}(\mathrm{f}) \tag{3.5}$$

where: ${}_iS_{yy}(f)$ is the contribution to the response PSD of mode *i*

$S_{xixi}(f)$ is the PSD of the generalised load of mode *i*

$H_i(f)$ is the FRF of mode *i*.

When the contributions of other modes are not significant near a peak, the above equation is reduced to the standard SDOF system adopted for curve-fitting (Equation 3.1). Since the full equation provides more accurate results, Macdonald (2000) proposed the equation for the contribution of a single mode, *r*, to the response PSD:

$$|H_r(f)|^2 S_{x_i x_r}(f) = S_{yy}(f) - \sum_{i \neq r} |H_i(f)|^2 S_{x_i x_i}(f) \tag{3.6}$$

Based on this equation, the IWCM was then adopted as summarised by Macdonald (2000) in Figure 3 below, and it has been used to conduct the system identification in this research.

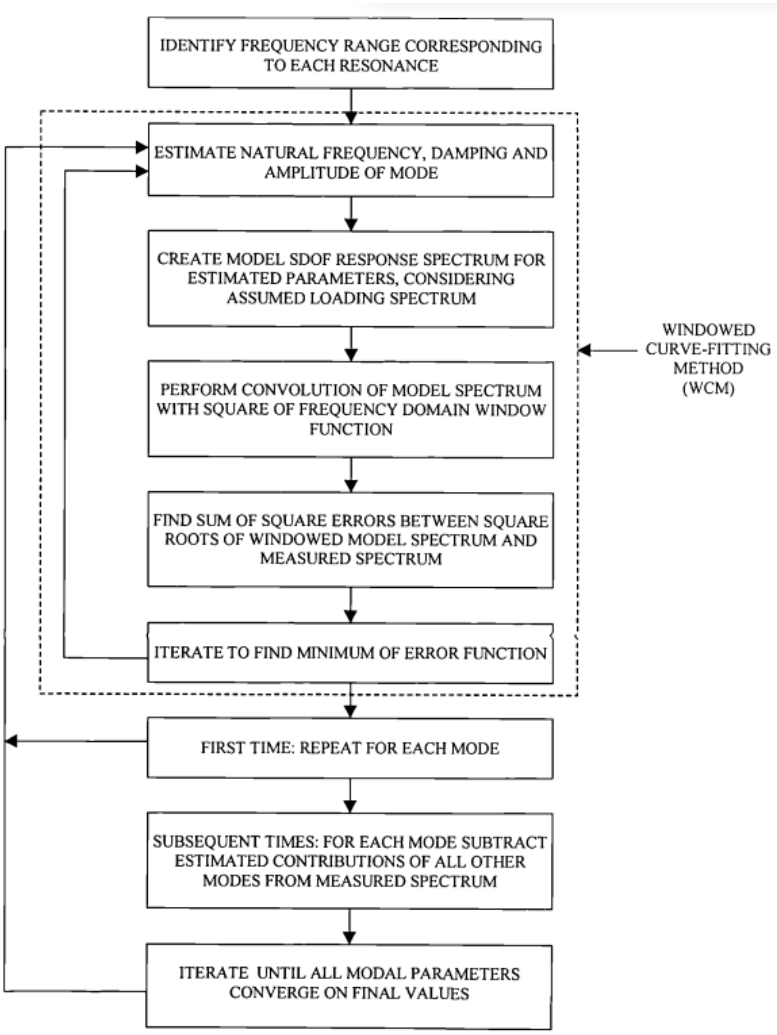

Figure 3.1. Steps of the IWCM, for calculation of modal parameters. [Macdonald (2000, p. 7-25)].

According to Macdonald (2000), the individual peaks are firstly fitted in the measured PSD to obtain initial estimates of the parameters of each mode. Then, for each mode the contributions of other modes are calculated based on the previously estimated parameters and subtracted from the measured PSD. Finally, improved estimates for each parameter are obtained by fitting a curve to the rest of the modes. These steps are iteratively carried out until the estimated parameters converges for the range of studied modes. Hence, added to the more accurate parameter estimation by removing the leakage from contiguous modes when fitting out the measured PSD, Macdonald (2000) highlighted that a main advantage of the ICWM with respect to other system identification methods, is that it enables the use of any specified loading spectrum.

3.1.2.2. *Frequency Domain Decomposition (FDD)*

FDD introduced by Brincker *et al*. (2000) is one of the most popular frequency domain system identification methods for OMA due to the high speed and ease of implementation. This method shares some common features in its baseline with the IWCM and other frequency domain techniques. Nevertheless, Brincker *et al*. (2000) highlighted that in FDD the spectral response is separated into a set of SDOF systems for each individual mode by applying a decomposition of the spectral density function matrix. Despite exact decomposition can be performed in the case of white noise assumption, close modes can be accurately identified in the presence of strong noise contamination of the signals. According to Brincker *et al*. (2000), once the PSD is estimated (Equation 3.1) in the matrix form, the PSD of the input, $S_{xx}(f)$, at discrete frequencies $f = f_i$ is decomposed by taking the Singular Value Decomposition (SVD) of the matrix:

$$S_{\mathrm{yy}}(f_i) = U_i S_i U_i^H \tag{3.7}$$

where: $U_i = [u_{i1}, u_{i2}, \dots, u_{im}]$ is a unitary matrix containing the singular vectors u_{ij}

S_i is a diagonal matrix containing the scalar singular values s_{ij}

^{H} is the complex conjugate and transpose

Founded on the theoretical basis of the method, a small number of modes are dominant at a given frequency range. Thus, assuming a dominating peak corresponding to the k^{th} mode, the PSD matrix at that frequency has a rank of one, and therefore one singular value is non-zero compared to the others (Gasparis 2019). Hence, the first singular vector u_{i1} of matrix U_{i} is related to the mode shape ϕ as provided by Brincker *et al*. (2000):

$$\phi = u_{i1} \tag{3.8}$$

In this regard, Brincker *et al*. (2000) stated that when there are two dominant modes, the first singular vector is always a good estimate of the mode shape of the strongest mode. According to Gasparis (2019), in the case of several closely spaced modes, the rank of PSD matrix is equal to the number of dominant modes in the corresponding frequency region; hence, the graphical representation is a standard approach in FDD to identify the location of resonance and obtain the natural frequency of the relative mode. Moreover, FDD offers a great advantage over other techniques that provide a batch of output PSDs, by summarizing all the modal information of the output PSDs on a smaller number of singular value functions (Gasparis, 2019).

3.1.3. Quasi-steady derivations of aerodynamic damping

There are different sources of damping in tall buildings, such as the structural material, structural joints and connections and foundations resulting in the so-called structural damping or the viscosity of the fluid resulting in the aerodynamic damping. However, it is difficult to identify its source when measuring the intrinsic damping from OMA. The hypothesis that the increase in damping with wind speed is ascribed to the aerodynamic damping was adopted in this investigation using experimental data for Tower 1. The measured damping has been assessed in this investigation in terms of the wind speed for different relative wind directions in the spirit of the across and along-wind quasi-steady aerodynamic damping analyses formulated by Kareem (1982) and Holmes (1996). The analysis has been based on the quasi-steady derivations of aerodynamic damping. Quasi-steady theory (or quasi-static theory) assumes that the aerodynamic force acting on a body is equivalent to the force on a rigid section of the body at the same angle of attack. Since the wavelengths related to the frequencies of aerodynamic loading are some orders of magnitude the width of the structure, this theory is useful for high reduced velocities. In these conditions, the approaching flow can be assumed to be locally steady. The aerodynamic damping on a section of a structure is obtained from sectional aerodynamic characteristics for the corresponding effective angle of attack in terms of a force coefficient and relative velocity.

Under various simplistic assumptions, aeroelastic forces caused by wind induced vibrations are nearly proportional to the velocity of the structure. These forces, which are considered as additional damping are referred to as ‘aerodynamic damping’. The structural

behaviour in each mode is illustrated by the total viscous damping:

$$\zeta = \zeta_{struct} + \zeta_{aero} \tag{3.9}$$

where: ζ_{struct} is the structural damping

ζ_{aero} is the aerodynamic damping

Based on quasi-steady theory, Davenport (1962) showed that the aerodynamic damping for vertical vibrations of a uniform horizontal rigid body in a wind normal to its axis is given approximately by:

$$\zeta_{aero,z} = \frac{\rho BU}{8\pi fm}\left[\frac{dC_L}{d\alpha}\right]_{\alpha=0} \tag{3.10}$$

where: ρ is the air density

B is the width of the structure

U is the wind speed

f is the frequency

m is the mass of the structure

C_L is the lift coefficient

α is the angle of attack of the wind

For horizontal vibrations (in the direction of the wind), it was also shown that the aerodynamic damping is approximately:

$$\zeta_{aero,x} = \frac{\rho BUC_D}{4\pi fm} \tag{3.11}$$

where: C_D is the drag coefficient

The aerodynamic damping for torsional vibrations is given by:

$$\zeta_{aero,\alpha} = \frac{\rho B^3 U}{16\pi fI}\left[\frac{dC_M}{d\alpha}\right]_{\alpha=0} \tag{3.12}$$

where: I is the polar second moment of mass of the structure per unit length

C_M is the moment coefficient

From quasi-steady theory equations, in any vibration mode the aerodynamic damping is proportional to the wind speed while it is inversely proportional to natural frequency. Thus, higher aerodynamic damping occurs at lower frequency modes.

Drag (C_D), lift (C_L) and moment (C_M) coefficients involved in the previous expressions of the aerodynamic damping are the three main aerodynamic coefficients. They are defined by:

$$C_D = \frac{F_D}{\frac{1}{2}\rho V^2 A}, \qquad C_L = \frac{F_L}{\frac{1}{2}\rho V^2 A}, \qquad C_M = \frac{F_M}{\frac{1}{2}\rho V^2 Ac} \tag{3.13}$$

where: V is the flow velocity

A is the area projected on a plane normal to the direction of flow

c is the distance between leading and trailing edges in the direction of flow

3.2. DESCRIPTION OF TOWERS AND MONITORING SYSTEMS

This section describes the main structural characteristics and the timeline of the monitoring and data collection program conducted by AKT II Ltd. for the two buildings monitored in this research, Tower 1 and Tower 2. A set of three Honeywell QA-700 accelerometers and an ultrasonic anemometer were installed by AKT II Ltd. on Tower 1 to monitor the effects of the wind on the structure from October 2017 for a period of about a year, giving a wide range of wind conditions.

The same accelerometer equipment was later installed by AKT II Ltd. at Tower 2, and it provided a set of measurements during a week at the end of January 2020. Wind conditions for Tower 1 have been obtained from readings of a Gill WindMaster ultrasonic anemometer installed by AKT II Ltd. at the top of the building, while Met Office (i.e., National Weather Service for the UK) data measured at Heathrow and London City airports has been considered for Tower 2.

3.2.1. Description of Tower 1 and monitoring system

This research firstly examined Tower 1, a 47-floor, 150 m-high building in London. Views of the structural arrangement of the tower are displayed in Figure 3.2. It consists of a reinforced concrete (RC) internal core with diagonal RC walls added to the perimeter of the internal core and tied into the floor slabs of each floor. Therefore, the slabs act as diaphragms that transfer wind loads into the walls. The structure is octagonal on plan, up to the 46th floor level, with triangular balconies on the four corners of the building.

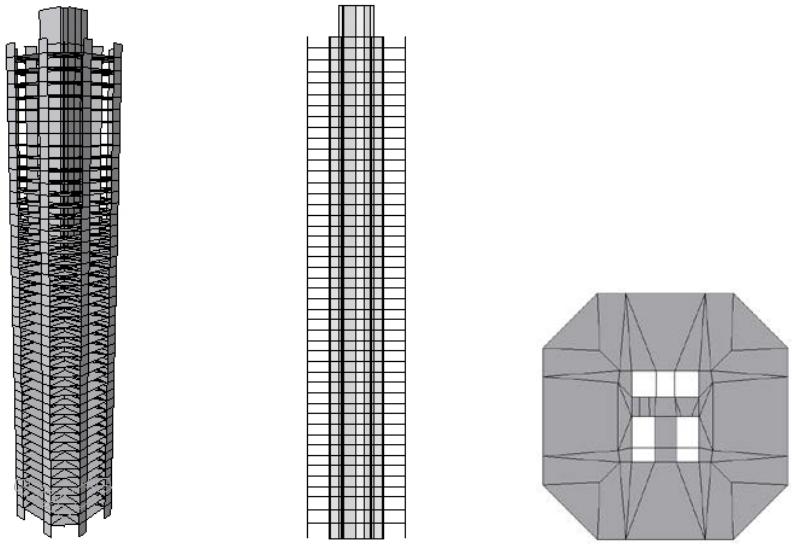

(a) Overview (b) Elevation (c) Plan

Figure 3.2. View of the structural arrangement of Tower 1.

Figure 3.3 shows views of the 45th to 47th floors with the locations of the instruments and the local co-ordinate system. The two top floors of the building are set back from the main façade, so the accelerometers were installed on the highest concrete slab level, in the external area on the 46th floor. The three accelerometers were installed on this floor by AKT II Ltd. in two orthogonal horizontal directions. Accelerometers at *A* and *B* recorded horizontal acceleration along the *x* direction, offset from each other to measure translational and rotational motion; accelerometer at *A* monitored motion also in the local *y* direction. The accelerations were acquired at a sampling rate of 61 Hz. True North coincides with the bottom right-hand side corner of the building.

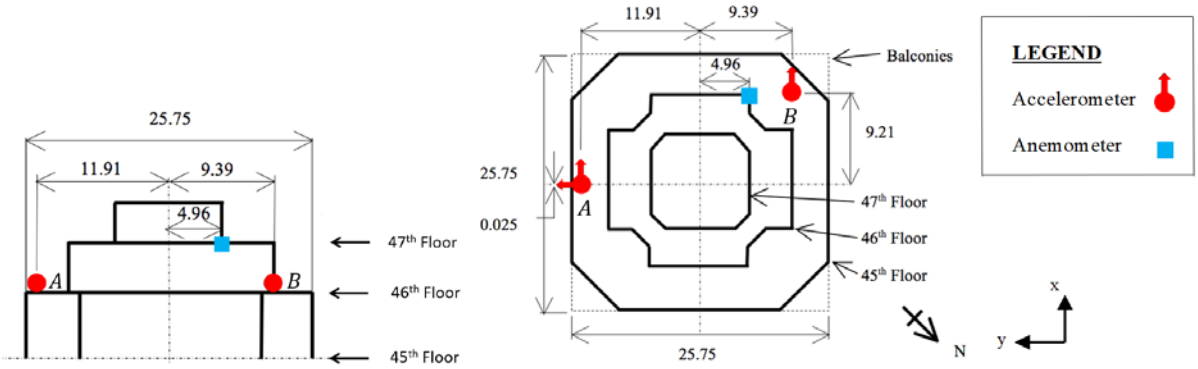

Figure 3.3. Views of the top three floors of Tower 1 showing the locations of the accelerometers and the anemometer and the local coordinate system (dimensions in m).

The wind velocity was measured at a sampling frequency of 1 Hz using a Gill WindMaster ultrasonic anemometer (blue marker in Figure 3.3), installed on a pole 3 metres above the 47th floor of the building. According to preliminary results on this building presented by Margnelli *et al*. (2018), the use of an ultrasonic anemometer allows the elimination of the vertical component of the wind that might be affected by the presence of the building and the obscuring structural elements (e.g., diagonal concrete shear walls or steel crown structure) that project above the anemometer level. The mean wind velocity and turbulence intensity used are therefore based on the components of the wind velocity in the horizontal plane. Wind directions are expressed as angles clockwise with respect to True North. Data from the accelerometer and anemometer measurements have been synchronised and saved in 1-hour long records. There are 2588 hourly records in total over the 12-month period between October 2017 and October 2018. A small number of wind records, 169, (7 % of the overall records) have also been obtained from the Met Office (2019) database periods when anemometer readings were unavailable. Although the monitoring system remained in place during the full monitoring period, data were not recorded continuously because of power shortages or constraints on the computer memory capacity according to AKT II Ltd. (personal communication, May, 2018). As it was detailed by Margnelli *et al*. (2018), the acceleration measurements were acquired through a custom built Arduino board which was connected to a PC, where data was stored on hard disk.

3.2.2. Description of Tower 2 and monitoring system

Tower 2 is a 57-floor building in London that stands 205 meters tall. The structure, which is cylindrical in shape, has a rectangular RC core with RC slabs supported by RC blade walls and columns. The same set of accelerometers used in Tower 1 were also installed by AKT II Ltd. on the top of the Tower 2, but in this case the accelerations sampling rate was 300 Hz. Figure 3.4 shows the plan of the 56th floor of Tower 2 with the location and orientation of the accelerometers. Similarly to Tower 1, two sensors at *A* and *B* monitored motion in Tower 2's local *x* direction, offset from each other to measure translational and rotational motion, and one sensor at A monitored motion in the local *y* direction. Overall 168 hourly acceleration records were measured during a week at the end of January 2020. Since there was not any anemometer installed in Tower 2 during this period of measurements, wind data used in this research has been obtained from Met Office records (Met Office, 2020) measured at the two closest airports around London (i.e., Heathrow and London City airports) to the site. Given the short length of

the measurements on this building, it has been only used for confirmation purposes. Heathrow and London City airports are located 30 km west and 4 km east of the Tower 2 respectively.

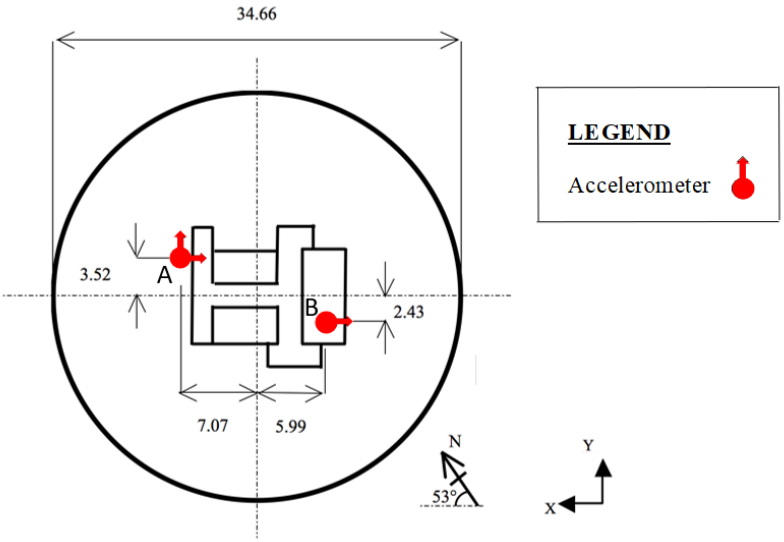

Figure 3.4. Plan of the Tower 2 showing locations of the instruments and the local co-ordinate system (dimensions in m).

3.3. CHARACTERISTICS OF THE WIND AT TOWER 1

The wind-induced response of a tall building is highly influenced by the atmospheric conditions. Therefore, this section illustrates the long-term wind conditions measured on top of Tower 1 (Figure 3.3), which provided a valuable set of data in order to assess the wind-induced response of the structure and its long-term variation. Also, this section seeks to justify the assumption of stationarity, which is investigated with a view to further spectral analysis and system identification. Moreover, since occupant comfort is directly related to wind-induced sway, monitoring of wind conditions is particularly important for residential buildings, such as Tower 1 and Tower 2. This section only presents the wind characteristics measured by the anemometer at the top of Tower 1, because there was not any anemometer installed in Tower 2 during the short period of measurements. Given the relative proximity between the two towers in London, it is assumed that the characteristics of the wind at the Tower 2 are relatively similar to those at Tower 1 during the winter season. There are 3580 hourly wind records in total over the 12-month period between October 2017 and October 2018. This number is higher than the number of hourly acceleration records (e.g., 2588; see Section 3.2.1) because there were periods when accelerometer readings were unavailable but the anemometer was still in operation.

3.3.1. Wind speed and direction

According to Stringer (1972), wind, as atmospheric motion, is defined by two main attributes: magnitude and direction, which are described in this section. The use of an ultrasonic anemometer allowed to decompose the components of the wind flow in the vertical and the two horizontal directions. Based on this components decomposition, Figure 3.5 shows a histogram of the 3580 hourly mean horizontal wind speeds measured over the 12-month period between October 2017 and October 2018. Although the monitoring period covered some moderate to severe storms (e.g., storms Ophelia and Brian on the 16th and 21st October respectively), the relative rarity of higher wind speeds is apparent, since the maximum hourly wind speed did not exceed 15 m/s. The full-scale wind velocities measured in this study are distorted by the presence of the building itself and may be different from the free stream velocity because the anemometer was located on top of the building. The value of the hourly-mean reference wind speed, V_{10r}, given by ESDU (2006) is 8.1 m/s, based on the top height of the tower (anemometer level) in urban terrain, which corresponds to the upper bound of the hourly wind speeds displayed in Figure 3.5. This phenomenon is embedded in the context of the Atmospheric Boundary Layer, which is characterised by the inhomogeneity of the wind flow for different heights above ground level, as described by the wind profile power law presented by Davenport (1965). According to the Beaufort Scale of Wind Force, WMO (1970), 3224 records (90 % of the overall records) are classified between calm (<0.5 m/s) and moderate breeze (5.5-7.9 m/s). The important results for higher wind speeds are therefore based on relatively few measurements. The maximum 1-hour average wind speed recorded, was 14.77 m/s (=33 mph), from 06:00 to 07:00 on Thursday 18/01/2018.

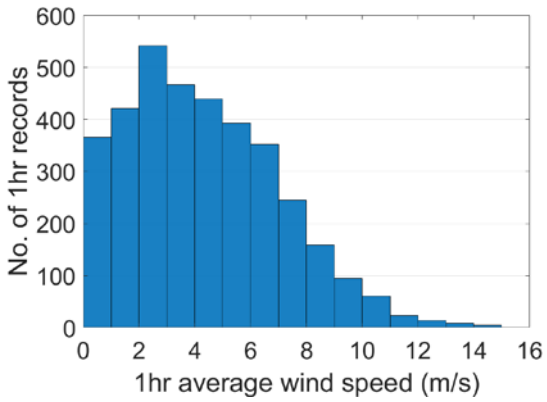

Figure 3.5. Histogram of 1-hour average wind speeds at Tower 1.

The wind speeds in terms of the wind direction for 1-hour record are shown in polar form in Figure 3.6. Wind directions are expressed as angles clockwise from normal to the building on the north side. True North coincides with the bottom right-hand side corner of the building, as displayed in Figure 3.3.

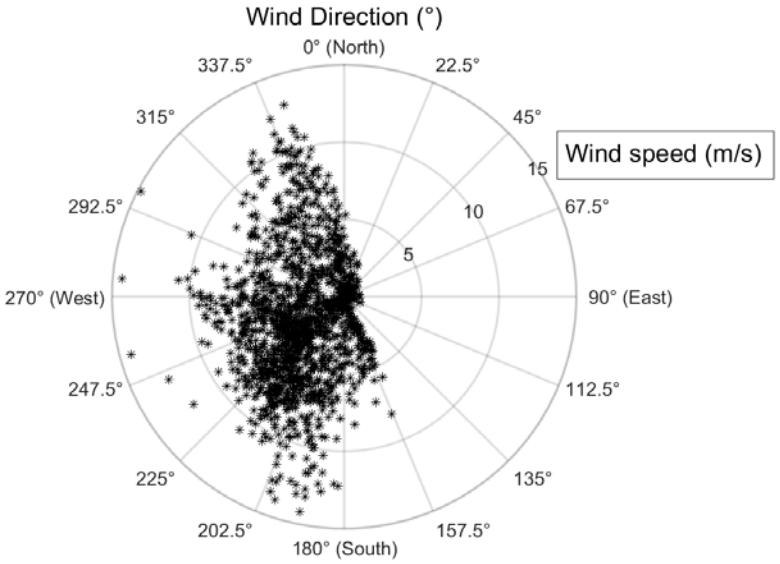

Figure 3.6. Polar plots of 1-hour average wind speeds in terms of wind direction.

The location of the building has a considerable effect on the local wind characteristics. In the east and northeast directions, within a 1-km radius, there are two other tall buildings of similar height in close proximity (90-150 m away) and dense urban areas of shorter tall buildings. The most frequent winds in southern England are typically from the south-west direction, and it is particularly notable that only a few wind instances from the east were experienced at the site during the measurements, particularly in the 0-150° wind direction range. The influence of other tall buildings in London might also increase this effect. More specifically, high 1-hour average wind speeds are concentrated in the 180-202.5° and 320-350° wind direction ranges. The measured wind velocity exhibited a large vertical angle of attack (mean 30°), presumably due to the proximity of the anemometer to the building itself.

3.3.2. Turbulence intensity

Since the response of the structure is significantly influenced by the wind loading, it is desired to gain deeper understanding on the loading characteristics. The horizontal wind speeds detailed previously represent just the measured wind speeds on one point on a vertical profile.

This is particularly relevant in urban environment, as it is the case in this study, where the interference effects of surrounding buildings are likely to affect the wind-induced acceleration of the towers. These interference effects are usually quantified by the turbulence intensity, which is defined by ESDU (1985) as the ratio of the standard deviation of the wind speed to the mean wind speed.

The relationship between the hourly longitudinal (with respect to wind direction) turbulence intensities and the wind speeds is displayed in Figure 3.7.

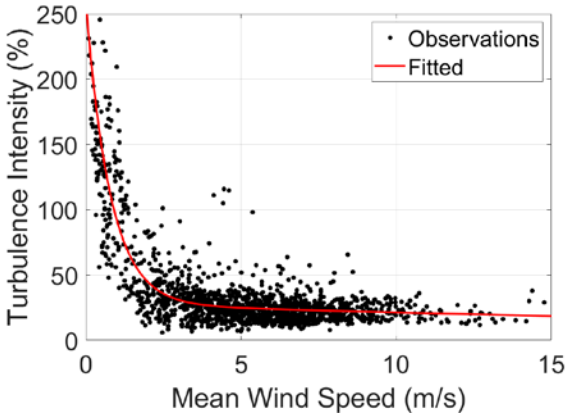

Figure 3.7. Observed (black markers) and fitted relationship (red curve) between turbulence intensities (for turbulence intensity <250%) and the corresponding 1-hour mean wind speeds in the Tower 1.

Since at low wind speeds the turbulence intensities are very large, only values below 250 % have been plotted to highlight the main trend. This relationship, which has been fitted by an exponential trendcurve, has the typical form found in literature and in the relevant IEC (2005). The longitudinal turbulence intensity from semi-empirical ESDU (1985) model derived for flat terrain with roughness change is 20 % while values between 18 and 16 % were obtained in the wind tunnel tests for the different wind directions. These results are coherent with the full-scale observations experienced in strong winds (over 8 m/s), for which the mean value was 22%.

In order to assess the interference effects of surrounding buildings, Figures 3.8 and 3.9 show the longitudinal turbulence intensities as a function of wind direction in polar form for turbulence intensities below 100 % and for wind speeds greater than 5 m/s, respectively. Although turbulence intensities of 100 % are quite high, it is still reasonable for an urban environment.

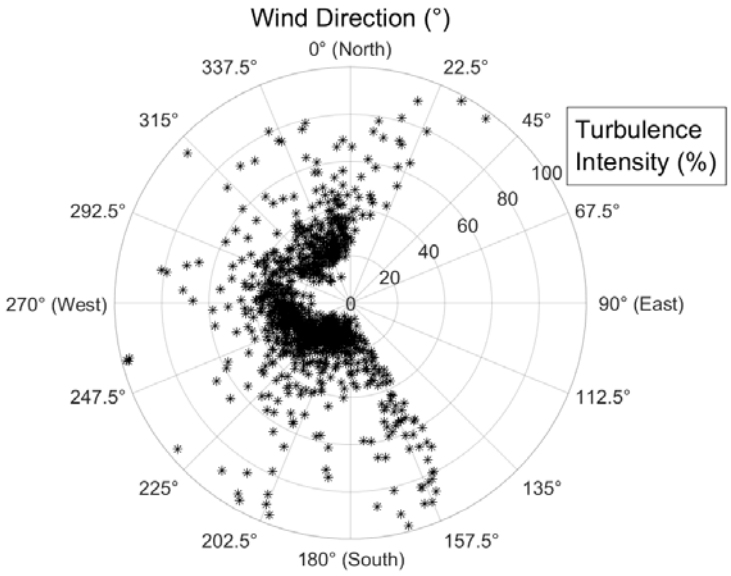

Figure 3.8. Longitudinal 1-hour average wind turbulence intensity as function of wind direction for turbulence intensity records <100%.

The turbulence intensity, which is relatively low at the sea due to its flat surface, tend to increase at inland locations as ground level increases and mountains, forests and structures affect the wind. For turbulence intensities below 100 %, there is a dependence on wind direction, as shown in Figure 3.8, and a weaker one on wind speed, as displayed in Figure 3.9. Lack of wind instances from the east were expected in Figure 3.8 because the overall wind records observed from the east in Figure 3.6 correspond to low wind speeds, which have turbulence intensities higher than 100 %.

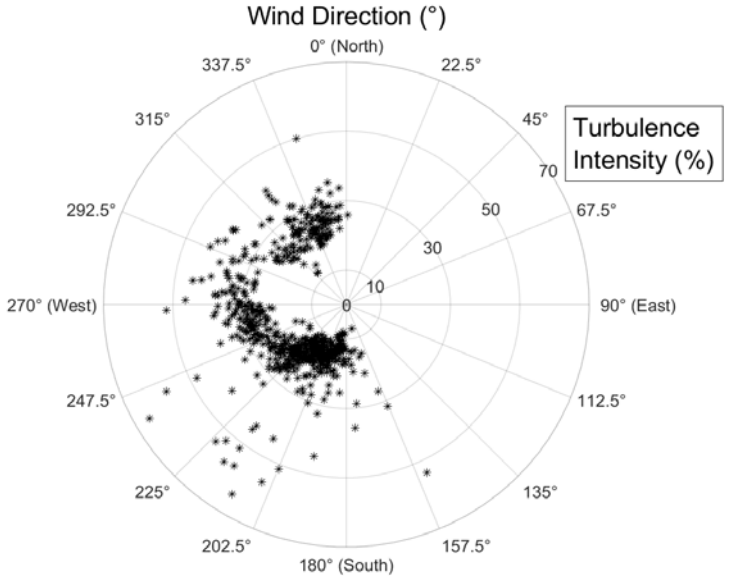

Figure 3.9. Longitudinal 1-hour average wind turbulence intensity as function of wind direction for wind speeds >5 m/s.

Turbulence intensity correlates the prevailing wind direction, either because of turbulence coming off the building itself, to do with the location of the anemometer, or it could be from the upstream fetch of the wind. Higher turbulence intensities are observed for north and south wind directions, which is assumed to be due to the proximity of other tall buildings. Alternatively, for higher wind speeds, it seems there is not a clear effect of the wind direction on the turbulence intensities. Therefore, it is expected that the parameter estimation on the Tower 1 is not biased by the measured wind direction, although it would be difficult to assess the response of the structure in the full range of wind directions due to the few wind instances measured from the east.

3.3.3. Stationarity of wind data

Given the statistical properties of the input signals in spectral analysis are assumed to be stationary, as described in Section 3.1.2, an analysis of the stationarity of the wind measured is presented in this section. Even though the wind loading measured on the top of tall structures can be classified as a stochastic non-stationary process when considered as a whole, Bendat and Piersol (2010) stated that, for analysis purposes, it is often possible to force the data to be at least piecewise stationary for periods of up to a few hours. Stationarity of the wind data was tested using the Kwiatkowski-Phillips-Schmidt-Shin (KPSS) test as described by Kwiatkowski *et al.* (1992). A significance level of 5 % was chosen to give a meaningful test. Virtually all of the wind speed records, more than 95 %, passed the test, indicating that statistically it is truly stationarity data.

Despite considering a shorter length of blocks within each hourly record, such as 10 or 20 minutes, would result in a higher fail rate, it seems reasonable to consider the wind data to be approximately stationary, as assumed by Simiu and Scanlan (1986). This qualifies the data to be further processed using standard system identification methods, such as the IWCM or the FDD method in order to conduct structural identification to extract the modal properties of the Tower 1. Given the relative proximity between the two monitored towers, it is assumed that the characteristics of the wind at the Tower 2 are similar to those at Tower 1, and consequently the adopted system identification methods are also compatible in the latter building.

3.4. SYSTEM IDENTIFICATION AND SPECTRAL ANALYSIS

3.4.1. Signal processing of Tower 1

Considering that frequency domain system identification methods for OMA require compatibility with the LTI (Linear Time-Invariant) assumption, it is important to provide comprehensive results at an acceptable level when performing system identification. According to Ruzzo *et al*. (2017) the mode shape and natural frequency estimates are not significantly affected by the record length, although too short records might lead to overestimations of the damping ratios. Hence, 1-hour long acceleration records were adopted in this research to ensure an accurate estimation of the modal parameters of the tower without being affected by the lack of stationarity. This is in accordance with the previous wind data analysis in Tower 1 based on hourly records.

Considering specifics of the sensor arrangement in Tower 1 shown in Figure 3.3, the measured accelerations were geometrically transformed to obtain the motion characteristics expressed relative to the centre of the building. This step effectively uncoupled the modal information into three nearly independent sets, each dominated by either motion in the *x*, *y* or torsional sense. After this, the positive one-sided acceleration PSDs were estimated for each 1-hour recording using the modified Welch's periodogram as detailed in (Marple, 1987). After initial exploration while aiming to capture sufficiently well the lowest frequency mode, each signal was windowed with a Hanning Window using 2^{12} samples (i.e. 67 s). The PSDs of the transformed signals of the accelerations in the *x* and *y* directions and the torsional acceleration of a typical record are shown in Figure 3.10 in the positive one-sided frequency range (0-30.5 Hz).

The mean wind speed of the selected 1-hour record was 10 m/s. Greater broadband noise can be observed for the torsional signal than for the *x* and *y* signals for this record. Above 5 Hz, all signals are smaller and the resonant peaks are less clear, although the slight increase in the signals above 20 Hz appears to be partly due to aliasing of other higher frequency components at that time. However, the source could also be localised excitation or local dynamics. Further, according to AKT II Ltd. (personal communication, May, 2018), the sources of the noise at the site were noted to be due to knocks caused by objects, doors banging, etc., which are expected to be mainly at high frequencies rather than at the low frequencies of the first few structural modes of interest.

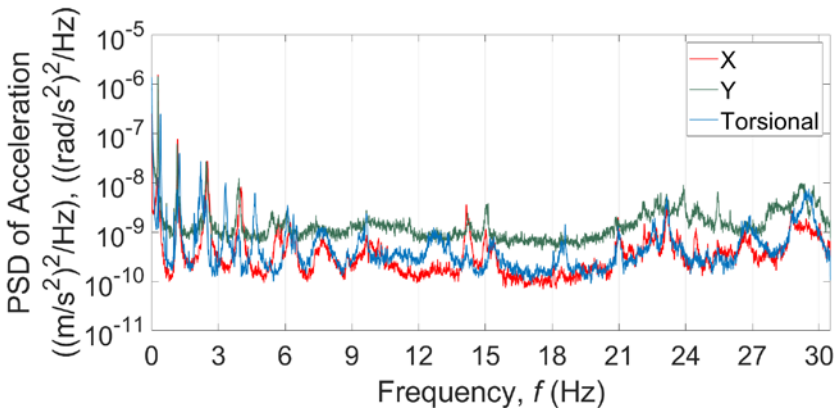

Figure 3.10. Typical PSDs of transformed *x*, *y* and torsional accelerations of a 1-hour record in the 0-30.5 Hz frequency range for Tower 1.

Figure 3.11 shows a zoom of Figure 3.10 in the frequency range 0-5 Hz, where there are clear resonant peaks at low frequencies. It shows four clear modes in each sway direction and five torsional modes below 5 Hz. The natural frequencies of the five torsional modes in this frequency range were relatively well spaced from those of the sway modes and consequently there is little evidence of coupling for the selected record. It was found that the natural frequencies in the *x* direction were slightly higher than those of the corresponding modes in the *y* direction. These slight differences were expected since, although the tower is close to being rotationally symmetric, there are small differences in the structure, mainly due to the configuration of the internal concrete cores.

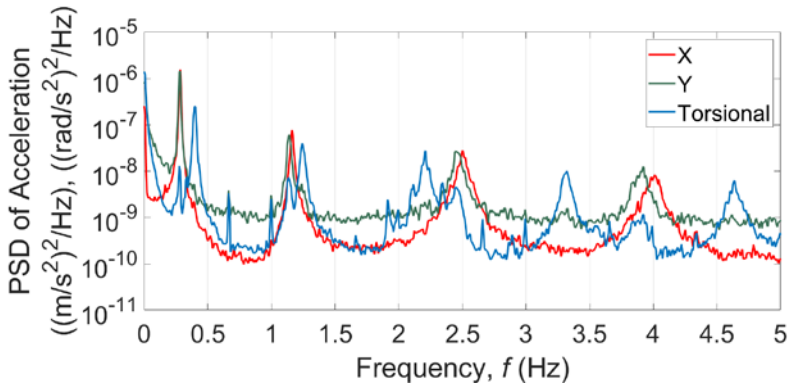

Figure 3.11. Typical PSDs of transformed *x*, *y* and torsional accelerations of a 1-hour record in the 0-5 Hz frequency range for Tower 1.

There are smaller peaks at 0.28 Hz, 1.13 Hz, 2.45 Hz and 3.92 Hz observed in the torsional PSD in Figure 3.11, corresponding to the natural frequencies of modes in the *y* direction, indicating that these modes are not purely translational and they also have a small torsional

component. Furthermore, there are additional small peaks at 0.66 Hz, 0.99 Hz, 1.9 Hz, 2.99 Hz and 4.32 Hz that does not appear to be associated with translational modes and they are probably due to harmonic loading at that frequencies, nonlinear effects or some other unaccounted phenomenon. These minor or "secondary" features are not investigated in this research.

The effect of the wind speed on the spectral response for Tower 1 is illustrated in Figure 3.12, which shows five PSDs corresponding to the measured acceleration based on a one-hour record at five different wind speeds (2, 4, 6, 8 and 10 m/s) for each motion component. In order to make different PSDs curves fully appreciable, Figure 3.12 shows the limited frequency range 0.1-3.5 Hz, where three clear translation modes and four torsional modes are visible.

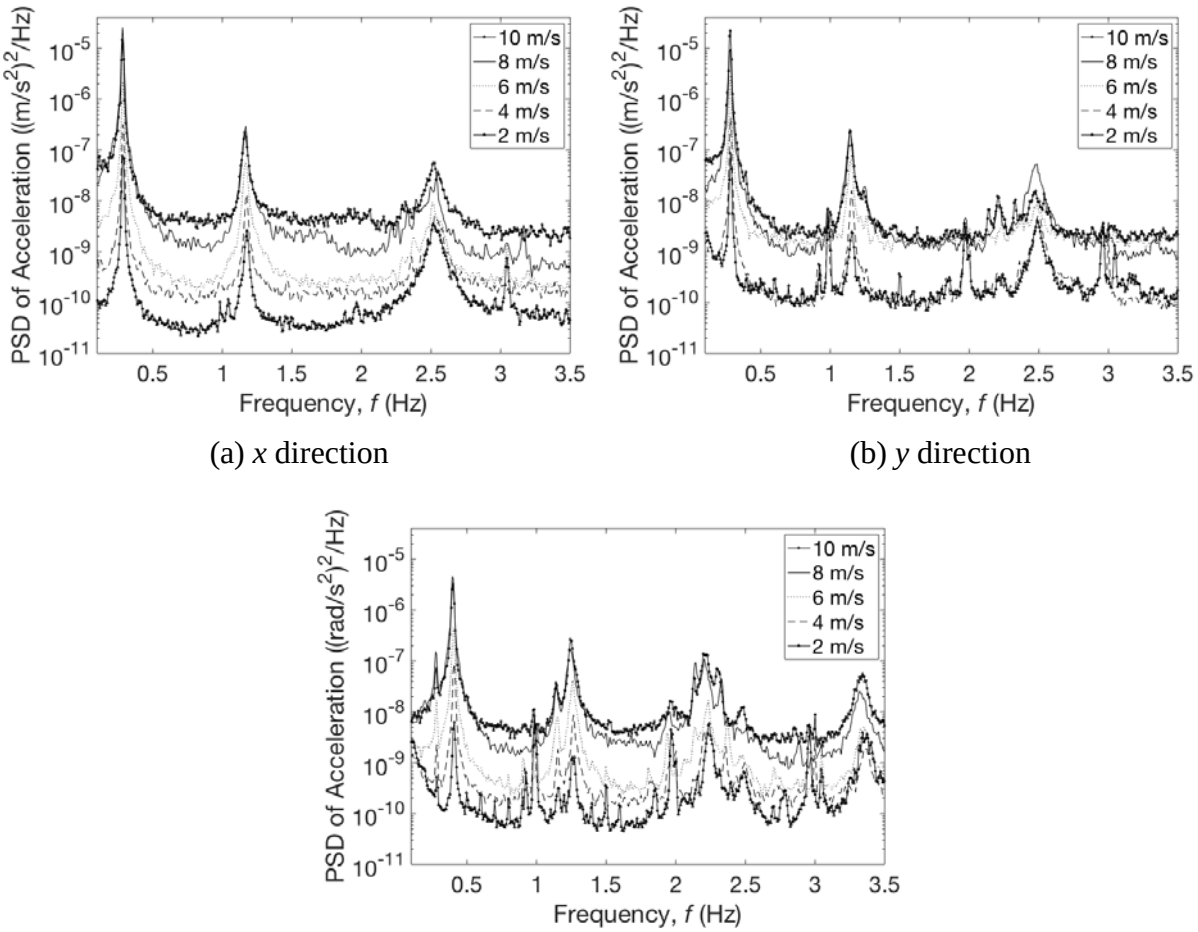

(a) *x* direction

(b) *y* direction

(c) torsional direction

Figure 3.12. PSDs of transformed acceleration in the *x*, *y* and torsional directions for selected records at different wind velocities for Tower 1.

As expected, while the resonant peaks in each PSD are aligned, the magnitudes of the acceleration PSDs increase with the increase in the mean wind velocity. It is also notable that

the peaks appear to be relatively broader for the higher wind velocity, implying possible higher total damping.

Although records measured up to 10 m/s have been considered, evidence of coupling of *x* and *y* motions cannot be found. However, it could theoretically occur due to aeroelastic coupling in stronger winds. Since the measured PSDs are inherently noisy, resonant peaks and vibration modes can be easier observed in the higher wind speed records.

3.4.2. Signal processing of Tower 2

Despite the accelerometers' arrangement in Tower 2 is analogous to Tower 1 (Section 3.2), the geometric transformation process of the motions relative to the centre of the building performed for Tower 1 did not result in a clear distinction of the structural modes of Tower 2. Thus, FDD method detailed by Brincker *et al*. (2000) (Section 3.1.2.2) was used for signal processing of the accelerometers data from Tower 2 due to difficulties in identifying closely spaced modes. The cross-spectral density matrix of the signal from each accelerometer was firstly estimated using the "*cpsd*" function in MATLAB®. Singular value decomposition of the cross-spectral density matrix was then performed in order to obtain the normalized mode shapes (i.e. relative contribution of *x*, *y* and rotational motion) of each mode, from which the generalized accelerations could be obtained in the frequency domain. Alternatively to the previously detailed geometric transformation for Tower 1, the singular value decomposition provided a solution allowing discrimination between the close modes found based on this mathematical tool. Figure 3.13 shows an example of the positive one-sided PSD of these accelerations of a typical record, where the decoupled modes can be clearly observed.

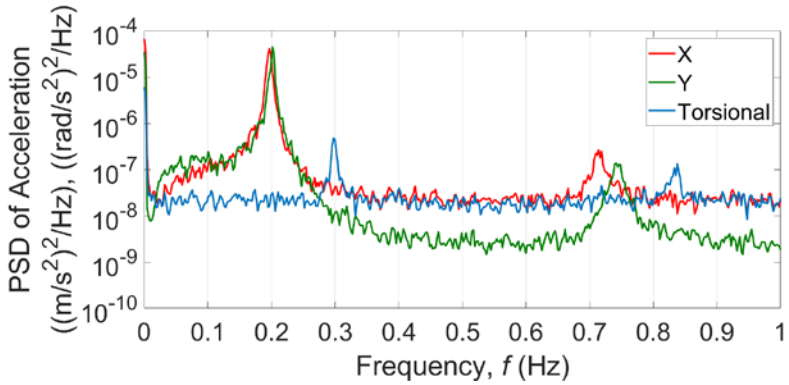

Figure 3.13. Typical PSDs of *x*, *y* and torsional generalised accelerations of a 1-hour record in the 0-1 Hz frequency range for Tower 2.

A clear dominant peak is observed close to 0.2 Hz for the generalised accelerations in the two translational directions. These seem to be the dominant components of motion since the torsional peaks are significantly smaller. Since the natural frequencies of the torsional modes below 1 Hz were relatively well separated from those of the sway modes, there is little evidence of coupling between translational and torsional motion in Tower 2. Given the natural frequencies in the *x* direction are slightly lower than in the *y* direction, similarly to Tower 1, it seems that there are slight differences in the structural properties in the orthogonal directions. To sum up, FDD was only used for intermediate steps in the signal processing of Tower 2 with the objective to prepare groundwork for the estimation of the modal parameters of the two buildings with the same technique. The mathematical identification of the closely spaced modes of Tower 2 enabled the implementation of the IWCM.

3.4.3. Application of the Iterative Windowed Curve fitting method (IWCM)

The identification of the natural frequencies and damping ratios from the estimated acceleration PSDs of the Tower 1 and Tower 2 was performed using the IWCM developed and first implemented by Macdonald (2000) within the studied frequency range for each building. As detailed by Macdonald (2000) in Section 3.1.2.1, an advantage of the IWCM over most other system identification methods is its suitability in the context of wind-excited OMA due to the consideration of a more appropriate loading spectrum while taking into account the contribution from adjacent modes in the curve-fitting process. Successful application of the IWCM to other structures by Macdonald and Daniell (2005) and Macdonald (2008), motivated the use of the IWCM in this research to provide a more accurate estimation of the parameters of individual modes.

Prior to the identification process, an 8^{th} order digital Butterworth high pass and a low pass filter with cut-off frequency 0.1 and 5 Hz respectively have been applied by implementing the "*butter*" function in MATLAB® to eliminate the very low frequency drift components of the signals. An example of the measured and fitted PSDs in the frequency range 0.1-4.5 Hz for the acceleration responses in the *x* direction of the Tower 1 is shown in Figure 3.14. However, the effect of aliasing, which originates when the signal is first digitised cannot be removed by applying this filtering method. The identification process provided the natural frequency and damping ratio estimates for each mode within the studied frequency range. The identified

differences in the natural frequencies in the *x* and *y* directions in this case ranged from 0.96% for the first mode pair to 2.47% for the fourth mode pair.

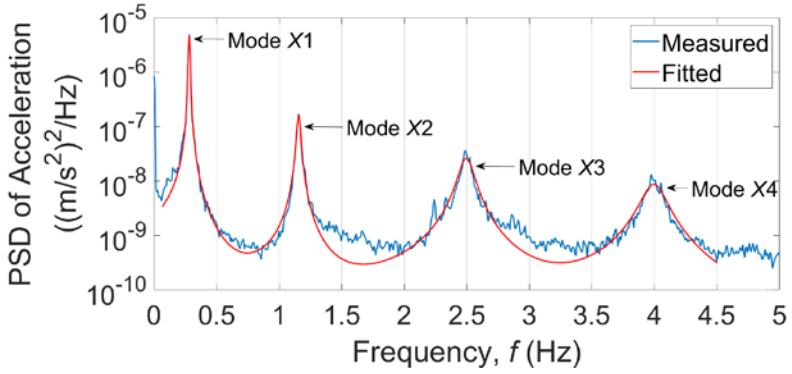

Figure 3.14. Typical measured and fitted PSD in the *x* direction for Tower 1.

The four modes of Tower 1 identified in the *x* direction are labelled as Mode *X1*, *X2*, *X3* and *X4*. PSDs for the other components of motion were treated similarly. In addition, the Root Mean Square (RMS) acceleration amplitude was obtained from the PSDs by integrating them over the frequency range of interest of the relevant resonant peak or consecutive peaks, as detailed by Bendat and Piersol (2010).

From the generalized accelerations measured at Tower 2 (Figure 3.12), there were difficulties in fitting accurately the PSDs for the torsional acceleration responses and the higher modes in the three components of motion using the IWCM because of the poorly defined peaks. However, Figure 3.15 shows that the measured PSDs of the acceleration responses in the *x* and *y* direction have been fitted precisely around the first dominant peak in the frequency range 0.1-0.3 Hz.

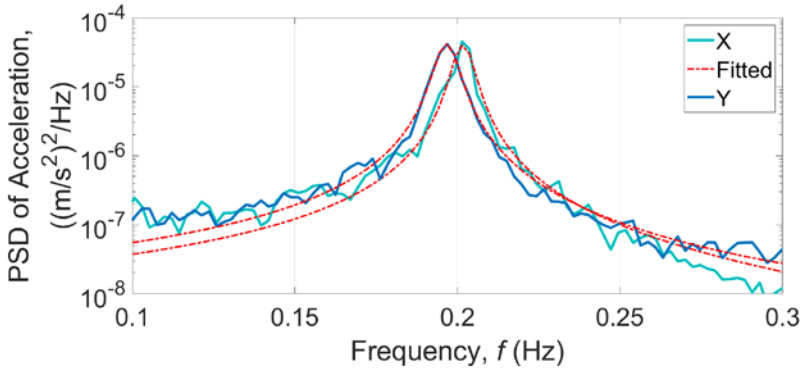

Figure 3.15. Typical measured and fitted PSD of the generalized accelerations in the *x* and *y* direction for Tower 2.

As is usual for full-scale ambient vibration data, the natural frequencies of the two structures were identified consistently between different records, with Coefficients of Variation of 0.2% or lower, for comparable wind conditions, but the damping ratios were much more variable due to the fundamental difficulty in estimating them accurately from individual records. The coefficient of variation between different damping ratios was up to 144%. However, using the large number of records available, underlying trends could be found. Therefore, the IWCM seems an appropriate technique to conduct an accurate estimation of the modal parameters of the two monitored buildings.

3.5. MODAL PARAMETERS

3.5.1. Introduction

With the aim of assessing the structural performance and the dynamic properties of the two tall buildings studied in this research, trends in the modal parameters, natural frequencies and damping ratios have been identified from vibrations measured on top of the structures in a range of wind conditions to provide an overview of the typical values in operation. Given the significantly shorter length of the measurements on Tower 2, the analysis of the results obtained from this building clearly plays a minor role and it has been used to confirm the results from Tower 1, which is the main subject of study in this section.

In order to quantify the effect of wind on the structures, the accelerometer and anemometer data were correlated in time and compared against each other. For each 1-hour record, the mean wind velocity is calculated, and the modal parameters are estimated as explained in Section 3.4. Regarding the symmetry of the two structures shown in Section 3.2, vibration modes are labelled as *Xi*, *Yi* and *Ti*, where the first letter corresponds to the dominant modal motion (i.e., *X*: translational along *x*, *Y*: translational along *y*, *T*: torsional around *z*), and *i* denotes the mode number. Although four modes for each direction were identified for Tower 1, results herein are presented only for the first vibration mode in each direction (i.e., *X1*, *Y1* and *T1*). This selection was made because such modes presented a higher correlation in the trends with the parameters of interest than the higher modes. Only the fundamental torsional modes *X1* and *Y1* were considered for Tower 2 due to the difficulties in fitting accurately the PSDs for the torsional acceleration and the higher modes in the three components of motion, as detailed in Section 3.4.

The two types of modal parameters adopted in this analysis, natural frequencies and damping ratios, were investigated with respect to a series of parameters using the methods of statistical regression with the objective to identify the most influential parameters in the wind-induced response of the system. The considered parameters included observation date (only for Tower 1), vibration amplitude, wind speed and wind direction. Despite temperature was also assessed, it did not show to be a relevant variable and it is not included in this chapter. Trends in the natural frequencies and damping ratios with the wind speed and acceleration amplitudes have been identified. The statistical regression was performed using the Curve Fitting Toolbox in MATLAB® and the coefficient of determination, R^2, as given in Wright (1921), was computed for each regression instance to assess its quality and to identify a potential cause-effect relationship between two variables in comparison with similar relationships. Considering results of the initial investigation, following analysis focuses on the effect of the wind speed, wind direction and acceleration amplitudes.

3.5.2. Natural Frequencies

The estimated natural frequencies of the two tall buildings are investigated in this section in relation to the wind speed, acceleration amplitude and time (only for Tower 1). Different measures of the amplitude (e.g., first mode RMS amplitude, overall RMS amplitude) were assessed for Tower 1; the RMS acceleration amplitude over the 0.1–4.5 Hz frequency range is identified as the most efficient parameter. Hence, the contribution of higher modes in the dynamic behaviour of the structure is taken into account. The first measurements on Tower 1 were taken in October 2017, when the building was structurally completed but construction works were still ongoing. The building started to be occupied at the end of 2017, and the first half of the floors were occupied by March 2018. Regression models are used to highlight the key trends in noisy data which, despite continuous monitoring, contain gaps between the recorded regions due to occasional power shortages and data storage errors. In the case of Tower 2, the RMS acceleration amplitude around the first dominant peak over the 0.1–0.3 Hz frequency range was considered.

3.5.2.1 *Analysis of natural frequencies for Tower 1*

The relationships between the estimated natural frequencies of this building, the RMS acceleration amplitude and the observation time corresponding to Mode *X1*, *Y1* and *T1* are

displayed in Figure 3.16.

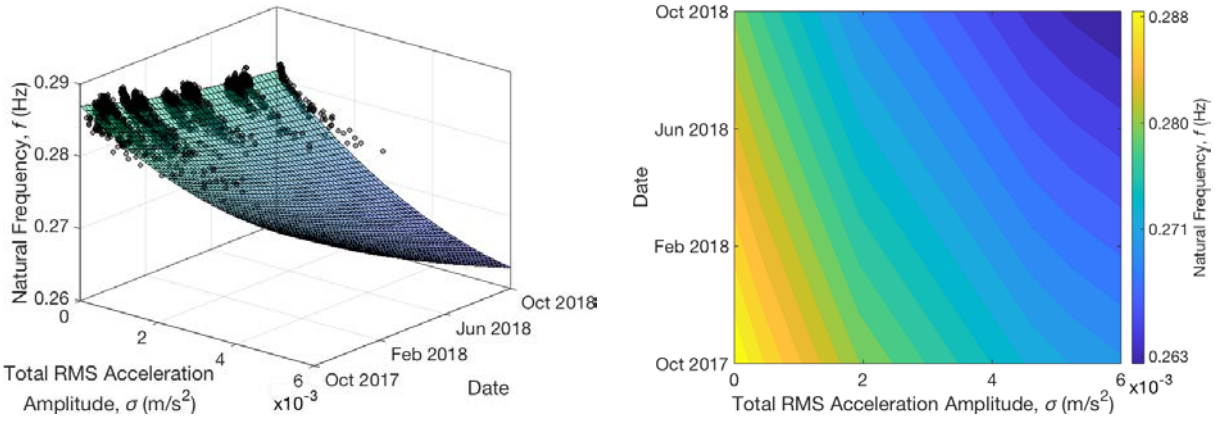

(a) Mode *X1* (R^2 = 0.862)

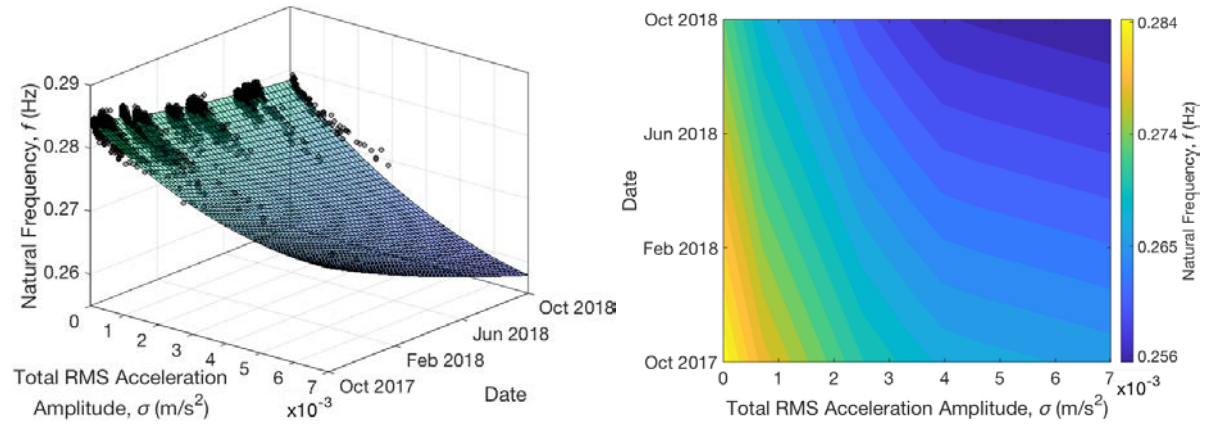

(b) Mode *Y1* (R^2 = 0.888)

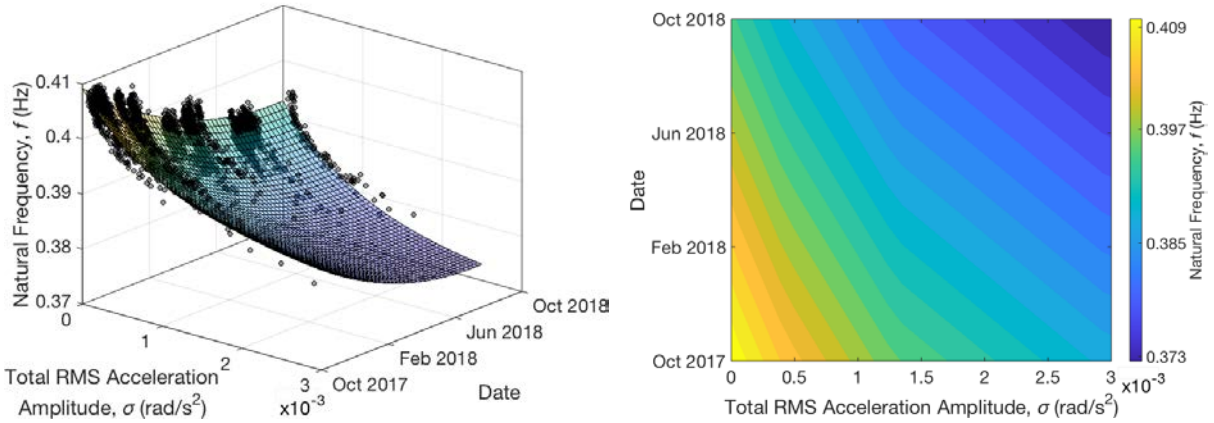

(c) Mode *T1* (R^2 = 0.917)

Figure 3.16. Observed (black markers) and fitted (surface) relationships between the natural frequencies, acceleration amplitudes and time, Mode *X1*, *Y1* and *T1*. Contour diagrams are displayed in the right-hand side of this figure.

It shows a gradual decrease of the natural frequency values with more recent observation dates and for increasing RMS acceleration amplitudes. The type of the fitting surface was selected after preliminary parameter assessment. Changes of the natural frequencies follow a decreasing trend with asymptotic tendency. The RMS amplitude effect is directly linked to the wind loading while the decrease of the natural frequency with the observation time is thought to be associated with the changing structural state. To elucidate the time-independent response characteristics further, this section compares the representation quality of the two regression models. Then, time-dependent behaviour and its causes are closely analysed in the next subsection 3.5.2.2.

Although the full-scale measurements were limited to 12 months, it is thought that the decrease in the rate of occupancy change and the consequent decreasing rate of the mass increments during the last months of the monitoring period, would ultimately result in stabilized frequency values after the monitoring ended, once the building was fully occupied. Therefore, an exponential asymptotic decay function with the time variable was chosen to fit the data. As a result of the previous considerations, especially their observed asymptotic character arising from two separate and distinct sources, the first regression model applies an equivalent functional forms to the date of measurement (in days from the first day of the measurement campaign) and the RMS acceleration amplitude in the following form:

$$f = f_0\left(1 - \alpha_t e^{-\beta_t t} - \alpha_\sigma e^{-\beta_\sigma \sigma}\right) \tag{3.14}$$

where: f is the natural frequency (in Hz),

f_0 is the estimated initial value of natural frequency at the start of the recording period (in Hz)

α_t and β_t are the constant parameters governing the eventual reduction in the natural frequency with time

t is the date of the measurements expressed here as number of days since the first measurement f_0 was taken

α_σ and β_σ are the constant parameters governing the eventual reduction in the natural frequency with amplitude

σ is the RMS acceleration amplitude (in m/s^2 or rad/s^2)

The values of the parameters of the fitted function (Equation 3.14) are displayed in Table 3.1 for each mode.

Table 3.1. Values of the fitted function parameters for the relationship between the natural frequencies, acceleration amplitudes and time.

	f_0 (Hz)	α_t	β_t	α_σ	β_σ
Mode *X1*	0.287	-0.008	1178	-1.207	0.009
Mode *Y1*	0.285	-0.009	928.5	-0.456	0.010
Mode *T1*	0.410	-0.025	381.5	-1.588	0.022

Noting the direct relationship between the wind loading and resulting structural responses, the second regression model uses a wind characteristic (1-hour mean wind speed) instead of the RMS acceleration along with an alternative functional form which is more appropriate in such case.

The relationship between the estimated natural frequencies of the building, the corresponding 1-hour mean wind speed and the observation date is presented in Figure 3.17. Similar to the previous relationship (Equation 3.14), a marked decrease in the identified natural frequencies as the wind speed increases can be observed for the different considered modes.

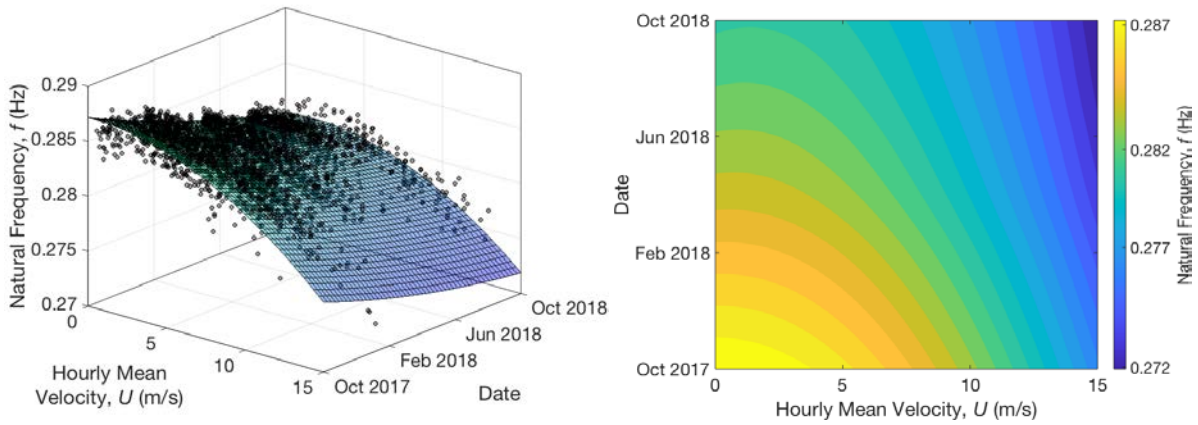

(a) Mode *X1* (R^2 = 0.759)

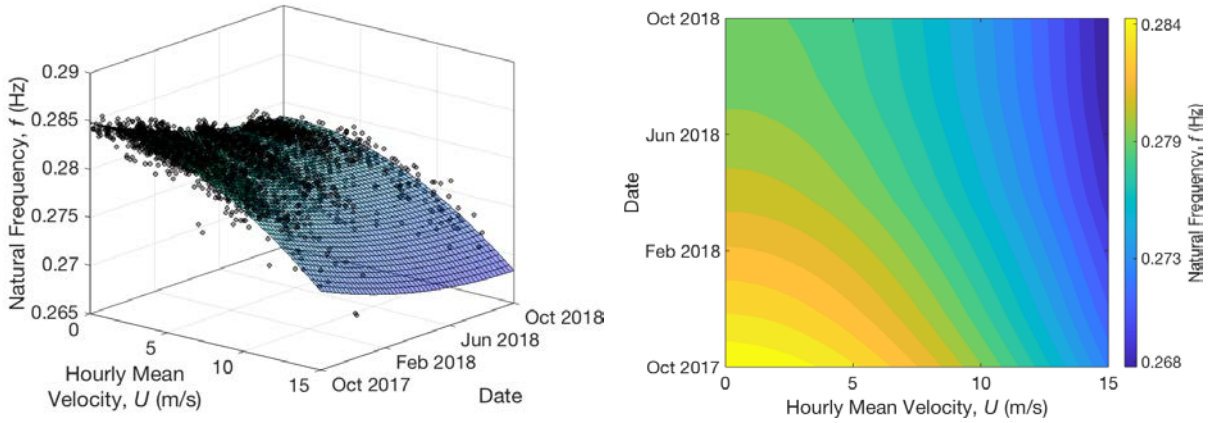

(b) Mode *Y1* (R^2 = 0.771)

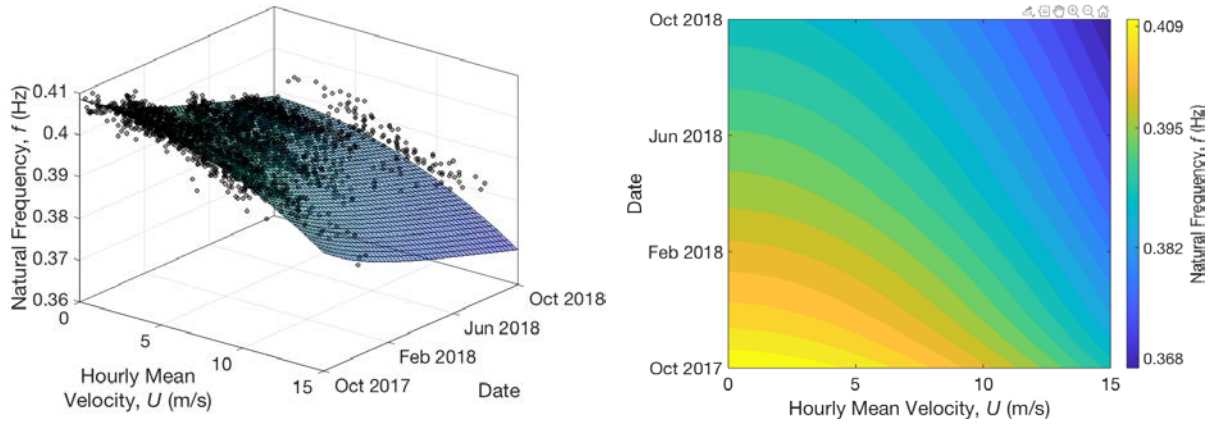

(c) Mode *T1* (R^2 = 0.864)

Figure 3.17. Observed (black markers) and fitted (surface) relationship between the natural frequencies, mean wind speed and time, Mode *X1*, *Y1* and *T1*. Contour diagrams are displayed in the right-hand side of this figure.

The relationship between the natural frequencies and the corresponding date of measurements and wind speed has been fitted by:

$$f = f_0\left(1 - \alpha_t e^{-\beta_t t} - \delta_U U^2\right) \tag{3.15}$$

where: f is the natural frequency (in Hz)

f_0 is the estimated initial value of natural frequency at the start of the recording period (in Hz)

α_t and β_t are the constant parameters governing the eventual reduction in the natural frequency with time

t is the date of the measurements expressed here as number of days since the first measurement f_0 was taken

δ_U is the constant parameters governing the eventual reduction in the natural frequency

with wind velocity

U is the hourly mean wind speed (in m/s)

It should be noted that the reduction in the natural frequency with wind velocity has been found to be best fitted by a square power in this case. The parameters values of the fitted function (Equation 3.15) are displayed in Table 3.2 for each mode.

Table 3.2. Values of the fitted function parameters for the relationship between the natural frequencies, 1-hour mean wind velocity and time.

	f_0 (Hz)	α_t	β_t	δ_U
Mode *X1*	0.287	-0.001	0.002	0.006
Mode *Y1*	0.285	-0.003	0.001	0.006
Mode *T1*	0.410	-0.093	0.002	0.018

It can be seen that model 1 is associated with higher R^2 values than to model 2. This demonstrates that the variation in the natural frequencies can be better explained by a change in the amplitude than by a change in wind speed. Assuming that both fitting functions are equally suitable for this problem, this implies that the natural frequency changes are particularly well represented when a deformation measure, the RMS acceleration amplitude in this case, is adopted. This conclusion indicates that the natural frequency variations are caused by the structural effect (e.g., softening under the large amplitude slip conditions at the structural interfaces) rather than an aerodynamic one. However, as it will be observed in Section 3.5.3.2, these two parameters are closely related to each other since higher wind speeds lead to higher amplitudes.

3.5.2.2 *Analysis of temporal changes in natural frequencies for Tower 1*

This section focuses on the temporal aspects of the identified natural frequencies and aims to clarify the origins of the observed changes. The natural frequencies for Mode *X1*, *Y1* and *T1*, after removing the amplitude-dependency, are plotted against the corresponding measurement date. Figure 3.18 shows the projected data onto the 2-dimensional date-frequency plane. The rate of the frequency decrease reduces with time. Since the natural frequency of oscillation in a mass-spring system is dependent on the stiffness and the mass of the structure, it is assumed

that the variation of these two variables might explain the decay in the frequencies with time. The possible phenomena in this case that might cause a reduction in the natural frequencies are the increase in the mass on the structure, softening due to concrete cracking and reduction of the foundation stiffness.

Since the structure was completed shortly before monitoring started, it is unlikely that softening due to cracking could have occurred in the early stages of the tower's lifetime, as it was noted by Bashor *et al*. (2012). Although the foundation stiffness reduction might affect the frequency response, there is insufficient data to quantify its conditions. Thus, this study focuses on the structure mass change. The mass levels can be further correlated with the changing rate of occupancy during the later months of monitoring. To enhance the detail of the analysis owing to its newly built character and despite its opposite influence on the natural frequencies, the concrete curing is also modelled using the standardised evolution of the concrete elastic modulus with time.

An asymptotic time-dependent regression model, akin to the model shown in equation 3.14, was used here. To assess the mode sensitivity, based on Figure 3.18, the relative frequency drops from the initial modelled values for *X1*, *Y1* and *T1* were obtained by comparing these values to the estimated frequency values at the end measurement time (denoted "Measurement end") and the predicted steady asymptotic values (denoted "Steady state asymptote"). The start and end date of the measurements correspond to the first day of measurements in October 2017 and the last day of measurements in October 2018, respectively. The frequency drops are summarised in Table 3.3, expressed relative to the corresponding initial values.

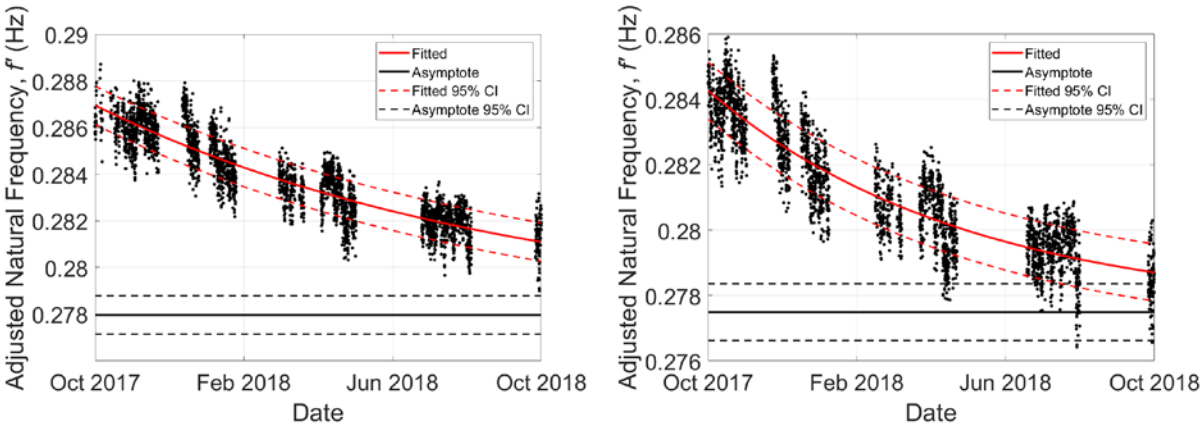

(a) Mode *X1* (R^2 = 0.779) (b) Mode *Y1* (R^2 = 0.766)

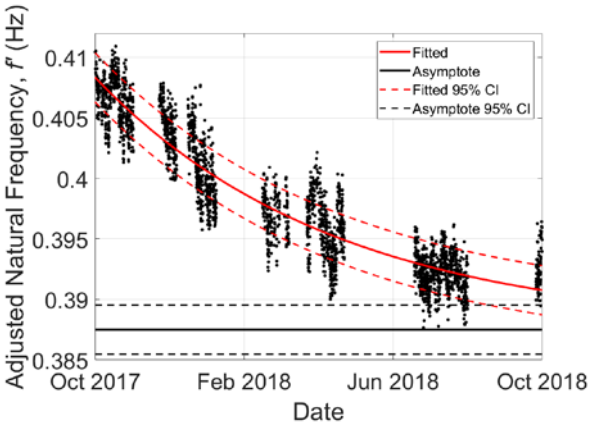

(c) Mode *T1* (R^2 = 0.869)

Figure 3.18. Variation of the observed (black markers) and fitted (red curves) adjusted natural frequencies (+95 % *CI*, -95 % *CI*) with the passage of time during the full monitoring period, Modes *X1*, *Y1* and *T1*. Steady state asymptotes (+95 % *CI*, -95 % *CI*) are also included (black lines).

The "Measurement end" frequency change expressed in percentage has been calculated from:

$$Measurement\ \ end = \frac{|f_0 - f_f|}{f_0} \times 100 \tag{3.16}$$

where: f_0 is the adjusted frequency value at the start date of the measurements

f_f is the adjusted frequency value at the end date of the measurements

while the "Steady state asymptote" frequency change has been estimated from the exponential asymptotic fitting by:

$$Steady\ \ state\ \ asymptote = \frac{|f_0 - f_a|}{f_0} \times 100 \tag{3.17}$$

where: f_0 is the adjusted frequency value at the start date of the measurements

f_a is the asymptote frequency value

Table 3.3. Percentage change (+95 % *CI*, -95 % *CI*) of the natural frequencies and the regression asymptotes with respect to the frequency values at the start date of the measurements.

	Mode *X1*	Mode *Y1*	Mode *T1*
Measurement end	2.04 % (1.39, 2.70) %	1.96 % (1.26, 2.66) %	4.31 % (3.11, 5.50) %
Steady state asymptote	3.13 % (2.76, 3.50) %	2.39 % (1.99, 2.78) %	5.10 % (4.40, 5.80) %

These quantities show a similar trend for both translational modes (*X* and *Y* modes). The notably larger values for the torsional modes (*T* modes), compared to those for the translational

modes, could arise from the additional mass being typically added close towards the outer edges of the building during the period of increasing building occupancy. Consequently, the change in the corresponding mass moment of inertia is more significant than the change in the mass, affecting thus the *X* and *Y* modes to the lesser extent.

A simple linear finite element (FE) model developed in *Midas Gen*® (MidasIT Co.) was used as a tool to support the analysis of the observations indicated above. This is a basic model-driven supporting analysis with the purpose of supplementing the observed experimental data. Based on Eurocode 2 a C30/37 strength concrete class has been adopted for the four main elements of the structure: the internal core, the shear walls, the floor slabs and the external walls. The floor diaphragms are considered to be rigid in their plane with the mass. The base of the structure is assumed infinitely rigid, and modelling of the deep foundation was not considered. Figure 3.19 displays the *X1*, *Y1*, and *T1* mode shapes for the nominal conditions at the start of the measurements, where only dead load was applied.

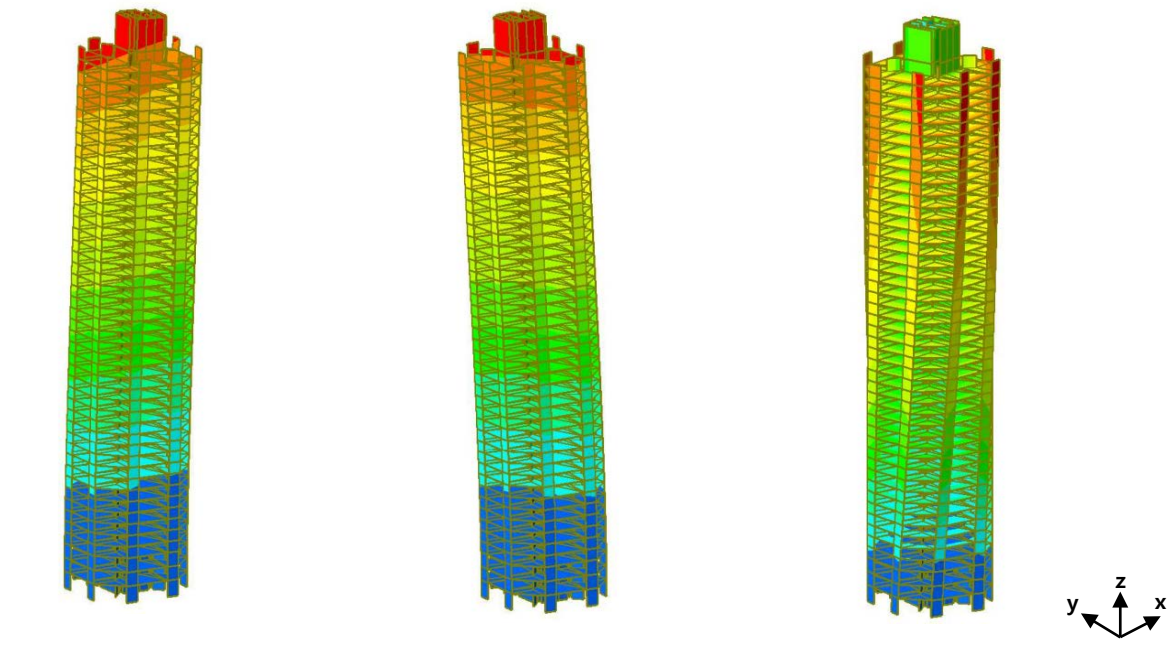

Mode *X1* (0.287 Hz) Mode *Y1* (0.292 Hz) Mode *T1* (0.454 Hz)

Figure 3.19. Estimated mode shape diagrams and natural frequencies for the first mode of each type from the finite element model at the start of the measurements.

Despite the simplicity of the model, they are only 0.2%, 2.4% and 10.2% higher than the estimated initial values of the natural frequency f_0 shown in Table 3.1 and obtained from the full-scale measurements of Mode *X1*, *Y1* and *T1*, respectively. The model has been able to capture the slight differences between the two translational modes identified from the full-scale

results due to the asymmetric structure in the orthogonal directions. Even though there are differences between the actual tower and its simplified model, this agreement in the modal behaviour is considered a satisfactory reliability test for the finite element model.

After the dead load was applied in the Finite Element Method (FEM) model, both occupancy rate and elastic modulus were modelled as time-dependent parameters. Both parameters were varied simultaneously to simulate the evolution of the natural frequencies of the structure at different stages. The occupancy rate was modelled by introducing additional mass and moment of inertia about the central axis for each floor. For this study, the contributing factors to the mass and inertia of each floor consisted of a self-weight and occupation component. The latter component was derived from Eurocode 1, where the value of the imposed characteristic uniformly distributed load (q_k) on floors in areas for domestic and residential activities in the UK is between 1.5 to 2.0 kN/m^2. Since most of the flats are under the rental status, it is assumed that the occupancy load is likely to be close to the lower limit of the imposed load. Assuming normal distribution and coefficient of variation of 0.35, the mean distributed mass loading on the floor diaphragm is 0.95 kN/m^2. The coefficient of variation has been selected to be within the upper range of the typical values used in design (0.1-0.35) with the objective to take the effect of the added mass on the structure into clear consideration.

The modulus of elasticity of concrete usually increases during the curing period in the first months after casting; two considered relationships are derived from Eurocode 2 and International Federation for Structural Concrete (2010), as shown in Figure 3.20 for concrete belonging to the C30/37 strength class with Quartzite aggregate.

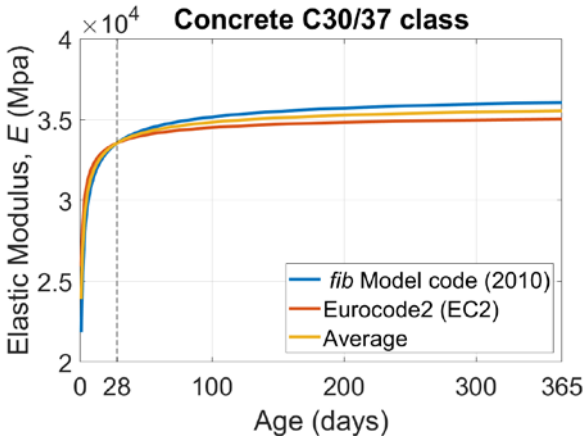

Figure 3.20. Development of the elastic modulus of elasticity of concrete as a function of time for two different standards and its averaged value.

In both cases, the elastic modulus reaches 90% of the final value 28 days from casting. For completeness, these relationships were used to compute the elastic modulus to be used in the FEM model. A resulting increase of around 4 % in the elastic modulus was applied in the model from the start of the measurements. Given that at least 2 months had passed since the end of the construction, this effect had only minor influence on the predicted trends with time.

The first half of the floors was occupied by March 2018. Further variations in the occupancy were not known explicitly. In the absence of other information, further assumptions were made regarding the rate and form in which the occupation changed in time. To align this study with Arakawa and Yamamoto (2004), it was assumed that the full occupancy of the building was reached in 60 months (October 2022) from October 2017. The 60-month interval was divided to six equal subintervals with the first interval ending in August 2018, close to the end of the monitoring period (September 2018).

The degree of occupancy was adjusted to the value that yielded the relative frequency decreases from the initial state (assumed to be unoccupied by October 2017) to be comparable and close to those drops observed during the overlapping monitoring period. This resulted to the assumption of the almost full occupancy, i.e., 42 floors out of 47 in total, occupied in August 2018. This constitutes a plausible state of occupation since the start of this process at the end of 2017. For the purposes of this study, the remaining part of the filling process was idealised such that the last five floors were filled at equal rate during the remaining five 10-month intervals.

The results of this study are summarised in Fig. 3.21 where the relative frequency drops of the first three modes from the full-scale measurements at the end of the measurements (Table 3.3) and the FE estimates at the six different stages and 60 months after the measurements started are compared under the above-described conditions. The asymptote values (Table 3.3) are also included. The estimated natural frequencies (i.e., filled markers connected by dotted lines in Figure 3.21) from the model (Figure 3.19) were the initial frequencies at the start of the measurements before applying any imposed mass.

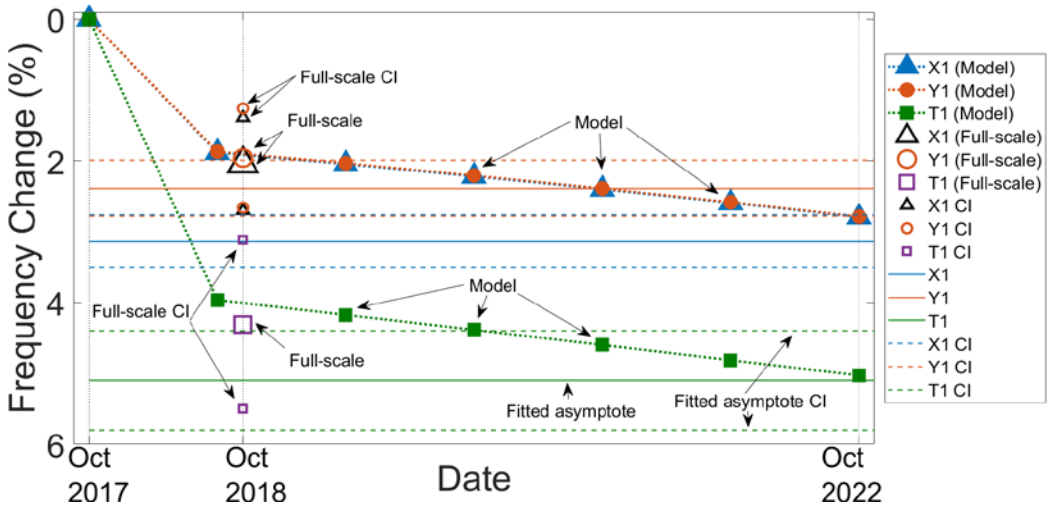

Figure 3.21. Percentage change of the measured full-scale natural frequencies for *X1*, *Y1* and *T1* compared with the estimates from the FEM model at different stages. Steady state asymptote frequency change values (Table 3.3) are also included.

Table 3.4 summarizes the "Steady state asymptote" frequency change in Table 3.3, the frequency changes over 60 months calculated by Arakawa and Yamamoto (2004) and the relative frequency drops from the initial modelled values for *X1*, *Y1* and *T1* in Figure 3.21 with respect to the estimated frequency values at 60 months after the measurement period started (denoted "Measurement 60 months (model)").

Table 3.4. Percentage change of the natural frequencies at 60 months and the regression asymptotes with respect to the frequency values from the FEM model at the start data of the measurements. Frequency changes from Arakawa and Yamamoto (2004) at 60 months for the first mode of each type are also included.

	Measurement 60 months (Model)	Steady state asymptote	Arakawa and Yamamoto (2004)
Mode *X1* (%)	2.79	3.13	3.51
Mode *Y1* (%)	2.78	2.39	2.77
Mode *T1* (%)	5.03	5.10	3.25

After imposing realistic occupying assumptions, it can be seen that the relative frequency drops based on the estimates provided by the FEM model at the end of the measurements are consistent with the asymptotic values expressed in relative terms. The asymptotic values can be described as the predictors for the full occupancy from the full-scale measurements. Despite

the significant differences in the study characteristics, such as the structural arrangement and the system identification method, the frequency changes over 60 months calculated by Arakawa and Yamamoto (2004) are comparable to the data and model-driven predictions presented in this research.

However, no reason for frequency variation was provided in that study. In this research, although there are significant differences between the Tower 1 and its model used as a support of the analysis, it seems that the long-term variation in the natural frequencies throughout the monitoring period can be attributed to the increasing added mass in the structure during the fitting out and the initial occupation of the building.

3.5.2.3 *Analysis of natural frequencies for Tower 2*

The estimated natural frequencies for Tower 2 are investigated in this section in relation to the acceleration amplitude and the wind speed in a similar way to the previous section for Tower 1, in order to provide a direct comparison of the effect of the wind on both structures. Because of the short length of the measurements on Tower 2, a variation of the natural frequency values with different observation dates was not observed in this case.

Due to the difficulties in fitting accurately the PSDs for the torsional acceleration responses, the analysis on Tower 2 only considers modal parameters for modes in the two translational directions, *X1* and *Y1*. Therefore, the RMS acceleration amplitude was obtained from the PSDs by integrating them over the 0.1-0.3 Hz frequency range of the first relevant resonant peak in each direction. It is noted that a main constraint in this analysis is the use of wind data from Met Office records (Met Office, 2020) measured at relatively distant locations at Heathrow and London City airports since there was not any anemometer installed in the Tower 2.

The relationship between the estimated natural frequencies of Tower 2 and the RMS acceleration amplitude for Mode *X1* and *Y1* is shown in Figure 3.22. Similarly to the equivalent relationship for Tower 1, it shows a gradual decrease of the natural frequency values for increasing RMS acceleration amplitudes despite limited data available for comparison. The values of the relative decrease in both towers are similar, accounting to approximately 5 %. Tower 2 is 37 % taller than Tower 1. The observed frequencies at low amplitudes in Tower 2 for Mode *X1* and *Y1* are 28 and 29 % lower respectively than in Tower 1. Since both buildings have similar core arrangements and building materials, it is expected that the difference in the

stiffness and consequently, in the natural frequencies of both structures is due to the difference in height. Given the RMS acceleration amplitude for this tower corresponds only to the first dominant peak, their hourly mean values are lower than the total RMS acceleration amplitude for the Tower 1.

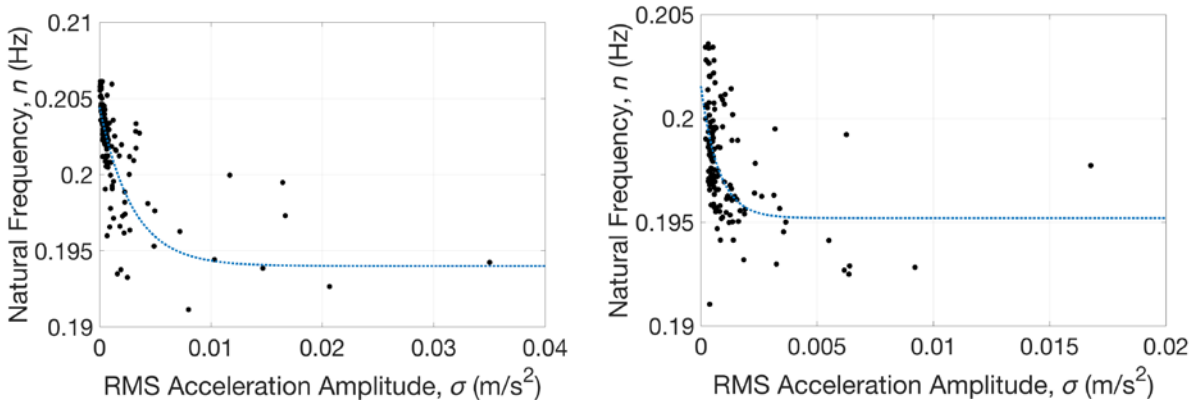

(a) Mode *X1* (R^2 = 0.62) (b) Mode *Y1* (R^2 = 0.30)

Figure 3.22. Observed (black markers) and fitted (blue curve) relationships between the natural frequencies and acceleration amplitudes, Mode *X1*, *Y1*. The coefficient of determination for each mode is also indicated.

The changes of the natural frequencies follow a decreasing trend with hints of an asymptotic tendency. Thus, the regression approach that models the relationship between the natural frequencies and the RMS acceleration amplitude is defined by:

$$f = f_0\left(1 - \alpha_\sigma e^{-\beta_\sigma \sigma}\right) \tag{3.18}$$

where: f is the natural frequency (in Hz)

f_0 is the initial estimated value of natural frequency at zero amplitude (in Hz)

α_σ and β_σ are the constant parameters governing the eventual reduction in the natural frequency with amplitude

α is the RMS acceleration amplitude (in m/s^2)

The values of the parameters of the fitted function (Equation 3.18) are displayed in Table 3.5 for each mode.

Table 3.5. Values of the fitted function parameters for the relationship between the natural frequencies and acceleration amplitudes.

	f_0 (Hz)	α_σ	β_σ
Mode *X1*	0.204	-1.953	5.19×10^{-4}
Mode *Y1*	0.202	-1.876	7.58×10^{-4}

The relationship between the estimated natural frequencies of Tower 2 and the wind speed for Mode *X1* and *Y1* is shown in Figure 3.23. The decrease in the identified natural frequencies as the wind speed increases is consistent with the results from Tower 1. Table 3.6 offers summary of the regression in Equation 3.19. Despite the wind data was obtained from relatively distant weather stations, the range of hourly mean wind speeds is similar to Tower 1, with values that did not exceed 15 m/s.

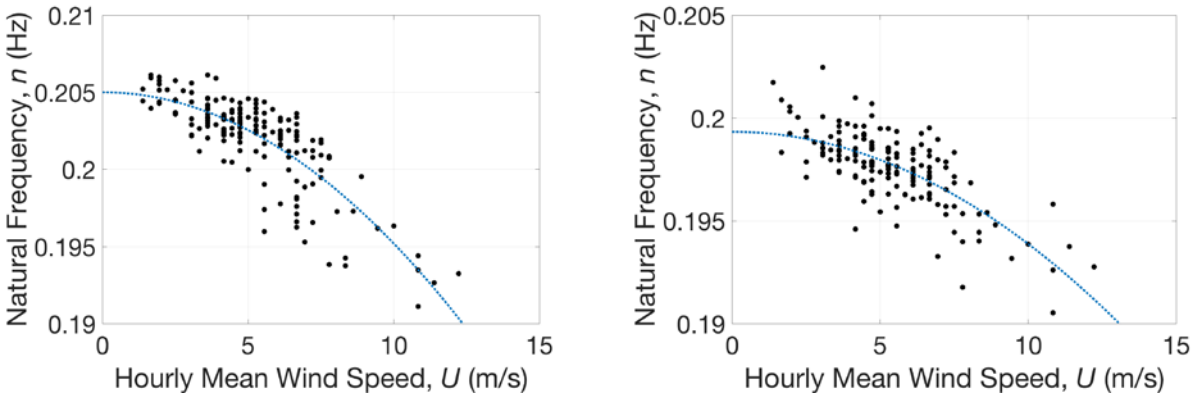

(a) Mode *X1* (R^2 = 0.63) (b) Mode *Y1* (R^2 = 0.23)

Figure 3.23. Observed (black markers) and fitted (blue curve) relationships between the natural frequencies and wind speeds, Modes *X1*, *Y1*. The coefficient of determination for each mode is also indicated.

The relationship between the natural frequencies and the corresponding wind speeds has been fitted by:

$$f = f_0(1 - \delta_U U^2) \tag{3.19}$$

where: f is the natural frequency (in Hz)

f_0 is the initial estimated value of natural frequency at zero amplitude (in Hz)

δ_U is the constant parameters governing the eventual reduction in the natural frequency with wind speed

U is the hourly mean wind speed (in m/s)

Table 3.6. Values of the fitted function parameters for the relationship between the natural frequencies and wind speeds.

	f_0 (Hz)	δ_U
Mode *X1*	0.205	9.81×10^{-5}
Mode *Y1*	0.199	5.45×10^{-5}

Although there is significant scatter in the data, this analysis provides confirming evidence that the natural frequencies of the two tall buildings studied in this research tend to decrease with the increase in the amplitude and wind speed linked to the wind loading. The drop in the natural frequencies with wind speeds follow a decreasing trend with hints of a quadratic tendency similarly to Tower 1 for an equivalent range of measured wind speeds. Despite this analysis on Tower 2 only considered the RMS acceleration amplitude for the first dominant peak, there is an equivalent decrease in the natural frequencies in comparison with Tower 1. Thus, it seems the variation in frequency is dominated by the amplitude response of the first mode, even though the contribution of higher modes might be also relevant. Given the RMS acceleration amplitude for this tower corresponds only to the first dominant peak, their hourly mean values are lower than the total RMS acceleration amplitude for the Tower 1. The R^2 value of the correlation between the natural frequency and wind speed is clearly lower than the corresponding value for the amplitude relationship for Mode *Y1*, but it is higher for Mode *X1*. However, the difference is very small. Regarding the objective of identifying the influential parameters in the wind-induced response of tall buildings, from the limited observed data of Tower 2 it is difficult to identify if the variation in natural frequency can be better explained by a change in amplitude or by a change in wind speed. This study showed that empirical estimates of the fundamental frequency of tall buildings vary with their height. For analogous structural core arrangements, the taller tower (Tower 2) is less stiff (or more flexible) and, consequently it has lower natural frequencies than the corresponding shorter building (Tower 1).

3.5.3. Damping ratio analysis

This section focuses on analysis of modal damping and influence of the key factors such

as the wind and dynamic response conditions. While the natural frequencies were found to be changing with time, and similar trends were also observed in published sources, e.g., Arakawa and Yamamoto (2004), this research did not identify conclusive variations of damping ratios with the observation date under the present conditions of the experimental and identification uncertainty. The identified damping ratios, however, were found to be sensitive to changes in the structural response and loading characteristics. The RMS acceleration amplitude was used to characterise the structural response and 1-hour mean wind speeds were used later to describe the changing wind loading intensity.

3.5.3.1 *Analysis of damping ratios for Tower 1*

Figure 3.24 shows the relationships between the damping ratios and the corresponding acceleration RMS values for Tower 1. Although there is a large scatter, an increasing trend in damping can be observed with increasing RMS amplitude for all three modes. A higher value of the coefficient of determination R^2 was obtained for Mode *X1* compared with Modes *Y1* and *T1* because of the comparatively smaller number of data points at the lower amplitudes, where the results are highly variable. Less well-defined growing trends were identified for the higher frequency modes.

Aiming to interpret the trends observed in the data, similar strategy to the one used in the previous sections is used. A regression model is adopted following the approach presented by Davenport and Hill-Carroll (1986) while considering the specifics of the identified data displayed in Figure 3.24, where near-zero response amplitudes, characteristic of small vibrations, clearly indicate the presence of non-zero damping ratio values.

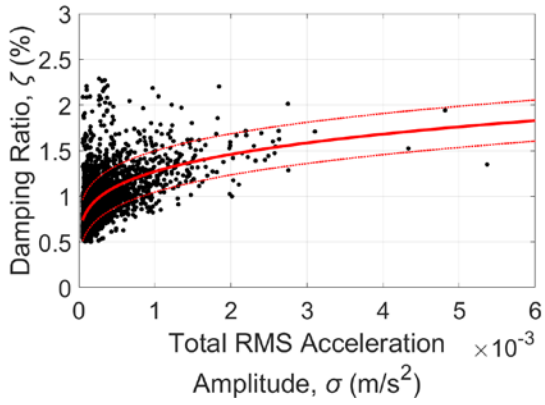

(a) Mode *X1* (R^2 = 0.341)

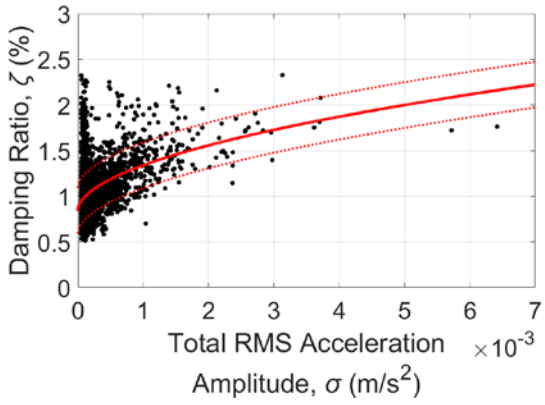

(b) Mode *Y1* (R^2 = 0.156)

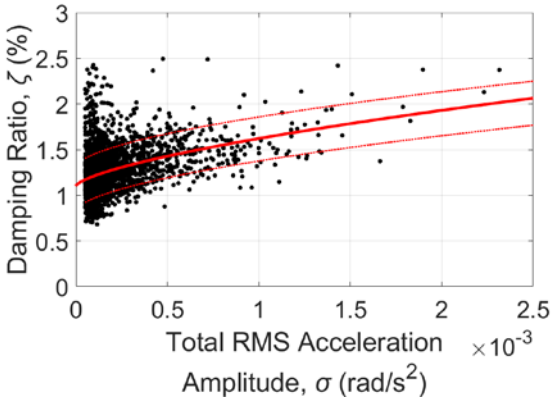

(c) Mode *T1* (R^2 = 0.156)

Figure 3.24. Observed (black markers) and fitted (red curve) relationships (+95 % *CI*, -95 % *CI*) between the damping ratios and acceleration amplitudes, Modes *X1*, *Y1* and *T1*. The coefficient of determination for each mode is also indicated.

Therefore, the exponential function is extended by an additional zero-amplitude term in the following form:

$$\zeta = \zeta_0 + \zeta_\sigma \sigma^\gamma \tag{3.20}$$

where: ζ is the damping ratio (in %)

ζ_0 is the damping ratio for zero amplitude (in %)

ζ_σ and γ are the constant parameters governing the eventual increase in the damping ratio with the RMS acceleration amplitude

σ is the RMS acceleration amplitude (in m/s^2 or rad/s^2)

The unknown coefficients are found using the nonlinear least square approach implemented in MATLAB®, and Table 3.7 lists the resulting parameter values for the three considered vibration modes.

Table 3.7. Values of the fitted function parameters for the relationship between the damping ratio and the RMS acceleration amplitude.

	ζ_0 (%)	ζ_σ	γ
Mode *X1*	0.73	5.41	0.24
Mode *Y1*	0.84	18.61	0.52
Mode *T1*	1.1	53.58	0.67

The estimation of the damping ratios is typically subjected to higher identification uncertainty compared to the estimation of natural frequencies. Consequently, the identification uncertainty and resulting data dispersion is larger. This variability is reflected in the R^2 values for the damping ratio regression, which are generally significantly smaller than those for the natural frequencies. For example, the R^2 values for the equivalent relationships of the natural frequencies, ignoring the time dependency (not discussed in the present study), extracted from Figure 3.16 are 0.345, 0.401 and 0.150 for Mode *X1*, *Y1* and *T1*, respectively. Aside from the question of adequacy of the fitting function, another important reason for comparatively low R^2 values is possible existence of another experimental factor that should be considered to explain the data. As visible in Figure 3.24, the low response amplitude value scatter suggests the possibility of another phenomenon influencing these values. To address this observation, next section offers a focused analysis of an alternative source behind the identified values of the damping ratios in the form of wind-structure aeroelastic interaction.

3.5.3.2. *Analysis of wind-structure interaction effects for Tower 1*

Motivated by the previous observations, the identified damping ratio values are studied against the 1-hour mean wind velocity data to check if the changes in the modal parameters are affected by wind-structure interaction and, later, by its directional characteristics.

A direct visual analysis was adopted initially. It was observed that the damping ratios of the first three modes showed a notable correlation with the wind speed measure; similar results were also found for higher modes. Figure 3.25 shows the relationships between the damping ratios of the first three modes and the corresponding 1-hour mean wind speed. Although there is a relatively large scatter in the data, an underlying trend of increasing damping ratio with increasing wind speed is observed.

A simple linear regression model is adopted in the spirit of the across and along-wind quasi-steady aerodynamic damping analyses formulated by Kareem (1982) and Holmes (1996) to provide the summary and comparative characteristics for the identified damping data. With this regression model, the gradient was adopted as a measure of the potential aeroelastic wind-structure coupling based on the study of aerodynamic damping on tall buildings presented by Davenport (1966).

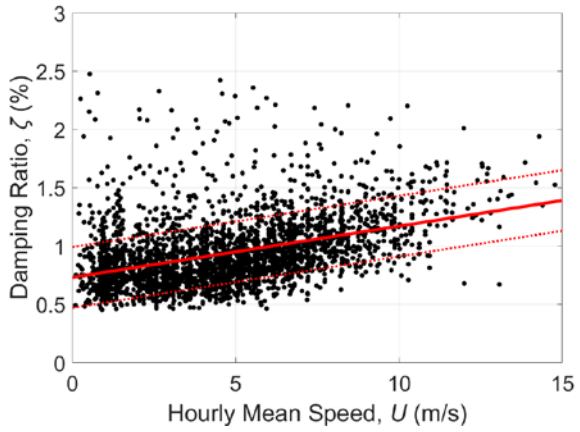

(a) Mode *X1* (R^2 = 0.16)

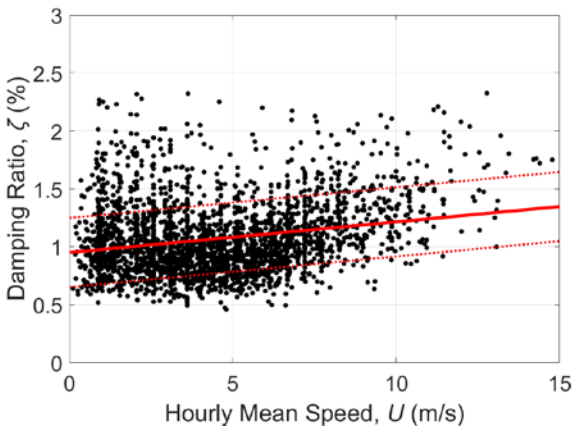

(b) Mode *Y1* (R^2 = 0.07)

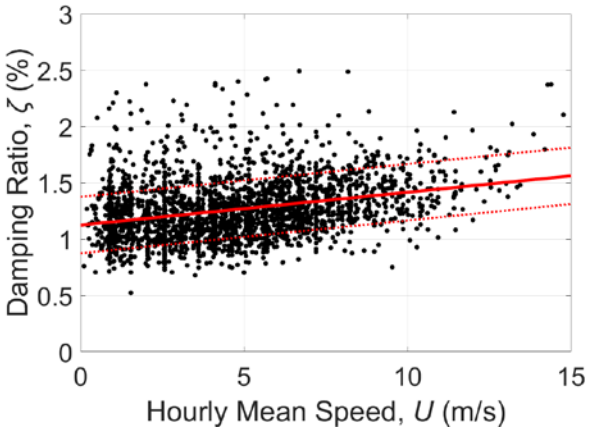

(c) Mode *T1* (R^2 = 0.10)

Figure 3.25. Observed (black markers) and fitted (red curve) relationships (+95 % *CI*, -95 % *CI*) between the damping ratios and wind speeds, Modes *X1*, *Y1* and *T1*.

Under the above theoretical assumptions, the total identified damping can be seen as the sum of the structural damping, which is associated with the no-wind conditions, and the aerodynamic damping increment associated with aeroelastic wind-structure interaction. As is the case in this study, if a linear relationship with the wind speed is assumed, the resulting damping gradient represents the rate at which aerodynamic damping ratio changes per unit wind speed. Table 3.8 offers summary of the linear regression in the form of the calculated structural damping ratios, apparent aerodynamic damping gradients and the corresponding R^2 for the first three investigated vibration modes. The linear function is expressed in the following form:

$$\zeta = \zeta_s + \zeta_a U \tag{3.21}$$

where: ζ is the damping ratio (in %)

ζ_s is the structural damping ratio, i.e. the damping ratio for zero wind speed (in %)

ζ_a is the aerodynamic damping gradient, i.e. the aerodynamic damping ratio per unit wind speed (in %s/m)

U is the hourly mean wind speed (in m/s)

Table 3.8. Values of the fitted function parameters for the relationship between the damping ratios and 1-hour mean wind speeds.

	Mode *X1*	Mode *Y1*	Mode *T1*
ζ_s (%)	0.73	0.95	1.12
ζ_a (%s/m)	0.04	0.03	0.04

It can be seen that the structural (zero wind speed) damping ratios broadly agree with the damping ratios for the (near) zero amplitudes from Table 3.7. Among these, the torsional Mode *T1* carries the highest value, most likely due to the most intense activation of the energy loss mechanisms caused by friction in structural joints and interfaces. Further, compared with Figure 3.24, the R^2 values here are notably lower mainly due to significant scatter in the identified damping values across the full range of wind speeds and, implicitly, wind directions.

To gain deeper understanding of the interactions between damping, wind speed and amplitude on the structure, a comparison between the RMS acceleration amplitude and the mean wind speed in logarithmic scale is displayed in Figure 3.26. Considering the large scatter of results for low wind speeds, presumably due to dynamic excitation mechanisms other than the wind, only data points for wind speeds above 6 m/s have been used for the fitting in Figure 3.26.

It can be noticed that the amplitude responses tend to increase monotonically directly proportional in logarithmic scale to the mean wind speed following a certain power relationship. This trend shows that the gradient of wind speed with acceleration amplitude correlate the gradient with damping. This correlation between damping, wind speed and amplitude makes difficult to disentangle the physical mechanisms behind the structural responses of tall buildings and is one of the root causes of the gap research around the amplitude-dependency behaviour of damping in tall structures.

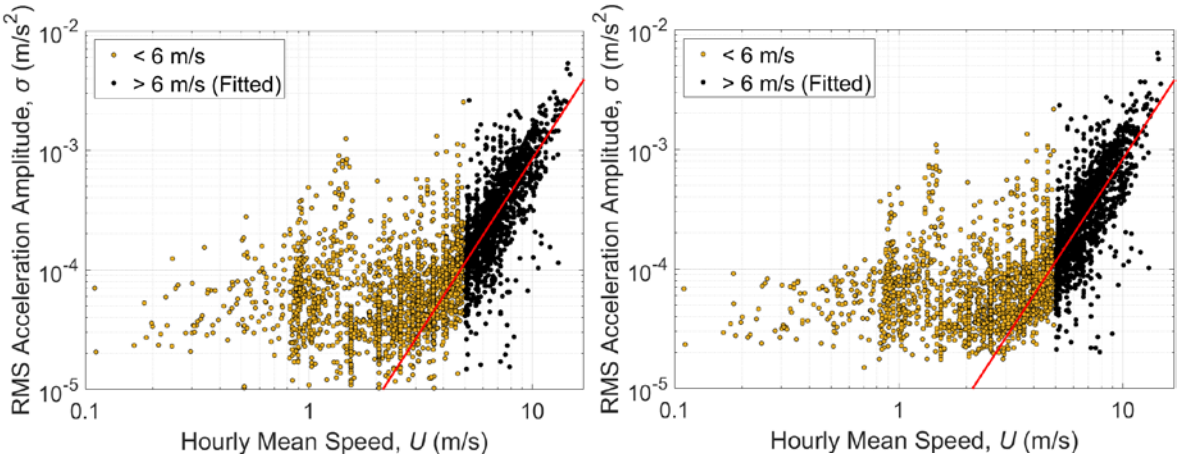

(a) Mode *X1* (b) Mode *Y1*

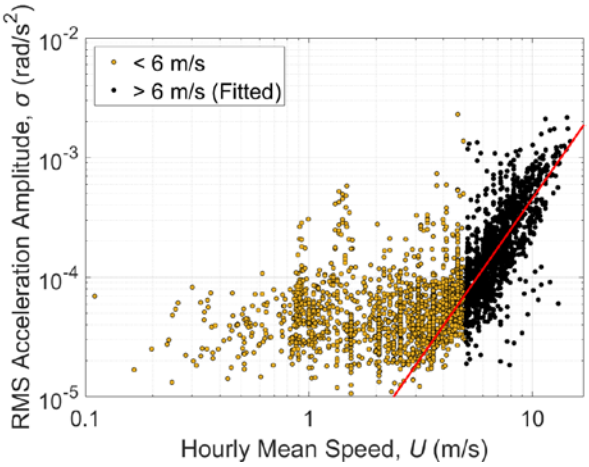

(c) Mode *T1*

Figure 3.26. Observed (yellow and black markers) and fitted (red curve only for wind speeds > 6 m/s) relationships between the RMS acceleration amplitudes in Mode *X1*, *Y1* and *T1*, and the corresponding 1-hour mean wind speeds.

To assess the power law relationship, the regression curves of the amplitude responses for each direction are defined by:

$$\sigma = \vartheta \ U^{\eta} \tag{3.22}$$

where: σ is the RMS acceleration amplitude (in m/s^2 or rad/s^2)

ϑ and η are the constant parameters governing the eventual increase in the amplitude with wind speed

U is the hourly mean wind speed (in m/s)

The estimated curve-fitting parameters of Equation 3.22 are shown in Table 3.9. Despite the datapoints in the three plots being scattered, there is a good agreement between the trendlines of the different motion modes.

Table 3.9. Values of the fitted function parameters for the relationship between the 1-hour mean wind speeds and acceleration amplitudes.

Mode *X1*	
ϑ [$m^{-1.88}/s^{0.88}$]	η [-]
2.15e-04	2.8806

Mode *Y1*	
ϑ [$m^{-1.86}/s^{0.86}$]	η [-]
2.15e-04	2.8643

Mode *T1*	
ϑ [$m^{-1.67}/s^{0.67}$]	η [-]
2.40e-04	2.6687

Whilst this can indicate lower ability of the wind-dependent aeroelastic mechanism or corresponding regression model to explain the data compared to the approach discussed in the previous section, it was deemed appropriate to assess the influence of the wind direction in the present context. To further scrutinise the effect of wind velocity, the impact of the wind direction on the damping ratios for the different modes was considered. When considering the wind directionality and assuming the aeroelastic origins of the observed damping variations, any characteristic differences observed consistently across the two pairs of the along and cross-wind scenarios could serve as an evidence for this mechanism being designated as the dominant source causing the damping ratio changes. The wind range directions were split into 45° data bins to determine potential aeroelastic behaviour differences. Based on the symmetry of the building, three different equivalent wind directions were considered, as displayed in Figure 3.27. Two bins correspond to winds in the *x* direction, perpendicular to the northeast and southwest façades (Wind *X*); another two bins coincide with winds in the *y* direction, perpendicular to southeast and northwest façades (Wind *Y*). The remaining four bins correspond to wind directed towards the corners of the building (Wind 45°). Since the building (Section “Description of Towers and Monitoring system”) has two orthogonal planes of symmetry, the apparent aerodynamic damping induced by the wind incident on two different parallel façades should be equivalent.

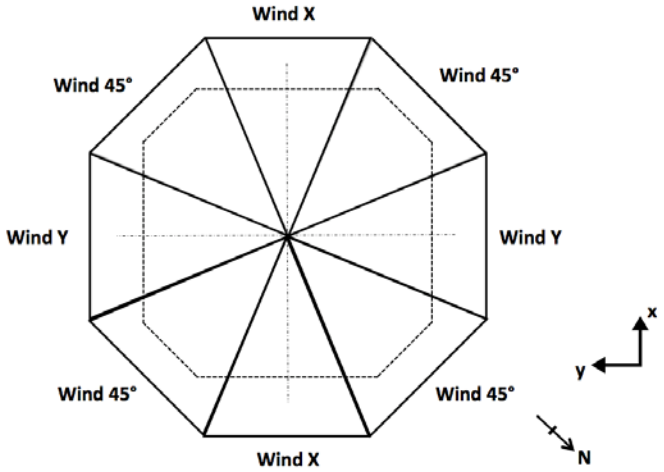

Figure 3.27. Plan of Tower 1 illustrating Wind *X*, *Y* and 45° direction ranges.

The relationships between the damping ratios and wind speed presented after splitting into the three different sets of plots according to the wind direction ranges for each investigated mode can be seen in Figure 3.28. The structural damping ratio (i.e., with no wind) was assumed to be equal for all plots corresponding to the same mode, regardless of the wind direction, so the least squares fitting was performed with this constraint. The values of the structural damping ratio, the apparent aerodynamic damping gradient and the corresponding R^2 values for each mode and wind direction are displayed in Table 3.10.

Table 3.10. Results of directionally sensitive wind-structure damping ratio analysis.

		Mode *X1*	Mode *Y1*	Mode *T1*
Structural Damping Ratio (%)		0.733	0.947	1.124
Wind *X*	Aerodynamic damping gradient (%s/m)	0.044	0.029	0.028
	R^2	0.156	0.091	0.088
Wind *Y*	Aerodynamic damping gradient (%s/m)	0.036	0.013	0.033
	R^2	0.061	-0.036	0.082
Wind *45°*	Aerodynamic damping gradient (%s/m)	0.044	0.029	0.029
	R^2	0.193	0.080	0.102

There, in general, a negative value of the R^2 indicates that the chosen model fits a studied dataset worse than a horizontal straight line. It is noted that the trends are highly influenced by

the damping ratio estimates at low wind speeds, particularly for Wind *Y*. Since a statistical test for significance of the relationship was adopted, the *p* value, as introduced by Pearson (1900), was computed for each relationship. It has been checked that for each estimation of the R^2 of a given relationship, $p < 0.05$, which means that the probability that the slope of the regression is equal to zero is low, and consequently it is meaningful to fit the data.

An underlying trend of positive apparent aerodynamic damping with increasing wind speed can be observed for all the modes and wind directions considered in Figure 3.28. This result is represented in Table 3.10 by the consistently positive values of the aerodynamic damping gradients.

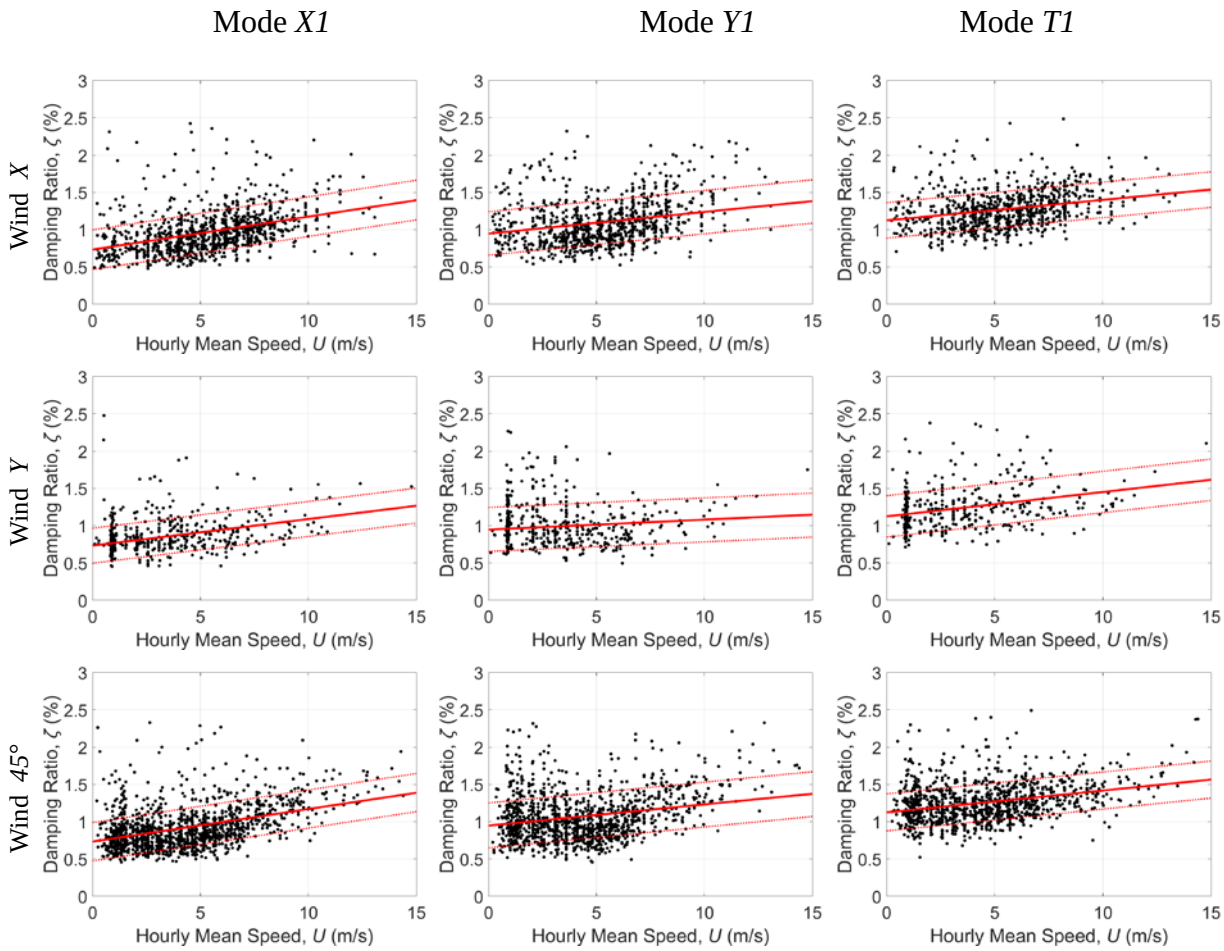

Figure 3.28. Observed (black markers) and fitted (red curve) results of directionally sensitive wind-structure damping ratio analysis.

However, when compared with Figures 3.25 and 3.26, even after taking the wind direction into account, the R^2 values in Table 3.10 are lower than those obtained for the corresponding modes and the assumed amplitude-damping relationships. Hence, overall, this selective

treatment of the wind speed factor did not lead to the regression scenario which explains the measured data better. Furthermore, following the arguments developed for the quasi-steady aerodynamic damping due to the across and along-wind vibrations formulated by Kareem (1982) and Holmes (1996), no qualitative or at least significant differences were observed between the across and along-wind scenarios due to the different mode-wind direction combinations. For example, in Figure 3.28 and Table 3.10, the apparent aeroelastic damping gradient for Mode *X1* is similar across all three wind direction classes, while the gradient Mode *Y1* and wind *Y* is notably lower, but there were fewer data points available for that specific case. Finally, despite the existence of the two nominally identical instances, in each scenario, of the along and across-wind aeroelastic wind-structure interaction, no notable similarities in the calculated damping trends were identified.

Hence, there is insufficient evidence that the wind direction is a factor which influences the identified damping ratios. Although the frequency-amplitude, frequency-wind speed and damping-amplitude relationships have been also evaluated in terms of different wind directions, little effect of wind direction on the identified building modes was found for any of them. In this research it might be concluded, therefore, that for the Tower 1, the wind-induced responses are dominated by the amplitude-dependent structural effects on the damping and natural frequencies.

3.5.3.3 *Comparative analysis of empirical damping models for Tower 1*

Given the above conclusion regarding the most likely origin of the damping ratio variation reached in the previous section, the obtained results were compared against the published empirical amplitude-damping relationships. Davenport and Hill-Carroll (1986), Jeary (1986) and Tamura *et al*. (2000) described amplitude-dependent behaviour of damping ratios, while Lagomarsino (1993), Fritz *et al*. (2009) and Bernal *et al*. (2015) only suggested a constant value of the damping ratio for a given building characteristics. Most of these authors have adopted the approximation for the fundamental frequency given by 46/H proposed by Ellis (1980), and Crowley and Pinho (2004). Furthermore, Tamura *et al.* (2000) asserted that the amplitude-dependent damping ratio might decrease after saturation and reaching the plateau. A ‘critical tip deflection’ concept was developed by Tamura (2006) to model and quantify this phenomenon. This behaviour was explained by an increase in slipping between contacting surfaces as the amplitude increases up to a certain point where friction becomes ineffective.

More recently, Spence and Kareem (2014) presented a data-driven probabilistic model to study the amplitude-dependent damping ratio and frequency relationships, combining both the viscous material damping and the predominant frictional damping of the building to explain both relationships simultaneously. In this research, following the full-scale super-tall building damping study presented by Li and Li (2018), the empirical models used include Davenport and Hill-Carroll (1986), Jeary (1986), Lagomarsino (1993), Tamura *et al.* (2000), Fritz *et al.* (2009) and Bernal *et al.* (2015). They are compared with the relationship based on the regression model introduced in Equation 3.20.

This updated empirical damping model follows the power-law form adopted from Davenport and Hill-Carroll (1986). An extra term is included to capture the structural damping ratio for the near zero-amplitude conditions. For the proposed model to be generally applicable, the parameters of the expression were obtained after fitting together the data from Modes *X1* and *Y1*. This expression was also found suitable for the equivalent relationships of the damping ratios for higher modes.

The formulas and the damping ratio estimates corresponding to the zero-amplitude, ζ_0, and to the maximum measured amplitude, $\zeta_{2.5x10^{-5}}$, are summarised in Tables 3.11 and 3.12.

Table 3.11. Damping ratio predictors proposed by previous amplitude-dependent studies and the proposed model.

Study (Amplitude-dependent)	Damping predictor	Estimated values from full-scale measurements		R^2	
		ζ_0 (%)	$\zeta_{2.5x10^{-5}}$ (%)	Mode *X1*	Mode *Y1*
Davenport and Hill-Carroll (1986)	$\zeta = 0.02 \left(\frac{1{,}000 \times \sigma_d}{H}\right)^{0.11}$	0	1.3	0.3	0.3
Jeary (1986)	$\zeta = 0.01 \times f + 10^{\frac{\sqrt{B}}{2}\left(\frac{x_H}{H}\right)}$	0.03	1.1	≈ 0	≈ 0
Tamura et al. (2000)	$\zeta = \frac{0.65}{H} + 400\frac{x_H}{H} + 0.0029$	0.7	2.4	0.2	0.2
Fritz et al. (2009)	$\hat{\zeta} = \frac{0.06}{\sqrt[4]{N}}$	2.3	2.3	≈ 0	≈ 0
Proposed Model	$\zeta = 1.185\left(\frac{\sigma_d}{H}\right)^{0.41} + 0.0058$	0.6	2.1	0.4	0.4

Table 3.12. Damping ratio predictors proposed by previous studies independent of vibration amplitude.

Study (Independent of vibration amplitude)	Damping predictor	Estimated values from full-scale measurements
		ζ_0 (%)
Lagomarsino (1993)	$\zeta_0 = 0.3192\ T + \frac{0.7813}{T}$	1.4
Bernal et al. (2015)	$\zeta = 0.012 + 0.0426\ e^{-0.013H}$	1.8

*Where ζ is the damping ratio, σ_d is the RMS displacement amplitude (in m), H is the building height (in m), ζ_0 is the damping ratio for zero amplitude, B is the building dimension (in m) at ground level in the direction of motion, x_H is the peak vibration amplitude (in m), f is the building natural frequency (in Hz), T is the building fundamental period (in sec), $\hat{\zeta}$ is the median damping ratio and N is the number of building stories.

Figure 3.29 illustrates the damping ratio trends for Mode *X1* and *Y1* with the dimensionless displacement measure denoted the tip drift ratio. To calculate it, once the displacement PSDs were computed by double integration of the acceleration RMS, the mode-specific RMS displacement amplitudes were obtained from the PSDs by their integration over the modal frequency range of interest. Each value of the hourly RMS displacement amplitude, σ, was converted to the peak displacement amplitude. The peak displacement amplitudes in the x and y directions, x_H and y_H, were found by multiplying the RMS displacement amplitude, σ, by $\sqrt{2}$. Finally, the dimensionless drift ratio represents the peak displacement amplitude divided by the height, H, of Tower 1.

Based on the R^2 value analysis, the updated prediction model, denoted the "Proposed Model" in Table 3.11, shows improved agreement with the present full-scale measurements. Given the reduced occurrence of the high-amplitude wind-driven displacement events, it should be noted that the low-amplitude results influence the parameter identification more significantly. Consequently, the predictive confidence of the proposed model in the high-amplitude regions is limited. The damping results shown in Figure 3.29 indicate that the damping ratios for the first mode in the x and y directions reach around 2% for the higher response amplitudes. Whilst not analysed here, damping ratios for the second and third modes in each direction at higher amplitudes reach between 2.5 and 3%.

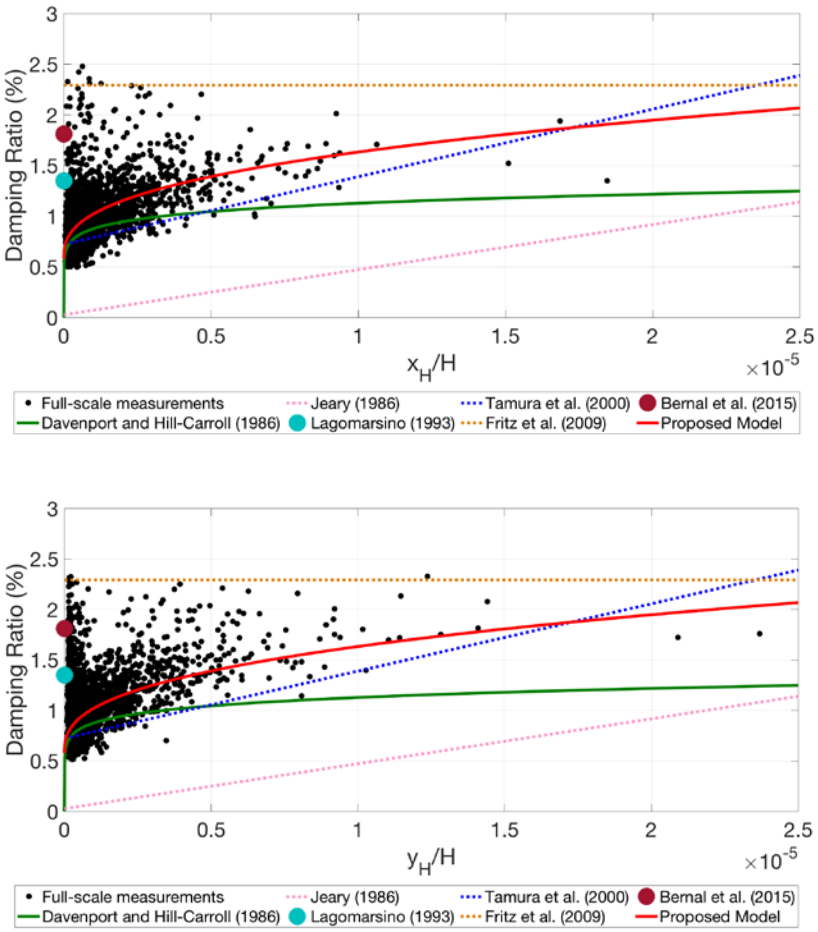

Figure 3.29. Amplitude-dependent damping ratios for the tower and seven chosen damping predictors.

This comparison shows that the forecast model established in Tamura *et al.* (2000) provided comparable structural damping ratio values while, according to the R^2 values, the prediction by Davenport and Hill-Carroll (1986) exhibited the closest amplitude tendency from all compared models.

3.5.3.4 *Analysis of damping ratios for Tower 2*

The estimated damping ratios for Tower 2 are investigated in this section in relation to the acceleration amplitude and the wind speed in a similar way to the previous section for natural frequencies. It aims to compare these results against the equivalent relationships for Tower 1 to understand the effects of wind on tall buildings. These two relationships of the estimated damping ratios in terms of two different variables in a independent structure are used to quantify the wind-induced response of the structure. Because of the short length of the

measurements on Tower 2, there is not enough amount of data to check the directional characteristics of the changes in the damping ratios. As detailed in Section 3.5.2.3, the analysis on Tower 2 only considers modal parameters for the first mode in the two translational directions, *X1* and *Y1*, for which the RMS acceleration amplitude was obtained from the PSDs by integrating them over the 0.1-0.3 Hz frequency range of the first relevant resonant peak in each direction.

The relationship between the estimated damping ratios of Tower 2 and the RMS acceleration amplitude for Mode *X1* and *Y1* that is displayed in Figure 3.30 shows an underlying trend of increasing damping ratio with amplitude. Most of the damping ratios observed at low amplitudes for Tower 2 are in the range between 1 and 2 %, which is consistent with the estimates from Tower 1. This might be due to the similarities in the structural arrangement. However, given the low amount of data measured at high amplitudes in this case, the amplitude-damping relationship is difficult to assess with high confidence.

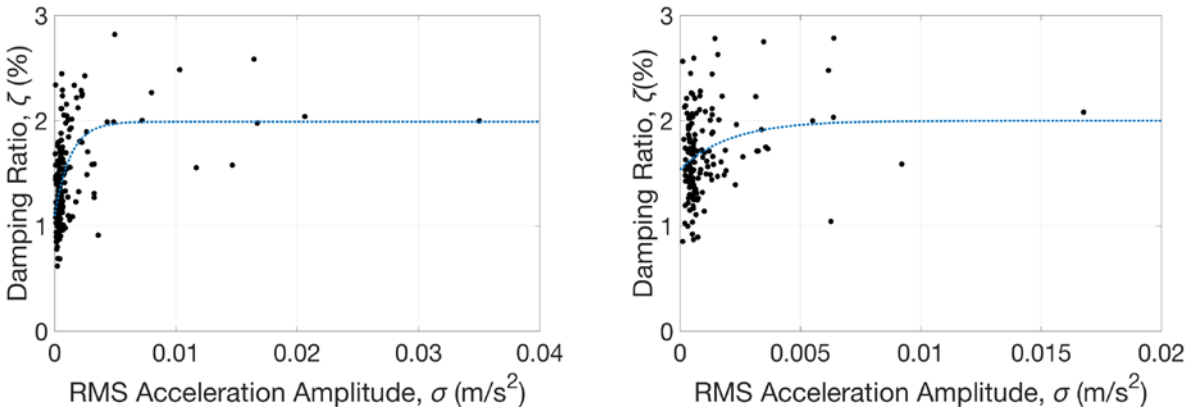

R^2 = 0.27 (a) Mode *X1* R^2 = 0.12 (b) Mode *Y1*

Figure 3.30. Observed (black markers) and fitted (blue curve) relationships between the damping ratios and acceleration amplitudes, Mode *X1*, *Y1*. The coefficient of determination for each mode is also indicated.

Variation of the damping ratio estimates of Tower 2 with the wind speed for Mode *X1* and *Y1* is shown in Figure 3.31. Although there is significant scatter in the individual cases, there is an obvious increase in the estimated damping ratios with the increasing wind speed that can be approximated by a simple linear regression model in the same way as for Tower 1.

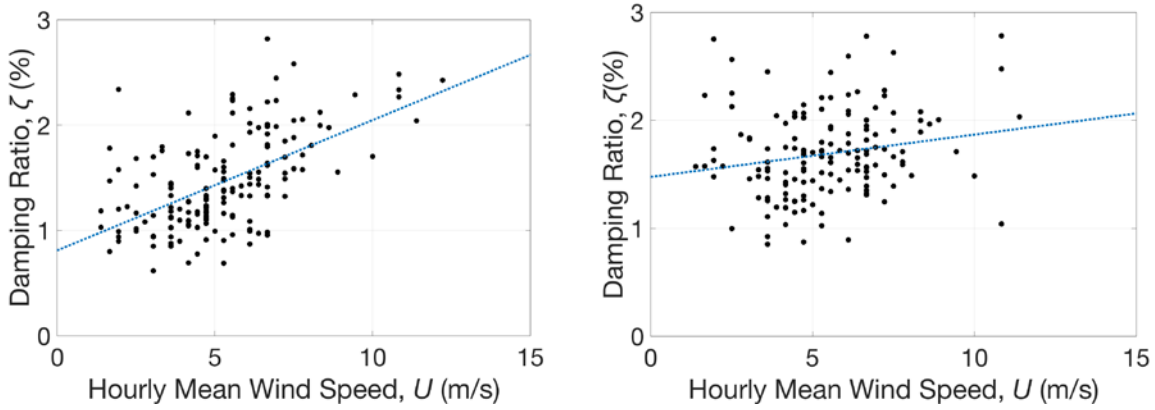

(a) Mode *X1* (R^2 = 0.30) (b) Mode *Y1* (R^2 = 0.04)

Figure 3.31. Observed (black markers) and fitted (blue curve) relationships between the damping ratios and wind speeds, Modes *X1*, *Y1*. The coefficient of determination for each mode is also indicated.

Regarding the objective of identifying the influential parameters in the wind-induced response of tall buildings, the analysis on Tower 2 seems to confirm the basic trends and observations on Tower 1 using an independent source in spite of the limitations related to the amount and apparent quality of the data. Similarly to the equivalent relationships for Tower 1, this analysis shows a gradual increase of the damping ratio values for increasing acceleration amplitudes and wind speed that is linked to the wind loading. The dissipation of energy and consequently mitigation of the oscillations associated with this increase has a positive effect on the integrity of the structure. As it was observed for Tower 1, there is evidence that the variation in the damping ratios in the Mode *Y1* can be better explained by a change in the acceleration amplitude than by a change in wind speed. However, considering the two sway motion directions from the limited observed data on this building, it is difficult to provide an overall conclusion on the main parameter influencing the damping of the structure. In addition, although the study on the natural frequencies showed that empirical estimates of the fundamental frequency of tall buildings with similar structural arrangements vary with their height, this research did not find a significant difference in the estimated damping ratios between the two studied buildings. This analysis on an independent building seems to confirm that the variation in the modal parameters, natural frequency and damping ratio is dominated by the amplitude response of the first mode, even though the contribution of higher modes might be also relevant.

3.6. DISCUSSION AND CONCLUDING REMARKS

3.6.1. Discussion

With the aim of studying the wind-induced vibrations on slender structures, the structural performance and the dynamic properties of a tall building in London (UK), Tower 1 (150 m), were investigated by measuring the wind-induced vibrations and associated wind conditions from a set of accelerometers and an ultrasonic anemometer. Results from Tower 1 were compared with similar, but shorter ones from another 205 m tall building (Tower 2), in the first two modes in each of the translational directions. The acceleration measurements and the corresponding wind conditions were analysed in both buildings to identify the most influential parameters that govern the wind-induced response of this type of systems and the reasons for variations in the structural modal parameters.

The identified modal parameters in the monitored buildings were evaluated in relation to a series of factors, including time, amplitude, wind speed and wind direction. Despite the shorter length of the measurements and the more scattered estimates observed for Tower 2, results in analogous sway motion directions from the two buildings agreed well. This increases confidence in the reliability of the identified results from Tower 1. The dominant effects in both structures were found to be amplitude in the case of natural frequencies and amplitude in the case of damping ratios. Given the lengthy duration of the measurements on Tower 1, it was also observed that time governed the frequency responses.

Similar trends to the ones presented in this analysis have been found for the modal parameters of higher modes (2^{nd} mode, 3^{rd} mode and 4^{th} mode). However, only results from the first mode of each type have been displayed in this chapter because they showed higher correlation with the investigated parameters than the results found for the higher modes. Previous results on the trends of the measured typical values of modal parameters under operation are relevant because they can be used to quantify the dynamic responses of other similar tall buildings. This technique is commonly adopted in design, because the dissipation of energy of a structure expressed as damping is directly related to the mechanical resonance represented by frequency.

Apart from the decrease in the natural frequencies observed with the increase in amplitude in both structures, there was a gradual drop of the natural frequency estimates in Tower 1 with the observation time over the twelve-month monitoring period for the first four modes in each

of the two sway directions and torsion. An asymptotic exponential regression model was used to fit the corresponding data. In summary, it was found that the sway modes asymptotically decreased by around 3% while the first torsional mode marked an asymptotic drop of up to 5% in the limit. A basic finite element model of Tower 1 was used to support the argument that the trends can be attributed to the increasing added mass in the structure during the fitting out and the initial occupation of the building. This novel analysis has been conducted in this investigation since limited literature has been published on the long-term variation of the modal parameters, natural frequencies and damping ratios of tall buildings in relation to environmental conditions or changes in the physical parameters of the system.

Despite the significant differences between the actual tower and the FEM model, its validity was established by achieving satisfactory agreement between its first three natural frequencies and the full-scale measurements as well as via qualitative agreement between the mode shape indicators implied by the post-processed acceleration PSDs and the calculated mode shapes. Overall, it has been shown that, based on realistic estimates of the occupancy and loading rooted in standards (Eurocode 1), the model has been able to match the observed values under the different fractions of the occupancy loading.

A trend of the increasing damping ratio with increasing response amplitude has been observed for the first three modes in each of the two sway directions and in torsion for Tower 1. Although there were more scattered results, similar trends have been also found for Tower 2 for the first three modes in each of the two sway directions. The data were approximated by an updated regression model combining the power law and the damping ratio constant corresponding to the near zero response amplitude. Aiming to identify the main source of damping, similar characteristics were investigated with respect to wind speed under the assumption of the aerodynamic damping being responsible for the experimental variations. The apparent aerodynamic damping gradient was used as the main feature to support the analysis whilst considering the different combinations of modal patterns and wind directions. This parameter was adopted by Davenport (1966) as a measure of the potential aeroelastic wind-structure coupling based on the study of aerodynamic damping on tall buildings presented. Principally, similar aerodynamic gradient trends have been identified in this research for the damping-wind speed relationships with respect to different wind orientations. Therefore, little evidence was found to support the aerodynamic damping arguments for the studied structural configuration. Instead, the amplitude-dependent structural effects were identified as the primary

source of the observed variations in the identified damping ratios.

However, it can be stated that the observed correlation between damping, wind speed and amplitude makes difficult to disentangle the physical mechanisms behind the structural responses of tall buildings and is one of the root causes of the gap research around the amplitude-dependency behaviour of damping in tall structures. In any case, the dissipation of energy and consequently mitigation of the oscillations associated with the increasing damping ratio with both the wind speed and amplitude has a positive effect on the integrity of the structures of the two monitored buildings. As an example to quantify this effect, the amplitude-dependent damping ratio values for Tower 1 were shown to range from 0.6% for the near zero amplitudes to 2.1% for the high amplitude conditions. Since occupant comfort is directly related to wind-induced sway in this type of structures, these findings are positive from both ultimate and serviceability points of view.

Moreover, this investigation has aimed to contribute to elucidate the main characteristics of the amplitude-dependent behaviour of the damping ratios for Tower 1. The new damping prediction model proposed based on the power-law model from Davenport and Hill-Carroll (1986), has been noted to differ from some of the most common models used in literature. Given the reduced occurrence of the high-amplitude wind-driven displacement events, it should be noted that the low-amplitude results influence the parameter identification more significantly. Consequently, the predictive confidence of the proposed model in the high-amplitude regions is limited. Despite the low amount of data measured at high amplitudes in Tower 2, there is a subtle trend which seems to confirm the observations in Tower 1.

Although it has been commonly described in literature that damping estimates, and to a lesser extent, natural frequencies, are susceptible to the loading assumption, the effect of the wind direction on the Tower 1 and the specific analysis on the new damping prediction model have been focused on the damping ratios estimates. This research has found that reliable estimates of both natural frequencies and damping ratios could be used for this type of slender structures subjected to wind loading. In summary, whilst the presented results are contextual and specific to these two structures, the demonstrated ability to use a simple monitoring system in combination with basic FEM model (for Tower 1), to establish the vibration characteristics, to elucidate their root causes and to interpret their variation forms a useful case study evidencing applicability of such tools in the through-life analysis and monitoring of the structural condition and health. Hence, this motivates the use of a similar approach to other types of slender

structures that are less stiff and more sensitive to the effect of the wind direction.

Finally, it should be noted that the full-scale wind velocities measured by the anemometer on top of Tower 1 might be distorted by the presence of the building itself and may be different from the free stream velocity because a possible shielding effect on the anemometer induced from the building. This might explain that the measured wind velocity exhibited a large vertical angle of attack (mean 30°). Moreover, the hourly-mean reference wind speed given by ESDU (2006) based on the top height of the tower (anemometer level) in urban terrain is 8.1 m/s, which is higher than most of the hourly full-scale observations. In addition, it is particularly notable that only a few wind instances from the east were experienced at the site during the measurements, so it has been assumed that the influence of other tall buildings in London might also increase this effect. This is related to the fact that the important results for higher wind speeds are therefore based on relatively few measurements.

3.6.2. Concluding remarks

In this study, data from a set of accelerometers and anemometers obtained by AKT II Ltd. (and additional weather stations wind data from Met Office) have been used to measure the wind-induced vibrations and associated wind conditions for two tall buildings in London (UK), Tower 1 (150 m) and Tower 2 (205 m). Aiming to quantify and elucidate the sources of the observed variations, the dynamic behaviour of the structures and the effect of wind direction and the orientation of the motion on the modal parameters have been investigated by considering the first three modes in each of the translational directions and torsion for different wind directions for Tower 1. Similarly, a minor supportive analysis for Tower 2 has considered the first two modes in each of the translational directions.

The main findings and conclusions of this study are:

- After evaluating the identified modal parameters in relation to a series of factors, including time, amplitude, wind speed and wind direction, the dominant effects in both monitored tall buildings have been found to be amplitude in the case of natural frequencies and amplitude in the case of damping ratios.
- There was a gradual drop in the natural frequency estimates for Tower 1 with the observation time over the twelve-month monitoring period for the first four modes in each of the two sway directions (around 3 %) and torsion (up to 5 %) in the limit. A basic finite element model for Tower 1 has been used to support the argument that the trends can be attributed to

the increasing added mass in the structure during the fitting out and the initial occupation of the building. Whilst its validity has been established by achieving satisfactory agreement between its natural frequencies estimates and the full-scale measurements, it has been also shown that based on realistic estimates of the occupancy and loading rooted in standards (Eurocode 1), the model has been able to match the observed values under the different fractions of the occupancy loading.

- Aiming to identify the main source of damping, similar characteristics have been investigated with respect to wind speed under the assumption that aerodynamic damping was responsible for the experimental variations. The apparent aerodynamic damping gradient for Tower 1 has been used as the main feature to support the analysis whilst considering the different combinations of modal patterns and wind directions. Principally, similar aerodynamic gradient trends have been identified for the damping-wind speed relationships with respect to different wind orientations. Therefore, little evidence has been found to support the aerodynamic damping arguments for the studied structural configuration. Instead, the amplitude-dependent structural effects have been identified as the primary source of the observed variations in the identified damping ratios.
- A new damping prediction model based on the power-law model from Davenport and Hill-Carroll (1986) has been proposed for Tower 1. Applying the qualitative evaluation of the coefficient of determination, R^2, this empirical model has shown to better represent the amplitude-dependent behaviour of the damping measures obtained from the full-scale measurements compared to the six selected damping models. Using the proposed damping model, the amplitude-dependent damping ratio values have been shown to range from 0.6% for the near-zero amplitudes to 2.1% for the high amplitude conditions.

CHAPTER 4. PRELIMINARY ANALYSIS OF MODEL-SCALE GALLOPING PROBLEM

4.1. INTRODUCTION AND THEORETICAL BACKGROUND

4.1.1. Introduction

In the light of the little effect that the wind direction was found to have on the responses of tall buildings (particularly Tower 1), as covered in Section 3.6, the investigation on the wind-induced vibrations on slender structures has been extended in this Chapter 4 to a less stiff and *a priori* more sensitive type of structure, i.e., overhead electricity transmission lines. The distinctly different characteristics of this system with respect to tall buildings (e.g., dimensions, stiffness properties, boundary conditions, etc.) might provide an opportunity to observe and quantify a direct effect of the wind on its dynamic responses.

Moreover, although these dynamic responses of tall buildings have been quantified based on modal parameter estimation from OMA (Operational Modal Analysis), this chapter presents a preliminary analytical study of the galloping problem in electricity transmission lines based on EMA (Experimental Modal Analysis). This controlled environment might enable the observation of the emergence of galloping as a mean of preparing the groundwork for a full-scale environment, where similar phenomena are expected.

The main aim of this research is to show how the analytical solutions of two 3-DOF quasi-steady aerodynamic force models of cable conductors provided by two different authors (Matsumiya *et al.* (2018) and He and Macdonald (2016) denoted in this research by Model 1 and 2 respectively) can be used in the prediction of galloping instability through the use of a simple controlled setting based on experimental wind tunnel test-data. It made use of observed aerodynamic characteristics of four-bundled conductors in static wind-tunnel tests conducted by Matsumiya *et al.* (2018). This study will prepare the groundwork for the analysis (presented in Chapter 5) of full-scale measurements on cable bundle transmission lines by focusing to understand the parameters that induce the emergence of galloping.

The overall structure displayed in Figure 4.1 illustrates a map of the methodology used in this analysis of model-scale galloping. A direct comparison between the prediction of galloping instability presented in this chapter and the full-scale measurements in Chapter 5 is sought, given they are both based on the same cable bundle geometry.

Previous work by H. Matsumiya on a four-bundled conductor was considered, where

galloping observations on full-scale ice-accreted sections (Matsumiya *et al*., 2012) were compared against numerical analysis (Matsumiya *et al*., 2013). These investigations presented by Matsumiya are part of an extensive research project conducted by the Central Research Institute of Electric Power Industry (CRIEPI) in several electric power transmission facilities in Japan. Moreover, Matsumiya *et al.* (2018) showed that motion in the individual subconductors from wind tunnel tests agreed well with the prediction of the dynamic response of the theoretical model provided by one of the two formulations presented in the study. Motivated by these findings, the research described in this chapter presents the eigenvalue analysis using analytically defined aerodynamic damping matrix to predict the galloping instability regions on transmission lines, on the basis of two existing three degrees of freedom (3-DOF) quasi-steady aerodynamic force models.

A useful and computationally efficient first point of analysis is sought with the adoption of this method, as illustrated in Figure 4.1. Firstly, the aforementioned Matsumiya *et al.* (2018) research was used to present a direct (analytical or numerical) linearization of the reference nonlinear model, for which time-history response analyses showed good agreement with the full-scale results from the wind tunnel tests.

However, Model 1 was specifically developed only for four-bundled conductors. Therefore, with the objective of using an approach with potential transferability to different geometric arrangements, the formulation developed by He and Macdonald (2016) was adopted in this study. It is a linear approximation of the problem that can be applied to any arbitrary geometry using the aerodynamic damping matrix that implicitly takes into account the effect of an aerodynamic centre. Thus, this study seeks to predict the galloping instability on transmission lines and find the position of this aerodynamic centre parameter from the experimentally observed aerodynamic characteristics of the bundle studied in Matsumiya *et al*. (2018).

These aerodynamic characteristics of the bundle were provided by Matsumiya *et al*. (2018) in the form of the steady-state aerodynamic drag, lift and moment coefficients measured in static wind tunnel test. Also, the present analysis will allow to check the accuracy of the He and Macdonald (2016) approach by comparing their results with those found in wind tunnel experiments.

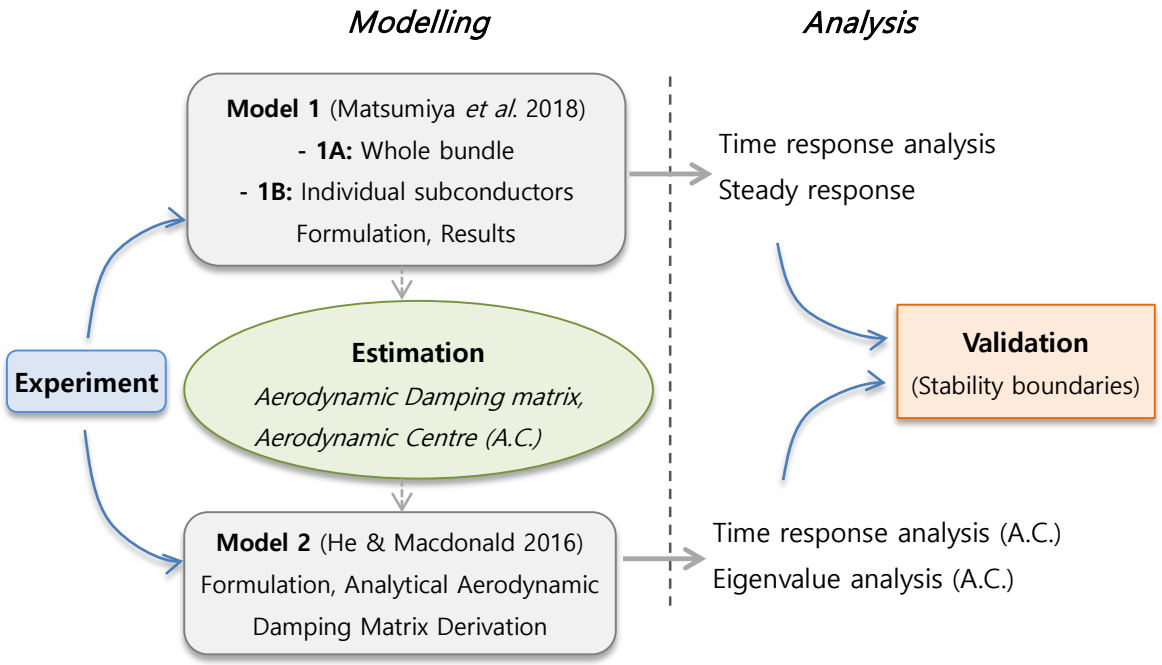

Figure 4.1. Structure of the research methodology.

It should be noted that this chapter firstly describes extensively the two existing reference formulations in Section 4.2. “Aerodynamic Force Formulations” as an introductory literature review part, including discussion of their differences and similarities and a comparison of their notations. This is followed by the novelty sections of this study: the estimation process of the position of an aerodynamic centre parameter addressed in Section 4.3 “Identification of the Position of an Aerodynamic Centre” and the analysis itself, developed to predict and understand the emergence of galloping which is presented in Section 4.4. “Analysis of Galloping Stability”.

4.1.2. Quasi-steady derivations of galloping

Theoretical background on quasi-steady theory is provided to understand the physical foundations of the two formulations considered in this analysis, developed by Matsumiya *et al.* (2018) (Model 1) and He and Macdonald (2016) (Model 2). One of the main advantages of quasi-steady theory is that the structural response, and therefore galloping behaviour, can be predicted without conducting dynamic tests. The static aerodynamic forces and moment coefficients of the system can be extracted from the static aerodynamic tests and then used in the analysis to predict the dynamic response of the aeroelastic structure. This section describes the derivation of the Den Hartog (1932) galloping criteria on the basis of a special Single Degree of Freedom (SDOF) case for pure across-wind motion. This theory aimed to describe the

conditions under a 2D body which can experience galloping.

Figure 4.2 shows the geometry of a bluff cross section with a reference dimension of the section perpendicular to the wind direction, *B*, subjected to wind flow, *U*, which is aligned with the horizontal principal structural axis, *x*. The motion of the body in the vertical direction is given by the vertical rate of displacement $\dot{y}$, and the angle, α, between the wind direction and the reference line on the body. The resulting aerodynamic forces acting on the body can be considered as quasi-steady forces, as functions of the relative angle of attack, α_{rel}, as illustrated in Figure 4.2. The velocity of the wind relative to the body is denoted by U_{rel} when it is in motion.

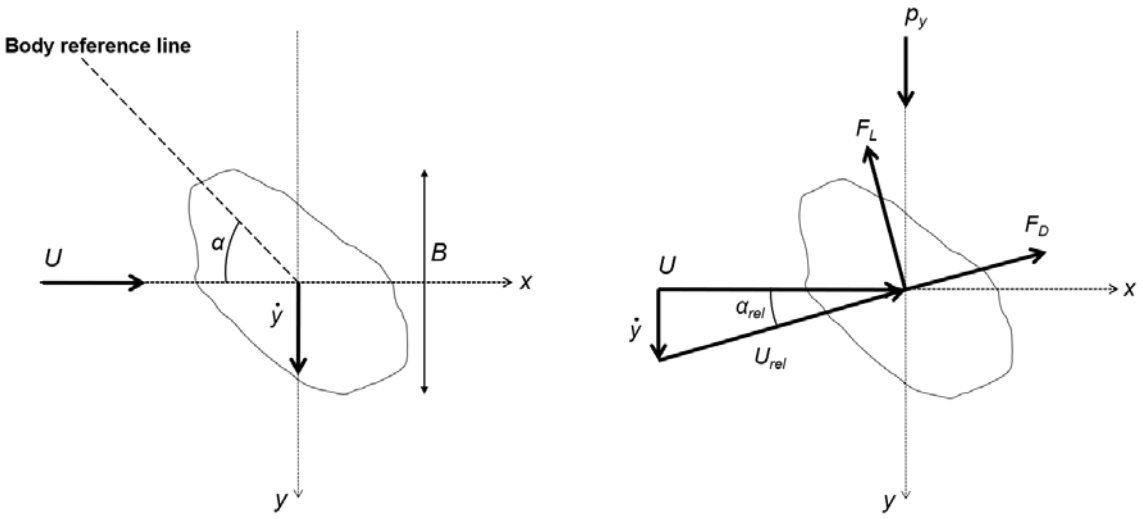

Figure 4.2. Geometry of a 1-DOF bluff section and the aerodynamic forces acting on it subjected to horizontal wind.

The first step of the classical Den Hartog derivation is to define the vertical component force on the body due to the wind force, per unit length:

$$p_y = -F_L cos(\alpha_{rel}) - F_D sin(\alpha_{rel}) \tag{4.1}$$

where the lift and drag forces per unit length can be expressed as:

$$F_L = \frac{1}{2}\rho U_{rel}^2 B C_L(\alpha + \alpha_{rel}) \tag{4.2}$$

$$F_D = \frac{1}{2}\rho U_{rel}^2 B C_D(\alpha + \alpha_{rel}) \tag{4.3}$$

and $C_D(\alpha)$ and $C_L(\alpha)$ are the steady-state aerodynamic coefficients, which can be obtained from static wind tunnel tests assumed for nominally 2D flow, as functions of the angle of attack, α.

For the general case where the vertical motion of the body is significantly smaller than the wind speed (e.g., $\dot{y} << U$), the relative velocity can be approximated as the wind velocity:

$$sin(\alpha_{rel}) \approx \frac{\dot{y}}{U}, \quad cos(\alpha_{rel}) \approx 1, \quad U_{rel} \approx U \tag{4.4}$$

Considering a Taylor expansion of the mean aerodynamic force around $\dot{y} = 0$:

$$p_y(\dot{y}) \approx p_y(\dot{y} = 0) + \frac{dp_y}{d\dot{y}}\Big|_{\dot{y}=0} \dot{y} = p_y(\alpha_{rel} = 0) + \frac{dp_y}{d\alpha_{rel}}\Big|_{\alpha_{rel}=0} \frac{\dot{y}}{U} =$$

$$= p_{y0} - \frac{1}{2}\rho U^2 B \left(\frac{dC_L}{d\alpha} + C_D\right)\frac{\dot{y}}{U} \tag{4.5}$$

The aerodynamic force is then defined as the static wind force for the case of no motion of the body, p_{y0}, minus the dynamic component of the motion of the body, which corresponds to the dynamic force. The dynamic component of the aerodynamic force on the body is proportional to its velocity, $\dot{y}$, which exactly represents the damping force in the equation of motion. Galloping might occur if the change in the force acting on the body due to its motion is in the same direction as its motion.

The damped equation of motion of the SDOF system considering the aerodynamic force in the vertical direction is:

$$M\ddot{y} + C\dot{y} + Ky = p_y \tag{4.6}$$

and can be rearranged as:

$$\ddot{y} + 2(\zeta + \zeta_{aero})\omega_n\dot{y} + \omega_n^2 y = \frac{p_{y0}}{M} \tag{4.7}$$

where p_{y0} is a constant that gives a constant displacement, ζ is the structural damping ratio and ζ_{aero} is the aerodynamic damping ratio, which is proportional to the wind speed and it is normally positive:

$$\zeta_{aero} = \frac{\rho UB}{4M\omega_n}\left(\frac{dC_L}{d\alpha} + C_D\right) \tag{4.8}$$

Since the structural damping ratio is usually positive, galloping instability would only occur when:

$$(\zeta + \zeta_{aero}) < 0 \tag{4.9}$$

and in this condition:

$$\frac{dC_L}{d\alpha} + C_D < 0 \tag{4.10}$$

This condition, when the system has negative aerodynamic damping ratio, is known as the Den Hartog galloping criterion, in which the system is dynamically unstable and the vibration amplitude might increase exponentially.

4.2. AERODYNAMIC FORCE FORMULATIONS

Although several studies have dealt with formulations to describe galloping mechanisms on overhead electricity transmission lines, this research considers two existing 3-DOF quasi-steady aerodynamic force models:

- Model 1: Matsumiya *et al*. (2018) formulations for four conductors within a bundle:
  - Model 1A: “Aerodynamic force formulation for four-bundled conductors”.
  - Model 1B: “Aerodynamic force formulation for each subconductor”.
- Model 2: He and Macdonald (2016) formulation for an arbitrary rigid cross-section.

Matsumiya *et al*. (2018) presented two formulations for four conductors within a bundle (Model 1A and 1B), for which steady aerodynamic coefficients were measured in static wind tunnel tests, while He and Macdonald (2016) developed a model of arbitrary rigid cross-section that directly takes into account the effect of an aerodynamic centre (Model 2). A significant difference between the formulations presented in each one of the two researches is that Model 2 can be applied to any arbitrary geometry, while Model 1 was designed specifically for four-bundled conductors. Thus, regarding future application to full-scale structures, Model 2 was adopted in this study because it seems a promising approach with potential transferability to different geometric bundle arrangements (e.g., one, two, three, five, six, etc. conductors within a bundle). Therefore, this section describes in detail the structural and aerodynamic models of the formulations considered in this research. Hence, all the equations presented in this section have been taken from Matsumiya *et al*. (2018) and He and Macdonald (2016) to provide the descriptions of Model 1 and 2 respectively.

4.2.1. Matsumiya *et al.* (2018) formulation (Model 1)

Matsumiya *et al.* (2018) developed a modelling technique based on quasi-steady theory to simulate physically the large-amplitude, low-frequency galloping motion of a 3-DOF four-bundled conductor. This technique adopted two different formulations. The first one, “Aerodynamic force formulation for four-bundled conductors” (Model 1A), will be detailed in Section 4.2.3.1. The second formulation, “Aerodynamic Force Formulation for each subconductor” (Model 1B), will be described in Section 4.2.3.2. The results in the appropriate directions (along wind, cross wind and torsional) of the structural system obtained from the Model 1A, where the motion of the whole cable bundle is considered, did not give good

agreement with the response of the dynamic wind tunnel test. Nevertheless, the results from the Model 1B, where the force in each individual conductor is taken, were consistent with the corresponding test results. Therefore, these findings motivated the use of this formulation as an initial reference to analytically predict the onset of galloping instability in this study.

4.2.2. Description of the experimental wind-tunnel model developed by Matsumiya *et al.* (2018) (Model 1)

This section describes the experimental wind tunnel arrangement developed by Matsumiya *et al.* (2018) in the study of Model 1. A rigid-body section supported by four elastic cords on each side with "low" rigidity represents the bundle, as shown in Figure 4.3. The setup enables the section model to be subjected to large amplitude and low frequency vibrations in the three directions of motion considered, *x*, *y* and *z*. The holding stay cord supports are free to rotate and adjust the angle of attack desired for the tests. Each elastic cord consists of a two-bundled urethane rubber rope of 3 mm. The wind tunnel tests were performed in an Eiffel-type wind tunnel with a width of 1.6 m and a height of 2.5 m. The section model, which is 1 m long (denoted by *l* in Figure 4.3), was set up centrally at 1 m distance of the leeward of the outlet of the wind on the wide-open test space.

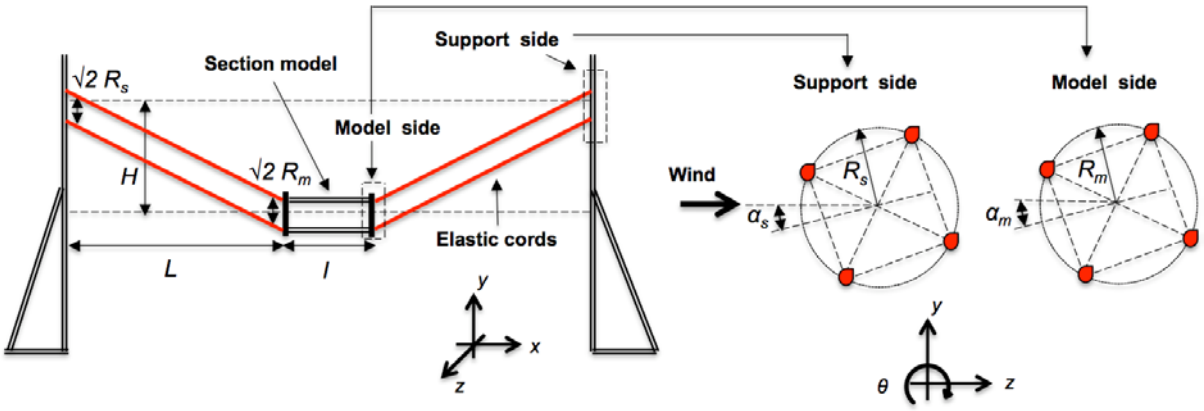

Figure 4.3. Definition of each parameter in the elastic model support system. [Adapted from Matsumiya *et al.* (2018)].

The turbulence intensity was less than 0.5% in a 1.2 m x 2 m (width and height respectively) area at a position of 0.5 m downstream of the outlet. A series of targets were attached to the sides of the section model in order to measure the vertical, horizontal and torsional displacements using a video tracking system. The wind is assumed to blow

horizontally and the horizontal direction, *x*, is defined along wind. The bundle is composed of four ACSR410 conductors, with a nominal cross-sectional area of 410 mm^2. The diameter of each subconductor is 28.5 mm and the distance between subconductors is 400 mm. There is an artificial snow accretion component with a sharp triangular tip on each subconductor, with a height that is half of the subconductor diameter, 14.25 mm, accounting for a maximum length of 42.75 mm.

For clarity of later description and better elucidation of nomenclature, Table 4.1 summarizes the parameters used in Model 1, their definitions and respective units of measurement. Positive vertical and horizontal displacements are considered in the upward and downwind directions respectively, with respect to the centre of the section model in the stationary condition, without wind speed. The distance between each elastic cord is $\sqrt{2}R_m$ on the section model side, and $\sqrt{2}R_s$ on the holding stay side. All of the cords are assumed to be identical, hence the parameters associated to them, such as mass (*m*), moment of inertia (*I*), length (*L*), tension (*T*) and axial rigidity (*EA*) are considered to be the same within each other. The self-weight of the elastic cords were ignored. A more detailed description of the wind tunnel arrangement was provided by Matsumiya *et al.* (2018).

Table 4.1. Nomenclature for parameters of Model 1. [Adapted from Matsumiya *et al*. (2018)].

Parameter	Definition	Unit
m	mass of the section model	Kg
I	mass moment of inertia of the section model	kg m^2
R_m	radius of the elastic chord support on the section model side	M
R_s	radius of the elastic cord support on the holding stay side	M
α_m	inclined angle of the elastic cord support on the section model side	Rad
α_s	inclined angle of the elastic cord support on the holding stay side	Rad
L	horizontal length of the elastic cords	M
l	length of the section model	M
H	sag (depth) of the section model from the support point in the stationary condition	M

T	tension in the elastic cords in the stationary condition	N
EA	axial rigidity of the elastic cords	N
y	vertical displacement	M
z	horizontal displacement	M
θ	torsional displacement (corresponds to the angle of attack in the wind direction)	M
D	diameter of the subconductor	M

4.2.3. Equations of motion of the structural model developed by Matsumiya *et al.* (2018) (Model 1)

The equations of motion of the structural model provided by Matsumiya *et al.* (2018) might exhibit nonlinear dynamic characteristics according to the oscillation amplitude. The 3-DOF differential equations for the vertical, horizontal and torsional motions are given respectively by:

$$m\ddot{y} + 2mC_y\dot{y} + 2\frac{T_1}{L_1}Y_1 + 2\frac{T_2}{L_2}Y_2 + 2\frac{T_3}{L_3}Y_3 + 2\frac{T_4}{L_4}Y_4 + mg = F_y \tag{4.11}$$

$$m\ddot{z} + 2mC_z\dot{z} + 2\frac{T_1}{L_1}Z_1 + 2\frac{T_2}{L_2}Z_2 + 2\frac{T_3}{L_3}Z_3 + 2\frac{T_4}{L_4}Z_4 = F_z \tag{4.12}$$

$$I\ddot{\theta} + 2IC_\theta\dot{\theta} + 2\frac{T_1}{L_1}R_1 + 2\frac{T_2}{L_2}R_2 + 2\frac{T_3}{L_3}R_3 + 2\frac{T_4}{L_4}R_4 = F_\theta \tag{4.13}$$

where: F_q $(q = y, z, \theta)$ is the aerodynamic force for each direction

y is the vertical displacement

z is the horizontal displacement

θ is the torsional displacement

m is the mass of the section model

I is the mass moment of inertia of the section model

C_q $(q = y, z, \theta)$ is the structural damping coefficient for each direction

T_i (i = 1, …,4) is the tension in the elastic cords at each instant

L_i (i = 1, …,4) is the length of the elastic cords at each instant

Positive values of displacement correspond to upward and downwind displacements from the centre of the section model in the stationary condition. The aerodynamic moment, F_θ, is

the sum of the static components plus the aeroelastic component. The terms that involve the T_i/L_i ratio are the structural terms related to the stiffness of the structural system because of the support geometry of the wires. The torsional angle, θ, is the instantaneous orientation of the conductor bundle. Y_i, Z_i, and R_i (i = 1, …,4) are the functions of the displacements related to the geometry of the wires and are expressed by Matsumiya *et al.* (2018) as follows:

$$\begin{aligned} Y_1 &= (y-H) + R_m \ sin\left(\tfrac{\pi}{4}+\theta\right) - R_s \ sin\left(\tfrac{\pi}{4}+\alpha_s\right) \\ Y_2 &= (y-H) - R_m \ cos\left(\tfrac{\pi}{4}+\theta\right) + R_s \ cos\left(\tfrac{\pi}{4}+\alpha_s\right) \\ Y_3 &= (y-H) - R_m \ sin\left(\tfrac{\pi}{4}+\theta\right) + R_s \ sin\left(\tfrac{\pi}{4}+\alpha_s\right) \\ Y_4 &= (y-H) + R_m \ cos\left(\tfrac{\pi}{4}+\theta\right) - R_s \ cos\left(\tfrac{\pi}{4}+\alpha_s\right) \end{aligned} \tag{4.14}$$

$$\begin{aligned} Z_1 &= z - R_m \ cos\left(\tfrac{\pi}{4}+\theta\right) + R_s \ cos\left(\tfrac{\pi}{4}+\alpha_s\right) \\ Z_2 &= z - R_m \ sin\left(\tfrac{\pi}{4}+\theta\right) + R_s \ cos\left(\tfrac{\pi}{4}+\alpha_s\right) \\ Z_3 &= z + R_m \ cos\left(\tfrac{\pi}{4}+\theta\right) - R_s \ cos\left(\tfrac{\pi}{4}+\alpha_s\right) \\ Z_4 &= z + R_m \ sin\left(\tfrac{\pi}{4}+\theta\right) - R_s \ cos\left(\tfrac{\pi}{4}+\alpha_s\right) \end{aligned} \tag{4.15}$$

$$\begin{aligned} R_1 &= (y-H)R_m \ cos\left(\tfrac{\pi}{4}+\theta\right) + zR_m \ sin\left(\tfrac{\pi}{4}+\theta\right) + R_m R_s sin(\theta-\alpha_s) \\ R_2 &= (y-H)R_m \ sin\left(\tfrac{\pi}{4}+\theta\right) - zR_m \ cos\left(\tfrac{\pi}{4}+\theta\right) + R_m R_s sin(\theta-\alpha_s) \\ R_3 &= -(y-H)R_m \ cos\left(\tfrac{\pi}{4}+\theta\right) - zR_m \ sin\left(\tfrac{\pi}{4}+\theta\right) + R_m R_s sin(\theta-\alpha_s) \\ R_4 &= -(y-H)R_m \ sin\left(\tfrac{\pi}{4}+\theta\right) + zR_m \ cos\left(\tfrac{\pi}{4}+\theta\right) + R_m R_s sin(\theta-\alpha_s) \end{aligned} \tag{4.16}$$

The relationships between the instantaneous tension, T_i, and length, L_i, of each elastic cord are given respectively by:

$$\frac{T_i}{L_i} = EA\left(\frac{1}{L_{i0}} - \frac{1}{L_i}\right) \tag{4.17}$$

$$L_i = \sqrt{L^2 + {Y_i}^2 + {Z_i}^2} \tag{4.18}$$

T_i (i = 1, …,4) in Equation 4.17 is the additional tension due to dynamics, while L_i (i = 1, …,4) is the instantaneous length when the tension is variable.

The static length of the elastic cord, L_{i0}, i.e. with no load applied, is derived from the length of the elastic cord in the stationary condition without wind, L_{ig}, and it is expressed as:

$$L_{i0} = \frac{EA}{T+EA} L_{ig} \tag{4.19}$$

where L_{i0} is the cut length

L_{ig} is the gravity stretch length

T is the tension in the elastic cords in the stationary condition

The tension, T, in the Equation 4.19 is the tension just due to the static weight of the model. L_{ig} is the length under the weight of the 4-bundle specimen hanging on it (with the gravity load acting on it). If both sides of the Equation 4.19 are multiplied by (T+EA)/EA, then the length in the stationary condition without wind is given by $L_{ig} = L_{i0}(1 + T/EA)$, where T/EA is the strain and 1+T/EA is the deformed length divided by the original length. Similarly, rearrange of Equation 4.17 gives $L_i = L_{i0}(1 + T/EA)$. L_{ig} can be calculated from the Equations 4.17, 4.18, 4.19 when $(y, z, \theta) = (0, 0, \alpha_m)$.

The linearized equations of motion can be derived using Equations 4.14, 4.15 and 4.16. When $R_m = R_s = \alpha_m = \alpha_s = 0$ without the application of any external forces, the natural frequencies are described by:

$$f_{z0} = \frac{1}{2\pi}\sqrt{\frac{g}{H}}, \quad f_{y0} = \frac{1}{2\pi}\sqrt{\frac{g}{H}}\sqrt{1 + \frac{EAH^2}{TL_g^2}}, \quad f_{\theta 0} = \frac{1}{2\pi}\sqrt{\frac{g}{H}}\frac{R_m}{r}\sqrt{1 + \frac{EAH^2}{2TL_g^2}} \tag{4.20}$$

$$\mathrm{L}_g = \sqrt{\mathrm{L}^2 + \mathrm{H}^2} \tag{4.21}$$

$$r = \sqrt{\frac{\mathrm{I}}{m}} \tag{4.22}$$

where: f_{z0} is the frequency of the horizontal motion [Hz]

f_{y0} is the frequency of the vertical motion [Hz]

$f_{\theta 0}$ is the frequency of the torsional motion [Hz]

L_g is the length of the elastic cord [m]

r is the radius of gyration of the section model around the x axis [m]

The tension, T, is given by:

$$T = \frac{mg}{8}\frac{L_g}{H} \tag{4.23}$$

The validity of the previous equations was confirmed by Matsumiya *et al.* (2018) with free vibration tests at a wind speed of 0 m/s. The natural frequency characteristics and the structural damping of the system were estimated by Matsumiya *et al.* (2018) from these tests. The responses were measured individually in each of the three directions after applying an initial displacement in one direction for each test, where the natural frequency and structural

damping of the model were found to change with the change in the oscillation amplitude. In addition, while a shift in the natural frequency with increasing amplitude was identified, particularly in the torsional direction, an increase in the structural damping ratio with amplitude was approximated by Matsumiya *et al.* (2018) by a linear relationship. There, the system response was found to be sensitive to the structural damping coefficients at different peak-to peak amplitudes.

Alternatively to the classical modelling of the damping force, $2\omega\zeta\frac{dq}{dt}$, the damping force determined in Model 1 has been expressed as $2mC_q\frac{dq}{dt}$, where the structural damping coefficient, C_q, is found by multiplying the logarithmic decrement, δ_q, by the natural frequency, f_q, expressed by:

$$C_q = \delta_q f_q \tag{4.24}$$

Therefore, the changes in the structural damping coefficient for each direction, C_q $(q = y, z, \theta)$, with the amplitude for each direction, A_q $(q = y, z, \theta)$, have been linearized in the following form:

$$C_q(A_q) = C_{q0} + C_{q1}A_q \tag{4.25}$$

where: C_{q0} $(q = y, z, \theta)$ is the structural damping coefficient at zero-amplitude

C_{q1} $(q = y, z, \theta)$ is the slope coefficient

The definition of the quasi-steady aerodynamic forces, drag (in N), lift (in N) and moment (in Nm), considered by Matsumiya *et al.* (2018) is given by:

$$Drag = \frac{1}{2}\rho U^2 A_l l C_{Df} \tag{4.26}$$

$$Lift = \frac{1}{2}\rho U^2 A_l l C_{Lf} \tag{4.27}$$

$$Moment = \frac{1}{2}\rho U^2 A_l B_l l C_{Mf} \tag{4.28}$$

where: ρ is the air density [kg/m^3]

U is the wind velocity [m/s]

l is the length of the section model [m]

C_{Df} is the drag aerodynamic coefficient

C_{Lf} is the lift aerodynamic coefficient

C_{Mf} is the moment aerodynamic coefficient

In the case of a four-bundled conductor, A_l and B_l are defined by $A_l = 4D$, $B_l = B$, where D is the conductor diameter [m] and B is the centre interval of the conductor [m]

4.2.3.1. *Aerodynamic force formulation for four-bundled conductors (Model 1A)*

In this first formulation presented by Matsumiya *et al*. (2018), the aerodynamic forces were measured on the whole bundle, based on the displacements of the centre midpoint of the bundle in the global coordinate system. On the basis of the quasi-steady theory, the predominant parameter to describe the motion of the section is the relative velocity between the wind and the body velocity, which is a function of the angle of attack. The steady aerodynamic coefficients of the individual subconductors are taken jointly. The quasi-steady aerodynamic forces, namely the drag, D_f , lift, L_f , and moment, M_f , are then given respectively by:

$$D_f = \frac{1}{2}\rho U_r^2 4Dl(-\ C_{Lf}(\phi_r)\ sin(\alpha_r) + C_{Df}(\phi_r)\ cos(\alpha_r)) \tag{4.29}$$

$$L_f = \frac{1}{2}\rho U_r^2 4Dl(C_{Lf}(\phi_r)\ cos(\alpha_r) + C_{Df}(\phi_r)\ \sin(\alpha_r)) \tag{4.30}$$

$$M_f = \frac{1}{2}\rho U_r^2 4BDlC_{Mf}(\phi_r) \tag{4.31}$$

The magnitude of the relative angle of attack, ϕ_r, and the relative wind speed, U_r, at the midpoint of all four conductors are:

$$\phi_r = \theta + \alpha_r \tag{4.32}$$

$$\alpha_r = \tan^{-1}\left(\frac{-\dot{y}}{U-\dot{z}}\right) \tag{4.33}$$

$$U_r^2 = (U-\dot{z})^2 + (-\dot{y})^2 \tag{4.34}$$

The angle between the horizontal axis and the direction of the relative wind speed, U_r, is given as α_r. Equations 4.29 to 4.31, which define the aerodynamic forces, do not involve the angular velocity. The drag, lift and moment are dependent on the relative wind speed, U_r, which is only a function of the vertical and horizontal velocity, $\dot{y}$ and $\dot{z}$, but not of the torsional velocity, $\dot{\theta}$. The steady aerodynamic coefficients of the four-bundled conductor, C_{Df}, C_{Lf} and C_{Mf}, respectively are functions of ϕ_r, which is a function of α_r. However, α_r is only a function of the vertical and horizontal velocity, $\dot{y}$ and $\dot{z}$, and does not depend on the torsional velocity, $\dot{\theta}$. Therefore, the relative angle of attack changes as the translational velocity changes, but without involving the torsional velocity if we neglect any change in the moment due to the angular velocity.

4.2.3.2. *Aerodynamic force formulation for each subconductor (Model 1B)*

The second formulation proposed by Matsumiya *et al*. (2018) considered the aerodynamic

force for each subconductor. The main difference between Model 1A and Model 1B is the way the rotational velocity is considered. Model 1A treats the whole section as a single cross-section, neglects the velocity of each subconductor due to rotation, and only takes into account the translational velocity of the centre of the bundle in the horizontal and vertical directions. Although the independent motion of each subconductor is not taken into account in Model 1B, the aerodynamic forces acting on each one are calculated separately. When the four-bundled conductors exhibit torsional motion, each subconductor exhibits velocity in a circumferential direction. This formulation describes the motion of each individual subconductor by accounting their local velocities including the component of each translational velocity due to the rotation about the centre of the bundle. The main parameters for this aerodynamic formulation are defined in Figure 4.4.

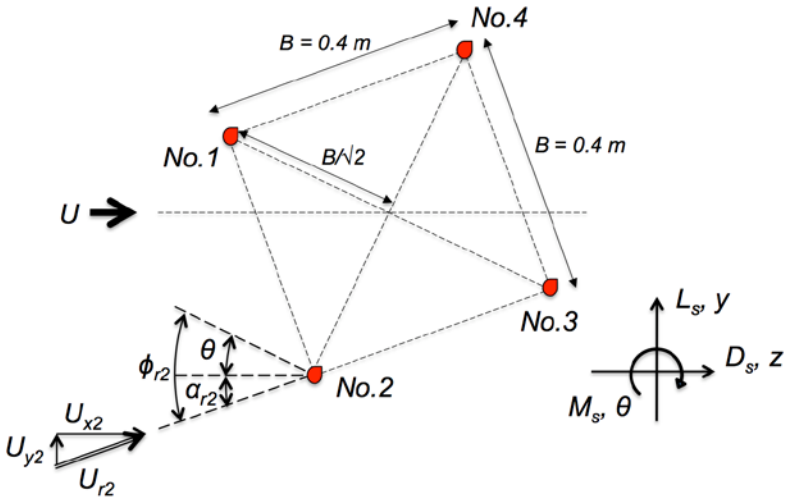

Figure 4.4. Definition of conductor number and each parameter for Model 1B. [Adapted from Matsumiya *et al.* (2018)].

The angle between the horizontal axis and the direction of the relative wind speed, U_{ri}, is given by α_{ri}. The relative angle of attack ϕ_{ri} and the relative wind speed U_{ri} for each subconductor (i = 1, …, 4) are derived as:

$$\phi_{ri} = \theta + \alpha_{ri} \tag{4.35}$$

$$\alpha_{ri} = \tan^{-1}\left(\frac{U_{yi}}{U_{zi}}\right) \tag{4.36}$$

$$U_{ri} = \sqrt{U_{yi}^2 + U_{zi}^2} \tag{4.37}$$

$$U_{y1} = -\dot{y} - \frac{B}{\sqrt{2}}\dot{\theta}cos\left(\frac{\pi}{4} + \theta\right), \qquad U_{z1} = U - \dot{z} - \frac{B}{\sqrt{2}}\dot{\theta}sin\left(\frac{\pi}{4} + \theta\right) \tag{4.38}$$

$$U_{y2} = -\dot{y} - \frac{B}{\sqrt{2}}\dot{\theta}sin\left(\frac{\pi}{4} + \theta\right), \qquad U_{z2} = U - \dot{z} + \frac{B}{\sqrt{2}}\dot{\theta}cos\left(\frac{\pi}{4} + \theta\right) \tag{4.39}$$

$$U_{y3} = -\dot{y} + \frac{B}{\sqrt{2}}\dot{\theta}cos\left(\frac{\pi}{4} + \theta\right), \qquad U_{z3} = U - \dot{z} + \frac{B}{\sqrt{2}}\dot{\theta}sin\left(\frac{\pi}{4} + \theta\right) \tag{4.40}$$

$$U_{y4} = -\dot{y} + \frac{B}{\sqrt{2}}\dot{\theta}sin\left(\frac{\pi}{4} + \theta\right), \qquad U_{z4} = U - \dot{z} - \frac{B}{\sqrt{2}}\dot{\theta}cos\left(\frac{\pi}{4} + \theta\right) \tag{4.41}$$

Unlike Model 1A, the aerodynamic forces for Model 1B, defined by Equations 4.42 to 4.44, take into account the angular velocity. The drag, lift and moment quasi-steady aerodynamic forces for each subconductor, D_{si}, L_{si} and M_{si}, (i = 1, …, 4), are dependent on the relative wind speed, U_{ri}, which is a function of the vertical, horizontal and torsional velocity, $\dot{y}$, $\dot{z}$ and $\dot{\theta}$. The steady aerodynamic coefficients for each subconductor, C_{Di}, C_{Li} and C_{Mi}, are functions of ϕ_{ri}, and therefore of α_{ri}, which is then a function of the vertical, horizontal and torsional velocity, $\dot{y}$, $\dot{z}$ and $\dot{\theta}$. Then, the relative angle of attack changes as the translational velocity changes involving the torsional velocity and taking into account the change in the moment due to the angular velocity.

The quasi-steady aerodynamic forces, D_s, L_s and M_s, of the bundle are defined by:

$$D_s = \sum_{i=1}^{4} D_{si} \tag{4.42}$$

$$L_s = \sum_{i=1}^{4} L_{si} \tag{4.43}$$

$$M_s = \sum_{i=1}^{4} M_{si} + \frac{B}{\sqrt{2}}(L_{s1} - D_{s2} - L_{s3} + D_{s4})cos\left(\frac{\pi}{4} + \theta\right) + \\ + \frac{B}{\sqrt{2}}(D_{s1} + L_{s2} - D_{s3} - L_{s4})sin\left(\frac{\pi}{4} + \theta\right) \tag{4.44}$$

The individual drag, D_{si}, lift, L_{si}, and aerodynamic pitching moment, M_{si}, (i = 1, …, 4), experienced by each one of the four subconductors are given by:

$$D_{si} = \frac{1}{2}\rho U_{ri}^2 Dl(-C_{Li}(\phi_{ri})\ sin(\alpha_{ri}) + C_{Di}(\phi_{ri})\ cos(\alpha_{ri})) \tag{4.45}$$

$$L_{si} = \frac{1}{2}\rho U_{ri}^2 Dl(C_{Li}(\phi_{ri})\ cos(\alpha_{ri}) + C_{Di}(\phi_{ri})\ sin(\alpha_{ri})) \tag{4.46}$$

$$M_{si} = \frac{1}{2}\rho U_{ri}^2 D^2 l C_{Mi}(\phi_{ri}) \tag{4.47}$$

where C_{Di}, C_{Li} and C_{Mi} (i = 1, …, 4) are the steady aerodynamic coefficients for each subconductor due to the action of each aerodynamic force, which are taken to be only functions of the relative angle of attack, ϕ_{ri}.

For the quasi-steady theory, the body is translated with certain velocity, from which the

relative velocity can then be obtained. But if the rotational velocity of the body is considered, some uncertainties are created because the relative velocities of each point in the cross-section are different (some parts of the body goes up while others goes down). With respect to Model 1A, when calculations are split into individual subconductors, as detailed in this Model 1B, each translational velocity can be locally identified due to the rotation about the centre because the distance to the centre of rotation is small. Any point of the bundle has a translational velocity equal to the angular velocity times the distance to the point from the centre of the bundle in the direction normal to the line between the point and the centre of the bundle. Since the size of the subconductors is small, the difference in the velocity of the different points across the section might be negligible, so the velocity is considered as the velocity at the centre point of each subconductor in order to use its local velocity due to that rotation. Nevertheless, it should be noted that strictly speaking, the outside part of a rotating conductor has a higher relative velocity than the inside part of the conductor. If each subconductor has a different velocity due to the rotation, then the translational velocity of the whole bundle is added (which is added equally to all of the subconductors) giving the total velocity of each subconductor. From the relative velocity and the steady aerodynamic coefficients for each subconductor measured by Matsumiya *et al.* (2018), the predictions of Model 1B were similar to the measured dynamic behaviour of this bundle in the full-scale test. Therefore, there is evidence that the predictions are good when the individual local velocities of each subconductor are considered.

4.2.4. Description of the model developed by He and Macdonald (2016) (Model 2)

He and Macdonald (2016) presented a two dimensional model of a 3-DOF body of arbitrary rigid cross-section to study the galloping stability based on the quasi-steady theory. This model makes use of the aerodynamic centre analogy. An aerodynamic centre represents the effect of the torsional velocity on the aerodynamic forces. The forces on the aerodynamic centre in the presence of translational and rotational motion are the same to the forces on the body if stationary with the same relative velocity between the wind and the aerodynamic centre. Therefore, given the formulation for Model 2, there is not any difference between the aerodynamic centre for models of a single conductor or for bundled conductors models.

The geometry of the body and the parameters involved in the system are shown in Figure 4.5. Alternatively to Model 1, which consists of four subconductors within the bundle, the geometry considered in Model 2 is not explicitly based on bundled conductors and it can be

easily applied to different geometric arrangements. The inertial coupling is not considered, so the elastic centre (point *O*) coincides with the centre of mass. This applies to symmetrical sections or lightly iced sections with negligible shift in the centre of mass due to ice.

There are two principal axes of the system, horizontal, *x*, and vertical, *y*, while θ is the rotation of the cross-section between the *x* axis and the dashed line in Figure 4.5, which is a reference line of the orientation of the shape of the body. The rotation of the cross-section, θ, includes the static rotation (due to the weight of the ice accretion or the mean wind load), θ_0, and a dynamic component, θ_d. The structural stiffness in the horizontal, vertical and torsional direction is given by k_x, k_y and k_θ respectively. The position of the aerodynamic centre for the section considered (point *A* in Figure 4.5), is defined by the distance from the elastic centre L_a, and γ_r which is the angle measured clock-wise from the reference line of the orientation of the shape of the body. The angle between the wind direction and the *x* axis is represented by α_0 while α is the angle between the wind direction and the body reference line such as $\alpha = \alpha_0 + \theta$.

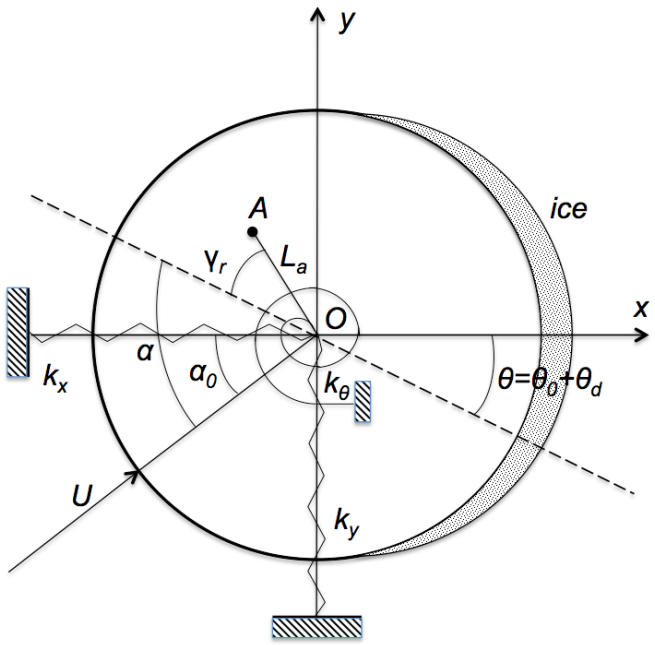

Figure 4.5. Cross-sectional model of the body and definition of parameters for Model 2. [Adapted from He and Macdonald (2016)].

There are three main directions in the structural arrangement, which are the direction of the principal axis, *x*, the direction of the wind velocity and the orientation of the body. If the cross-section of the bundle is square, the reference line of the orientation of the shape of the body goes through the middle of the square, and it is not necessarily the same as the *x* direction.

If the bundle is rotated due to a higher amount of ice in one side, the principal axes are dependent on the support structure, which is the rest of the transmission lines, i.e., the catenary. Generally, there are two main axis, vertical and horizontal, but when the mean wind goes across the section, there is no longer sagging in the vertical plane, since it is sagging in an inclined plane because both the wind and the gravity are acting simultaneously. Strictly speaking, the structural axes under these circumstances are in the plane of the sag and normal to it, so without wind the bundle is just sagging vertically.

Figure 4.6 highlights the velocity components of the model, the mean wind velocity, the components of velocity of the aerodynamic centre and the relative velocity between the wind and the aerodynamic centre. The mean wind velocity, U, is measured at an angle α_0 from the *x* axis, while the components of the translational velocity of the body in the *x* and the *y* directions are given by $\dot{x}$ and $\dot{y}$ respectively. The component of velocity of the aerodynamic centre due to the rotational velocity of the section is denoted as $U_{rot} = L_a\dot{\theta}$. The resultant of all these previous components is then the relative velocity, U_{rel}. The relative angle of attack is defined by α_{rel}.

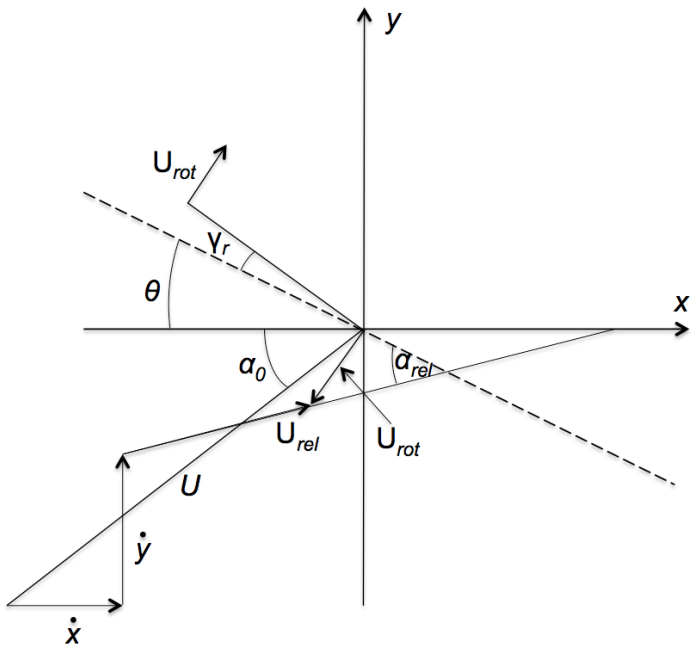

Figure 4.6. Definition of the velocity components and related angles of the Model 2. [Adapted from He and Macdonald (2016)].

For clarity of later description and better elucidation of nomenclature, Table 4.2 summarises the nomenclature for parameters used in Model 2 and their definitions.

Table 4.2. Nomenclature for parameters of Model 2.

Parameter	Definition
x, y	principal structural axes of the system
θ	rotation of the cross-section measured between the *x* axis and a reference line
θ_0	static rotation of the shape due to the weight of ice or the mean wind load
θ_d	dynamic component
k_x, k_y, k_θ	structural stiffnesses
L_a	aerodynamic centre radius
γ_r	aerodynamic centre angle from the body reference line
α	angle between wind direction and body reference line
α_0	angle between wind direction and *x* axis
α_{rel}	angle between relative velocity and reference line
U	mean wind velocity at an angle of α_0 with respect to *x*
U_{rel}	relative velocity (resultant of U and U_{rot} components)
U_{rot}	component of velocity of the aerodynamic centre due to the rotational velocity of the section

The analytical study of torsional galloping based on the quasi-steady theory raises two problems: the aerodynamic forces on an arbitrary geometry are dependent on the angle of attack and the angular velocity, and the relative velocity as well as the angle of attack vary along the section of the body. There is no precise theoretical method to take into account the effect of the rotational velocity on bluff bodies based on the linear quasi-steady analysis. Therefore, to represent these effects, the aerodynamic centre parameter was first introduced by Slater (1969) and Blevins and Iwan (1974) on the basis of the three-quarter chord point in flutter instability analysis of airfoils (Bisplinghoff and Ashley, 1962). An aerodynamic centre is a point for which the relative velocity between the wind and that point, combined with the static force coefficients, emulates the force on the body in the presence of translational and rotational motion. Therefore, the forces on the aerodynamic centre in the presence of that motion are the same to the forces

on the body if stationary with the same relative velocity of the wind. Considering a situation in 2 dimensions, where the body has some translational and rotational velocity, i.e. 3 components of velocity, the position of an aerodynamic centre can be found on that body or beyond the body. The major motivation for the use of the aerodynamic centre parameter is to find a position for which, during the dynamic test, the relative velocity of that point matches the actual observed behaviour of the structure.

According to He and Macdonald (2016), the assumption of the existence of an aerodynamic centre has been found to be true in certain conditions, such as, generally, in the presence of a high enough reduced velocity. The way the analysis was conducted by He and Macdonald (2016) implies that there is not any difference between considering aerodynamic centre for single conductor or for the whole bundle. For a given cross-sectional shape of, for example a collection of four conductors in a bundle, the conductors stay in the same position relative to the rigid cross-section and the mass remain constant for any other cross-sectional shape. This assumption was taken a stage further by He and Macdonald (2016) by considering there is a rotation velocity of the body.

Therefore, the relative velocity between the wind and any point in the body is different depending on its position relative to the centre of rotation. Then, the relative velocity is varying over the cross-section depending on the direction of the wind (upwards, downwards). So, according to He and Macdonald (2016), the basic quasi-steady theory does not correctly hold under these circumstances. However, He and Macdonald (2016) performed some wind tunnel experiments considering the previous assumption with the aim to make it work for Model 2 and assess if it models the situation well enough.

The analytical results obtained by He and Macdonald (2016) were fairly consistent with the wind tunnel measurements. However, measured data were limited to one set of natural frequencies without changing stiffness or other properties and without quantifying the magnitude of the vibrations obtained. The wind tunnel results were based on rectangular prisms with different aspect ratios based on the data from Norberg (1993). For both square and rectangular sections of the prisms, the location of the aerodynamic centre was taken as half of the long side of the section, with the orientation of the aerodynamic centre aligned with the wind velocity according to the conventional approximation, described by Nakamura and Mizota (1975).

4.2.5. Aerodynamic force formulation developed by He and Macdonald (2016) (Model 2)

This section shows the aerodynamic force formulation and the derivation of the aerodynamic damping matrix, as detailed by He and Macdonald (2016), which will be used in this research to conduct the estimation of the position of the aerodynamic centre parameter and the analysis of galloping stability.

In this Model 2, which treats the whole bundle as a single cross-section, the aerodynamic forces, drag, lift and moment on it are dependent on the velocity of an aerodynamic centre, which is some place relative to the centre of that cross-sectional shape. They are given by:

$$F_x = \frac{1}{2}\rho {U_{rel}}^2 D(-C_L(\alpha_{rel})\ sin(\alpha_{rel}-\theta) + C_D(\alpha_{rel})\ cos(\alpha_{rel}-\theta)) \quad (4.48)$$

$$F_y = \frac{1}{2}\rho {U_{rel}}^2 D(C_L(\alpha_{rel})\ cos(\alpha_{rel}-\theta) + C_D(\alpha_{rel})\ sin(\alpha_{rel}-\theta)) \quad (4.49)$$

$$F_\theta = \frac{1}{2}\rho {U_{rel}}^2 D^2(C_M(\alpha_{rel})) \quad (4.50)$$

where F_q $(q = x, y, \theta)$ are the drag, lift forces and aerodynamic moment respectively

ρ is the density of air

U_{rel} is the relative velocity

D is a reference dimension of the body

$C_D(\alpha_{rel})$, $C_L(\alpha_{rel})$ and $C_M(\alpha_{rel})$ are, respectively the drag, lift and moment coefficients of the cross-section, which are taken to be only functions of the relative angle of attack, α_{rel}

θ is the angle measured between the x axis and a reference line

Similarly to the formulation developed in Model 1, the aerodynamic coefficients are functions of only the relative angle of attack. The magnitude of the instantaneous relative wind velocity and the relative angle of attack are given, respectively, by:

$$U_{rel} = \sqrt{\left(U\,sin(\alpha_0) - \dot{y} - \dot{\theta}L_a cos(\gamma_r+\theta)\right)^2 + \left(U\,cos(\alpha_0) - \dot{x} - \dot{\theta}L_a sin(\gamma_r+\theta)\right)^2} \quad (4.51)$$

$$\alpha_{rel} = arctan\left(\frac{U\,sin(\alpha_0)-\dot{y}-\dot{\theta}L_a cos(\gamma_r+\theta)}{U\,cos(\alpha_0)-\dot{x}-\dot{\theta}L_a sin(\gamma_r+\theta)}\right) + \theta \quad (4.52)$$

where: U is the mean wind velocity

α_0 is the angle between wind direction and x axis

$\dot{x}, \dot{y}, \dot{\theta}$ are the horizontal, vertical and rotational velocities respectively

L_a is the aerodynamic centre radius from O

γ_r is the angle between the line from O to the position of the aerodynamic centre and the body reference line

The galloping instability is considered by applying the Taylor expansion (Zeidler, 2013) to the aerodynamic forces and moment in the three directions of motion considered (represented respectively by the second, third and fourth terms in Equations 4.53 to 4.55) about the static equilibrium values (represented by the first term in Equations 4.53 to 4.55):

$$F_x = F_x|_{\dot{x}=\dot{y}=\dot{\theta}=\theta_d=0} + \dot{x}\frac{\partial F_x}{\partial \dot{x}}\Big|_{\dot{x}=\dot{y}=\dot{\theta}=\theta_d=0} + \dot{y}\frac{\partial F_x}{\partial \dot{y}}\Big|_{\dot{x}=\dot{y}=\dot{\theta}=\theta_d=0} + \dot{\theta}\frac{\partial F_x}{\partial \dot{\theta}}\Big|_{\dot{x}=\dot{y}=\dot{\theta}=\theta_d=0} \tag{4.53}$$

$$F_y = F_y|_{\dot{x}=\dot{y}=\dot{\theta}=\theta_d=0} + \dot{x}\frac{\partial F_y}{\partial \dot{x}}\Big|_{\dot{x}=\dot{y}=\dot{\theta}=\theta_d=0} + \dot{y}\frac{\partial F_y}{\partial \dot{y}}\Big|_{\dot{x}=\dot{y}=\dot{\theta}=\theta_d=0} + \dot{\theta}\frac{\partial F_y}{\partial \dot{\theta}}\Big|_{\dot{x}=\dot{y}=\dot{\theta}=\theta_d=0} \tag{4.54}$$

$$F_\theta = F_\theta|_{\dot{x}=\dot{y}=\dot{\theta}=\theta_d=0} + \dot{x}\frac{\partial F_\theta}{\partial \dot{x}}\Big|_{\dot{x}=\dot{y}=\dot{\theta}=\theta_d=0} + \dot{y}\frac{\partial F_\theta}{\partial \dot{y}}\Big|_{\dot{x}=\dot{y}=\dot{\theta}=\theta_d=0} + \dot{\theta}\frac{\partial F_\theta}{\partial \dot{\theta}}\Big|_{\dot{x}=\dot{y}=\dot{\theta}=\theta_d=0} \tag{4.55}$$

The chain rule is used to evaluate the derivatives:

$$\frac{d()}{d\dot{x}} = \frac{\partial()}{\partial U_{rel}}\frac{dU_{rel}}{d\dot{x}} + \frac{\partial()}{\partial \alpha_{rel}}\frac{d\alpha_{rel}}{d\dot{x}} \tag{4.56}$$

$$\frac{d()}{d\dot{y}} = \frac{\partial()}{\partial U_{rel}}\frac{dU_{rel}}{d\dot{y}} + \frac{\partial()}{\partial \alpha_{rel}}\frac{d\alpha_{rel}}{d\dot{y}} \tag{4.57}$$

$$\frac{d()}{d\dot{\theta}} = \frac{\partial()}{\partial U_{rel}}\frac{dU_{rel}}{d\dot{\theta}} + \frac{\partial()}{\partial \alpha_{rel}}\frac{d\alpha_{rel}}{d\dot{\theta}} \tag{4.58}$$

The resulting full aerodynamic damping matrix, C_a, for the 3-DOF model is composed by rearranging the nine terms of the derivatives and is given by:

$$C_a = -\begin{bmatrix} \frac{\partial F_x}{\partial \dot{x}} & \frac{\partial F_x}{\partial \dot{y}} & \frac{\partial F_x}{\partial \dot{\theta}} \\ \frac{\partial F_y}{\partial \dot{x}} & \frac{\partial F_y}{\partial \dot{y}} & \frac{\partial F_y}{\partial \dot{\theta}} \\ \frac{\partial F_\theta}{\partial \dot{x}} & \frac{\partial F_\theta}{\partial \dot{y}} & \frac{\partial F_\theta}{\partial \dot{\theta}} \end{bmatrix}_{\dot{x}=\dot{y}=\dot{\theta}=\theta_d=0} \tag{4.59}$$

The elements in the previous Jacobian matrix (Equation 4.59) physically represent the change in the vertical, horizontal and moment forces due to a unit velocity of the body in the vertical, horizontal and torsional directions from a stationary position. This matrix then results in:

$$C_a = \frac{\rho DU}{2}\begin{bmatrix} 2C_D & 2C_L & (C_L' + C_D) & (C_L - C_D') & 0 & 0 \\ 2C_L & -2C_D & (C_L - C_D') & -(C_L' + C_D) & 0 & 0 \\ 0 & 0 & 0 & 0 & 2DC_M & DC_M' \end{bmatrix} \begin{bmatrix} c^2 & cs & L_a s_{\alpha\theta\gamma} c \\ -cs & -s^2 & -L_a s_{\alpha\theta\gamma} s \\ s^2 & -cs & -L_a c_{\alpha\theta\gamma} s \\ cs & -c^2 & -L_a c_{\alpha\theta\gamma} c \\ c & s & L_a s_{\alpha\theta\gamma} \\ -s & c & L_a c_{\alpha\theta\gamma} \end{bmatrix} \tag{4.60}$$

where $c = cos\,(\alpha_0)$, $s = sin\,(\alpha_0)$, $c_{\alpha\theta\gamma} = cos\,(\alpha_0 + \theta_0 + \gamma_r)$ and $s_{\alpha\theta\gamma} = sin\,(\alpha_0 + \theta_0 + \gamma_r)$

C_D, C_L, C_M are, respectively, the drag, lift and moment coefficients with respect to the angle of attack. C_D', C_L', C_M' are, respectively, the "rates of change" of drag, lift and moment coefficients with respect to the angle of attack.

The aerodynamic coefficients and their rates of change are estimated at the angle between the wind and the shape in the static equilibrium configuration about which the dynamic stability is considered, i.e. at $\alpha_0 + \theta_0$ $(= \alpha$ for $\theta_d = 0)$.

The angle between the wind direction and the *x* axis, α_0, is only relevant if the direction of the wind is not along one of the main axes. In this analysis, the aerodynamic damping matrix is considered in relation to the structural principal axes, *x*, and therefore the dynamic response is ignored at this stage. When $\alpha_0 = 0$, the wind direction is along the *x*-axis. In this special case, the aerodynamic damping matrix, C_a, is presented as:

$$C_a = \frac{\rho DU}{2}\begin{bmatrix} 2C_D & -(C_L - C_D') & L_a\left[C_D s_{\theta\gamma} - (C_L - C_D')c_{\theta\gamma}\right] \\ 2C_L & (C_L' + C_D) & L_a\left[C_L s_{\theta\gamma} + (C_L' + C_D)c_{\theta\gamma}\right] \\ 2DC_M & DC_M' & DL_a\left[2C_M s_{\theta\gamma} + C_M' c_{\theta\gamma}\right] \end{bmatrix} \tag{4.61}$$

where $c_{\theta\gamma} = cos\,(\theta_0 + \gamma_r)$ and $s_{\theta\gamma} = sin\,(\theta_0 + \gamma_r)$

Figure 4.7 illustrates the velocity-related parameters of the model, the mean wind velocity, U, and the relative velocity between the wind and the aerodynamic centre, U_{rel}, in the stationary condition, e.g. $\dot{x} = \dot{y} = \dot{\theta} = \theta_d = 0$ and for the special case when $\alpha_0 = 0$.

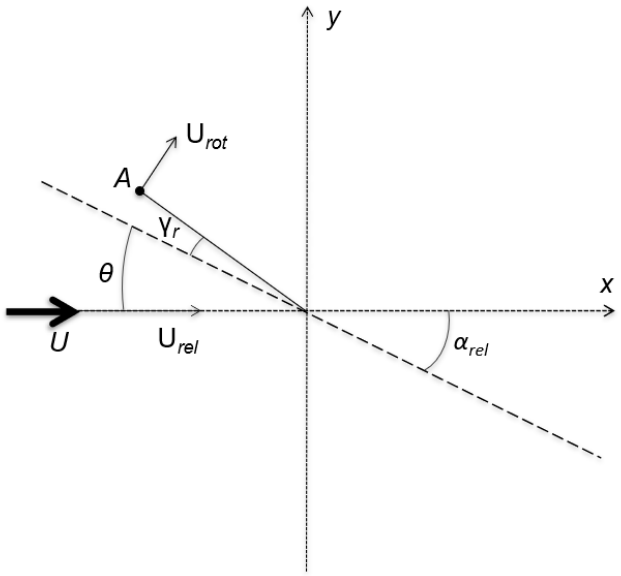

Figure 4.7. Definition of the velocity components and related angles of the Model 2 in the stationary conditions.

The detailed derivation of the elements of the aerodynamic damping matrix is explained by taking the bottom left element as an example. Physically, the bottom left element of the Jacobian matrix represents the change of the moment due to a unit velocity of the body in the horizontal direction from stationary position, which is along the same direction as the wind. According to Equations 4.59 and 4.61:

$$-\left[\frac{\partial F_\theta}{\partial \dot{x}}\right]_{\dot{x}=\dot{y}=\dot{\theta}=\theta_d=0} = \frac{\rho D U}{2} * 2DC_M \tag{4.62}$$

This element can be derived as follows. Firstly, the equation of the static aerodynamic moment induced by the wind blowing along the horizontal direction of the model (Equation 4.50) is considered:

$$F_\theta = \frac{1}{2}\rho U_{rel}^2 D^2 C_M(\alpha_{rel}) \tag{4.63}$$

where the relative velocity is given by:

$$U_{rel} = U - \dot{x} \tag{4.64}$$

Therefore, the relative velocity is substituted into the equation of the aerodynamic moment, which can be expressed as:

$$F_\theta = \frac{1}{2}\rho(U-\dot{x})^2 D^2 C_M = \frac{1}{2}\rho(U^2 - 2U\dot{x} + \dot{x}^2) D^2 C_M \tag{4.65}$$

If the horizontal displacement, $\dot{x}$, is very small compared with the magnitude of the wind speed, U, then $\dot{x}^2$ is negligible, hence:

$$F_\theta = \frac{1}{2}\rho(U^2 - 2U\dot{x})D^2C_M \tag{4.66}$$

The change in the aerodynamic moment from what it was only with the wind speed, U, without any horizontal velocity, $\dot{x}$, would be the same, e.g. U^2. This change, U^2, then cancels out, resulting in:

$$-\left[\frac{\partial F_\theta}{\partial \dot{x}}\right]_{\dot{x}=\dot{y}=\dot{\theta}=\theta_d=0} = \frac{F_\theta}{\dot{x}} = \frac{\frac{1}{2}\rho(-2U\dot{x})D^2C_M}{\dot{x}} = -\frac{\rho DU}{2} * 2DC_M \tag{4.67}$$

4.2.6. Comparison of notation between Model 1 and Model 2

In order to conduct further analysis based on Model 1 and Model 2, their formulations are studied in parallel to assess their compatibility. The differences in notation of some relevant parameters are summarised in Table 4.3.4.

Table 4.3. Comparison between Model 1 and Model 2 nomenclatures for parameters.

Parameter	Model 1	Model 2
Relative wind velocity	U_r	U_{rel}
Relative angle of attack	ϕ_r	α_{rel}
Horizontal force	D_f	$F_x 4l$
Vertical force	L_f	$F_y 4l$
Moment	M_f	$F_\theta 4Bl/D$
Stationary torsional displacement/ Support orientation	θ_0	α_s

In Model 1 it is assumed that wind blows horizontally and that the horizontal direction, *x*, is defined along the wind direction. However, Model 2 differs from this assumption since the mean wind velocity, U, is measured at an angle α_0 from the horizontal axis, *x*. The velocity-related parameters from both formulations are only equivalent for the special case that α_0 = 0 for the Model 2 formulation. If $\alpha_0 = 0$, then $\dot{x}$ is in the same direction as the mean wind velocity, U, and then the horizontal component is given by $U - \dot{x}$. In addition, Model 1 neglected the component of velocity of the aerodynamic centre due to the rotational velocity of the section, U_{rot}, so the reference line is just defined by θ rotated from the horizontal axis, *x*.

By simplifying the equation of the relative angle of attack according to the formulation from Model 2, α_{rel}, it can be compared with the equivalent expression developed in Model 1, ϕ_r.

The conductor diameter, D, defined in Model 1 (Equations 4.29 to 4.31) does not represent the same parameter as the reference dimension of the body, D, described in Model 2 (Equations 4.48 to 4.50). The reference dimension considered in Model 2 is *D*, which is denoted in this analysis as D_M. The reference dimension considered in Model 1 is 4*D*, represented by D_H. Therefore, $4D_H = D_M$. The relationship between both variables is given by $D(\text{Model } 1) = D(Model\ 2)/4$. Finally, the aerodynamic forces developed Model 1 includes a factor of length, *l*, because the total force is considered whereas the aerodynamic forces developed in Model 2 are expressed in terms of force per unit length. Despite the differences in notation and geometry, the two formulations Model 1 and Model 2 have been found to be compatible and suitable to conduct further analysis.

4.3. IDENTIFICATION OF THE POSITION OF AN AERODYNAMIC CENTRE

Following the strategy presented at the beginning of this chapter, the analysis conducted in this section takes as a baseline starting point the aerodynamic damping matrix presented in Model 2 (Equation 4.61). Then, the aerodynamic damping matrix for the formulation presented in Model 1B, based on the quasi-steady theory aerodynamic forces for each subconductor, was derived according to the approach detailed in Model 2.

The first two columns of both aerodynamic damping matrices obtained by each selected strategy physically represent the change in the vertical, horizontal and moment forces due to a unit velocity of the body in the vertical and horizontal directions. Therefore, these two columns agree exactly, while the third column of the matrix presented in Model 2 is a function of two unknown parameters, L_a and γ_r, representing the position of an aerodynamic centre, which is not considered in Model 1.

An aerodynamic centre represents the effect of the rotational velocity on the aerodynamic forces. It is therefore important to identify the unknown parameters which characterise the position of the aerodynamic centre, as used in Model 2. The identification can be achieved with the help of the nominal equivalency established between the individual elements of the two aerodynamic damping matrices. The identification process itself will use minimisation of the

difference, or residuals, obtained between the selected components of both damping matrices, whilst using the analytical expressions derived later in this chapter in combination with experimentally observed aerodynamic characteristics of the bundle studied in Matsumiya *et al*. (2018).

4.3.1 Derivation of the new aerodynamic damping matrix according to the Matsumiya *et al.* (2018) formulation following He and Macdonald (2016) approach

The Taylor expansion (Zeidler, 2013) is a linearization method, which in a 3D problem, is used to approximate the value of a function with two independent variables, $\dot{x}$ and $\dot{y}$, to an established point. This approximation can be done by considering a plane tangent to the surface on the established point, $f(\dot{x}_0, \dot{y}_0)$, in which the function is linearized. According to the Taylor expansion method, the slope of the plane can be obtained by using 1st order derivatives. After the derivative with respect to this curve is calculated, partial derivatives of the function with respect to the two independent variables are estimated, $\partial f/\partial \dot{x}$ and $\partial f/\partial \dot{y}$, resulting in multiple tangents if they are calculated analytically. Numerically, the tangents at the established point (where $\dot{x} = \dot{x}_0$ and $\dot{y} = \dot{y}_0$) represent the slope of the plane that gives two angles. Ultimately, the function is approximated to the desired point as the value of the function in that point plus their partial derivatives with respect to $\dot{x}$ and $\dot{y}$ (where $\dot{x} = \dot{x}_0$ and $\dot{y} = \dot{y}_0$). The actual points are given by the slope of the tangent plane multiplied by the distance $\dot{x} - \dot{x}_0$:

$$f(\dot{x},\dot{y}) = f(\dot{x}_0\ ,\dot{y}_0) + \frac{\partial f}{\partial \dot{x}}\Big|_{\substack{\dot{x}=\dot{x}_0 \\ \dot{y}=\dot{y}_0}} (\dot{x}-\dot{x}_0) + \frac{\partial f}{\partial \dot{y}}\Big|_{\substack{\dot{x}=\dot{x}_0 \\ \dot{y}=\dot{y}_0}} (\dot{y}-\dot{y}_0) + \\ + H.O.T.(Higher\ \ Order\ \ Term) \tag{4.68}$$

Better approximations could be obtained by considering higher order derivatives, which would result in shapes different than a plane, such as parabolic.

In a matrix form, the expression that includes the Jacobian matrix is given by:

$$\begin{bmatrix} F_x \\ F_y \end{bmatrix} = \begin{bmatrix} F_{\dot{x}_0} \\ F_{\dot{y}_0} \end{bmatrix} + \begin{bmatrix} \frac{\partial F_x}{\partial \dot{x}} & \frac{\partial F_x}{\partial \dot{y}} \\ \frac{\partial F_y}{\partial \dot{x}} & \frac{\partial F_y}{\partial \dot{y}} \end{bmatrix} \begin{bmatrix} \dot{x}-\dot{x}_0 \\ \dot{y}-\dot{y}_0 \end{bmatrix} + H.O.T.(Higher\ \ Order\ \ Term) \tag{4.69}$$

The Jacobian matrix corresponds to the linear term in the Taylor Expansion. In the Taylor Expansion the static term is the 1st term, which is basically the static equilibrium around the vibrations, and gives the forces when there is no velocity of the body, i.e. the forces on the static body. Therefore, the velocities in the different directions and the dynamic rotation are zero

($\dot{x}, \dot{y}, \dot{\theta}, \dot{\theta}_d = 0$). The rotation of the cross-section, θ, is also zero because there is not aerodynamic stiffness on the body. The next term of the Taylor expansion is the Jacobian matrix, which correspond to the changes in the forces and moment with respect to the velocity of the body in the three different directions considered, $\dot{x}$, $\dot{y}$ and $\dot{\theta}$. It is represented by the partial derivatives with respect to the velocities of the body multiplied by these velocities ignoring higher order terms ($\dot{x}^2, \dot{y}^2, \dot{\theta}^2$ ...).

The dynamic and the structural effects of the system (stiffness, axes orientation) are ignored by making the assumption that the wind remains along the horizontal direction. However, the effect of the different orientations of the body (ignoring its rotation) is considered by the estimation of the Jacobian matrix for each orientation of the body using the aerodynamic coefficients measured in the static test conducted in Model 1. In these tests, the body was rotated through a series of angles of attack, for which the aerodynamic coefficients were measured. Since Model 1 neglects the change of the moment in relation to the angular velocity, the elements of the right-hand column of the corresponding aerodynamic damping matrix are all zeros.

Therefore, in order to progress the proposed identification strategy, the new aerodynamic damping matrix according to Model 1 for each subconductor was derived following Model 2 linearisation approach for the special case where $\alpha_0 = 0$. The horizontal axis of the system is assumed to be along the wind for this special case, thus $\theta = \alpha$. The dynamic response is not considered at this stage with the aim to establish the equivalence of the dynamic forces where the principal structural axes are ignored. The first step involves definition of both cases, including their corresponding notation, such that they represent the equivalent conditions. Taking Model 1 formulation as a source, it is considered $\theta = \alpha_s + \theta_d$, where α_s is the static angle of attack and θ_d is the dynamic rotation, for $\theta_d = 0$. Taylor expansion of the aerodynamic forces and moment about the values of the static solution is applied to the analytical expressions derived in Model 1:

$$D_s = D_s|_{\dot{x}=\dot{y}=\dot{\theta}=\theta_d=\alpha_0=0} + \dot{x}\left.\frac{\partial D_s}{\partial \dot{x}}\right|_{\dot{x}=\dot{y}=\dot{\theta}=\theta_d=\alpha_0=0} + \\ + \dot{y}\left.\frac{\partial D_s}{\partial \dot{y}}\right|_{\dot{x}=\dot{y}=\dot{\theta}=\theta_d=\alpha_0=0} + \dot{\theta}\left.\frac{\partial D_s}{\partial \dot{\theta}}\right|_{\dot{x}=\dot{y}=\dot{\theta}=\theta_d=\alpha_0=0} \tag{4.70}$$

$$L_s = L_s|_{\dot{x}=\dot{y}=\dot{\theta}=\theta_d=\alpha_0=0} + \dot{x}\left.\frac{\partial L_s}{\partial \dot{x}}\right|_{\dot{x}=\dot{y}=\dot{\theta}=\theta_d=\alpha_0=0} +$$

$$+\dot{y}\frac{\partial L_s}{\partial \dot{y}}\Big|_{\dot{x}=\dot{y}=\dot{\theta}=\theta_d=\alpha_0=0}+\dot{\theta}\frac{\partial L_s}{\partial \dot{\theta}}\Big|_{\dot{x}=\dot{y}=\dot{\theta}=\theta_d=\alpha_0=0} \tag{4.71}$$

$$M_s = M_s|_{\dot{x}=\dot{y}=\dot{\theta}=\theta_d=\alpha_0=0}+\dot{x}\frac{\partial M_s}{\partial \dot{x}}\Big|_{\dot{x}=\dot{y}=\dot{\theta}=\theta_d=\alpha_0=0}+ +\dot{y}\frac{\partial M_s}{\partial \dot{y}}\Big|_{\dot{x}=\dot{y}=\dot{\theta}=\theta_d=\alpha_0=0}+\dot{\theta}\frac{\partial M_s}{\partial \dot{\theta}}\Big|_{\dot{x}=\dot{y}=\dot{\theta}=\theta_d=\alpha_0=0} \tag{4.72}$$

The chain rule is used to derive the aerodynamic damping matrix by evaluating the derivatives where there is an implicit dependency on the aerodynamic conditions and flow kinematics. It is expressed as:

$$\frac{d()}{d\dot{x}} = \frac{\partial()}{\partial U_{ri}}\frac{dU_{ri}}{d\dot{x}}+\frac{\partial()}{\partial \phi_{ri}}\frac{d\phi_{ri}}{d\dot{x}} \tag{4.73}$$

$$\frac{d()}{d\dot{y}} = \frac{\partial()}{\partial U_{ri}}\frac{dU_{ri}}{d\dot{y}}+\frac{\partial()}{\partial \phi_{ri}}\frac{d\phi_{ri}}{d\dot{y}} \tag{4.74}$$

$$\frac{d()}{d\dot{\theta}} = \frac{\partial()}{\partial U_{ri}}\frac{dU_{ri}}{d\dot{\theta}}+\frac{\partial()}{\partial \phi_{ri}}\frac{d\phi_{ri}}{d\dot{\theta}} \tag{4.75}$$

The resulting full aerodynamic damping matrix, C_a, is composed by rearranging the 9 terms of the derivatives following the standard linear matrix notation pertinent to the velocity-dependent terms and is expressed as:

$$C_a = -\begin{bmatrix} \frac{\partial D_s}{\partial \dot{x}} & \frac{\partial D_s}{\partial \dot{y}} & \frac{\partial D_s}{\partial \dot{\theta}} \\ \frac{\partial L_s}{\partial \dot{x}} & \frac{\partial L_s}{\partial \dot{y}} & \frac{\partial L_s}{\partial \dot{\theta}} \\ \frac{\partial M_s}{\partial \dot{x}} & \frac{\partial M_s}{\partial \dot{y}} & \frac{\partial M_s}{\partial \dot{\theta}} \end{bmatrix}_{\dot{x}=\dot{y}=\dot{\theta}=\theta_d=\alpha_0=0} \tag{4.76}$$

The equivalent aerodynamic damping matrix is then derived as:

$$C_a = \frac{\rho D_M U}{2}\begin{bmatrix} \frac{1}{2}*\Sigma C_{Di} & \frac{1}{4}*(-\Sigma C_{Li}+\Sigma C'_{Di}) & Element\ (1,3) \\ \frac{1}{2}*\Sigma C_{Li} & \frac{1}{4}*(\Sigma C'_{Li}+\Sigma C_{Di}) & Element\ (2,3) \\ \frac{{D_M}^2}{2B}*\Sigma C_{Mi}+ISC(3,1) & \frac{{D_M}^2}{4B}*\Sigma C'_{Mi}+ISC(3,2) & Element\ (3,3) \end{bmatrix} \tag{4.77}$$

where: $\Sigma C_{Di} = C_{D1} + C_{D2} + C_{D3} + C_{D4}$ $\quad \Sigma C'_{Di} = C'_{D1} + C'_{D2} + C'_{D3} + C'_{D4}$

$\Sigma C_{Li} = C_{L1} + C_{L2} + C_{L3} + C_{L4}$ $\quad \Sigma C'_{Li} = C'_{L1} + C'_{L2} + C'_{L3} + C'_{L4}$

$\Sigma C_{Mi} = C_{M1} + C_{M2} + C_{M3} + C_{M4}$ $\quad \Sigma C'_{Mi} = C'_{M1} + C'_{M2} + C'_{M3} + C'_{M4}$

The conductor diameter, D, defined in Model 1 (Equations 4.29 to 4.31) is denoted in this analysis by D_M, not to be confused with the reference dimension of the body, D, described in Model 2 (Equations 4.48 to 4.50). The relationship between the conductor diameter, D_M, and the reference dimension of the body according to Model 1 formulation, D, is given by $D_M = D/4$:

$$\begin{aligned} Element(1,3) = \frac{B}{4} * cos(\alpha_s) * (C_{D1} - C_{D2} - C_{D3} + C_{D4}) \; + \\ + \; \frac{B}{8} * cos(\alpha_s) * (C'_{D1} + C'_{D2} - C'_{D3} - C'_{D4} - C_{L1} - C_{L2} + C_{L3} + C_{L4}) + \\ + \; \frac{B}{4} * sin(\alpha_s) * (C_{D1} + C_{D2} - C_{D3} - C_{D4}) + \\ + \; \frac{B}{8} * sin(\alpha_s) * (-\; C'_{D1} + C'_{D2} + C'_{D3} - C'_{D4} + C_{L1} - C_{L2} - C_{L3} + C_{L4}) \end{aligned} \tag{4.78}$$

$$\begin{aligned} Element(2,3) = \frac{B}{8} * cos(\alpha_s) * (C_{D1} + C_{D2} - C_{D3} - C_{D4} + C'_{L1} + C'_{L2} - C'_{L3} - C'_{L4}) + \\ + \frac{B}{4} * cos(\alpha_s) * (C_{L1} - C_{L2} - C_{L3} + C_{L4}) + \\ + \frac{B}{8} * sin(\alpha_s) * (-C_{D1} + C_{D2} + C_{D3} - C_{D4} - C'_{L1} + C'_{L2} + C'_{L3} - C'_{L4}) + \\ + \; \frac{B}{4} * sin(\alpha_s) * (C_{L1} + C_{L2} - C_{L3} - C_{L4}) \end{aligned} \tag{4.79}$$

$$\begin{aligned} Element(3,3) = \frac{{D_M}^2}{8} (2C_{M1} - 2C_{M2} - 2C_{M3} + 2C_{M4} + C'_{M1} + C'_{M2} - C'_{M3} - C'_{M4}) + \\ + ISC(3,3) \end{aligned} \tag{4.80}$$

The ISC (Individual Subconductor Contribution) expressions, $ISC(3,1)$, $ISC(3,2)$ and $ISC(3,3)$ are derived from quasi-steady aerodynamic moment of the bundle (Model 1, Equation 4.44):

$$\begin{aligned} ISC(3,1) = \frac{D_M}{4} * cos(\alpha_s) * (C_{D1} - C_{D2} - C_{D3} + C_{D4} + C_{L1} + C_{L2} - C_{L3} - C_{L4}) + \\ + \frac{D_M}{4} * sin(\alpha_s) * (C_{D1} + C_{D2} - C_{D3} - C_{D4} - C_{L1} + C_{L2} + C_{L3} - C_{L4}) \end{aligned} \tag{4.81}$$

$$\begin{aligned} ISC(3,2) = \frac{D_M}{8} * [cos(\alpha_s) * (C_{D1} + C_{D2} - C_{D3} - C_{D4} + C'_{D1} - C'_{D2} - C'_{D3} + C'_{D4} - C_{L1} + C_{L2} + \\ + C_{L3} - \; C_{L4} + C'_{L1} + C'_{L2} - C'_{L3} - C'_{L4}) + \; sin(\alpha_s) * (-\; C_{D1} + \; C_{D2} + \; C_{D3} - C_{D4} + C'_{D1} + \\ + \; C'_{D2} - C'_{D3} - \; C'_{D4} - C_{L1} - \; C_{L2} + C_{L3} + \; C_{L4} - C'_{L1} + C'_{L2} + C'_{L3} - \; C'_{L4})] \end{aligned} \tag{4.82}$$

$$\begin{aligned} ISC(3,3) = \frac{BD_M}{16} * [3C_{D1} + 3C_{D2} + 3C_{D3} + 3C_{D4} + \; C'_{L1} + C'_{L2} + C'_{L3} + \; C'_{L4} + (C'_{D1} + C_{L1} - \\ - C'_{D2} - \; C_{L2} + \; C'_{D3} + \; C_{L3} - \; C'_{D4} - \; C_{L4}) * cos(2\alpha_s) + (C_{D1} - C'_{L1} - \; C_{D2} + \; C'_{L2} + \; C_{D3} - \\ - C'_{L3} - \; C_{D4} + \; C'_{L4}) * sin(2\alpha_s)] \end{aligned} \tag{4.83}$$

This resultant matrix is compatible with the equivalent aerodynamic damping matrix presented in Model 2 (Equation 4.61). The first two columns of both matrices are identical numerically while the third column of the matrix according to Model 2 includes the parameters

related to the position of an aerodynamic centre. Thus, the third column is the part of the aerodynamic matrices that is considered to contain the key relationship needed to experimentally identify the parameters, which can be used to define the position of an aerodynamic centre.

4.3.2 Experimental wind-tunnel data measured by Matsumiya *et al*. (2018) (Model 1)

There are a whole series of wind tunnel tests conducted by Matsumiya *et al.* (2013) on the described bundle in Model 1, but the key results have been obtained from the static wind tunnel tests in terms of different angles of attack presented in Matsumiya *et al.* (2018). The aerodynamic forces, drag, lift and moment of each individual subconductor within the bundle normal to flow were measured by Matsumiya *et al.*, (2011) for different angles of attack through a surface-pressure measurement test at wind speed within the range 10 to 20 m/s and Reynolds number of 2.0 and 3.9×10^4 respectively.

The force balance measurements were obtained by Matsumiya *et al.* (2018) on the overall conductor leading to estimates of the steady aerodynamic coefficients of the four-bundled conductor. However, for the individual subconductors the force balance tests were only performed on one of the four subconductors and therefore their results have not been used in this research.

The steady aerodynamic coefficients of the four-bundled conductor, C_{Df}, C_{Lf} and C_{Mf}, and individual subconductors, C_{Di}, C_{Li} and C_{Mi}, and their rates of change, C'_{Df}, C'_{Lf} and C'_{Mf}, and C'_{Di}, C'_{Li} and C'_{Mi} estimated by Matsumiya *et al.* (2018) are shown in Figures 4.8 to 4.11 in terms of the angle of attack for the 0-180° range. The rate of change of the aerodynamic coefficients is calculated as the local gradient of the coefficient with respect to the angle using finite difference method (FDM) based on linear interpolation, as described by Smith (1965). For certain wind directions there is one conductor directly behind another and when it rotates a bit there is no longer directly downwind so receives more of the wind directly. This is the cause of dips for certain wind direction and certain conductors in Figures 4.8 to 4.11.

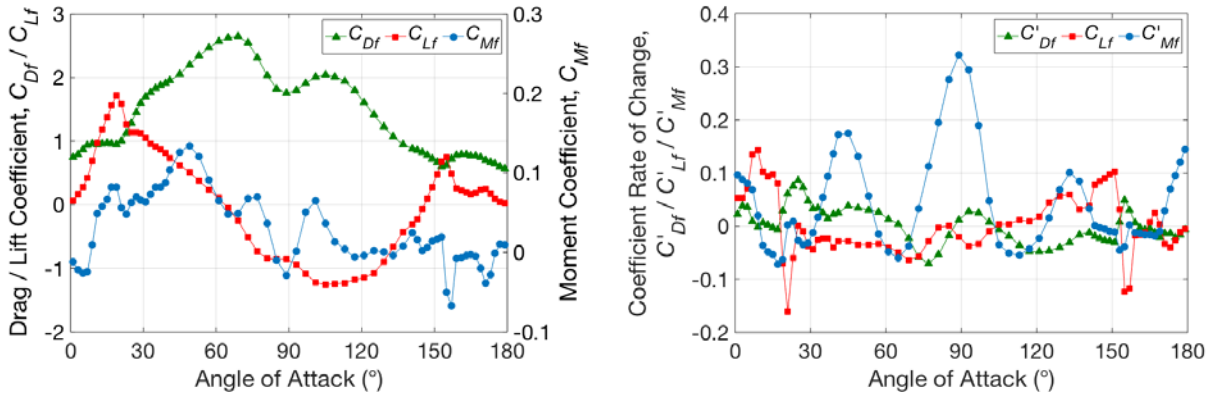

Figure 4.8. Aerodynamic coefficients of the whole bundle and their rates of change. [Adapted from Matsumiya *et al*. (2018)].

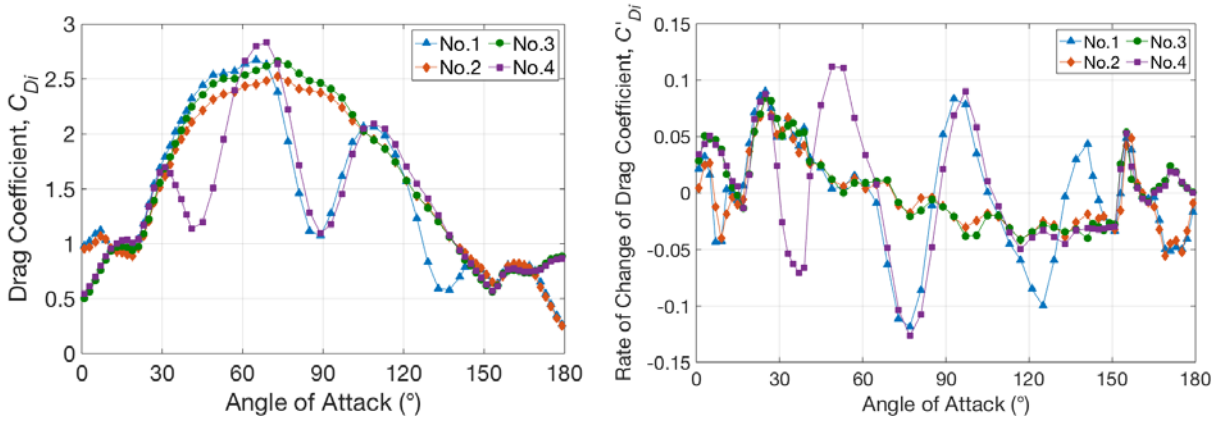

Figure 4.9. Aerodynamic drag coefficients for each subconductor and their rates of change. [Adapted from Matsumiya *et al*. (2018)].

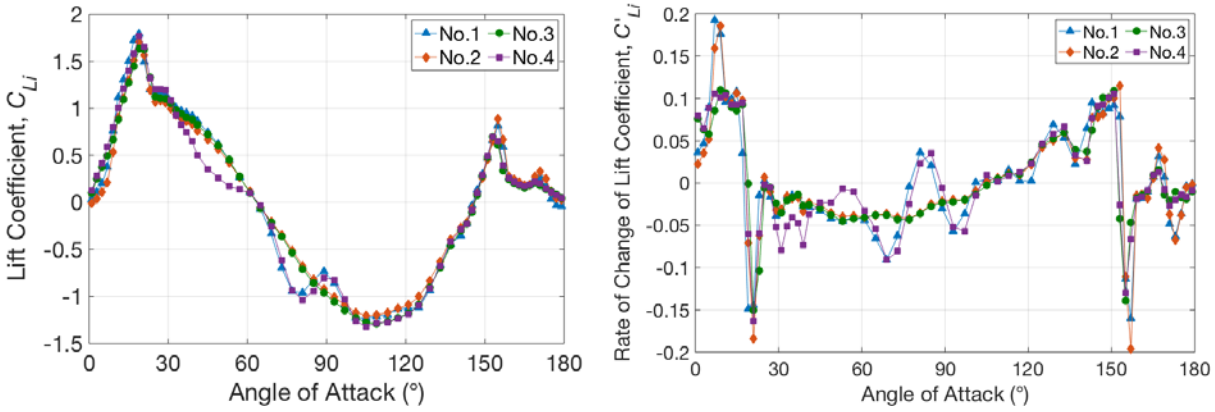

Figure 4.10. Aerodynamic lift coefficients for each subconductor and their rates of change. [Adapted from Matsumiya *et al*. (2018)].

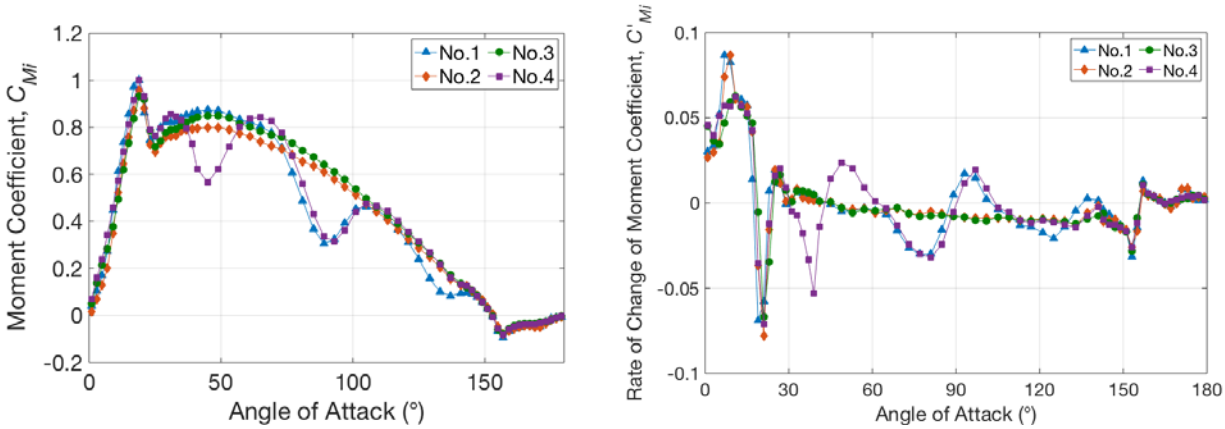

Figure 4.11. Aerodynamic moment coefficients for each subconductor and their rates of change. [Adapted from Matsumiya *et al*. (2018)].

The steady aerodynamic coefficients of the four-bundled conductor and individual subconductors have been used in this research to estimate the position of an aerodynamic centre.

4.3.3 Estimation of the position of the aerodynamic centre parameter

The two parameters that define the position of an aerodynamic centre, L_a and γ_r, are present in the third column of the aerodynamic damping matrix presented in Model 2 (Equation 4.61), which was compared against the corresponding column of the equivalent aerodynamic damping matrix derived from Model 1 (Equation 4.77). Note that L_a is the aerodynamic centre radius from *O*, which is the elastic centre of the section model that coincides with the centre of mass as well as the axes' origin. According to the bundle geometry illustrated in Model 2 (Figure 4.5), the point *O* would be located at the centre of the bundle. γ_r is the angle between the line from *O* to the position of the aerodynamic centre and the body reference line. L_a and γ_r were firstly obtained by reducing the difference between the third column of the corresponding two matrices through the process of the least squares error minimisation.

The elements of the right-hand side of the aerodynamic damping matrix presented in Model 2 (denoted by *H* in Equation 4.61) and the equivalent elements of the aerodynamic damping matrix derived for the formulation presented in Model 1 (denoted by *M* in Equation 4.77) according to the approach detailed in Model 2, are compared in the following form:

$$\begin{cases} H\ (1,3) = M\ (1,3) \\ H\ (2,3) = M\ (2,3) \\ \frac{1}{D_M} H\ (3,3) = \frac{1}{D_M} M\ (3,3) \end{cases} \Rightarrow \begin{cases} L_a\left[C_D s_{\theta\gamma} - (C_L - C'_D) c_{\theta\gamma}\right] = Element\ (1,3) \\ L_a\left[C_L s_{\theta\gamma} + (C'_L + C_D) c_{\theta\gamma}\right] = Element\ (2,3) \\ \frac{1}{D_M}\left(D L_a\left[2C_M s_{\theta\gamma} + C'_M c_{\theta\gamma}\right]\right) = \frac{1}{D_M}\left(Element\ (3,3)\right) \end{cases} \tag{4.84}$$

where $c_{\theta\gamma} = cos\,(\theta_0 + \gamma_r)$ and $s_{\theta\gamma} = sin\,(\theta_0 + \gamma_r)$

The top two elements of the system (1,3 and 2,3) correspond to the change in the aerodynamic force in the horizontal and vertical directions with respect to the rotational velocity component of the body, while the bottom element (3,3) correspond to the change in the aerodynamic moment force with respect to the rotational velocity component of the body. In order to make all of the compared rows compatible and have the same physical interpretation, the bottom row is multiplied by an inverse of the characteristic dimensional factor *D*.

Then, the values of the L_a and γ_r parameters are obtained for the lowest value of the following least squares type of the optimisation cost function shown below:

$$\min_x \left|\left|f(x)\right|\right|_2^2 = \min_x (f_1(x)^2 + f_2(x)^2 + f_3(x)^2) \tag{4.85}$$

where:

$$f(x) = \begin{bmatrix} f_1(x) \\ f_2(x) \\ f_3(x) \end{bmatrix} = \begin{bmatrix} [H\ \ (1,3)] - [M\ \ (1,3)] \\ [H\ \ (2,3)] - [M\ \ (2,3)] \\ \left[\frac{1}{D}H\ \ (3,3)\right] - \left[\frac{1}{D}M\ \ (3,3)\right] \end{bmatrix} \tag{4.86}$$

Then:

$$\min_x \left|\left|f(x)\right|\right|_2^2 =$$

$$= \sqrt{\left[[H\ \ (1,3)] - [M\ \ (1,3)]\right]^2 + \left[[H\ \ (2,3)] - [M\ \ (2,3)]\right]^2 + \left[\left[\frac{1}{D}H\ \ (3,3)\right] - \left[\frac{1}{D}M\ \ (3,3)\right]\right]^2} \tag{4.87}$$

A minimum value of the sum of squares of the functions can be found from the expression in the Equation 4.87. Each angle of attack for which the aerodynamic coefficients were measured, is used to find one pair of the values of the L_a and γ_r parameters.

By equating the quasi-steady aerodynamic forces from the entire four-bundled conductor formulation (Equations 4.29 to 4.31) and from the individual subconductors formulation (Equations 4.45 to 4.47), the relationships of the steady aerodynamic coefficients used in each formulation are given by:

$$C_{Df} = \frac{1}{4} * (C_{D1} + \ C_{D2} + \ C_{D3} + \ C_{D4}) \tag{4.88}$$

$$C'_{Df} = \frac{1}{4} * (C'_{D1} + \ C'_{D2} + \ C'_{D3} + \ C'_{D4}) \tag{4.89}$$

$$C_{Lf} = \frac{1}{4} * (C_{L1} + \ C_{L2} + \ C_{L3} + \ C_{L4}) \tag{4.90}$$

$$C'_{Lf} = \frac{1}{4} * (C'_{L1} + \ C'_{L2} + \ C'_{L3} + \ C'_{L4}) \tag{4.91}$$

$$C_{Mf} = \frac{D}{4B} * (C_{M1} + \ C_{M2} + \ C_{M3} + \ C_{M4}) + \frac{1}{4\sqrt{2}} * sin\left(\frac{\pi}{4} + \theta\right) * (C_{D1} + C_{L2} - C_{D3} - C_{L4}) +$$

$$+\frac{1}{4\sqrt{2}} * cos\left(\frac{\pi}{4}+\theta\right) * (C_{L1} - C_{D2} - C_{L3} + C_{D4}) \quad (4.92)$$

$$C'_{Mf} = \frac{D}{4B} * (C'_{M1} + C'_{M2} + C'_{M3} + C'_{M4}) +$$
$$+\frac{1}{4\sqrt{2}} * sin\left(\frac{\pi}{4}+\theta\right) * (C'_{D1} - C_{L1} + C'_{L2} + C_{D2} - C'_{D3} + C_{L3} - C'_{L4} - C_{D4}) +$$
$$+\frac{1}{4\sqrt{2}} * cos\left(\frac{\pi}{4}+\theta\right) * (C'_{L1} + C_{D1} - C'_{D2} + C_{L2} - C'_{L3} - C_{D3} + C'_{D4} - C_{L4}) \quad (4.93)$$

The values of the identified L_a and γ_r parameters for each experimentally studied angle of attack are shown in Figure 4.12. There seems to be an approximately periodic pattern for the values of L_a every 45°. There are three relatively large local maxima values of L_a at 0, 90 and 180°, and two smaller maxima at 45 and 135° angle of attack. The maximum value of L_a at 180°, 0.2 m, is equal to the distance from the centre of the bundle to the mid-point of the square sides. It can be observed that the position of an aerodynamic centre is close to the edges only every 45° angle of attack whilst it is approximately around the mid-point of the bundle for the rest of the angles of attack. However, there is little evidence of a clear pattern of the γ_r values.

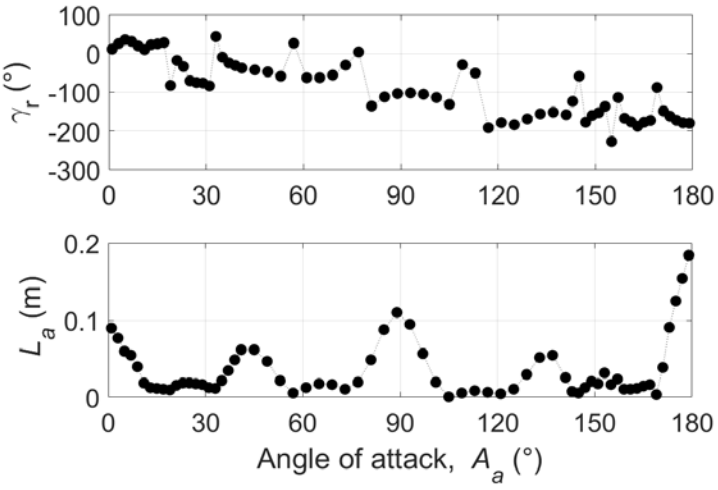

Figure 4.12. Variation of the L_a and γ_r estimates in terms of the angle of attack.

Since there was little evidence of a clear trend of the γ_r values in Figure 4.12, a different display of the results was adopted next. In Figure 4.13, for each considered angle of attack, the identified γ_r estimates are visualised with the markers, which are sized according to the values of the corresponding L_a parameters. The emerging trend is highlighted by adopting a linear fit which is also weighted in terms of the corresponding L_a values, for the full range of the angle

of attacks, as already implied by the provided visualisation.

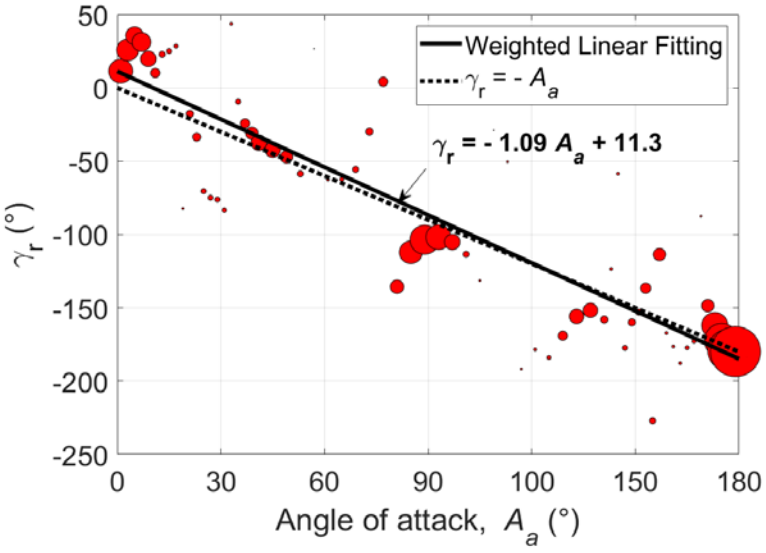

$R^2 = 0.60$

Figure 4.13. Weighted linear fitting of γ_r and its apparent trend with respect to the angle of attack.

In this approach, the larger the value of L_a is, the larger the size of the marker is, thus mostly the estimates at the previously discussed "special" angles, i.e., (0, 45, 90, 135 and 180°), determine the overall trend. The weighted linear regression fit adopted in MATLAB® provides the slope of -1.09 which well approximates the apparent trend in the plot. Therefore, γ_r is approximately equal to the negative magnitude of the angle of attack. The corresponding coefficient of determination of the regression, R^2, as given in Wright (1921), is 0.60. A common approximation of an aerodynamic centre from previous literature was defined by He and Macdonald (2017, p. 323) as "*a fixed point on the principal axis in the x direction with L_a equal to the largest offset of the perimeter of the section from the elastic centre (i.e. the sum of the radius of the cable and the greatest ice thickness)*". The observed trend confirms this approximation only in the proximity of the "special" angles, i.e., (0, 45, 90, 135 and 180°), where its position is on the principal axis. However, for the rest of the angles of attack, it can be stated that an aerodynamic centre is located near to the mid-point of the bundle. Despite the weighted linear fit provides the intercept of 30.7°, it is considered to be due to the higher number of datapoints above the apparent trendline. The use of these results for validation purposes will be done in the next section by comparing the outputs from both formulations.

The position of an aerodynamic centre relative to the geometry of the bundle is further

illustrated in Figure 4.14 for the selected angles of attack (1, 23, 45, 69, 89, 113, 137, 159 and 181°). These are the closest angles to the 45° increments of the angle of attack, for which the value of L_a seems to be influenced, and their intermediate positions at 22.5° increments (0, 22.5, 45, 67.5, 90, 112.5, 135, 157.5 and 180°). For the other angles, the estimates of L_a are smaller and the values of γ_r, which indicates the orientation of an aerodynamic centre, can be neglected because the position of an aerodynamic centre approximates to the mid-point of the bundle.

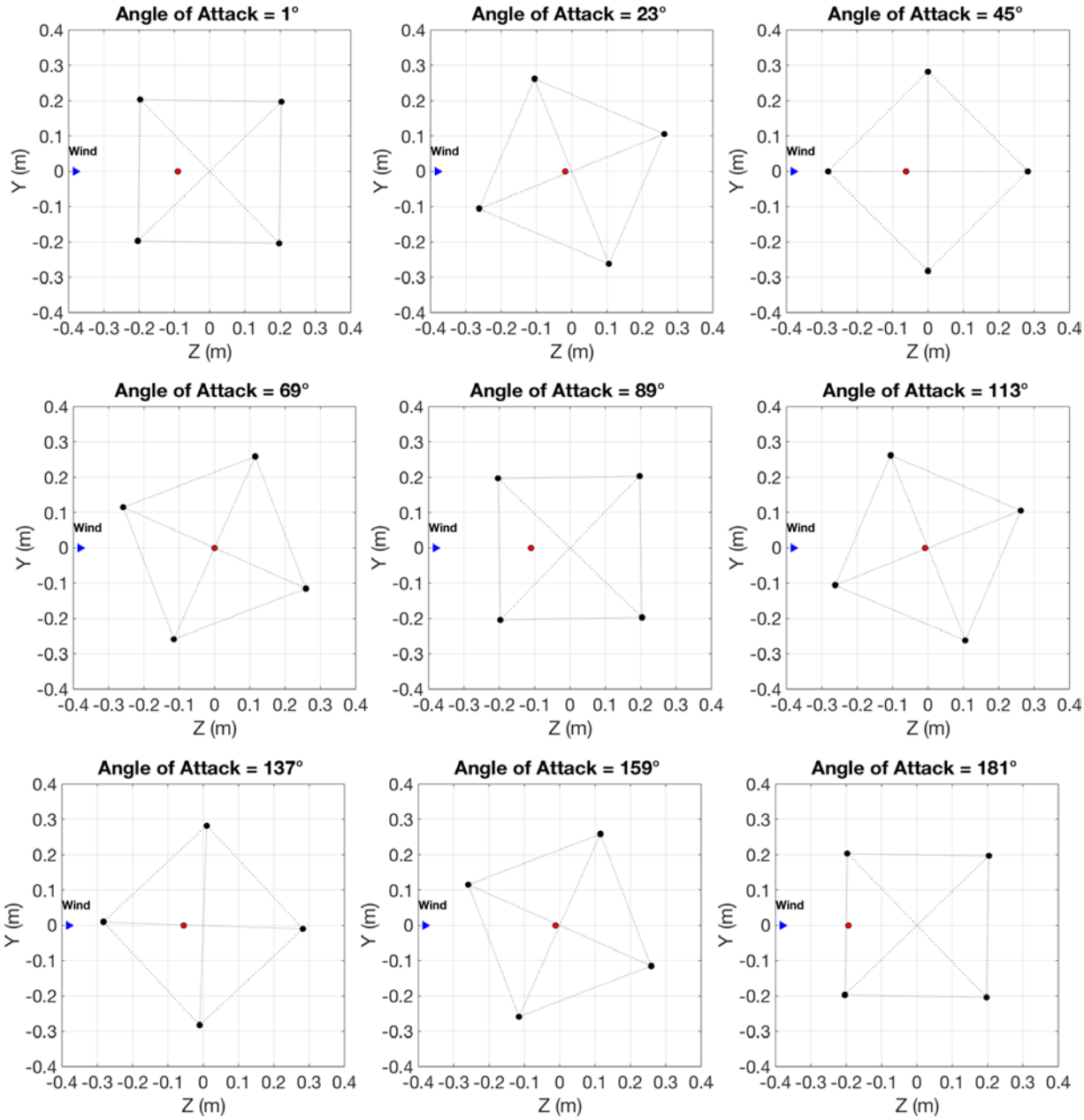

Figure 4.14. Variation of the position of the aerodynamic centre (red) relative to the geometry of the bundle for selected angles of attack.

What is special about each 45° angle of attack is that it makes L_a to be a maximum there. It can be noticed that for each multiple of 45° angle of attack there is at least one sub-conductor directly behind another. For 0, 90 and 180°, there are two sub-conductors directly behind another, while at 45, 135° one (on the leeward corner) is directly downstream of another one (on the windward corner). For all the other angles there is no sub-conductor stream-wise overlap. At these selected angles, i.e., (0, 45, 90, 135 and 180°), where some form of the stream-wise overlap is observed, it can be seen that a rotational motion will cause a relatively large change in the induced aerodynamic forces (represented by large L_a), since the sub-conductor sheltered, or shadowed, by another will then go in and out of a region with greater local wind velocity. This behaviour is supported by the shape of the plot in Figure 4.12. There, the peak regions are found to be sharper than the valley regions. Thus, the subconductors shadowing or subconductor sheltering from the wake are seen as a cause of the increased local sensitivity to the changing conditions and this is effectively observable through the narrow shape of the peaks in Figure 4.12.

On the other hand, the valleys are seen as the regions corresponding to the intermediate multi-conductor bundle locations, and they are not comparably affected by the small variations in the angle of attack. In the instance of a large ice accretion, this sensitivity might be reduced since the boundaries of the wake would become larger. In future analysis, the conductor's wake spread, or its influence, might be characterised by the relative narrowness of the peak regions.

When there are one or more subconductors directly downstream of another one, a large value of L_a is observed in this work, whereas if there is not any subconductor directly downstream of another one, then L_a is close to zero. In those cases, the torsional velocity changes the aerodynamic forces very little. If all of the subconductors are exposed to the wind and they are rotated by a small amount, but they are still exposed to the wind, then the forces are going to be similar. If one is sheltered by another one is directly downstream of it, and are rotated by a small amount the one downstream then pops out the wake and experiences greater wind action. The wind the downstream one is experiencing is quite sensitive to the angle, because from small rotation it comes out of the shelter and experiences the wind. In that case, the torsional motion will cause a bigger difference in the aerodynamic forces.

4.4. ANALYSIS OF GALLOPING STABILITY

The formulation proposed by He and Macdonald (2016) (Model 2) is explored in comparison with the formulation for the aerodynamic forces measured in each one of the four subconductors within the bundle presented by Matsumiya *et al*. (2018) (Model 1B), which showed good agreement with the wind tunnel measurements. Using two different methods of analysis, this section studies the results obtained from the two aerodynamic force formulations, applying the identified position of an aerodynamic centre in the previous section developed for Model 2.

Specifically, the calculated stability regions and steady-state responses are compared between the two models to assess the effect of this parameter in the results. This first method of analysis also provides a point of support to compare the calculated boundary regions with those from the eigenvalue analysis. It has been identified that the galloping instability was mainly driven by the torsional displacement of the bundle, and at a lower extent, by the wind speed. Furthermore, the critical wind speed (i.e., the wind speed at which galloping emerges) has been found to be governed by the lift force acting on the body section expressed in the form of lift coefficient.

This analysis uses a simple controlled setting to prepare groundwork for full-scale measurements on the same cable bundle geometry in Chapter 5. It is also aimed to find similarity between the results obtained from Model 1B, which were consistent with wind tunnel experiments from Model 2, with the objective of assessing the argument that the latter is a reliable approach in the analysis of galloping stability. This analytical prediction approach of the galloping stability used the steady aerodynamic coefficients of the four-bundled conductor and individual subconductors measured by Matsumiya *et al.* (2018) in wind tunnel test (Section 4.3.2).

With the objective to adopt analogous conditions to those provided by Matsumiya *et al*. (2018), Table 4.4 shows the associated parameters of the two different test cases considered in Model 1, namely: Case 1 and Case 2. The sag of the section model from the support point in the stationary condition, H, is different for each test case. It implies that the total length of the elastic cords can be different for each case for the same horizontal length, L. Different air densities, ρ, were considered to take into account the temperature pressure effect.

Table 4.4. Parameters used in Model 1. [Adapted from Matsumiya *et al*. (2018)].

Parameter	Case 1	Case 2
m	6.692 kg	6.692 kg
I	0.535 kg m^2	0.535 kg m^2
L	6.255 m	6.255 m
$\sqrt{2}R_m = \sqrt{2}R_s$	0.400 m	0.400 m
EA	176.4 N	176.4 N
H	1.725 m	1.560 m
T	30.8 N	33.9 N
U	6.7 m/s	10.2 m/s
ρ	1.21 kg/m^3	1.20 kg/m^3
α_s	0-35°	0-35°
f_{y0}	0.450 Hz	0.456 Hz
f_{z0}	0.379 Hz	0.399 Hz
$f_{\theta 0}$	0.416 Hz	0.428 Hz

It should be noted that despite the wind tunnel simulations were conducted at high Reynolds numbers (e.g., between 2.0 and 3.9×10^4; see Section 4.3.2), which may be representative of galloping of the full-scale structure in the field, for the present analysis, the actual Reynolds number may not be so important, since the aerodynamics of sharp-cornered sections are generally insensitive to it (He and Macdonald, 2016). The aerodynamic coefficients of conductors with any noncircular cross-section are dependent on the Reynolds number and its effect has been considered in some 3DOF models in literature, such as Gjelstrup and Georgakis (2011) to determine the occurrence of galloping. However, this results in complicate formulations and it has been neglected in both Model 1 and 2.

4.4.1. Nonlinear performance of the system with galloping regions

The amplitudes identified from the time series of displacements were used by Matsumiya

et al. (2018) to illustrate the dynamic response of the system for Model 1. With the objective to use an approach to predict the galloping stability on transmission lines with potential transferability to different geometric arrangements, the formulation developed by He and Macdonald (2016) (Model 2) was adopted in this research. Therefore, using as a reference the analytical results obtained from Model 1 presented in Matsumiya *et al*. (2018), they were compared with the analytical amplitudes estimated in this research from Model 2, which have not been previously provided by He and Macdonald (2016), for the purpose of assessing its suitability in future studies.

In order to conduct a direct comparison, analogous conditions (e.g., test cases, input and output parameters, etc.) were adopted in this investigation. The analysis of the time responses has been conducted by solving the equations of motion of the structural model (Equations 4.11 to 4.13) using the standard solver for ordinary differential equations (ODEs) "*ode45*" function in MATLAB®. He and Macdonald (2016) did not provide the equations of motion of the structural model in Model 1. Therefore, given the compatibility between the two formulations (Model 1 and Model 2), the 3-DOF differential equations for the vertical, horizontal and torsional motions presented by Matsumiya *et al.* (2018) have been also used in this analysis for Model 2. Despite the changes in the structural damping coefficient with the amplitude involved in these equations were linearized in Model 1, this study used constant values of structural damping coefficients independent of the amplitude. Initial perturbation in the system was applied by Matsumiya *et al*. (2018) for some test cases in Model 1 in the three different directions considered, as shown in Table 4.5. According to Matsumiya *et al*. (2018) "*"without I.D." indicates measurements of the response after disengaging the model from the stationary position by holding it softly against the wind (i.e., without initial displacement) and "with I.D." indicates measurements of the response after applying a large initial displacement*". This perturbation has been replicated in the analysis of amplitudes based on Model 2.

Table 4.5. Initial displacements considered by Matsumiya *et al.* (2018).

With Initial Displacement (With I.D.)	Case 1	Case 2
Vertical	-0.5 m	-0.5 m
Horizontal	0.5 m	0.5 m
Torsional	45°	45°

4.4.1.1. *Structural characteristics of the Model 1 support system without wind*

This section describes in detail the structural characteristics of the Model 1 support system in the stationary condition (i.e., without wind, U = 0 m/s). These characteristics are particularly relevant in the analysis of the galloping stability because they are related to some of the input and output parameters in the time-history response analysis considered by Matsumiya *et al*. (2018).

The orientation of the supports, α_s, is measured relative to the horizontal direction. The orientation of the conductor bundle, α_m, is also measured relative to the horizontal direction, in the static case without wind. The centre of mass of the wind tunnel conductor bundle is in the centre of the model, so there is no moment on the section when it is just under gravity loading. If the spacings and the radius of the support chords are the same on the supports as on the bundle ($\sqrt{2}R_m = \sqrt{2}R_s$ and $R_m = R_s$ respectively), then $\alpha_m = \alpha_s$, as it will be demonstrated next. If the spacings are different, these two angles are not generally the same, but they should still be similar.

The torsional angle, which is the instantaneous orientation of the conductor bundle, θ, is measured relative to the horizontal direction. It can include components due to rotation of the supports, the mean wind and vibrations. In the static case without wind, $\theta = \alpha_m$. The mean torsional angle is the mean value of θ, which is the static equilibrium orientation, i.e. if there are no vibrations. If there are vibrations, because of nonlinearly the mean torsional angle is not necessarily quite the same as the static equilibrium orientation, but it would be expected to be close.

The relationship between α_s, α_m and θ is studied in detail because these parameters were considered by Matsumiya *et al*. (2018) as input control variables for Model 1 and therefore, they are typically used to illustrate the comparison of the results in this research. Considering a special case, their relationship is firstly addressed. For $\alpha_s = 0°$, the stationary condition without wind (U = 0 m/s) is assumed, so $\theta = \alpha_m$ since the section is symmetric. The spacings and the radius of the support chords are assumed to be the same on supports as on the bundle, so $\sqrt{2}R_m = \sqrt{2}R_s$ and $R_m = R_s$. Without adding any extra mass, it seems reasonable that in this case $\alpha_m = 0°$. L_{ig}, which is the length of the chord in the stationary condition, can be then calculated when $(y, z, \theta) = (0°, 0°, \alpha_m)$. Values of L_{i0}, which are constant for a given sag in

the stationary condition, *H*, have been found to be 5.522 m for Case 1 and 5.407 m for Case 2. Under these conditions, it has been found that $\theta = 0°$ when $\alpha_m = 0°$.

When the supports are rotated by a known amount without wind, the bundle rotation is unknown, because the orientation of the cables and therefore their tension is going to change. So it would seem reasonable that the rotation of the body approximates the rotation of the supports, but it might not be quite the same. Therefore, solving the system for this special case gives the instantaneous vertical (*y*), horizontal (*z*) and torsional (θ) displacements of the section for a range of α_s values for Case 1 and Case 2. Figure 4.15 shows the relationship between the support orientation for no wind conditions and the torsional displacement obtained after solving the system. It is assumed that for this case the torsional displacement is the same as the orientation of the bundle, i.e. $\theta = \alpha_m$. It can be noticed in Figure 4.16 that the displacement in the torsional direction in the stationary condition without wind is equal to the orientation of the conductor bundle, so $\alpha_s = \theta$. Given that for this case, $\theta = \alpha_m$, it can be also stated that the orientation of the supports is equal to the orientation of the conductor bundle $(\alpha_s = \alpha_m)$. Since the trends for Case 1 and Case 2 are apparently the same, it seems that the sag in the stationary condition does not have an effect on this relationship.

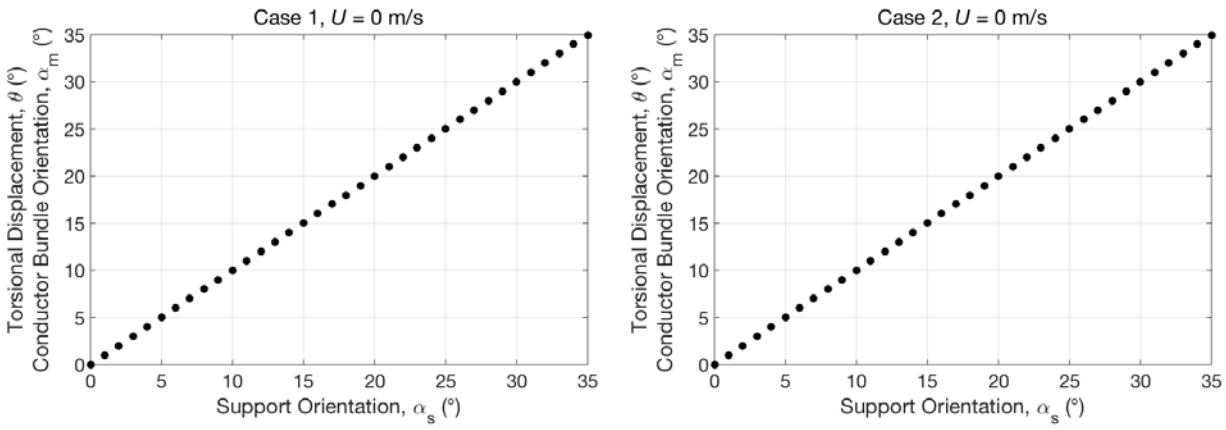

Figure 4.15. Orientation of the supports and torsional displacement relationship for *U* = 0 m/s, Case 1, Case 2.

Given the centre of mass of the conductor is in the middle of the section, the length and the tension of the cables remain constant when the supports and the bundle are rotated by the same angle. The vertical component of those wires is the same as it was before rotated, so in that case the rotation of the model is equal to the rotation of the supports, $R_m = R_s$. Physically, it makes sense that under these circumstances the total vertical force and the moment equals the weight of the body setting equilibrium.

Finally, when wind velocities are applied to the special case described previously, a component due to the rotation of the supports or a component due to the wind might be added. Drag is generated causing a deflection along wind, which probably induces a very small rotation to the bundle. Figure 4.16 shows that the torsional displacement is different than the support orientation angle, particularly when the support orientation angle is between 8° and 20°, which is the stalling angle (20°) according to Matsumiya *et al*. (2018). The calculated analytical results are compared with the experimental results for Model 1 from time history analysis of wind tunnel tests. These displacements identified experimentally by Matsumiya *et al*. (2018) correspond to the mean values measured without applying any initial displacement. Matsumiya *et al*. (2018) obtained the response amplitudes from the time-history analyses when the amplitudes and the structural damping coefficient have almost reached a steady state. Although the static equilibrium and the mean torsion of the dynamic response would be expected to be similar, they might not be necessarily the same. At $\alpha_s = 0°$ there is a small change in the torsional displacement, which is highlighted in the plot in Figure 4.16. Given the symmetry of the bundle, without applying any rotation, there is not any moment on the section. However, because of the three dimensional geometry of the body, when downwind deflection is induced, the cable is no longer vertical and it swamps a little bit causing a small rotation. Comparing the results from the Case 1 and Case 2, it can be stated that the higher the wind speed applied is, the larger negative torsional displacement is measured. In a more general case, when the supports rotate and the rotation angle of the body is not 0°, there will be a moment on the body inducing more rotation.

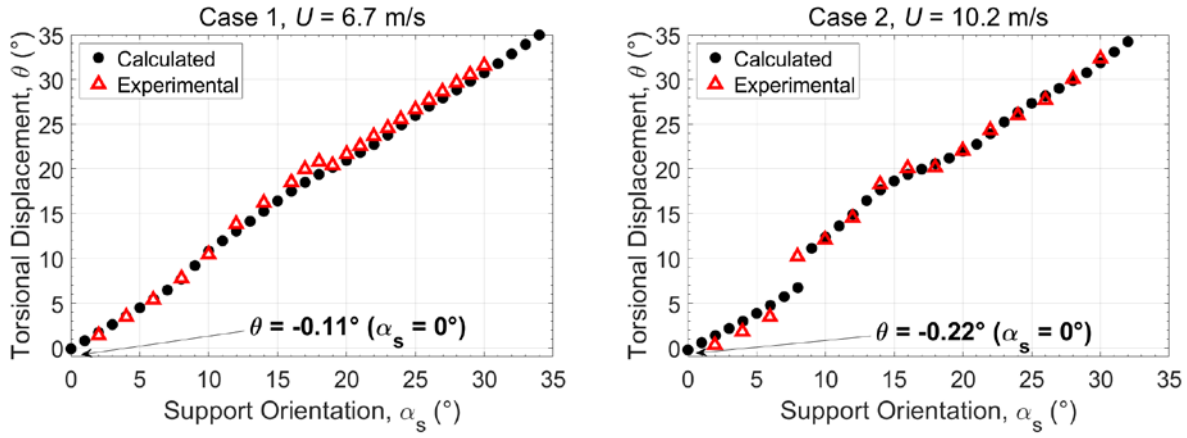

Figure 4.16. Orientation of the supports and torsional displacement relationship for U = 6.7 m/s, Case 1, and U = 10.2, Case 2.

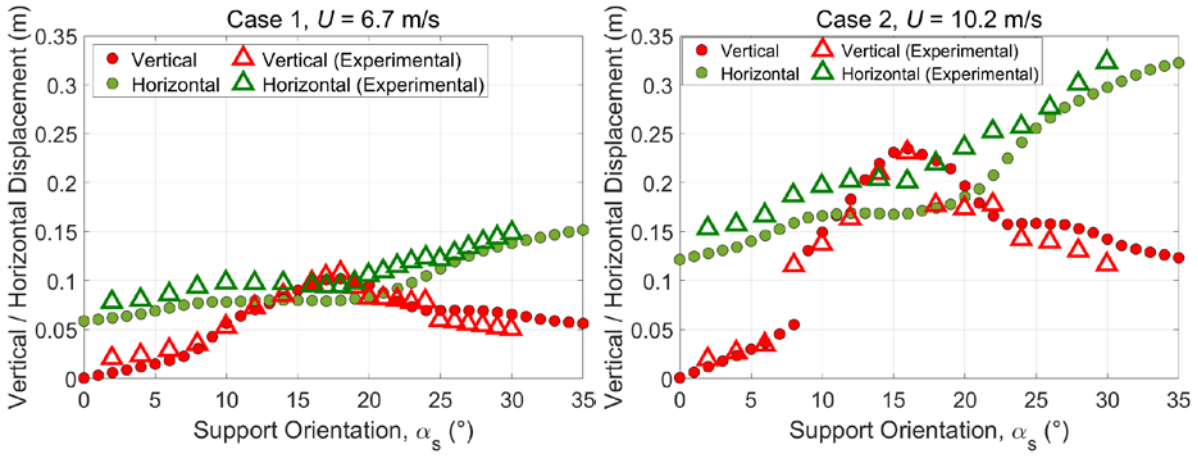

Figure 4.17. Orientation of the supports and torsional displacement relationship for U = 6.7 m/s, Case 1, and U = 10.2, Case 2.

Similarly, the vertical and horizontal static displacements for a range of support orientations are plotted in Figure 4.17, where they are compared with the experimental dynamic response presented by Matsumiya *et al*. (2018) from time history analysis of wind tunnel tests. The overall trend of the displacements is coherent with the results from the time history analysis, although the time-averaged horizontal displacements are slightly higher than the static horizontal results obtained in this analysis.

4.4.1.2. *Aerodynamic force formulation for four-bundled conductors (Model 1A)*

Although Model 1A did not show good agreement with the full-scale results from the wind tunnel tests and it does not seem suitable to be used in future studies, it has been firstly considered in this section in order to provide a broader comparison.

The analytical dynamic response of the system is illustrated by the time series of displacements displayed in Figure 4.18, for Case 1 (Table 4.4) as an example, at $\alpha_s = 23°$ without initial displacement. From the right-hand side plot in Figure 4.16 (Case 2), the orientation of the supports, α_s, is approximately 23° when the torsional displacement, θ, is 24.5°, which is the last value of the mean torsional displacement below 25° where Matsumiya *et al*. (2018) measured the highest vertical, horizontal and torsional total amplitude. The value of $\theta = 24.5°$ was selected in order to avoid numerical errors and uncertainties that might arise around the peak or the turning point of the trend. For a sinusoidal response, the $2\sqrt{2}$ factor multiplied by the standard deviation of an integer number of cycles corresponds to the total peak-to-peak amplitude.

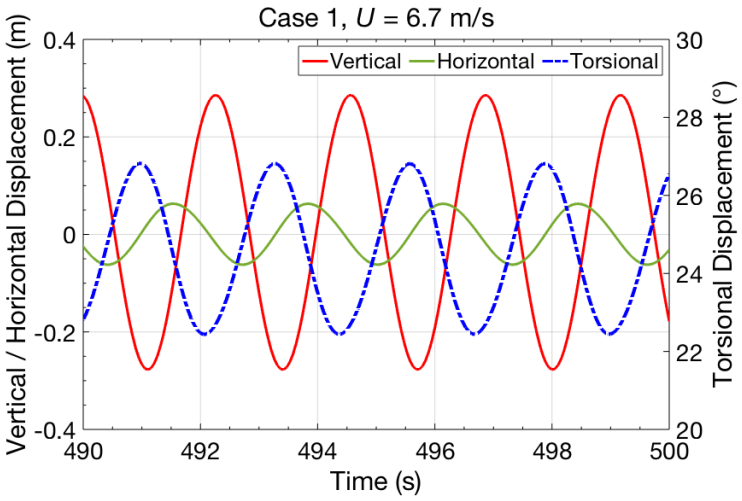

Figure 4.18. Time series of displacement from time history analyses for Model 2 for α_s = 24°, Case 1.

Figures 4.19 to 4.21 show (for Case 1 and Case 2 respectively, as detailed in Table 4.4) the comparison between the amplitudes from time-history analyses based on the Model 1A ("Aerodynamic force formulation for four-bundled conductors") and Model 2. Since this formulation considered in Model 1A treats the whole section as a single cross-section and neglects the motion of each subconductor due to rotation, the third column of the aerodynamic damping matrix is set to be zero (e.g. $L_a = 0$). By making this assumption, the torsional motion does not change the aerodynamic forces. The values of the initial vertical, horizontal, and torsional displacements applied in the plots that are denoted by "With I.D." are -0.5 m, 0.5 m, and 45° respectively.

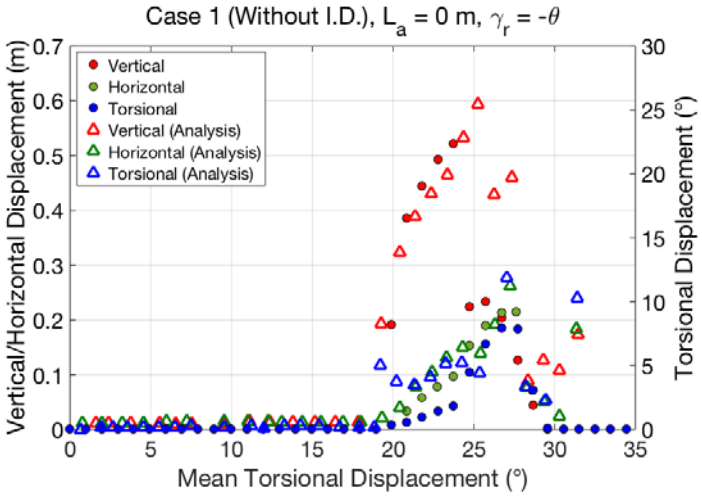

Figure 4.19. Comparison of the analytical total amplitude of each displacement from time history analyses for Model 1A and Model 2, without I.D. (initial displacement) for U = 6.7 m/s, Case 1.

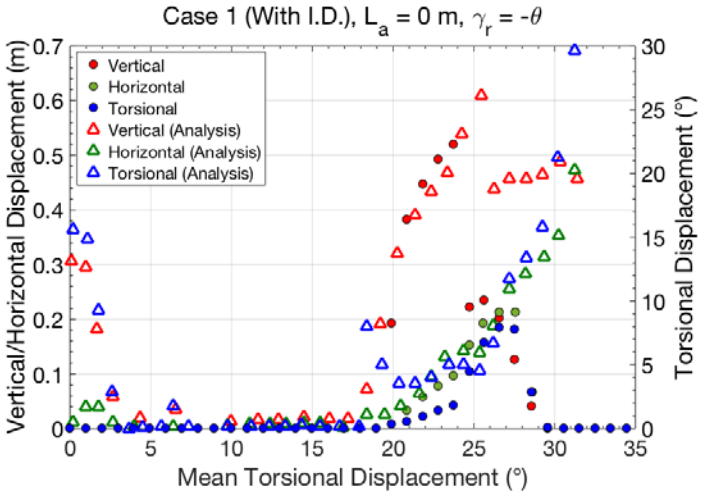

Figure 4.20. Comparison of the analytical total amplitude of each displacement from time history analyses for Model 1A and Model 2, with I.D. (initial displacement) for U = 6.7 m/s, Case 1.

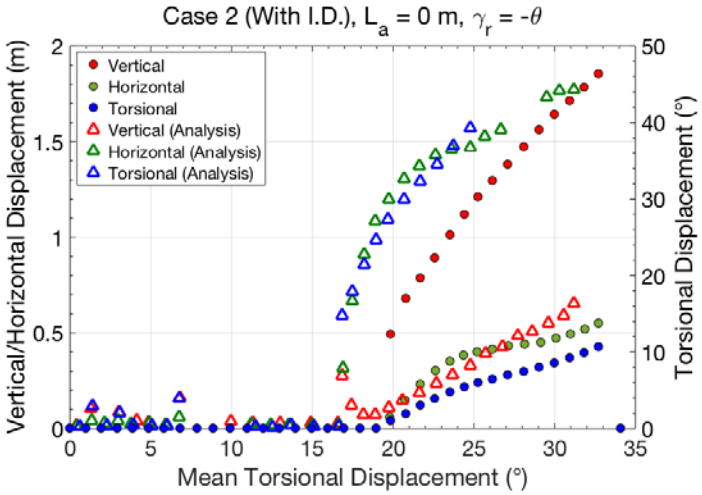

Figure 4.21. Comparison of the analytical total amplitude of each displacement from time history analyses for Model 1A and Model 2, with I.D. (initial displacement) for U = 10.2 m/s, Case 2.

The amplitudes and stability boundaries identified for the vertical (red) and horizontal components (green) based on the formulation presented in Model 2 agree fairly well with the results obtained in Model 1A. However, the comparison of the amplitudes for the Case 2 in Figure 4.21 shows apparent discrepancies. Apart from the amplitude-dependent modelling of the damping, the assumption that the orientation of the supports is equal to the orientation of the bundle ($\alpha_s = \alpha_m$) made in Model 1, which was taken into account in this analysis, are the only differences between the two different estimation methods. These assumptions are then considered to be the cause of the differences in the amplitudes.

4.4.1.3. *Aerodynamic force formulation for each subconductor (Model 1B)*

Figures 4.22 and 4.23 show (for Case 1 and Case 2 respectively, as detailed in Table 4.4) the comparison between the amplitudes from time-history analyses based on the Model 1B ("Aerodynamic force formulation for each individual subconductor") and Model 2. The position of an aerodynamic centre was derived from the L_a and γ_r, values displayed in Figure 4.12 in terms of the angle of attack. The values of the initial vertical, horizontal, and torsional displacements applied in each plot that are denoted by "With I.D." are -0.5 m, 0.5 m, and 45° respectively.

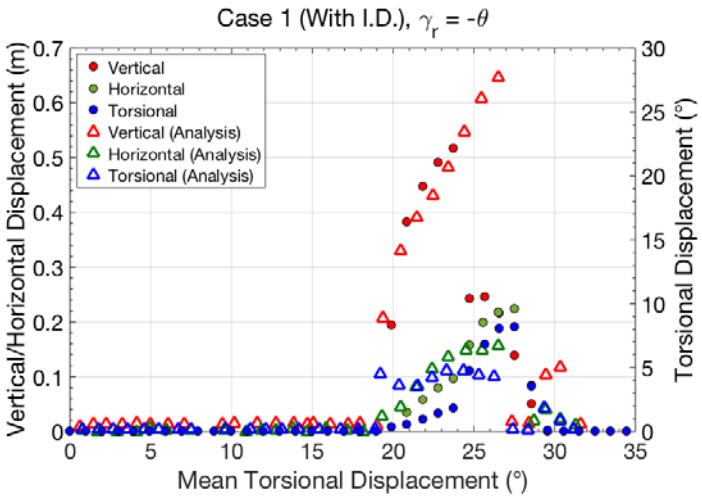

Figure 4.22. Comparison of the analytical total amplitude of each displacement from time history analyses for Model 1B and Model 2, with I.D. (initial displacement) for U = 6.7 m/s, Case 1.

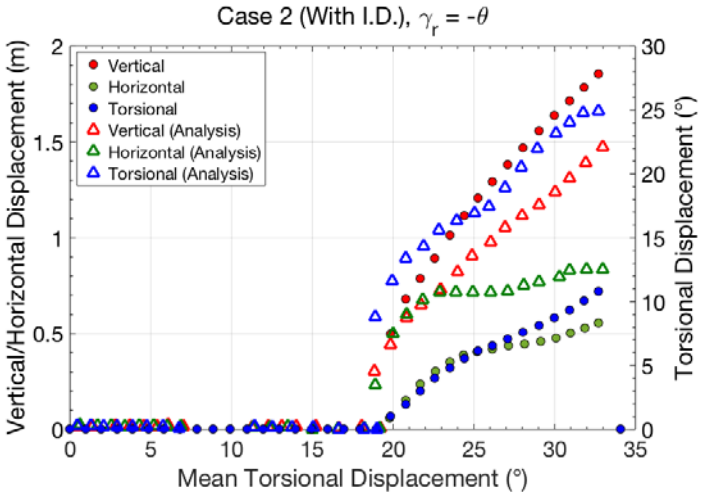

Figure 4.23. Comparison of the analytical total amplitude of each displacement from time history analyses for Model 1B and Model 2, with I.D. (initial displacement) for U = 10.2 m/s, Case 2.

The amplitudes and stability boundaries identified for the vertical (red) and horizontal components (green) based on the formulation presented in Model 2 agree fairly well with the results obtained in Model 1B, which showed good agreement with the full-scale results from the wind tunnel tests. It is assumed that the discrepancies observed for the torsional components (blue) in the Case 1 and the components for the Case 2 are related to the difficulties in modelling the damping accurately considering Model 1 linear approximation approach. In addition, some discrepancies in the results might be related to the assumption that $\alpha_s = \alpha_m$ made by Matsumiya *et al*. (2018) in Model 1, which was not taken into account in this analysis. The effect of the aerodynamic centre by including the fitted values of the two parameters, L_a and γ_r that define its position slightly improved the match between both models with respect to the previous results obtained in Model 1A using the formulation for the whole bundle (Section 4.4.1.1). However, there are still some discrepancies in the amplitudes for Case 2 throughout the whole range of mean torsional displacements considered.

4.4.2. Analytical solution for the galloping stability

An alternative approach to the time-history response analyses is developed in this chapter based on the eigenvalue analysis utilising the analytically defined aerodynamic damping matrix. The first model is a direct linearization of the 3-DOF nonlinear model presented in Model 1 considering the aerodynamic forces measured in each one of the four subconductors. The second explored model is a linear approximation of the problem using the parameters of the model related to the position of the aerodynamic centre, which were previously obtained in Figure 4.12 according to the formulation proposed in Model 2. The eigenvalue analysis is related to the Jacobian matrix calculated at the point where the displacements and velocities give a static solution i.e. no change with time, for which the velocities of the body in the different directions are zero. The Jacobian matrix is then calculated at the static equilibrium position in order to assess the perturbations to the static equilibrium. In dynamic systems where the static equilibrium is explored, small vibrations are studied around the static equilibrium. This way the change on the system is assessed about the conditions in which the system would be without being forced.

The solution for the galloping stability of the 3-DOF system is found through its eigenvalue analysis. The equation of motion in the matrix form is rearranged into a linear form of 1st order differential equations rather than 2nd order differential equations to be solved by an

Ordinary Differential Equation (ODE) solver. Rearrangement is performed by using the matrix A, as it is shown below. The solutions of this equation are basically the solutions of the equation of motion:

$$\begin{Bmatrix} \dot{\underline{X}}_1 \\ \dot{\underline{X}}_2 \end{Bmatrix} = A \begin{Bmatrix} \underline{X}_1 \\ \underline{X}_2 \end{Bmatrix} \tag{4.94}$$

Solving the equation of motion (Equation 4.94 before) for $\dot{\underline{X}}_2$:

$$M\dot{\underline{X}}_2 = -C\underline{X}_2 - K\underline{X}_1,\ \dot{\underline{X}}_2 = -M^{-1}C\underline{X}_2 - M^{-1}K\underline{X}_1 \tag{4.95}$$

where displacements, $\underline{X}$, and velocities $\dot{\underline{X}}$, are expressed in the form of two 3-by-1 vectors. The mass, M, damping, C, and stiffness, K, matrices are given by M, C and K respectively. The form of the stiffness matrix, K, is linearized for low amplitudes. The total damping matrix, C, consists of the sum of the aerodynamic damping matrix, C_a, and the structural damping matrix, C_s.

Therefore, the form of the matrix A is given by:

$$A = \begin{bmatrix} 0 & I \\ -M^{-1}K & -M^{-1}C \end{bmatrix},\ \begin{Bmatrix} \dot{\underline{X}}_1 \\ \dot{\underline{X}}_2 \end{Bmatrix} = \begin{bmatrix} 0 & I \\ -M^{-1}K & -M^{-1}C \end{bmatrix} \begin{Bmatrix} \underline{X}_1 \\ \underline{X}_2 \end{Bmatrix} \tag{4.96}$$

where I is the identity matrix.

The displacements and velocities can be represented by a harmonic motion as follows:

$$\begin{Bmatrix} \underline{X}_1 \\ \underline{X}_2 \end{Bmatrix} = \{\underline{\phi}\} e^{\lambda t},\ \begin{Bmatrix} \dot{\underline{X}}_1 \\ \dot{\underline{X}}_2 \end{Bmatrix} = \{\underline{\phi}\} \lambda e^{\lambda t} \tag{4.97}$$

where $\underline{\phi}$ is the mode shape vector and λ is equivalent to sinusoidal motion with exponential growth or decay.

Assuming the solutions of the equation of motion are given by the Equation 4.96 (*A* matrix) and displacements and velocities vectors are substituted into it, the eigenvalues of the matrix A, and consequently, the resultant eigenvector can be found:

$$\lambda\underline{\phi} = A\underline{\phi},\quad (A - \lambda I)\underline{\phi} = 0,\quad |A - \lambda I| = 0 \tag{4.98}$$

If λ is expressed as a complex number:

$$\lambda = a + ib,\quad e^{\lambda t} = e^{at}e^{iwt} \tag{4.99}$$

the real part of the eigenvalue, *a*, indicates the state of the vibrations. Positive values of the real part correspond to growing vibrations, while negative values indicate vibration decay. Without

wind, the complex conjugate pairs of eigenvalues, $a + bi$, are related to the natural frequencies and damping ratios. The imaginary parts correspond to the angular natural frequencies for each degree of freedom, ω_x, ω_y and ω_θ while the real parts represent the terms $-\omega_x\zeta_x$, $-\omega_y\zeta_y$ and $-\omega_\theta\zeta_\theta$, which are directly related to the structural damping of each degree of freedom. Therefore, for no wind conditions, there is not any aerodynamic damping, and hence, it is expected that all the real parts of the eigenvalues are negative because only the structural damping can be involved. In the case that there is not any structural damping, the total damping and the real parts of the eigenvalues would be zero.

In order to follow the analytical solution approach derived in Model 2, the 3-DOF equations of motion presented in Model 1 are converted into the matrix form for the Model 2 formulation. The eigenvalue analysis linearizes the aerodynamic forces with the aerodynamic damping matrix and the structural stiffness force terms about an equilibrium position. These terms effectively become a constant times the displacements in the three directions considered for each case. The functions of the displacements related to the geometry of the wires are given by the nonlinear terms Y_i, Z_i, and R_i, which are functions of y, z and θ. This implies that the resultant stiffness matrix is a full matrix opposite to the analysis presented in Model 2, where the elements of the matrix, "*KX*", "*KY*" and "$K\theta$", are uncoupled and therefore the matrix is diagonal (He and Macdonald, 2016).

The numerical calculation of the Jacobian matrix of the six states function matrix is used to check the stability conditions for the static solution obtained from the time-history analysis. It is assumed that for small amplitudes, time-history analysis should agree with the stability analysis using the Jacobian matrix. The eigenvalue analysis indicates the stability of the solutions around the static equilibrium of the function by linearizing the problem around that static solution.

When the body is under stationary conditions, the small vibrations might grow (unstable) or die down (being static) for certain mean angles of attack and wind speeds. The time-history analysis starts close off from the static equilibrium, and it assesses whether the vibrations die down (stable) to that static equilibrium or they grow (unstable). The focus of the previous comparisons with the results presented in Model 1 was the steady-state amplitudes from time-history analysis. However, it should be noted that the Jacobian matrix is not related to the steady-state amplitudes. Opposite to the measurements of the amplitude analysis, which would involve non-linearity of probably both the structure and the aerodynamics, the eigenvalue

analysis identifies the stability conditions based on the aerodynamic damping.

The following sections provide the prediction of galloping instability of the 3-DOF system based on the eigenvalue analysis for Model 1B, which showed good agreement with the full-scale results from the wind tunnel tests, and for Model 2. The instability boundaries found in this analysis are compared against the boundaries observed from previous analysis of amplitudes from the time series of displacements presented in Section 4.5.1. The eigenvalue analysis of the numerical Jacobian matrix conducted by using the "*numjac*" function in MATLAB®, was found to be sensitive to the input threshold vector of significance for the static solution. Small perturbations in the values of the static solution were observed to have a significant effect in the evaluation of the partial derivative of the function resulting in large discrepancies in the magnitudes of the real parts of the complex conjugate pairs of eigenvalues. Although the values for the threshold vector are not known in advance, in theory, the smaller the better. In order to perform the numerical calculation of the Jacobian matrix, an investigation of the best perturbation level was conducted to stablish the right approximation of the local slope via secant and minimise noise or other effects.

4.4.2.1. *Aerodynamic force formulation for each subconductor (Model 1B)*

With the objective to provide a direct comparison, Figure 4.24 shows the variation of the real parts of the complex conjugate pairs of the eigenvalues at the static equilibrium position in terms of the equivalent range of torsional displacements. The positive values of the real parts of each eigenvalue pair, which indicate the galloping instability, are highlighted in yellow. The vertical dashed lines define the boundaries of the galloping region which corresponds to the non-zero amplitudes identified for Model 1B in the previous analysis of amplitudes from the time series of displacements presented in Section 4.4.1.3.

It is noticeable that this linearization approach predicts the galloping stability regions accurately based on the range of torsional displacements and supports the nonlinear time domain analysis despite an initial displacement was applied in the time-history analysis. Based on the differences between the results for Case 1 and 2, there is evidence that the increase in the wind speed and the tension of the cables, and a decrease in the sag of the bundle, increases the range of instability torsional displacements.

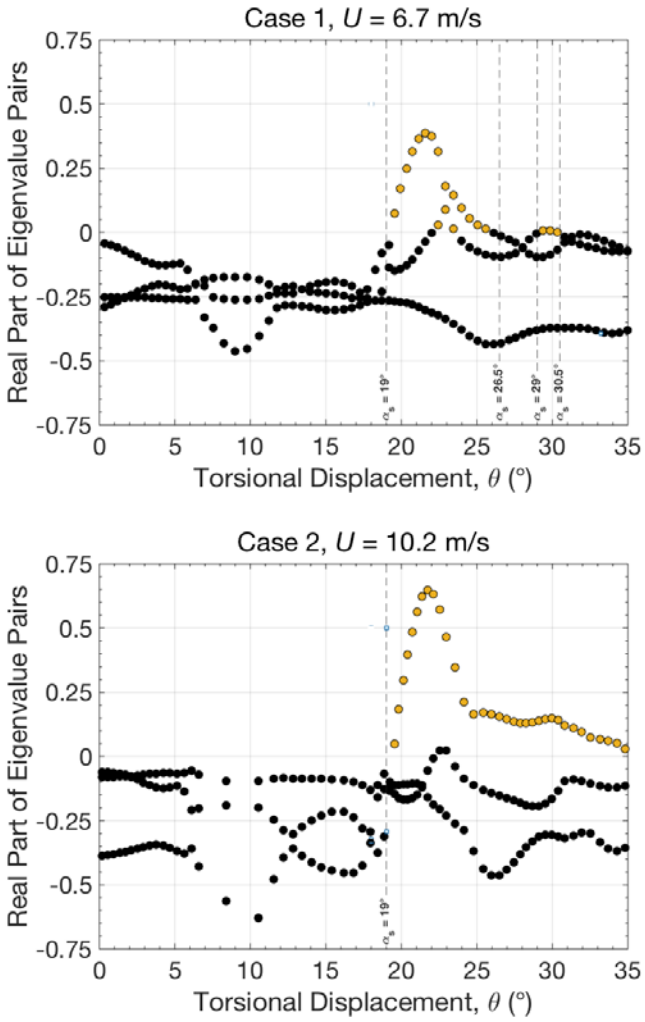

Figure 4.24. Variation of the real parts of the complex conjugate pairs of eigenvalues as the torsional displacement is varied, Case 1, Case 2. Vertical dashed lines define the non-zero amplitude boundaries identified in Model 1B from time-history analyses.

Figure 4.25 shows the eigenvectors in a scaled complex plane for two significant torsional displacements (e.g. 19.6 and 21.6° for Case 1 and 19.5 and 21.8° for Case 2), which corresponds to the point where the system first shows unstable behaviour (first positive real parts of the eigenvalue pairs) and where it is most unstable (maximum real parts of the eigenvalue pairs) according to the eigenvalue analysis shown in Figure 4.24. The three eigenvectors were normalized with respect to the magnitude of the largest component and rotated to aligned with the horizontal axis in order to make them numerically comparable.

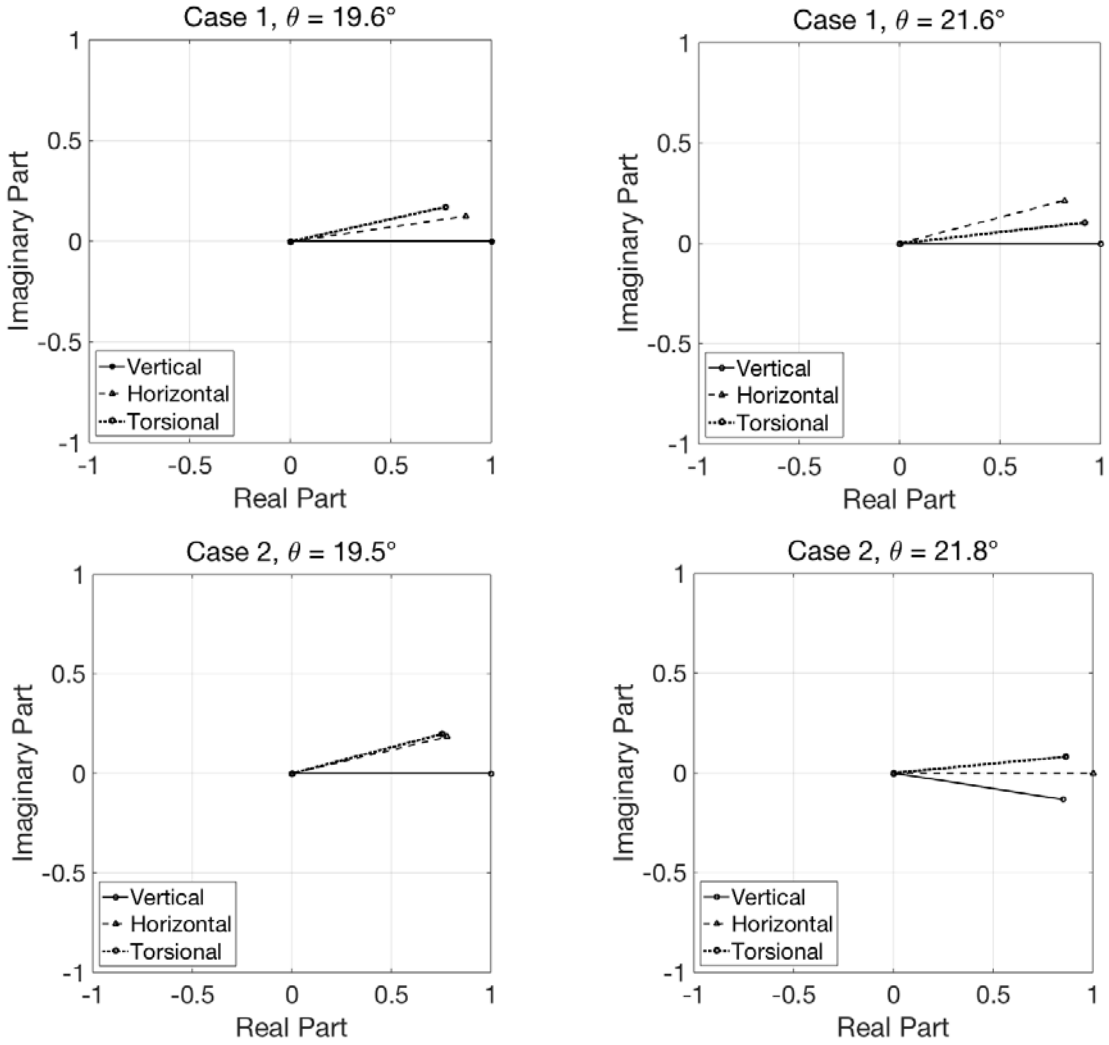

Figure 4.25. Complex conjugate pairs of eigenvectors for selected torsional displacements from Figure 4.24, Case 1, Case 2.

For Case 1, it is observed that for both torsional displacements, the motion is dominated by the vertical component in accordance with the steady-state amplitudes from the time-history analyses shown in Figure 4.23. Therefore, as it was expected, the corresponding curve of the real parts of the eigenvalue pairs that shows the maximum value between 19 and 25° torsional displacements in Figure 4.24, is dominated by the vertical motion. The results for Case 2 agree with the corresponding amplitudes identified from the time series of displacements in Figure 4.23, where it was noted that vibrations are dominated by motion in both the vertical and horizontal directions for torsional displacement close to 20°. For higher torsional displacements it was observed that the vertical component is clearly predominant.

The real parts of the complex conjugate pairs of eigenvalues of the Jacobian matrix at the static equilibrium position, taking a selected torsional displacement of 18° as an example, are

displayed in Figure 4.26 in terms of the wind speed for Case 1. The data points corresponding to the positive real parts of the eigenvalue pairs are highlighted in yellow over the shadowed blue area to illustrate the range of wind speeds where instability occurs. The galloping behaviour for the selected mean torsional displacement of 18° is observed for wind speeds greater than 9 m/s. Results presented by Matsumiya *et al*. (2022) on full-scale measurements of a bundle within a transmission line span with the same geometric arrangement as the wind-tunnel model described in Model 1, confirmed that galloping occurred when the wind speed was over 9 m/s.

The decrease in the aerodynamic damping in the vertical direction with the increase in the wind speed is illustrated by the increasing magnitudes of the real parts. On the other hand, aerodynamic damping in the horizontal and torsional directions is observed to decrease with the increasing wind speed.

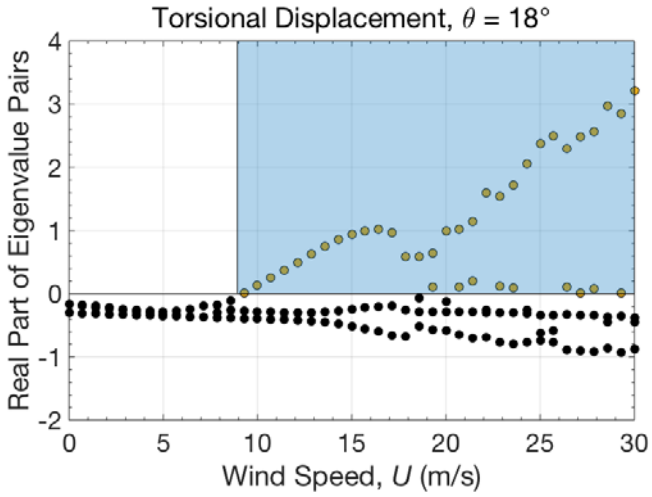

Figure 4.26. Variation of the real parts of the complex conjugate pairs of eigenvalues as the wind speed is varied for θ = 18° (Case 1).

On the basis of the previous relationship displayed in Figure 4.26, the critical wind speed, U_{crit}, was plotted for different torsional displacements in Figure 4.27 for Case 1 and 2. The critical wind speed is the value of the wind speed where the real parts of the eigenvalue pairs first become positive, and hence it might be used to define the instability boundaries of the system. It was found that the critical wind speeds in the range of torsional displacements between 0 and 9° are extremely large (e.g. around $1x10^7$ m/s), indicating the system is extremely stable for small torsional displacements and no realistic critical wind speed exists.

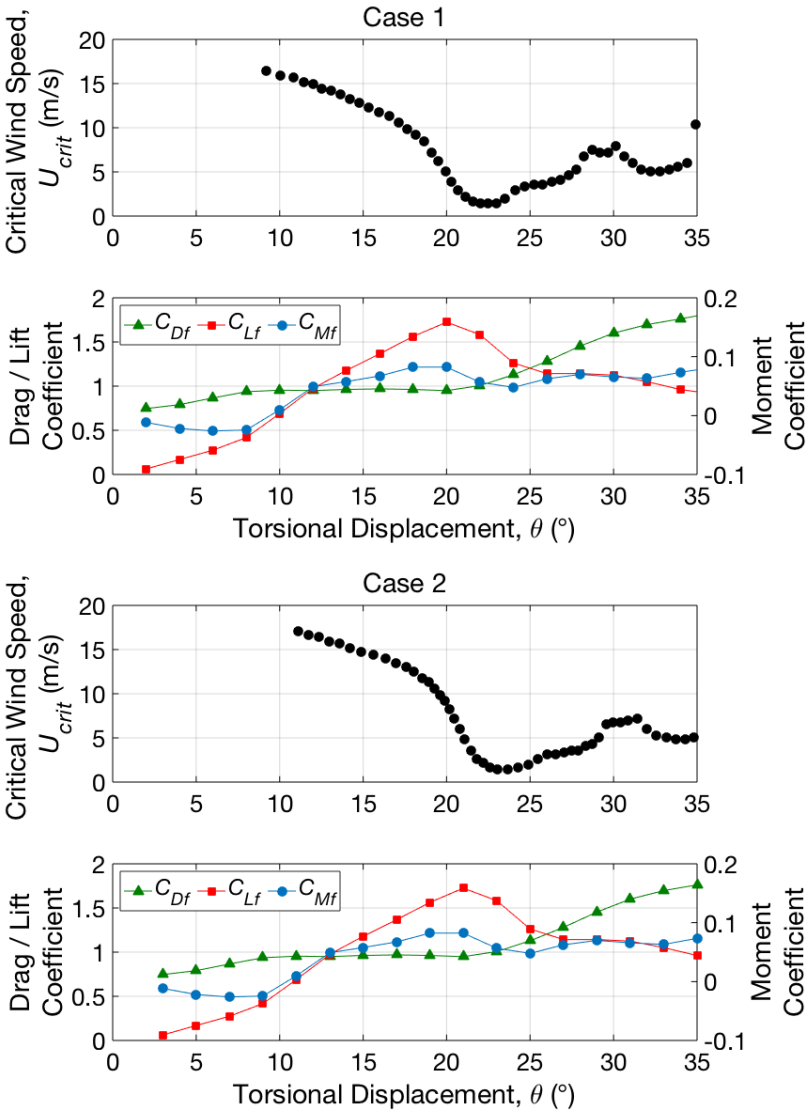

Figure 4.27. Variation of the critical wind speed and aerodynamic force coefficients as the torsional displacement is varied, Case 1, Case 2.

Below each of the subplots of the critical wind speed for Case 1 and 2 they are displayed the aerodynamic coefficients in relation to the torsional displacement to illustrate the relationship between the values of the critical wind speed and the lift coefficient measured on the bundle. From the time-history amplitudes analyses, the dominant motion was observed to be in the vertical direction. It seems that the critical wind speed is mainly governed by the magnitude of the lift coefficient showing an inversely proportional relationship in the range of torsional displacement considered. This trend matches with the classical definitions and formulations of galloping, such as those presented by Den Hartog (1932) detailed in Section 4.1.2 and CIGRE (2007), which relates the large-amplitude aeroelastic vibration with the lift force acting on an asymmetrical body section.

4.4.2.2. *He and Macdonald (2016) formulation (Model 2)*

This section assesses the galloping stability of the system through its eigenvalue analysis based on the formulation presented in Model 2, where the model parameters are related to the position of an aerodynamic centre. The eigenvalue analysis is compared with the analytical results of the total amplitudes from time-histories shown in Section 4.4.1.

Figure 4.28 shows the real parts of the complex conjugate pairs of eigenvalues of the Jacobian matrix at the static equilibrium position for each support orientation for the Case 1.

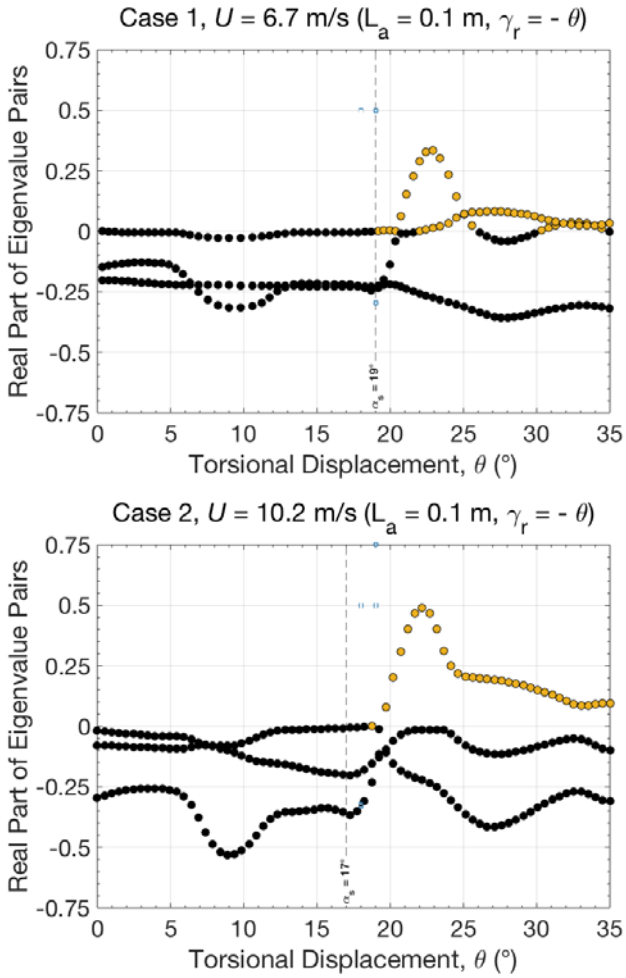

Figure 4.28. Variation of the real parts of the complex conjugate pairs of eigenvalues as the torsional displacement is varied, Case 1, Case 2. Vertical dashed lines define the non-zero amplitude boundaries identified in Model 2 from time-history analyses.

The L_a and γ_r, values that define the position of an aerodynamic centre were derived from the results displayed in Figure 4.12 in terms of the angle of attack. According to the relationship found in Figure 4.13, γ_r can be approximated to be equal to the negative

magnitude of the angle of attack. The positive values of the real parts of each eigenvalue pair are highlighted in yellow in Figure 4.28, while the vertical dashed lines define the start of the galloping region as identified in Figure 4.22. The prediction of the torsional displacement at which the galloping instability region starts based on the eigenvalue analysis agrees fairly well with the analytical amplitudes obtained from the time-history analysis, which showed good agreement with the analytical and full-scale results published by Matsumiya *et al*. (2018) from the wind tunnel tests.

However, results for Case 2 do not give such precise results. Although the discrepancy is relatively small, it is expected that if the stability locations are perturbed there would not be a good match of results. Moreover, it seems that the identified position of an aerodynamic centre does not lead to an accurate prediction of the instability for the set of parameters considered. Compared with Case 1, it is observed that in Case 2 the increase in the wind speed and the tension of the cables, and a decrease in the sag of the bundle, reduces the range of instability torsional displacements.

Figure 4.29 shows the eigenvectors in a scaled complex plane for two significant torsional displacements (e.g., 19.2 and 22.9° for Case 1 and 19.5 and 21.8° for Case 2), which corresponds to the point where the system first shows unstable behaviour (first positive real parts of the eigenvalue pairs) and where it is most unstable (maximum real parts of the eigenvalue pairs) according to the eigenvalue analysis shown in Figure 4.24. The magnitudes of the eigenvalues are normalized with respect to the magnitude of the largest component. The vertical component dominates the motion in both cases.

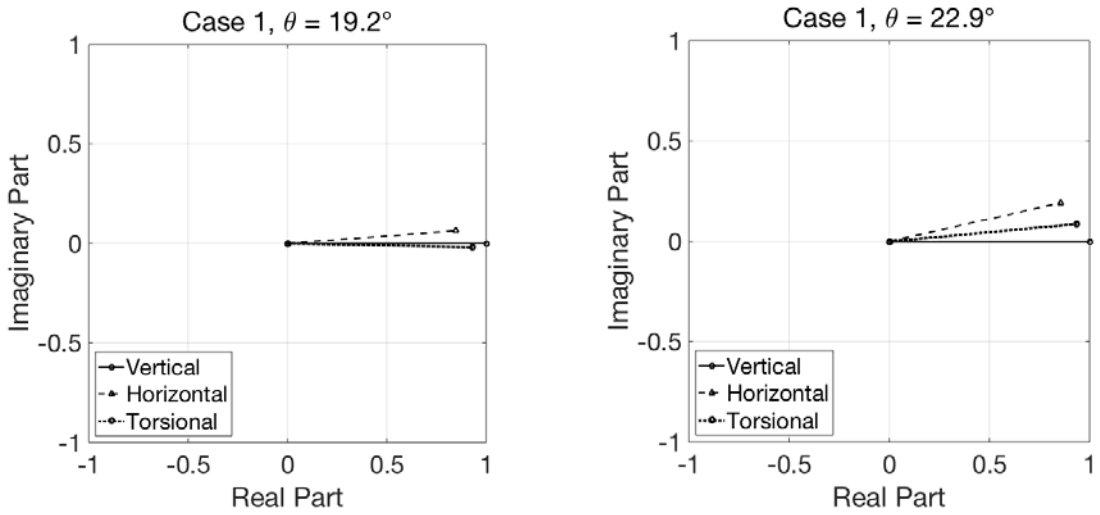

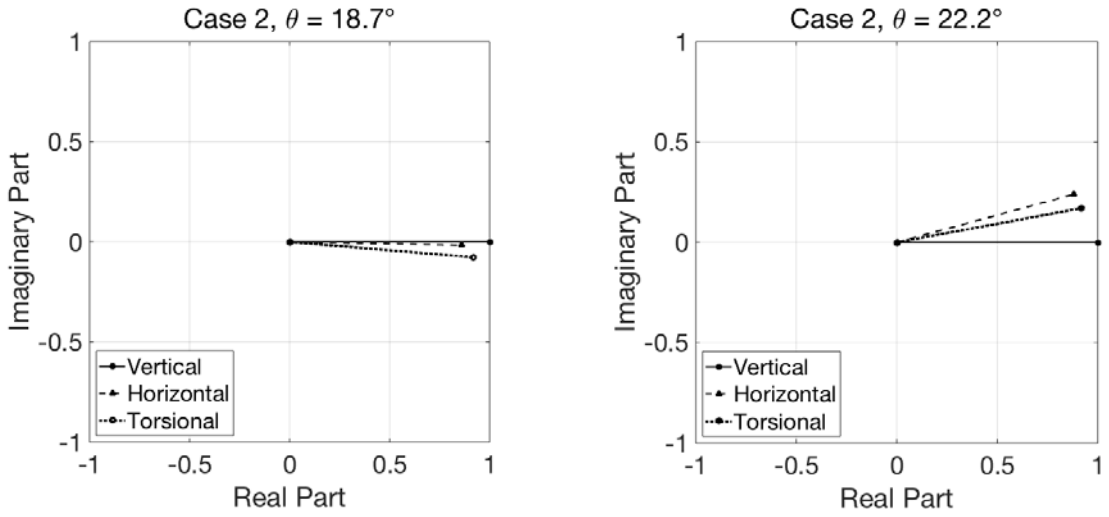

Figure 4.29. Complex conjugate pairs of eigenvectors for selected torsional displacements from Figure 4.28, Case 1, Case 2.

Despite the uncertainties related to the modelling of the structural damping and the initial perturbation of the system, this study suggests that the explored approach offers a useful and computationally efficient first point of analysis for identification and assessment of the galloping instability regions on the adopted 3-DOF model. These galloping instability regions, which were predicted based on the experimental steady-state aerodynamic drag, lift and moment coefficients measured in static wind tunnel test, agree relatively well with the reference analytical results obtained from Model 1B, which were consistent with the full-scale results from the wind tunnel tests.

4.5. DISCUSSION AND CONCLUDING REMARKS

4.5.1. Discussion

Alternatively to full-scale monitoring, this study suggests that the explored strategies offer a useful and computationally efficient first point of analysis for identification and assessment of the galloping instability regions. The instability regions found with the help of this approach have been identified for two different test conditions. Unlike the results from the wind-induced vibrations of tall buildings, the dynamic response of this cable structure showed a high sensitivity to the effect of the wind direction, illustrated in this analysis by the torsional displacement of the cable bundle. This distinctly behaviour is assumed to be due to the different

characteristics of this system with respect to tall buildings (e.g., dimensions, stiffness properties, boundary conditions, etc.). The relationship between the critical wind speed (i.e., the wind speed at which galloping emerges) and the magnitude of the experimental measured aerodynamic lift coefficient has confirmed the classical definitions and formulations of galloping (Den Hartog, 1932; CIGRE, 2007), where the condition of galloping instability is governed by the lift force acting on the body section expressed in the form of lift coefficient. In this regard, it was also observed that the simultaneous increase in the wind speed and the tension of the cables, and a decrease in the sag of the bundle, reduces the range of instability torsional displacements. These instability boundaries agree with the results obtained from the steady-state time-history response analyses of the model developed by Matsumiya *et al*. (2018), which showed good agreement with the full-scale results from the wind tunnel tests.

The behaviour estimated using the model from He and Macdonald (2016), which assumes the existence of the aerodynamic centre, is also relatively consistent with the results observed in the reference and linearized model. It is, therefore, found to be a promising approach to predict the onset of the galloping instability at full-scale. Furthermore, since the results obtained from Model 1 were consistent with Model 2 and wind tunnel experiments, it seems that it is a reliable approach in the analysis of galloping stability. This might lead to potential transferability to multiple future studies in full-scale measurements because it can be applied to an arbitrary bundle geometric section. In future work, it might be also applied to other types of slender structures, such as tall buildings. Although it should be noted that only two test cases were considered and slight discrepancies were observed in one of them, they have been assumed to be because the aerodynamic nonlinearities define the stability boundaries. Hence, the linear stability does not have a direct effect in the results when initial perturbation is applied to the system. In addition, modelling of the additional amplitude-dependent damping structural damping, which has been simplified in the presented model seems to be a source of discrepancies.

The identification of the position of an aerodynamic centre, which was used to represent the rotational velocity effects of the cross-section in several theoretical models, has provided a deeper understanding of its physics. This study presents novel results because its position under varying conditions has not been yet defined theoretically in literature. Based on experimental data from wind tunnel tests, the position of an aerodynamic centre, as adopted by He and Macdonald (2016), was found in terms of its relative position within the adopted bundle and

for different angles of attack. Assuming the wind to be along the principal axis of the system in the horizontal direction, the position of an aerodynamic centre was found to be approximately at the mid-point of the bundle for those angles of attack, for which there is no sub-conductor directly behind another one else. The mid-point of the bundle coincides with the elastic centre and the centre of mass. For those angles of attack for which there is at least one sub-conductor directly behind another, its position was found to be aligned with the wind direction towards the edge of the bundle upwind. It is assumed that the rotational motion cause a relatively large change in the forces, since the subconductor sheltered by another will then go into or out of a region with greater local wind velocity.

Although the use of the identified position of an aerodynamic centre has provided relative good agreement with the analytical and full-scale results published by Matsumiya *et al*. (2018) from the wind tunnel tests for one of the two test cases considered, this is of limited use because higher discrepancy and evidence of insensitivity to its different positions was observed in the other case. This might be because the range of stable boundaries depends on the static conditions, so the effect of the different positions of an aerodynamic centre based on L_a and γ_r parameters plays a role in the galloping cases whilst in the stable regions it might not be relevant.

Since limited parameter space has been taken as a reference, a more extended analysis would provide more conclusive findings. It might be possible to quantify this effect in further analysis using a simple model of the wake and knowing the mean wind speed downstream of one subconductor. If this downwind subconductor moves to a different location in that wake, it might be assessed the changes in the wind speed, the change in the force acting on it and in the drag, lift and moment on the overall bundle. If this can be done for the case of a bundle of subconductors where it can be modelled considering a discrete aerodynamic body, but the wind experiencing is dependent on the upstream conditions, maybe it could come with a theoretical reason where L_a and γ_r are what they are. In the case of a solid section, whether it is rectangular or bridge section it would include additional effects because the aerodynamic centre is different, but in the case of bundle, maybe an explanation can be found. In addition, it might be possible to predict the behaviour of different shapes of bundles, such as triangular, octagonal if a way of modelling them is found.

This analytical study has sought to disentangle the influence of the individual parameters that induce the emergence of galloping in a more straightforward controlled setting. This

environment enabled the observation of the emergence of galloping to prepare the groundwork for a full-scale environment, where similar phenomena are expected. The wind-induced instabilities will be analysed in detail to get appropriate appreciation when setting up the full-scale monitored data assessment plan on the same cable bundle geometry.

4.5.2. Concluding remarks

The main aim of this research has been to show how the analytical solutions of the 3-DOF quasi-steady aerodynamic force models of cable conductors provided by two different authors (i.e., Matsumiya *et al*., 2018; He and Macdonald, 2016) can be used in the prediction of galloping instability through the use of a simple controlled setting based on static wind tunnel test-data on four-bundled conductors presented by Matsumiya *et al*. (2018). This study has focused on understanding the parameters that induce the emergence of galloping in overhead electricity transmission lines. It has been performed by means of an eigenvalue analysis using the analytically defined aerodynamic damping matrix to predict the stability boundaries, whilst taking as a reference the two existing quasi-steady aerodynamic force models presented by Matsumiya *et al*. (2018) and He and Macdonald (2016), which implicitly takes into account the effect of an aerodynamic centre.

The main findings and conclusions of this study are:

- A new position of an aerodynamic centre for four-bundled square conductors in transmission lines has been found in terms of its relative position within the cross section for different angles of attack based on static wind tunnel test-data. Assuming the wind to be along the principal axis of the system in the horizontal direction, the position of an aerodynamic centre has been found to be approximately at the mid-point of the bundle for those angles of attack for which there is not any sub-conductor directly behind another. For those angles of attack for which there is at least one sub-conductor directly behind another, its position has been found to be aligned with the wind direction towards the edge of the bundle upwind. It is assumed that the rotational motion causes a relatively large change in the forces, since the subconductor sheltered by another will then go into or out of a region with greater local wind velocity. However, for the analysis conducted in this research based on the limited parameter space taken as a reference, the new identified position of the aerodynamic centre parameter has not changed the results significantly.
- The instability regions found with the help of the eigenvalue analysis agree with the results

obtained from the steady-state time-history response analyses of the model developed by Matsumiya et al. (2018), which showed good agreement with the full-scale results from the wind tunnel tests. The behaviour estimated using the model from He and Macdonald (2016), which assumes the existence of the aerodynamic centre, is also relatively consistent with the results observed in the reference and linearized model. It has been, therefore, found to be a promising approach to predict the onset of the galloping instability.

- It has been identified from the eigenvalue analysis that the galloping instability was mainly driven by the torsional displacement of the bundle, and at a lower extent, by the wind speed. Furthermore, the critical wind speed (i.e., the wind speed at which galloping emerges) has been found to be governed by the lift force acting on the body section expressed in the form of lift coefficient. Moreover, the analytical critical wind speed agrees with the full-scale observations on the same bundle geometry provided by Matsumiya *et al*. (2022).

CHAPTER 5. ANALYSIS OF FULL-SCALE MEASUREMENTS ON ELECTRICICTY TRANSMISSION LINES

5.1. INTRODUCTION AND THEORETICAL BACKGROUND

5.1.1. Introduction

In line with the analytical study presented in Chapter 4 on the galloping problem in overhead electricity transmission lines, the investigation presented in Chapter 5 provides a follow-up of the research at full-scale based on the same bundle geometry. In the context of the overall research aim of this Thesis, this study is an opportunity to gain better understanding on the wind-induced vibrations in slender structures by assessing other kind of structure different from tall buildings in Chapter 3 with different characteristics (e.g., dimensions, stiffness properties, flat urban vs. mountainous rural environment).

Given the several aforementioned negative structural effects caused by galloping (Literature Review), it is paramount to better design galloping mitigation solutions and improve inspection and maintenance. Therefore, it is essential to accurately predict the dynamic behaviour to develop a robust maintenance work strategy and reduce the frequency of inspections. However, inspection and maintenance are complicated, because of the wind-induced excitations, the high-voltage electricity, and the large ground clearance. Hence, in line with the monitoring system used in tall buildings, which consisted only in three accelerometers and an anemometer, this analysis highlights the importance of the use of a minimalist monitoring approach. The tools and elements of methodologies from tall buildings are adapted to a more challenging setting in this study to identify the limits of their applicability, assess usefulness and, ideally, propose further refinements and improvements. Hence, full-scale measurements have been taken with the objective to understand the dynamic response of transmission lines, particularly under extreme events such as galloping. Factors that influence the occurrence of galloping are the tension of the conductors, vibration amplitude, the mode of displacement, the ice accretion and the wind conditions.

The focus of this chapter is to conduct the full-scale investigation in order to identify trends in the ambient vibrations in a range of atmospheric conditions with the objective to analyse the typical values in operational conditions. This is a relevant analysis based on valuable data because, although galloping can be observed at wind-tunnel scale, as observed in

Chapter 4, the identification of a set of detailed conditions under which full-scale galloping occurs from field observations is challenging to simulate in the wind tunnel. The variables that might influence the dynamic response of the structure include the pre-tension in the conductor cables, vibration amplitude, vibration modes, wind conditions, ice accretion shape and distribution. Since several months of recording are available, the variation of the wind-induced response has been analysed in order to identify the most influential parameters in the dynamic response of the system, with a specific focus on the galloping events. These findings have been compared with the equivalent results obtained from experimental wind-tunnel data in Chapter 4.

This chapter examined full-scale measurements on a four-bundled conductor within a transmission line span in Japan (Tsuruga test line). Some preliminary results on the test line were presented by Matsumiya *et al.* (2017), Matsumiya *et al.* (2022a) and Taruishi and Matsumiya (2022) in the context of an extensive research project conducted by the Central Research Institute of Electric Power Industry (CRIEPI) in several electric power transmission facilities in Japan. Previous research discussed the incidence conditions of galloping with special emphasis on the suppression effect of loose spacers under ice accretion conditions. The monitoring system included an industrial television (ITV) camera, LED lamps, GPS sensor and inclinometers. From them, Matsumiya *et al.* (2022a) and Taruishi and Matsumiya (2022) also used tension meters to identify a clear relationship between the tension variation and the vertical displacement amplitude of a vibration mode for which large galloping was observed.

The main motivation of previous research was to identify the conditions under which galloping occurred based on tension data neglecting displacement measurements. Although the displacements were identified using an ITV camera, they could only be obtained over a limited period because of the poor visibility during night-time, blinding blizzard or thick fog conditions. In addition, the installation, calibration and maintenance of tension meters are cheaper and less demanding than for ITV cameras, LED lamps and GPS sensors. Therefore, it was desirable to estimate the occurrence of galloping and the dynamic properties in general from tension measurements rather than displacements. Thus, the results from full-scale measurements displayed in the present study have been obtained from two tension meters and an anemometer installed on the target span to monitor the effects of the wind on the structure from December 2018 to April 2019, giving a wide range of conditions. These results have been used to make

technical claims about what the system experiences and assess the extent to which the methodology is sufficient to analyse the galloping phenomenon.

The objectives of analysis are unique and different from previous investigations because the assessed response of the structural system in this investigation is based on the natural frequencies estimates rather than on the displacements amplitudes or accelerations. The research on the Tower 1 presented in Chapter 3 found that reliable estimates of both natural frequencies and damping ratios could be used for that type of slender structures subjected to wind loading. However, it has been expected the modal parameter estimation of the monitored four-bundled conductor to be more susceptible to the loading assumption given it is a more complex nonlinear system.

This analysis adopts the use of a simple linear Finite Element Method (FEM) model as a tool that enables the interpretation of the dynamic behaviour of the system from the full-scale observations. The first 15 modes have been estimated in the original structure without modifying its structural parameters before assessing their variation with a mass increase of up to 100% to simulate the effect of ice and snow accretion on the bundle. The results obtained from this analysis are used to support the observations of the actual experiments. Compared with the study in tall buildings (Chapter 3), the analysis in transmission lines has not reached the level of physical fidelity experienced in the behaviour of the full spectrum of the modes.

5.1.2. Theoretical background of poly-reference least-squares complex frequency-domain (pLSCF) or “PolyMAX” and Stabilisation diagram

This section briefly presents the theory behind the poly-reference least-squares complex frequency-domain (pLSCF) method or PolyMAX (i.e., commercial name) that has been selected and adapted in this study as the baseline system identification method. It has been primarily used in the present analysis to identify the modal properties of the system and accompanied, to a lesser extent, by the IWCM developed by Macdonald (2000), which was extensively detailed in Section 3.1.2.1.

The poly-reference least-squares complex frequency-domain (pLSCF) method is a non-iterative frequency-domain method that evolved from the least-squares complex frequency-domain (LSCF) method (Van der Auweraer *et al.*, 2001; Guillaume *et al.*, 2003; Peeters *et al.*, 2004) used in EMA. The stabilisation diagram is the most important advantage of pLSCF over previous parameter estimation techniques according to Peeters *et al.* (2004). It is constructed to

discriminate between structural and *spurious* modes of the structure under test in a context of closely space modes. It was developed on the assumption that the real structural modes provide similar frequencies, damping ratios and mode shapes with the sequential increase in the model order.

The use of pLSCF and stabilisation diagrams particularly in the context of OMA and PSDs, is embedded in SSI (Stochastic Subspace Identification Method) technique. Since then, that community moved on to the use of the transmissibility functions, which are commonly used to construct the stabilisation diagrams for OMA of civil engineering structures. To perform the modal parameter estimation, the pLSCF fits a rational fraction of two polynomials on each response auto/cross- PSD (Gasparis, 2019). Using the so-called right matrix-fraction model, the PSD and CPSD (Cross Power Spectral Density) matrix representation as a sum of modal contribution derived from expression given by Schanke (2105) is expressed as:

$$[S(\omega)] = [B(\omega)][A(\omega)]^{-1} \tag{5.1}$$

where $S(\omega)$ is the PSD matrix

$B(\omega)$ is the numerator matrix polynomial

$A(\omega)$ is the denominator matrix polynomial

The numerator and denominator matrixes polynomial for each measurement channel $o = 1 \ldots l$ are defined as:

$$[B(\omega)] = \sum_{r=0}^{p} \Omega_r(\omega)[\beta_{or}] \tag{5.2}$$

$$[A(\omega)] = \sum_{r=0}^{p} \Omega_r(\omega)[\alpha_r] \tag{5.3}$$

where $\Omega_r(\omega)$ is the polynomial basis function

p is the polynomial order

β_{or} and α_r are the polynomial coefficients corresponding to the unknown real parameters to be estimated

Derived from the algorithm of the LSCF method, the basis function is chosen:

$$\Omega_r(\omega) = e^{j\omega\Delta tr} \tag{5.4}$$

where Δt is the sampling time

In the context of OMA, where output-only data is considered, physical modes can be determined after the stabilisation diagram is constructed to discriminate *spurious* modes on the basis of stable physical λ_i and unstable $-\lambda_i$ poles. According to Guillaume (2006), by taking the Fourier Transform of the positive time samples only, the unstable poles will not occur in the half (or positive) power spectra $S(\omega)$ (Equation 5.5):

$$[S(\omega)] = \sum_{i=1}^{n} \frac{\{v_i\} < k_i^T >}{j\omega - \lambda_i} + \frac{\{v_i^*\} < k_i^H >}{j\omega - \lambda_i^*} \tag{5.5}$$

where $i = 1 \ldots n$, where n is the number of modes

$*$ indicates the complex conjugate of a matrix

H indicates the complex conjugate transpose of a matrix

$\{v_i\} \epsilon \mathbb{C}^l$ are the mode shapes

$< k_i^T > \epsilon \mathbb{C}^m$ are the operational reference vectors

λ_i are the poles

The operational reference vector is a function of the modal parameters and the power spectral matrix of the unknown input forces (Guillaume, 2006).

In EMA (Experimental Modal Analysis), the measured frequency response function FRF requires the initial guess of the modes, which comes from the stabilisation diagram. The FRFs are fitted according to Peeters *et al*. (2008) by:

$$[H(\omega)] = \sum_{i=1}^{n} \frac{\{v_i\} < l_i^T >}{j\omega - \lambda_i} + \frac{\{v_i^*\} < l_i^H >}{j\omega - \lambda_i^*} \tag{5.6}$$

where $[H(\omega)] \epsilon \mathbb{C}^{l \times m}$ is the FRF matrix considering m inputs and l outputs

$i = 1 \ldots n$, where n is the number of modes

$*$ indicates the complex conjugate of a matrix

H indicates the complex conjugate transpose of a matrix

$\{v_i\} \epsilon \mathbb{C}^l$ are the mode shapes

$< l_i^T > \epsilon \mathbb{C}^m$ are the modal participation factors

λ_i are the poles

ξ_i are the eigenfrequencies (in rad/s)

ω_i are the damping ratios

In the context of the pLSCF's algorithm, the *modalsd* function in MATLAB® provides the estimates in the stabilisation diagram on the basis of some level of tolerances, which are estimated by comparing consecutive approximating orders that correspond to the number of poles. The order of the fitted system is increased progressively with the right mathematical structure, but it is derived from physics. The difference between poles is estimated in the sense of complex numbers. The real part corresponds to the damping ratio, while the imaginary part corresponds to the natural frequency. The poles, in complex conjugated-pairs, λ_i, λ_i^*, are defined by Peeters *et al*. (2008) as:

$$\lambda_i, \lambda_i^* = -\xi_i \omega_i \pm j\sqrt{1-\xi_i^2}\omega_i \tag{5.7}$$

where λ_i are the poles

$i = 1 \ldots n$, where n is the number of modes

ξ_i are the eigenfrequencies (in rad/s)

ω_i are the damping ratios

A starting estimate for the optimisation algorithm is performed before an approximated function is fitted on it, and it returns newly found modal natural frequencies and damping ratios that might be very close to the ones provided. According to Peeters *et al*. (2008) the mode shapes and the residuals can be found from the linear least-squares solutions of the following expression given by:

$$[H(\omega)] = \sum_{i=1}^{n} \frac{\{v_i\} < l_i^T >}{j\omega - \lambda_i} + \frac{\{v_i^*\} < l_i^H >}{j\omega - \lambda_i^*} - \frac{[LR]}{\omega^2} + [UR] \tag{5.8}$$

where $[H(\omega)] \epsilon \mathbb{C}^{l \times m}$ is the FRF matrix considering m inputs and l outputs

$i = 1 \ldots n$, where n is the number of modes

$*$ indicates the complex conjugate of a matrix

H indicates the complex conjugate transpose of a matrix

$\{v_i\} \epsilon \mathbb{C}^l$ are the mode shapes

$< l_i^T > \epsilon \mathbb{C}^m$ are the modal participation factors

λ_i are the poles

ξ_i are the eigenfrequencies (in rad/s)

ω_i are the damping ratios

5.2. DESCRIPTION OF SITE AND MONITORING SYSTEM

The Tsuruga Test line is located in a mountainous area in central Japan, 10 km from the Sea of Japan, as shown in Figure 5.1. In particular, full-scale monitoring has been conducted on a target span of the line between two towers, denoted Tower 2 and Tower 3, for which the azimuth angle (i.e. angle with respect to the polar north, measured clockwise) is 100°. It is approximately 700-850 above sea level on a higher position with respect to the northwards ground surface (i.e., the prevailing wind direction), which has a slope of around 27° as described by Matsumiya *et al.* (2022a). Since transversal wind and in-cloud icing are expected, this span is a good choice to observe galloping a priori. Although measurements have been taken on this

line for several years, in the context of an extensive research project conducted by the Central Research Institute of Electric Power Industry (CRIEPI) in several electric power transmission facilities in Japan, only records provided by CRIEPI between December 2018 and March 2019 are presented in this study. Previous studies on different spans of the Tsuruga Test line were conducted by Yukino *et al*. (1995) and Gurung *et al*. (2003). The findings on this electricity transmission line have potential transferability to sites in Europe with similar atmospheric and terrain conditions.

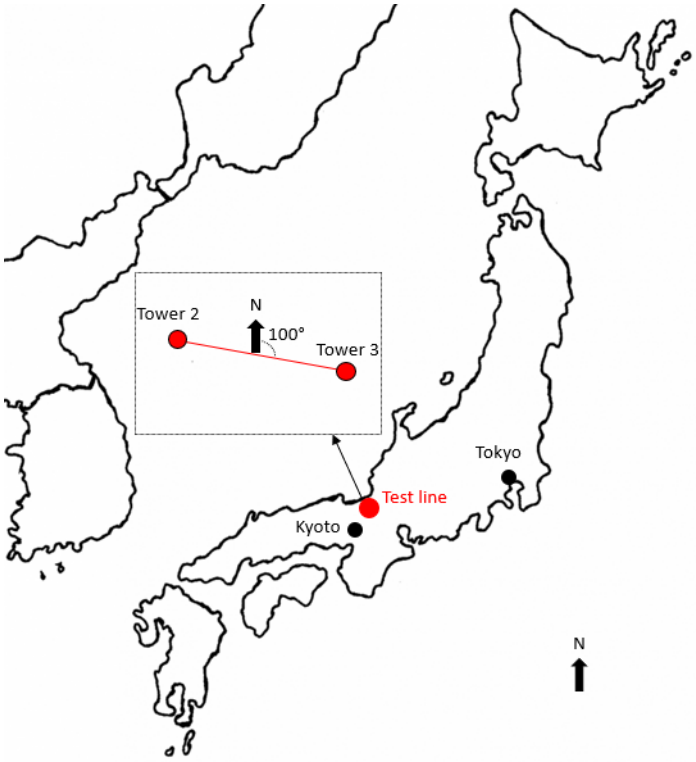

Figure 5.1. Location map of the test line and orientation. [Adapted from Matsumiya *et al.* (2022a)].

Figure 5.2 shows the approximate structural arrangement of the target span, which is composed of three phases (e.g., Phase A, B and C), and the location of the monitoring equipment. At the time of the measurements considered in this study, loose and normal spacers were installed at Phase A and C, respectively. Standard spacers are rigid connectors that maintain the distance between multi-bundled conductors. Measurements were taken in Phase A and C, but only Phase C has been assessed in this study. The conductor bundle of Phase C is connected to Towers 2 and 3 by tension-type supports. The span length of Phase C, the sag and the height difference between the Tower 2 and Tower 3 are 345, 10.8 and 95 m, respectively. Phase C is 40 m above ground level.

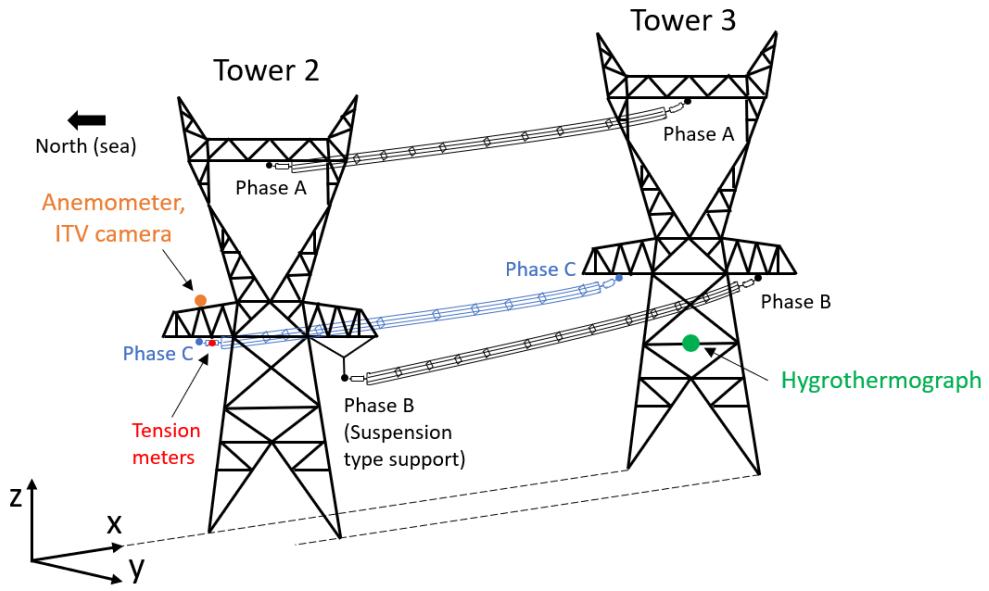

Figure 5.2. Sketch of the target span and the location of the monitoring equipment.

The square-shaped bundle is composed of four ACSR410 (Aluminium conductor steel-reinforced cable) conductors, with a diameter of 28.5 mm and a nominal cross-sectional area of 410 mm^2 for each sub-conductor, as illustrated in Figure 5.3. They are connected at twelve spacers weighting 8 kg each, and the distance between sub-conductors is 400 mm. Line spacers are commonly used in bundles to avoid contact between the sub-conductors. According to Japanese Industrial Standards Committee (1994), this type of commercial cable is made of concentric layers of twenty-six grouped aluminium (4.5-mm diameter and 413.4 mm^2 overall cross-sectional area) and a core of seven galvanised steel wires (3.5-mm diameter and 67.3 mm^2 overall cross-sectional area).

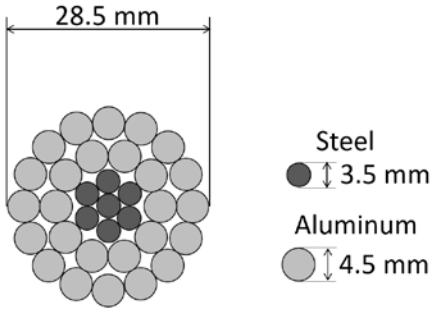

Figure 5.3. Cable cross-section of ACSR410 sub-conductor.

The weight of each sub-conductor, the mass density, the modulus of longitudinal elasticity and the linear expansion coefficient are 1.673 kg/m, 3479.617 kg/m^3, 81.984 GPa and

$18.9x10^{-6}$ $(°C)^{-1,}$ respectively. According to H. Matsumiya and S. Taruishi (personal communication, October, 2022), the initial pretension load on the bundle measured previously to the installation of the monitoring equipment is approximately 90 kN (i.e. 22.5 kN per each individual sub-conductor), while its breaking load is 136 kN.

The monitoring equipment is composed of a vane anemometer, an industrial television camera (ITV) and two tension meters installed in Tower 2 and a hygrothermograph in Tower 3, as shown in Figure 5.4. Their main characteristics and their exact location are discussed later in detail. The two tension meters are the key instruments in the present study, from which the main results are derived. The anemometer, tension and hygrothermograph recordings were acquired continuously and correlated in time. In order to use the anemometer and tension measurements for further processing, the data were saved in 1-day long records. The hygrothermograph measured the temperature, in degrees Celsius, and the relative humidity, expressed as a percentage, for every 10 minutes. The anemometer and the ITV camera have been installed on a pole at the east side of the north cross-arm of Tower 2 at the height of 40 m from ground level. The ITV camera was used by Matsumiya *et al.* (2012), Taruishi *et al.* (2021), Matsumiya *et al.* (2022a) and Taruishi and Matsumiya (2022) to monitor the displacements of the bundle and note the presence of ice accretion on the cables at a rate of 10 FPS (Frames per second). In this study it has been only used to verify the occurrence of galloping.

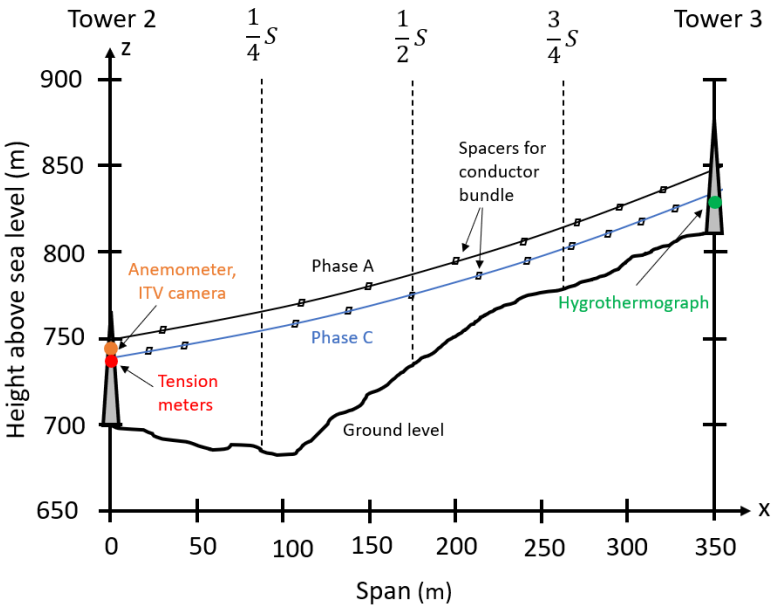

Figure 5.4. Profile of the target span and the location of the monitoring equipment. [Adapted from Matsumiya *et al.* (2022a)].

The vane-type anemometer consists of a propeller and a wind vane. The wind vane is a device that always points towards the wind direction, and in this case, it measures the horizontal component of the wind direction clockwise relative to the north from 0 to 360°, as shown in Figure 5.5. When the wind direction is 10°, the wind is perpendicular to the line. The sampling frequency of the anemometer is 20 Hz.

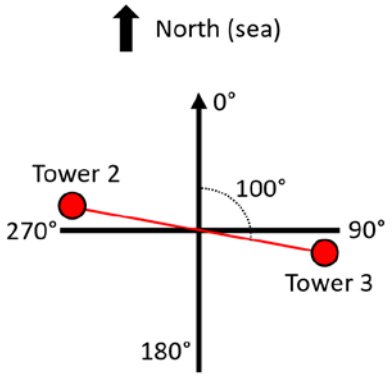

Figure 5.5. Wind direction convention relative to the test line.

The tension meter, with a sampling frequency of 20 Hz, are of the strain gauge type, so the tension of a cable is inferred from the strain of the cable, which is related to its electrical resistance, as described by Keil (2017). Figure 5.6 shows the location of the two tension meters on a hinge joint at the insulators (the weight of each insulator is 956 kg), which are connected to the tower and to the four-bundled conductor by pinned supports.

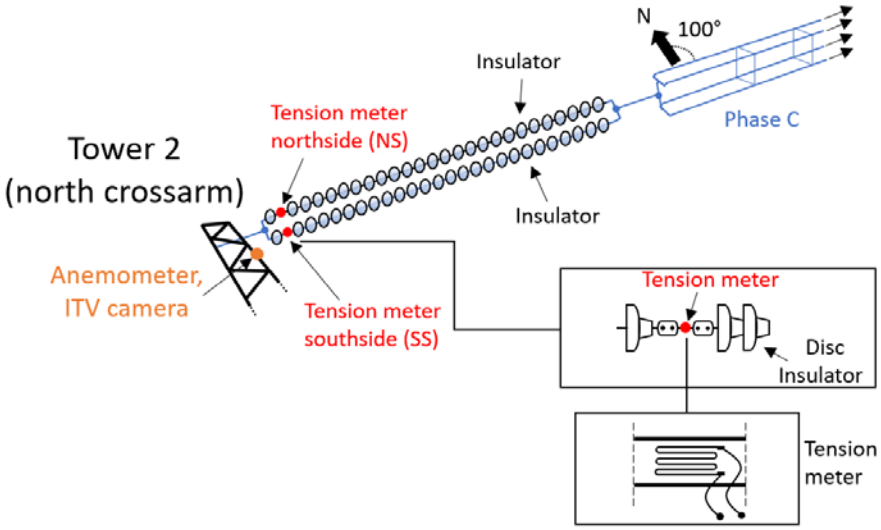

Figure 5.6. Detailed arrangement of the monitoring equipment at Tower 2.

The addition of tension loads from the two sensors, which are named Northside support (NS) and Southside support (SS), is equivalent to the total load on the Phase C bundle.

Rubio-Gómez *et al*. (2021) discussed some drawbacks of this approach, such as that the measured tension might differ from the real tension when the bundle orientation is not aligned with the insulators, the requirement of a wire cable supply or the latency and lack of synchronism if non-wire signal is used. Moreover, due to severe weather conditions, the monitoring system has been affected by lighting and shortages of the power supply that uses solar panels. These shortages have interfered with some tension measurements for a few hours and with readings from the hygrothermograph for several days.

5.3. OVERVIEW OF THE OBSERVATIONS

5.3.1. Description of data

Although measurements on this site have been taken since 2017, only records between 2018/12/01 and 2019/04/01 (e.g. 121 daily records) are considered in this analysis. The format and the main characteristics of the raw measured data have determined the handling process of the data. Tension measurements (in kN) from Northside support (*NS*) and Southside support (*SS*) tension meters were saved in 1-day long records for further processing of the data. An overview of the extent of the database (e.g. 121 daily records) is further detailed in Section 5.6. The tension loads measured by the sensors correspond to the load on the insulators excluding the pretension load on the bundle, which is approximately 90 kN (i.e. 22.5 kN per sub-conductor). The pretension load was measured on the bundle before the installation of the tension meters. The overall 121 1-day long records have been classified based on the peak-to-peak tension loads. The different classes are described as follows:

- Most of the measurements correspond to the 78 non-galloping records. Two main types of non-galloping records have been distinguished:
  - 70 non-galloping records which have relatively low tension force, with a well-defined response resulting in clearly clustered frequencies. The peak-to-peak loads for this type of records mostly lie in the range ± 2 kN.
  - 8 non-galloping records under higher excitation force where the identified frequencies are consequently scattered. The loads for long periods within each daily record can reach ± 6 kN.

- There are 18 observed galloping events listed by Matsumiya *et al.* (2022a) involving 36 daily records, where high tension forces have been largely measured, and the frequencies seem to be dominated by the limit cycle frequencies of the galloping oscillation and its harmonics. The peak-to-peak loads from the time series of tension for this type of records (Figure 5.25) are usually larger than ± 8 kN. However, it is noted that for some records, tension loads are just between -2 and +3 kN.
- Finally, seven files have been neglected because unreliable signals are present during the majority of the record due to power shortage.

A comparison between standard behaviour (i.e., relatively low tension force) and extreme event (e.g., higher excitation force) of non-galloping records is provided to highlight the different responses of the system and motivate further split into non-galloping and galloping regimes. Two typical files for each one of the two scenarios have been selected as an example in Figure 5.7, where the time series of the tension are displayed. It is noted that for most of the monitoring period of most records the tension load of the SS is higher than in the NS, probably because the bundle is slightly inclined towards the north side.

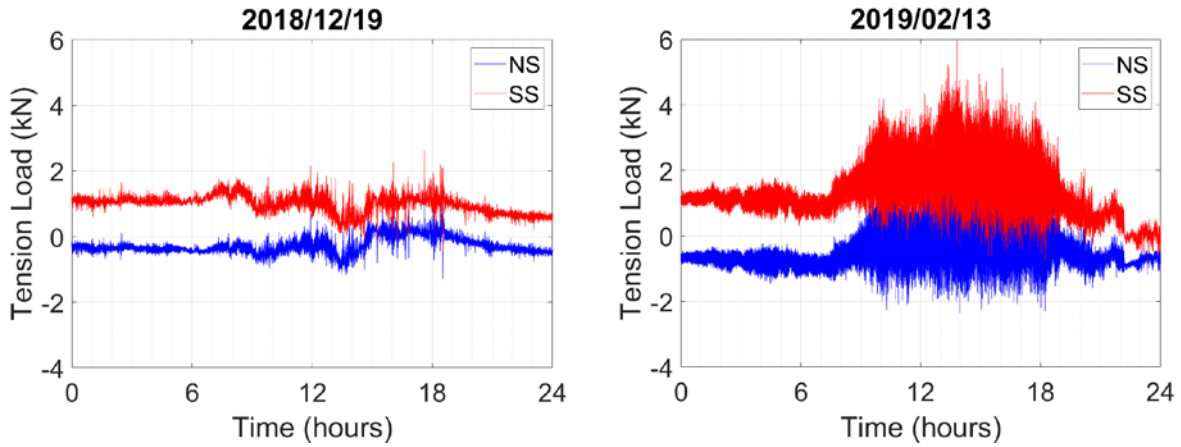

Figure 5.7. Time series of low (left-hand side) and high (right-hand side) tension load of non-galloping records.

The left-hand side plot shows the standard non-galloping record which have relatively low tension force, with peak-to-peak loads in the range ± 2 kN. Since galloping is a complex phenomenon where there are various mechanisms involved, a large peak-to-peak tension load amplitude might not necessarily be an indication of galloping, as displayed in the right-hand

side plot. Peak values in this type of record under higher excitation force have been found to be up to ± 6 kN.

5.3.2. Environmental conditions

Figure 5.8 shows the 10-minute statistics average temperature and relative humidity for the monitoring period taken into account. The overall mean temperature and relative humidity are 1.4 °C and 94.5 %, respectively. The mean temperatures for each month are 2.5, -0.8, 0.4 and 3.3 °C, respectively. The maximum temperature, 15 °C, was measured on 2018/12/04 at 19:30 and 19:40 while the minimum temperature, -5.6 °C, was measured on 2019/02/10 at 07:40, 07:50, 08:00 and 08:20. The mean daily variation in temperature between the maximum and minimum temperature for each month are 4.5, 3.7, 5 and 6.1 °C respectively. The maximum temperature variation within one day was measured on 2019/03/29, where it oscillated between -1 and 12.6 °C.

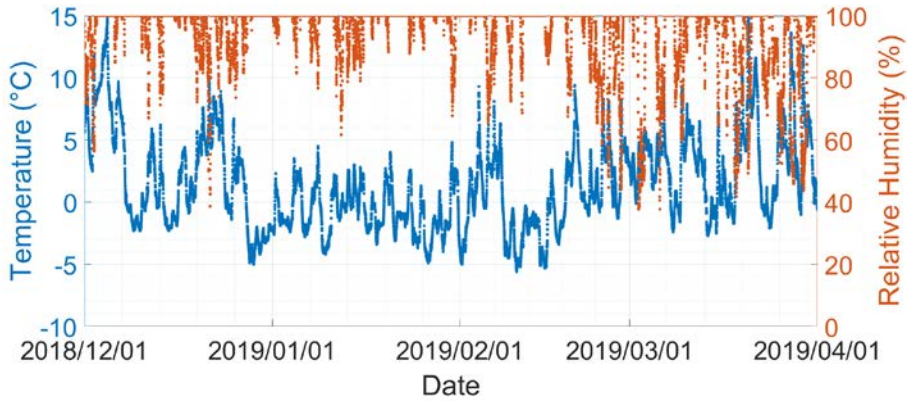

Figure 5.8. 10-minute statistics average temperature and relative humidity for the full monitoring period.

The 10-minute statistics average wind direction and wind speed at the Tsuruga Test line site during the winter season are displayed in Figure 5.9. North (between 315 and 45°) is the prevailing wind direction in 43, 54, 52 and 29 % of the 10-minute statistics for December, January, February and March, respectively. The wind speed has been found to be relatively uniform over the monitoring period since the mean values for each month are 5.7, 6.2, 6.2 and 6.0 m/s, respectively. However, it has been found to be highly variable over each day. The maximum variation in wind speed within one day was measured on 2019/03/04, ranging between 0.2 and 17.8 m/s. Wind measurements conducted in the proximity of Tower 2 by Horiguchi and Mitsuta (1994) found that the wind blowing-up angle was approximately 13°

and 6° at 30 and 160 m above the ground level, respectively, while the maximum mean wind speed was measured at about 40 m above the ground.

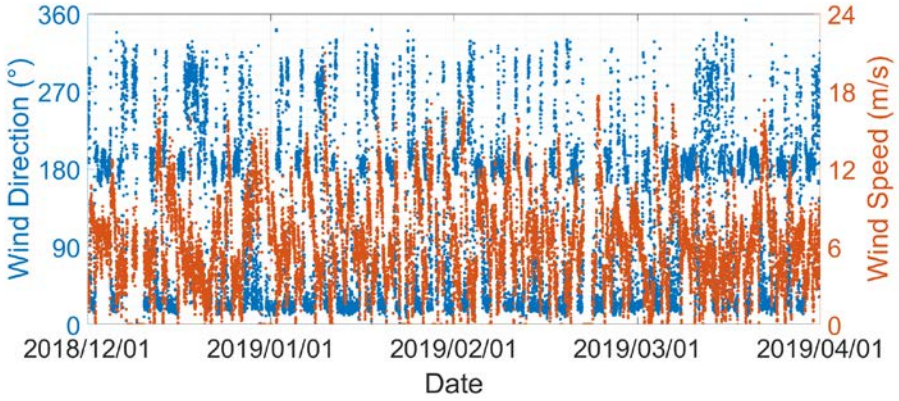

Figure 5.9. 10-minute statistics average wind direction and wind speed for the full monitoring period.

During the winter season, prevailing winds blow from Siberia from north to south, causing heavy snowfalls on the site of the test line. In most cases, icing and subsequent galloping on the Tsuruga line occurred when the ice accretion was detected with wind from the north. However, Matsumiya *et al*. (2022a) found that in a few cases, wind direction reversed once the ice accretion was already formed on the sub-conductors. Also, in the majority of the cases of galloping, Matsumiya *et al*. (2022a) observed ice and snow accretion formed on the sub-conductor, particularly on the leeward side. The amount and distribution of ice accretion on transmission lines are difficult to quantify, so its occurrence on the studied test line has been based on visual inspection. Ice accretion on the bundle has been generally observed to build up during between ten and twenty minutes at temperatures below -4 °C while melting and shedding started to occur at approximately 0 °C, lasting between ten minutes and one hour. Ice shedding on this site is mainly caused by the increase in temperature rather than the motion of the cable. The weight of ice accretion on each conductor has been estimated to be approximately between 0.3 and 0.5 kg/m by Matsumiya *et al*. (2022a), which represents 18 and 30% of the mass of the conductor. On the basis of the parametric analysis from the FEM model (Section 5.4.2), the added mass on the bundle leads to a decrease on the natural frequencies. To sum up, these observations highlight that the atmospheric conditions have a significant effect on the dynamic response of the system, mainly due to the combined action of wind and ice accretion. A more detailed analysis of these conditions and the quantified responses might illustrate the importance of the effects on the structure.

5.4. FINITE ELEMENT METHOD ANALYSIS

5.4.1. Finite Element Method (FEM) model

The analysis of full-scale data has been supported by the use of a FEM model of the bundle to predict and understand the observed responses of the structures. It provides an overview of the data with the aim to use later a suitable identification method. The FEM analysis has been conducted in OpenSees® software using the corotational finite element technique accounting for the cross-sectional bending and torsional stiffness terms, as detailed by Belytschko and Hasieh (1973). This technique was developed by De Souza (2000) for OpenSees® and denoted as "Corotational Coordinate Transformation", where it was noted that this method is used in large displacement-small strain problems.

The finite element mesh of the bundle is defined according to the structural arrangement detailed in Section 5.2 where *x* (axial), *y* (horizontal) and *z* (vertical) directions are adopted, as shown in Figures 5.10 and 5.11. The squared bundle has been modelled as a three-degree of freedom (i.e., vertical, horizontal and torsional) elastic beam in three-dimensional space with fully restrained supports.

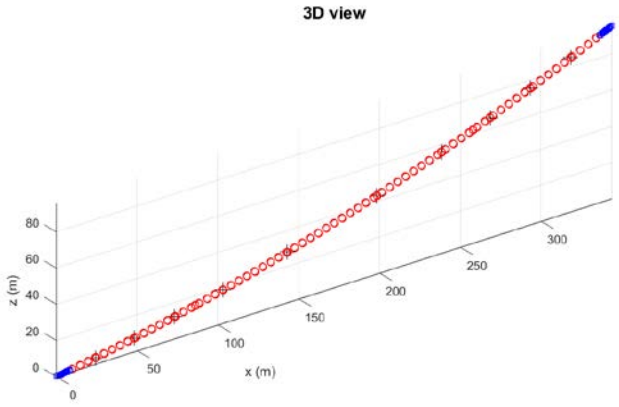

Figure 5.10. General arrangement of the FEM model. Red and blue markers correspond to the cable and insulator elements, respectively.

The geometry of the bundle was modelled based on visual approximation rather than real measurements, and its initial shape can be better described by a polynomial function rather than a catenary. The horizontal length of the model (e.g. span) is 343.9 m, and the overall length of the single conductor is 341.56 m. A total of 316 equally horizontally spaced beam finite elements are considered for each conductor. The maximum sag (point to line) is 11.95 m, and

the maximum sag (vertical distance) is 12.41 m. The vertical distance between both ends is 95.8 m, and the temperature during the analysis is set to 0 °C in the software. The links representing the spacers illustrated in Figure 5.4 have been modelled as beams. Selected characteristics of the model are summarised in Table 5.1.

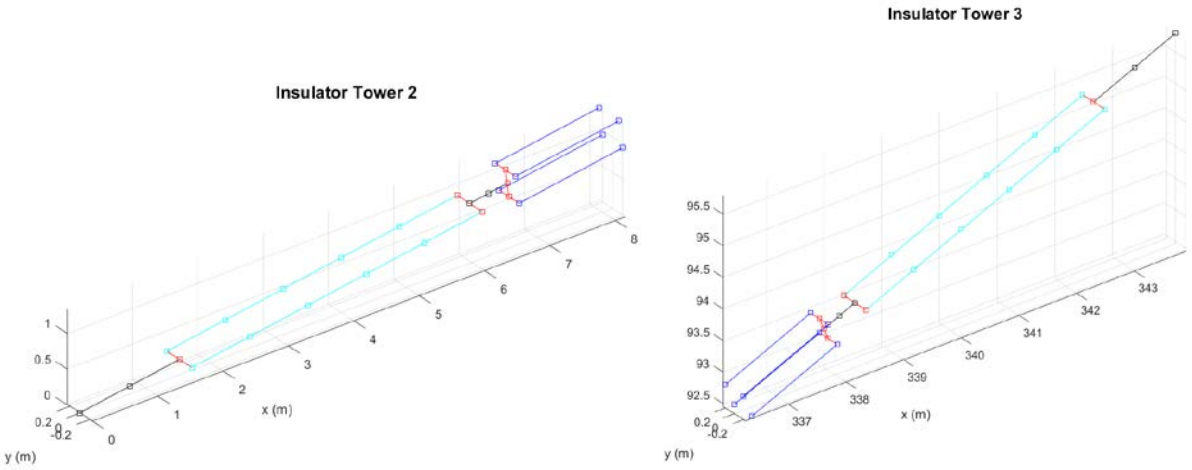

Figure 5.11. Detail of insulators at Tower 2 (left-hand plot) and Tower 3 (right-hand plot). Pale blue, dark blue and red elements correspond to the insulators, Phase C bundle and pinned connections respectively.

Table 5.1. Main characteristics of the FEM model.

Type of conductor	ASCR410 (four-bundled)
Spacing of conductor cables	0.4 m
Span	343.9 m
Sag (Line to point)	11.95 m
Type of element	Conductors and insulators: elastic beam element spacer: elastic beam element
Number of elements	316 per conductor
Boundary condition	Fully restrained connections at both edges

The static analysis was performed using the Euler-Bernoulli beam theory before conducting the modal analysis, but the measured full-scale pretension load has not been applied to the model because the system is already subjected to the initial deformation due to the self-weight. Since the wind flow was not adopted in this analysis, the structural modes depend only on the structure itself and are independent of the wind load. Although fully restrained supports

were applied to the model, it was observed that they behaved similarly to pinned supports because of the large inertia of the bundle. Despite these boundary conditions are different to the full-scale geometry, and they might affect the actual flexural rigidity of the bundle, it is assumed that this does not have a great impact on the results.

In FEM analysis, the modal mass participations are usually displayed for all calculated modes following modal frequency estimation. The modal participation mass or effective modal mass is generally used to quantify the significance of a vibration mode of a structure. As detailed by Williams (2016), derived from the equation of motion of a discrete dynamic system, the modal participation mass for mode *i* in each degree of freedom *p* can be estimated (in % of units of mass) by:

$$M_{p,i} = \frac{{L_i}^2}{M_i} \times 100 \tag{5.8}$$

where L_i is the excitation factor

M_i is the generalised mass

The modal participation masses are used in this study to quantify the mass, and the subsequent force, that is transmitted to the connectors due to this mode in different directions. The sum over all of the modes is equivalent to the total mass of the structure. Table 5.2 summarises the first 15 identified modes of the bundle, their modal participation masses for values lower than 90% and their motion description. These include the first five structural modes in the horizontal (out-of-plane), six in the vertical (in-plane) and four in the torsional direction, where the plane is defined as a plane of sag. The motion of the modes has been identified with the help of the mode shape diagrams displayed in Figure 5.12 and in the Appendix "FEM Mode Shapes". The proximity of close frequencies, such as those corresponding to Modes 2 and 3, 4 and 5 or Modes 10 and 11 indicates that the IWCM developed by Macdonald (2000) might not be appropriate to identify the modal parameters of the structure. The 1st mode at 0.161 Hz, *Y1*, and its near harmonics in the horizontal (out-of-plane) direction at 0.320, 0.479, 0.632 and 0.775 Hz are clearly observed in Table 5.2.

Table 5.2. Summary of the frequency values, modal participation masses and description of the first fifteen vibration modes obtained from the FEM Model. Significant mass participations are highlighted in bold font.

Mode Number	Frequency (Hz)	MX longitudinal (%)	MY horizontal (%)	MZ vertical (%)	MR torsion(%)	Description
1	0.161	0.000	**49.802**	0.000	0.001	1st mode *Y* (*Y1*)

2	0.319	1.449	0.000	0.013	0.000	1st mode *Z* (*Z1*)
3	0.320	0.000	0.000	0.000	0.000	2nd mode *Y* (*Y2*)
4	0.399	0.427	0.000	**5.986**	0.005	2nd mode *Z* (*Z2*)
5	0.400	0.004	0.000	0.050	0.616	1st mode *R* (*R1*)
6	0.433	0.000	0.004	0.000	0.015	2nd mode *R (R2*)
7	0.479	0.000	**10.087**	0.000	0.001	3rd mode *Y* (*Y3*)
8	0.566	0.000	0.064	0.001	0.479	3rd mode *R* (*R3*)
9	0.573	1.516	0.000	**17.552**	0.000	3rd mode *Z* (*Z3*)
10	0.630	0.834	0.000	0.268	0.000	4th mode *Z* (*Z4*)
11	0.632	0.000	0.001	0.000	0.000	4th mode *Y* (*Y4*)
12	0.718	0.000	0.005	0.000	0.003	4th mode *R* (*R4*)
13	0.775	0.000	**13.464**	0.000	0.000	5th mode *Y* (*Y5*)
14	0.824	1.425	0.000	**17.743**	0.000	5th mode *Z* (*Z5*)
15	0.867	1.869	0.000	0.616	0.000	6th mode *Z* (*Z6*)

The estimated mode shapes from the FEM model have been used to help to interpret the nature of the modes. In addition, they might be compared with full-scale measurements presented in later sections and observations from video images conducted by Matsumiya *et al.* (2022a) to assess the performance of the model. Figure 5.12 illustrates the mode shapes of some relevant modes identified from the FEM model.

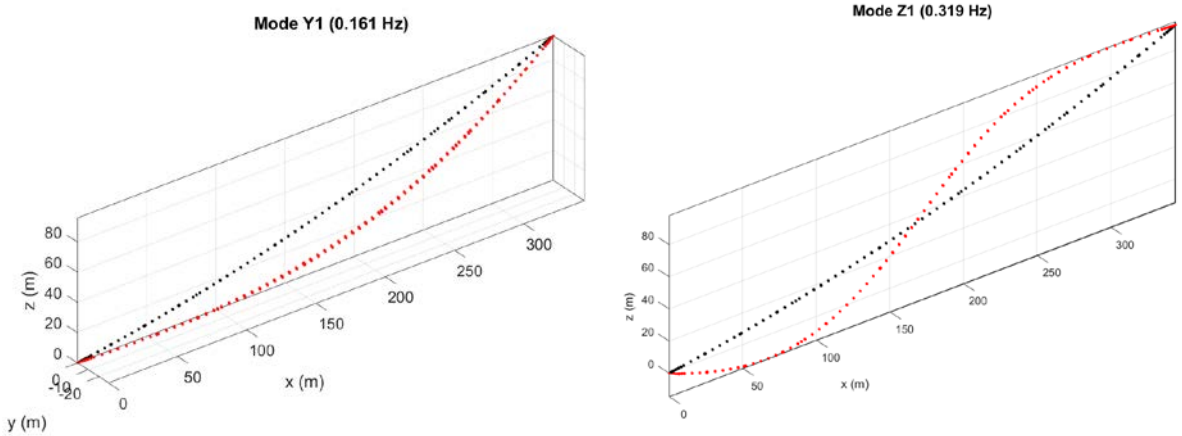

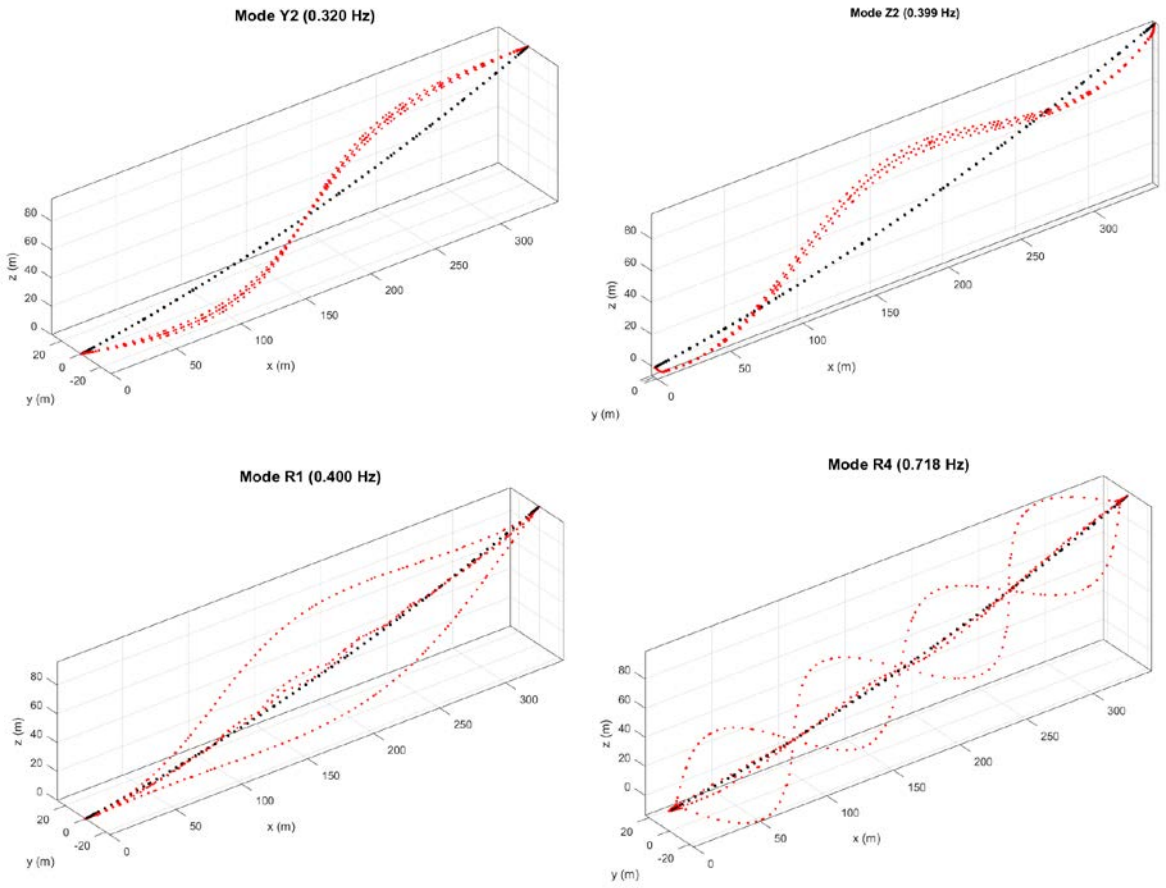

Figure 5.12. Mode shape diagrams of Modes *Y1*, *Z1*, *Y2*, *Z2*, *R1* and *R4*. Initial (black) and deformed (red) bundle geometry are displayed.

The predicted Mode *Y1* is 1-loop/span out-of-plane (horizontal) mode. Modes between 0.3-0.4 Hz are important because results presented by Matsumiya *et al*. (2022a) indicated the occurrence of galloping in that frequency range, where the FEM model has identified 2-loop/span vertical mode (Mode *Z1*) at 0.319 Hz and 2-loop/span mode out-of-plane (Mode *Y2*) at 0.320 Hz.

These two twin modes are the same shape in two different directions, vertical and horizontal, where Mode *Z1* absorbs the participation mass and the same mode with the same frequency approximately, Mode *Y2*, with ~0 % participation mass, is less clear. The low values of the modal participation masses for some modes, such as Mode *Y2* and *Y4* is typical in antisymmetric modes where half of the mass contributes to the dynamic of the system in the positive direction while the other half contributes in the negative direction, resulting in zero participation mass.

There is evidence of torsional displacement triggering in the galloping vibrations at about 0.4 Hz, where there is coupling between pseudo vertical (Mode *Z2*) and torsional (Mode *R1*) 1-loop/span mode. Matsumiya *et al*. (2022a) also stated that galloping was also observed in the two-loop/span mode around 0.7 Hz from the images and power spectrum density of displacements and tensions. However, in that frequency range the FEM Model has identified Mode *R4*, 4-loop/span torsional mode.

The FEM is not used in this chapter to create a perfect or high-quality model; instead it is used to provide better interpretation of the data and improve the overall analysis. Nevertheless, the predicted modes from the FEM Model shown in Table 5.2 agree relatively well with the spectral analysis conducted by Matsumiya *et al.* (2022a) on Phase C, where some modes could be identified from the PSDs of the bundle tension load and displacements for a 10-minute long period on a typical case record. Peak frequencies corresponding to different modes were obtained by Matsumiya *et al.* (2022a) at approximately 0.16, 0.35, 0.42, 0.70 Hz. The consistency in the results increase confidence in the use of the model to estimate useful response parameters given the complexity of the system.

5.4.2. Parametric study

A parametric study of the model has been conducted by increasing the sectional mass of the bundle from 0 up to the additional 100 % to assess how the natural frequencies change when exposed to this parameter effect. Since in-cloud icing frequently occurs in the Tsuruga test line during the winter season, this parametric study aims to simulate the conditions where the mass of the ice or snow accretion is notable relative to the mass of the bundle. Although Matsumiya *et al*. (2022a) estimated from video images that the maximum mass of ice accretion might represent 30 % of the mass of the conductor, 100 % is chosen here in order to simulate an extreme ice accretion event and to see clear trends.

Uniformly distributed mass on the bundle has been adopted, neglecting eccentricity. In this study, pre-stress analysis was done for each case before eigenvalue analysis was conducted. Summarised values of the estimated frequencies are displayed in Figure 5.13 for 10 % mass increments.

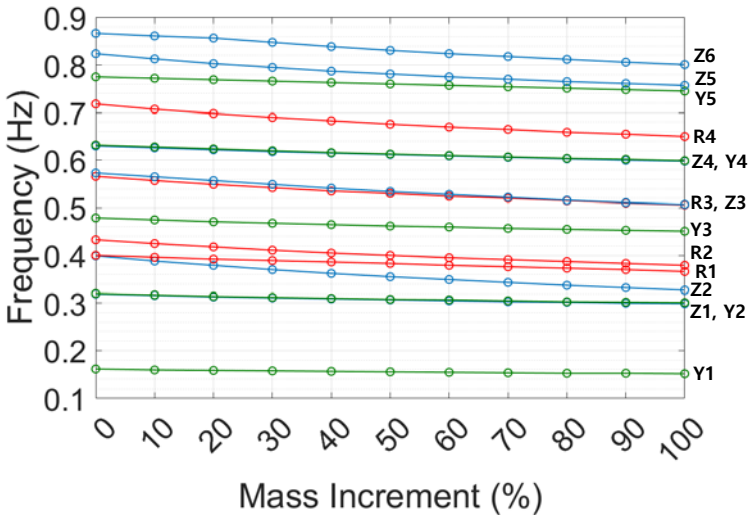

Figure 5.13. Variation of the frequencies of the first 15 vibration modes for 10 % mass increments. Mode type is included for horizontal modes (green), vertical modes (red) and torsional modes (blue).

The addition of mass to the cable mainly affects the torsional and vertical modes, while the horizontal modes barely change. Table 5.3 displays the overall frequency decrease (in %) for the 100 % mass increment. It provides a direct comparison to highlight the most sensitive modes due to the increase in mass. The average decrease in the frequencies of the first 15 vibration modes with an increase in the mass of 100 % is 5.4, 9.4 and 10.2 % in the horizontal, vertical and rotational directions, respectively.

Table 5.3. Frequency decrease (%) of the first 15 vibration modes for 100 % mass increments.

Mode Number	*Y1*	*Z1*	*Y2*	*Z2*	*R1*	*R2*	*Y3*	*R3*	*Z3*	*Z4*	*Y4*	*R4*	*Y5*	*Z5*	*Z6*
Frequency change (%) for 100 % mass increment	6.3	6.2	6.0	17.9	8.3	12.4	5.8	10.7	11.5	5.1	5.2	9.4	3.8	8.1	7.6

Several studies (Joly *et al*. (2012), Jayatunga *et al*. (2015), Sen and Mittal (2015), Sourav and Senn (2020)) examined the combination of galloping and vortex-induced vibration of square cylinders mainly using direct numerical simulation. They concluded that the amplitude of motion for this type of section decreased significantly when the mass ratio between the fluid and the solid was decreased. In the same line, Han and De Langre (2022) confirmed the galloping behaviour in this type of structure even at a low mass ratio. However, few full-scale studies are available to provide a comparison level of the effect of added ice or snow masses in

the natural frequencies of transmission lines. These phenomenum has been investigated analytically for a long time; Mersenne's laws published in his 1636 work *Harmonie universelle* (Steinhaus, 1999, p. 301) derived the general equation of oscillation of a string, from which it can be stated that the natural frequency is inversely proportional to the square root of the mass per length.

A decrease on the resonant vertical, horizontal and angular frequencies was observed by conducting parametric tests both experimentally and theoretically by Noël *et al.* (2008). Also, Havard (1979b) found that the variation of torsional natural frequencies of a single conductor was induced by the increase in mass and wind speed due to the moment on the section, for which the torsional frequencies were more sensitive than the vertical ones. Although uniformly distributed mass has been considered, it is likely that ice accretion distributes unevenly along the overall span in the Tsuruga test line due to the vast length of the span and the height difference between both ends.

This might have a significant effect in the variation of the frequencies, but it is difficult to quantify because of the lack of measured mass distribution in full-scale. However, the results above will be compared with the full-scale results to assess whether it can be confirmed the variation in the natural frequencies of the bundle with the increase in mass associated to the ice accretion that is predicted by the finite element model.

5.5. SYSTEM IDENTIFICATION

5.5.1. Initial considerations: suitability of tension measurements

The system identification in the present study has been performed based on the measurements from the strain gauge sensors detailed in Section 5.2. Historically, accelerometers have been more commonly used for modal testing than strain gauges due to their ease of use. Despite the differences in the monitoring system, it is expected that it leads to the same natural frequencies and modal damping values as if it had been processed using acceleration sensors, such as in the analysis of tall buildings in Chapter 3. However, where it definitely differs from accelerometers whether it is OMA (Operational Modal Analysis) or EMA (Experimental Modal Analysis) is the interpretation of the identified mode shapes, as detailed by Dos Santos *et al.* (2014). The novel arrangement of tension meters adopted in this study is a potentially innovative approach that presents a big opportunity to be applied for

different types of modes since strain modes can be calculated and plotted. The strain-based mode shapes look different from the standard mode shapes, which, ultimately, are normalised "displacements".

Nevertheless, strain-based OMA has been successfully used to obtain mode shapes, particularly in lightweight structures prone to fatigue failure (Jiang *et al.*, 2019; Tarpo *et al.*, 2019). This increases confidence in the use of tension meters to predict reliable results in the Tsuruga line.

The format and the main characteristics of the raw measured data have determined the handling process of the data and the choice of the system identification method. Tension measurements (in kN) from Northside support (NS) and Southside support (SS) tension meters were saved in 1-day long records for further processing of the data. The tension loads measured by the sensors correspond to the load on the insulators excluding the pretension load on the bundle, which is approximately 90 kN (i.e. 22.5 kN per sub-conductor). The pretension load was measured on the bundle before the installation of the tension meters.

5.5.2. Pre-processing and stationarity

This section describes the preliminary analysis conducted to assess the outlook of the raw measured data with the objective to develop the system identification strategy. A typical 1-day long record corresponding to the 2019/03/12 has been considered as an example. The tension load profile measured by NS and SS tension meters is shown in Figure 5.14.

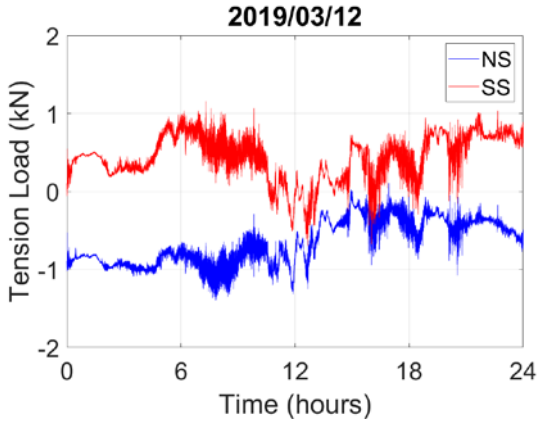

Figure 5.14. Time series of tension load for the typical non-galloping record measured by Northside Support (NS) and Southside Support (SS) tension meters.

It is noted that for most of the monitoring period, the tension load of the SS is higher than in the NS, probably because the bundle is slightly inclined towards the north side.

In OMA techniques, stationarity of the process is usually assumed. However, Gasparis (2019) explained that the stationarity assumption in wind-excited systems is probably violated since the wind speed is not steady. Thus, random or stochastic non-stationary process might require compatible system identification methods. Alternatively, Bendat and Piersol (2010) stated that, for analysis purposes, it is often possible to force the data to be at least piecewise stationary even though it is nonstationary when considered as a whole. The addition of the two channels (NS + SS), which gives the overall tension on the bundle, has been selected to conduct a preliminary analysis of the signal in Figure 5.15, where it has been broken down into 10-minute long blocks.

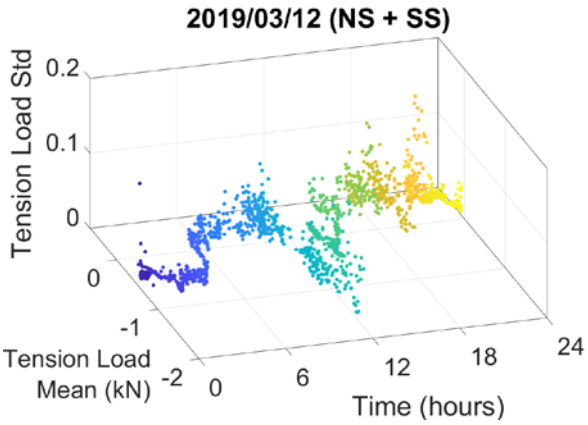

Figure 5.15. Mean and standard deviation for the typical non-galloping record.

It has shown that the mean value and the standard deviation of the signal fluctuate even within each block. If the signal was stationary there would be a concentrated cluster of points stationary in time indicating that the mean and the standard deviation do not change through the time. Since these features have been observed in the whole set of records, there are evidences that those signals might be disqualified from being stationary. Nevertheless, the use of piecewise approach by breaking down the data into shorter windows, as shown in Figure 5.15, has been recommended by Bendat and Piersol (2010) to avoid performing stationary nonstationary data analysis procedures.

Considering specifics of the sensor arrangement in Phase C shown in Figure 5.6, the measured tensions were arithmetically transformed to obtain the motion characteristics expressed relative to the insulators on the Tower 2. Figure 5.16 summarises the spectral analysis

of the tension force for the record on 2019/03/12 in the frequency range 0-0.9 Hz for both differential (NS - SS) and addition handling (NS + SS) of the two channels. These plots offer a first overview of the excited modes of vibration of the structure.

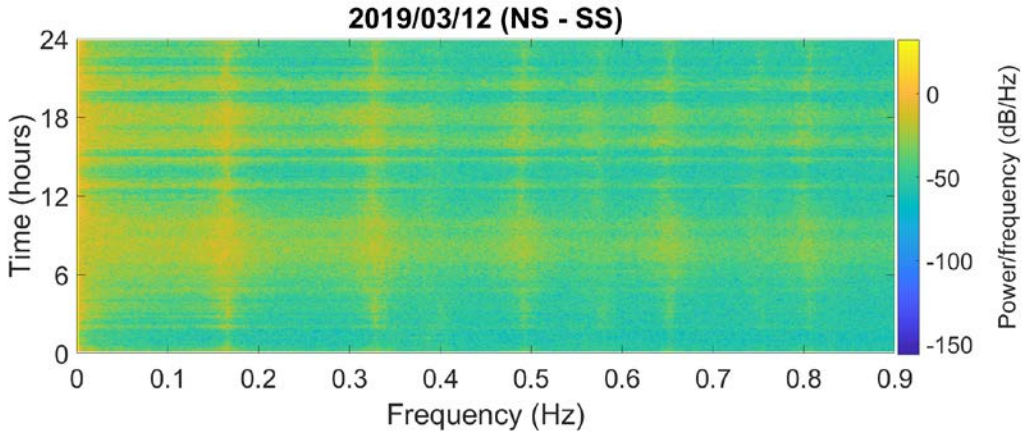

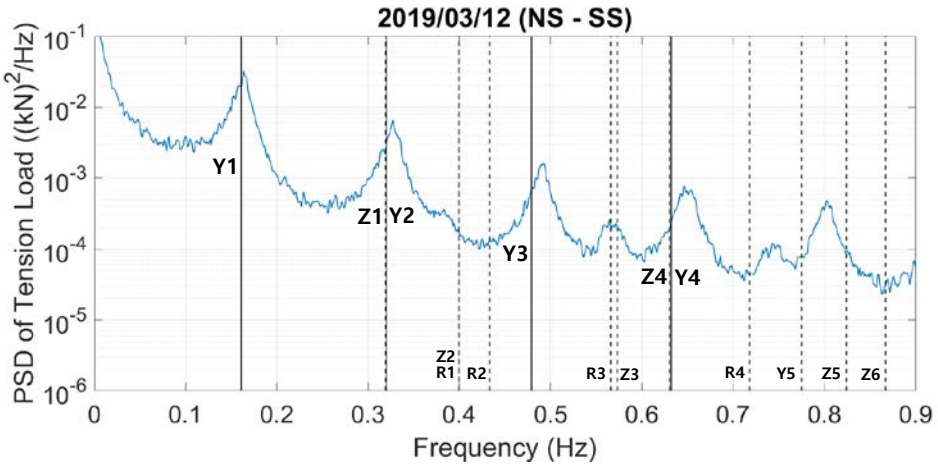

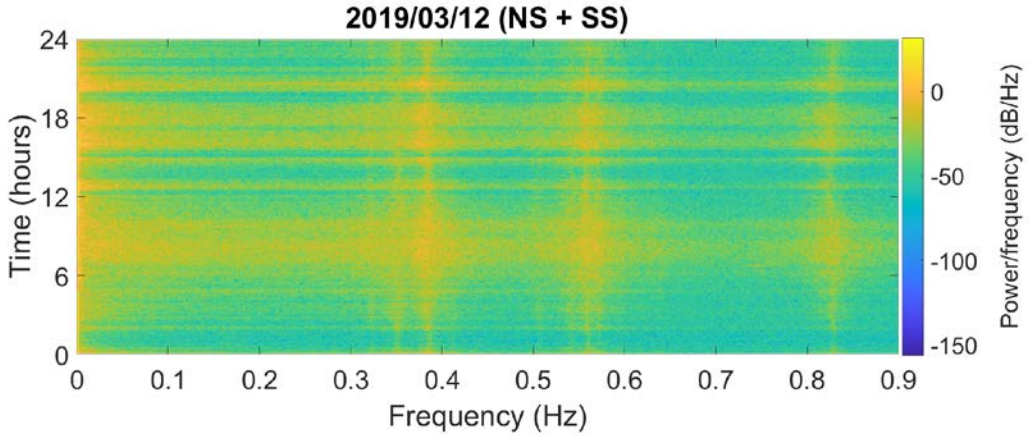

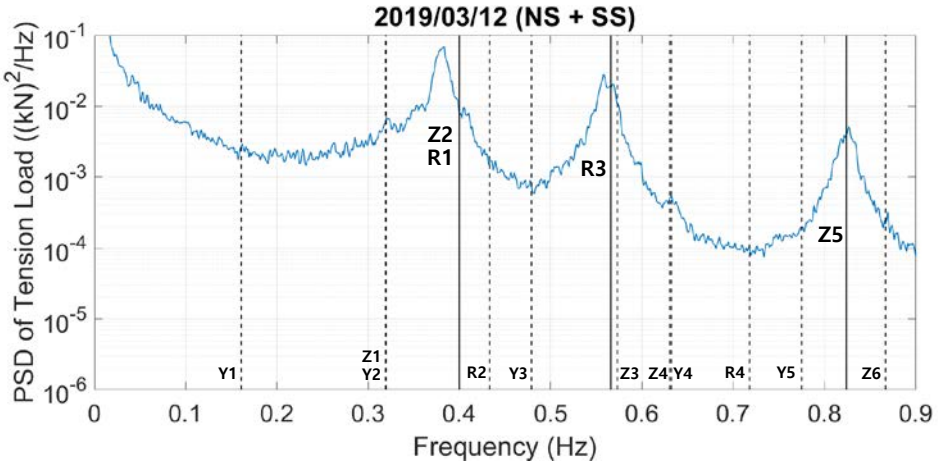

Figure 5.16. PSDs and spectrograms of the tension load for subtraction (top) and addition (bottom) of channels for the typical non-galloping record. Predicted modes from the FEM model are superimposed (vertical lines).

For each combination of channels, the spectrogram is derived using the short-time Fourier transform and the estimated positive one-sided tension Power Spectral Densities (PSDs) from the modified Welch's periodogram, as it was detailed by Marple (1987). Since this method splits up the signal into overlapping segments, they can be considered as quasi-stationary stochastic processes. This implies that the stationarity assumption might not be violated and the PSD of tension load can be calculated.

The spectrograms are displayed with the frequency values aligned in the horizontal axis. In the spectrograms, the time is on the vertical axis, and colour patches define the amplitude of each frequency component at successive times. The STFT length considered is 2^{14} samples (13.65 minutes), windowed with a Hamming Window, and an overlap of 4000 samples (i.e. 3.3 minutes). These parameters have been selected to provide comprehensive results by selecting a suitable duration of the time-series to ensure an accurate estimation of the modal parameters which are not biased by the nonstationary processes. The frequency values of the modes identified from the FEM model (Table 5.2), which are close to the main peaks in the PSDs, have been superimposed on the plots.

This preliminary approach indicates that there is good agreement between the spectrograms and the PSDs of tension and they can be used in the identification of potential modes. Five and three clear peaks are observed below 0.9 Hz from the channel subtraction and addition, respectively. Differential handling of the northside support sensor and the southside support sensor seems to reveal more clearly the modes that involve horizontal movement

because it creates differential action in the sensors. On the other hand, the addition of the two channels provides a better observation of the vertical and torsional motions. The combination of both actions gives all of the modes that are visible with this equipment.

The FEM model enables confirmation of the nature of some of the mode shapes identified in this spectral analysis from full-scale measurements. For example, modes *Y1*, *Z1* (or *Y2*), *Y3*, *Z4* (or *Y4*), *R3* and *Z5* are relatively close to the main peaks of the PSDs for the selected file. There is also a less clear peak at 0.57 Hz close to modes *R3* and *Z3*. However, some modes identified from the FEM model are not observed either in the spectrograms or in the PSDs. The low horizontal spectral power bands observed mainly around 8 and 16 hours correspond to long wind speed drops in the time domain. A higher spectral power band might be due to noise in some other regions. This preliminary approach based on the spectrogram and the PSDs of tension highlights several clear modes and, therefore, motivates the identification process to provide the modal parameter estimation.

5.5.3. Iterative Windowed Curve fitting method (IWCM)

The identification of the natural frequencies and damping ratios from the estimated acceleration PSDs was successfully applied to the two monitored tall buildings in Chapter 3 using the IWCM developed by Macdonald (2000). With the aim to replicate the system identification process and obtain the modal parameters of the system, this method has been applied to the measured tension load from the standard record measured on 2019/03/12. This method was extensively detailed in Section 3.1.2.1.

An example of the fitted positive one-sided tension PSDs (Figure 5.16) of the tension load for the record on 2019/03/12 is shown in Figure 5.17 in the frequency range 0.1-0.9 Hz for the differential (NS - SS) and addition handling (NS + SS) of the two channels. It is found that four and two clear peaks of the signals from the channel subtraction and addition respectively can be fitted. As it was previously observed, in an equivalent frequency range, there are more modes, and they are more closely spaced compared to the estimated PSDs of acceleration on tall buildings (Figures 3.11 and 3.13). As a comparison, the PSD of acceleration of a typical 1-hour-long record for Tower 1 in Chapter 3 was fitted precisely because there is only one mode below 1 Hz for each motion component.

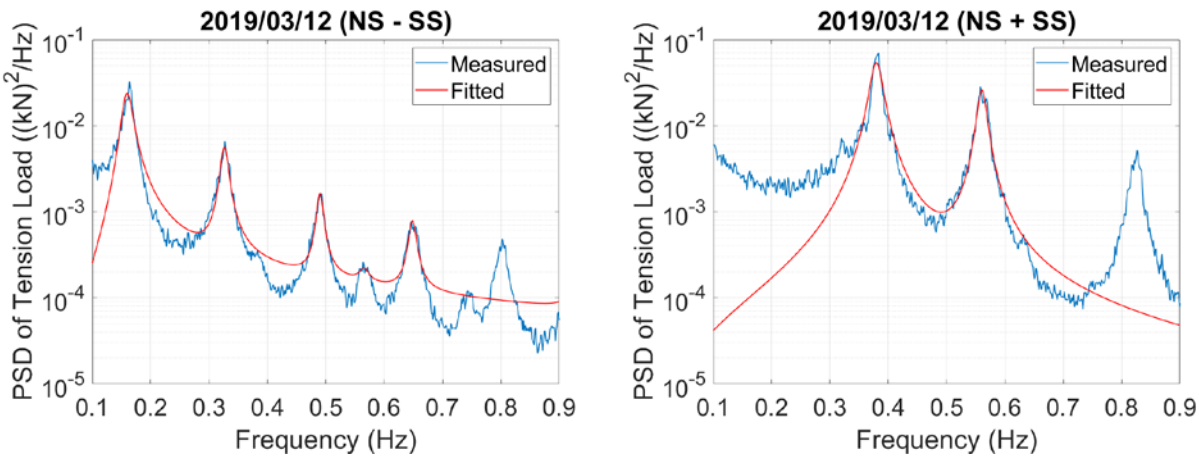

Figure 5.17. Measured and fitted PSDs of the tension load for subtraction (left-hand side) and addition (right-hand side) of channels for typical non-galloping record.

Although there are some parameters that can be adjusted in the IWCM algorithm for different types of spectral responses and analyses, such as the frequency range or the number of modes to be fitted, this method struggles to perform the fitting of higher modes accurately. This is particularly evident for the estimated PSD from channel subtraction, due to the proximity of several peaks where visible. In its standard form, the IWCM assumes well-separated modes, and it fits the PSD with a number of 1-DOF PSDs, where each 1-DOF PSD corresponds to a single previously localised modal peak.

This assumption is acceptable in systems with well-separated modes. However, in the present study, the situation is much more complex because not only that some modes are closely spaced but some of them are difficult to observe. From the curve-fitting of the PSDs of the tension responses in Figure 5.17, the natural frequency and damping ratio for the observed modes are summarised in Table 5.4.

Table 5.4. Summary of the frequencies and damping ratios from IWCM fitted PSDs.

Mode Number	1	2	3	4	5	6
Frequency (Hz)	0.159	0.326	0.380	0.490	0.561	0.566
Damping ratio (%)	6.33	2.23	3.04	1.29	1.54	1.69

The main challenge has been found to be the large amplitude files, where there are different regimes in which the system switches into various nonlinear responses. In those

conditions, it would not be appropriate to consider large data segments, estimate the PSD and analyse them assuming linear behaviour.

5.5.4. Poly-reference least-squares complex frequency-domain (pLSCF) or PolyMAX and Stabilisation diagram

A series of difficulties and limitations have been encountered in applying the ICWM to identify modal parameters of the system. Therefore, an alternative method has been adopted. The choice of the method has been mainly driven by:

- The ability to differentiate between very close modes and provide easy-to-interpret results in a context of very close modes.
- Reduce the manual pre-processing as much as possible, given the presence of nonlinearities and the lack of stationarity conditions, with the aim to make it less influenced by subjective assumptions.
- A shorter-term analysis has been conducted with the aim of selecting more steady or stationary subsets, considering the shortest acceptable interval
- Increase automatisation of the analysis to process large amounts of data (i.e. continuous 4-month long period).

The poly-reference least-squares complex frequency-domain (pLSCF) method or PolyMAX (i.e., commercial name) has been selected and adapted in the present analysis. The pLSCF has been commonly used for OMA since its development, sometimes in comparison with other techniques.

For example, based on full-scale measurements on a suspension bridge, similar modal parameter estimates were found from pLSCF and SSI by Peeters *et al.* (2006). Despite the nonstationary character of the wind and traffic excitation, it was concluded that pLSCF was easier to automate and yielded more clear stabilisation diagrams than SSI. However, there are two main uncertainties in the use of pLSCF in the present study. As detailed by Guillaume *et al*. (1996), this algorithm is nominally designed to work with FRFs, but the quantities analysed are PSD, which, broadly, are related to conj($H(\omega)$)·$H(\omega)$, where $H(\omega)$ is a particular FRF and ω is the frequency. Since the frequency response functions and the positive power spectra can be parametrised in the same way (Peeters, 2007), the PSD can be used to construct stabilisation diagrams in the case of OMA. The use of PSD in *modalsd* function in MATLAB® has an appropriate grounding in system identification theory, as explained by Cauberghe (2004) and

Schanke (2105), and it has been applied in a two-step process, first mode detection using modalsd and then PSD fitting accounting for wind spectrum. Application of pLSCF on auto/cross PSD for wind and wave excitation by Gasparis (2019) resulted in an unstable non-structural identified mode, but it was stated that it was probably due to the wave load rather than due to the wind.

Secondly, stabilisation diagram is identified through FRF estimation, which is based on white noise input that ignores the fact that the wind creates excitation. Moreover, it is difficult to approximate the input loading by a Gaussian white noise process in this case. Since the dynamic behaviour of the bundle is mainly influenced by wind load, the excitation is "grey" or "coloured". This might lead to harmonic and *spurious* modes frequencies being mistaken for structural modes while failing to identify weakly excited modes. Considering OMA on offshore wind turbines, Gasparis (2019, pp. 4-5) stated that "*In general, wind loads approximate such a flat, broadband frequency spectrum and therefore, white noise assumption is not largely violated*" and supported that coloured noise contribution might influence identification in case where wave loading dominates wind load.

The use of pLSCF for OMA on offshore wind turbines by El-Kafafy *et al*. (2014) was supported by assuming linear time-invariant conditions and the suitability of the white noise assumption based on the low risk of harmonic frequencies for low (10 m/s) and constant wind. Although several studies justified the use of non-white inputs, Reynders (2012) confirmed that when the operational forces are not modelled as white noise, pLSCF suffers from bias in the estimates.

Despite these uncertainties, pLSCF can still give a useful estimate for OMA of the full-scale measurements from the Tsuruga line. This method has been applied to the measured tension data in this case study in order to obtain the modal parameters of the system. A stabilisation diagram is first constructed to quickly identify the modes of the structure. The stabilisation diagram of the addition and subtraction of the tension load channels corresponding to the typical non-galloping record measured on 2019/03/12 is shown in Figure 5.18 in the frequency range 0-0.9 Hz. The same positive one-sided tension PSDs estimated previously (Figure 5.16) has been used in this analysis.

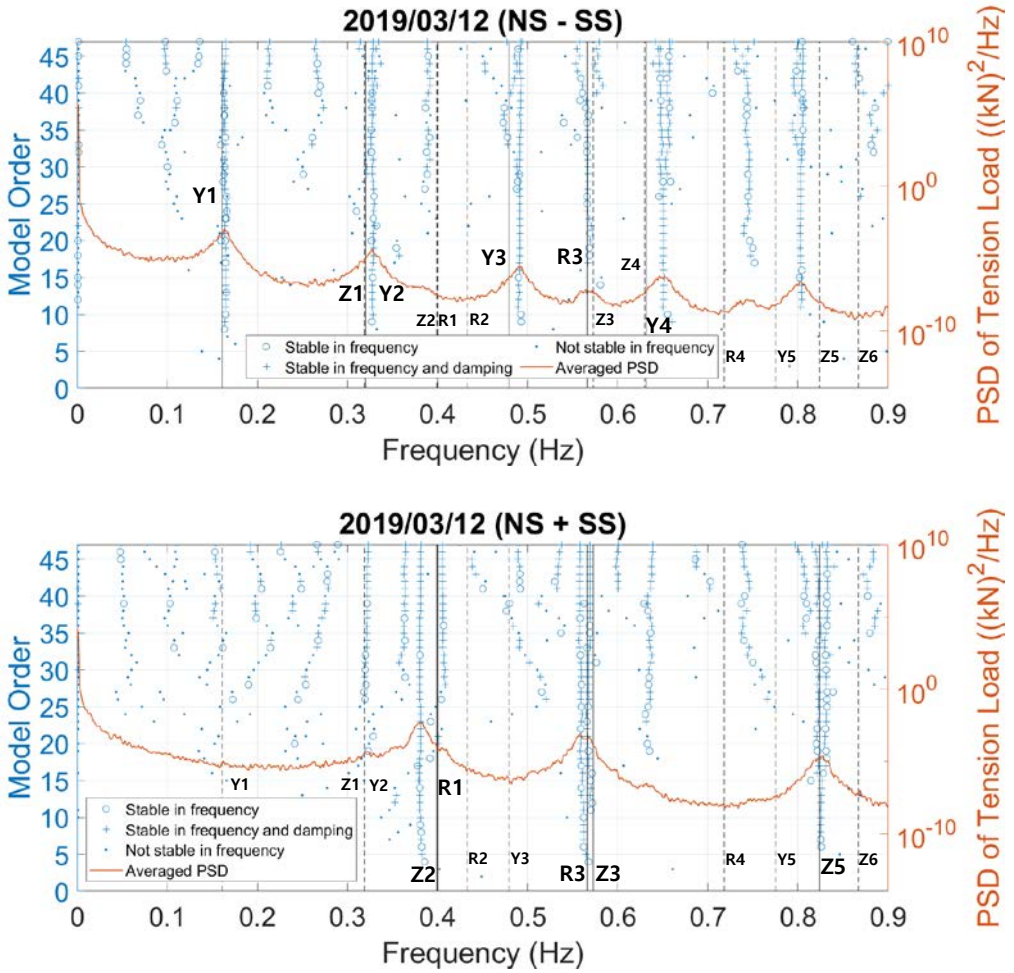

Figure 5.18. Stabilisation diagram of subtraction (top) and addition (bottom) of channels for the typical non-galloping record. Predicted modes from the FEM model are superimposed (vertical lines).

The maximum number of modes to be identified is set to 46. In this case, the poles are classified as stable in frequency and damping if their natural frequencies and damping ratios change by less than 0.7 and 3 %, respectively. These bounds are lower than the "default" used as typical stability criteria (i.e., 1 and 5 % respectively) provided by Peeters *et al*. (2008). This level of error has been selected to ensure that the results are comprehensive of an acceptable level to provide an accurate estimation of modal parameters. There is no *rule of thumb* for selecting an exact number of modes.

Different authors have considered different maximum model order numbers, for example, 65 by Peeters *et al.* (2006) and 32 by El-Kafafy *et al.* (2014). In addition, with the aim to distinguish between *spurious* and structural modes, Boroschek and Bilbao (2018) proposed a minimum number of objects to 1/3 of the total number of model orders for a stable column to

be considered as a valid mode. The frequency values of the modes identified from the FEM model (Table 5.2) that are close to the apparent real physical modes from the stabilisation diagram have been superimposed on the plots.

The stabilisation diagram shown in Figure 5.18 illustrates the main strength of pLSCF method in this case study; its ability to show patterns that might not be identified through simpler spectral analysis, such as spectrograms and PSDs (Figure 5.16 and 5.17 respectively). In the present study, this is related to local and close modes. Generally, higher modes are supposed to be more sensitive to changes that are induced by gravity, and consequently, they are more separated. The low modes are particularly prone to be quite close; therefore, the evidence of very close modes is identified through a stabilisation diagram below 0.9 Hz. As a comparison, the IWCM is not able to work at such a level of detail in these circumstances. There is evidence of some close modes, for example, around 0.33, 0.56 and 0.8 Hz, where it is suggested that there are either one or two modes as it gets to higher order (around 35) of approximated modes.

It can be inferred that modes come from different motions or subsystems. The emergence of different modes around a model order 35 is probably something that is visible to a limited extent with the used instrumentation. The changes of trends in clusters of points belonging to a particular mode can be observed at higher frequencies, although in these regions, there are different close modes that start to overlap because their wind-induced observability decreases. There is a weaker observed mode at 0.75 Hz that probably comes from the swaying of the sagged conductor or it might be related to the dynamic tower system, although it has not been identified from the FEM model.

5.5.5. Natural frequencies

With a view to automating the analysis and assessing a wide range of events, including galloping, each 24-hour-long file has been analysed with the help of the stabilisation diagram by subdividing it in segments to identify important frequencies within the signal. It is expected that by using piecewise approach by breaking down the data into shorter windows the *spurious* modes vary through the record, but the structural modes remain stable under low excitation. The stabilisation diagrams have been combined together, one next to the other, acting as an extension of the spectrogram of the short-time Fast Fourier Transform of the force signal, where

considering the LTI (Linear Time-Invariant) system assumption implied by the previous methodology, the shortest viable level of analysis using this approach has been sought.

According to Ruzzo *et al.* (2017) the mode shape and natural frequency estimates are not significantly affected by the record length, although too short records might lead to overestimations of the damping ratios. These publications motivate the minimum length of the signal in which the PSD of the signal can still be reasonably estimated, but it is not violating significantly the stationary assumption.

With the aim to establish the acceptable significant analysis length that are chosen from within the whole set, Ruzzo *et al.* (2017) have recommended using, as a *rule of thumb*, in cases where non-stationarity is an issue, at least 160 natural periods of the fundamental mode, i.e. the lowest mode. In the present study, the fundamental mode is around 0.16Hz, and the natural period is about 6 seconds, so 200 cycles would correspond to 1200 seconds, which is 20 minutes.

Figure 5.19 shows the evolution of the natural frequencies over the record on 2019/03/12. It is used as an example to show the estimation of the natural frequencies in this study. The estimates have been obtained from the stabilisation diagram for short windows of 200 cycles of the fundamental mode (approximately 20 minutes) across the entire daily record. The overlap between each slice is chosen to be 5 minutes. The four highest fitting model order results within the 25-order range have been considered to be included in this analysis. A shorter number of cycles would not provide enough information to reveal clearly the first mode while it would still give information about higher modes.

This analysis shows that some modes remain stationary through the time resulting in the concentrated frequency estimates. This is particularly clear for Mode *Y1*. However, between 1 and 2 hours, there is a large variation in the frequencies and an apparent switching of modes. From the addition of channels, there is evidence of two close modes between 0.35 and 0.4 Hz that apparently merge in some regions. Also, given the scattered results, it seems there are two close modes at 0.57 Hz (*R3* and *Z3*). Clear, distinct natural frequencies have been identified in low amplitude regimes, while scattered natural frequencies are observed under higher amplitude conditions.

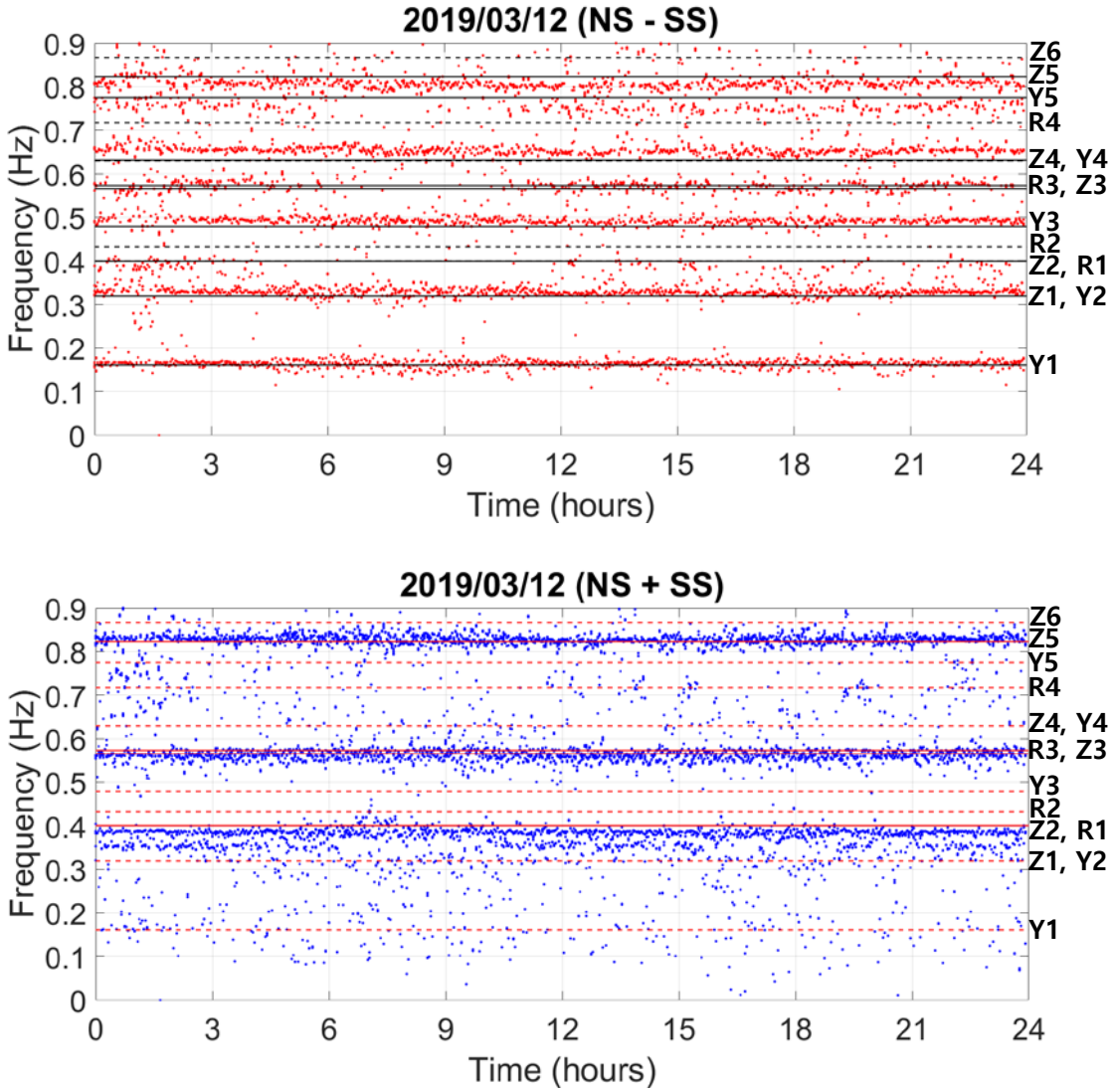

Figure 5.19. Natural frequencies estimates through the typical non-galloping record. Predicted modes from the FEM model are superimposed (horizontal lines).

5.5.6. Modal damping

In comparison with natural frequencies, one of the main problems arising when conducting damping estimation is that it leads to more uncertainties. As noted in Chapter 3, although natural frequencies can be properly estimated from short duration records with little effect of the white noise loading assumption, accurate damping estimates require consideration of the average characteristics of the response of longer measurement periods. Sudden large changes are usually found in the full-scale tension or displacement time-histories in transmission lines, particularly when subjected to galloping or high excitation. Gao *et al.* (2023) noted that this might affect the accuracy of damping identification and lead to biased estimates.

In addition, modal damping estimation is negatively influenced by the nonlinearity of the aerodynamic damping characteristic, which is dominant in transmission lines, since the structural damping of conductors is very low, as stated by Zanelli *et al.* (2022). The aerodynamic damping is associated with aeroelastic wind-structure interaction, which is more difficult to assess in this type of structures. Alternatively, despite damping ratios were more challenging to measure accurately than natural frequencies for comparable wind conditions in the system identification conducted for tall buildings (Chapter 3), it was found that the wind-induced responses for Tower 1 were dominated by the amplitude-dependent structural effects since little influence of wind direction was observed for the identified damping ratios.

Free vibration tests have been frequently conducted to measure the vibration characteristics of the four-bundled conductor in test lines in Japan. Damping ratios between 0.5 and 4 % were measured by Yukino and Kuze (2001), while Shimizu and Sato (2005) obtained values between 0.5 and 2 %. In addition to the estimation of the natural frequencies of a four-bundled conductor by means of excitation tests to validate the FEM modelling, Taruishi *et al.* (2021) obtained the damping ratios of the vertical and horizontal vibrations. In these tests, the correlation between the aerodynamic damping and wind speed was studied.

The damping ratio estimated using the IWCM (Table 5.4) in the considered bundle at the Tsuruga Test Line showed values between 6.33 and 3.04 % for the first three modes. These are notably higher than the previous estimates from literature. It is likely that the discrepancy is caused to the previously detailed uncertainties in the estimation of full-scale damping in transmission lines. The violation of the LTI assumption affects the shape of the spectral peaks, and consequently, it might lead to biased damping estimation. As detailed in Chapter 3, it has a more significant effect on the estimation of damping ratios compared with natural frequencies. If the system identification method based on the pLSCF is conducted, damping from the stabilisation diagram would come out much more fuzzy than the frequencies. Therefore, if multiple results are combined in the same way as it has been done for frequencies, the results are more difficult to associate with specific vibration modes. Due to observability issues, it has been noted that in many cases one sensor is not able to identify some of the frequencies while the other does very well. If the data from both sensors are combined (e.g., NS ± SS), and one of the sensors provides messy measurements, combination action would find an intermediate result that might spoil good quality measurements. This type of uncertainties particularly affects the damping estimation. Given the uncertainties around the damping estimation, this analysis

has been based on the frequency responses and it has not considered the modal damping of the system, which is left for future research.

5.6. ANALYSIS OF NATURAL FREQUENCIES

With the aim of assessing the structural performance and the dynamic properties of the bundle studied in this research, trends in the natural frequencies have been identified from vibrations measured by the two tension meters in a range of wind conditions to provide an overview of the typical values in operation. Based on the distinct classes of 1-day long records, summarised in Section 5.3.1 in terms of the peak-to-peak tension loads, two different analyses of the natural frequencies have been adopted in this section for non-galloping and galloping records.

5.6.1. Non-galloping records

This section conducts a global analysis of the records where galloping was not observed. Based on the different loading scenarios, this section considers long-term trends formed from 1-day statistics.

A comparison between standard behaviour (left-hand side plot) and extreme event (right-hand side plot) of non-galloping records is shown in Figure 5.20. The time series of the tension load and the estimated natural frequencies are displayed in Figure 5.20. It shows that for low excitation regimes, the natural frequencies are more concentrated because the system behaves as if it was in the state of small vibrations, and it complies well with the linearity assumptions. On the other hand, as it moves to higher excitation regimes, the system response becomes more nonlinear, and the results identified with this analysis normally used for linear systems become more scattered. It is then noted that the identification of the natural frequency parameter is not equally applicable in those circumstances.

One of the likely reasons is that this larger motion creates larger fluctuations in the axial loading which then causes changes in the observed dynamics in the system. The nonstationary effect can be also noticed by observing how the tension excitation at the start of the record 2019/02/13 starts to create a response which contains a mode at approximately 0.27 Hz, which is known to be related to the dynamic tower system. This mode, which has not been identified

from the FEM model, is usually only visible with the addition of the channels under a moderately high excitation load.

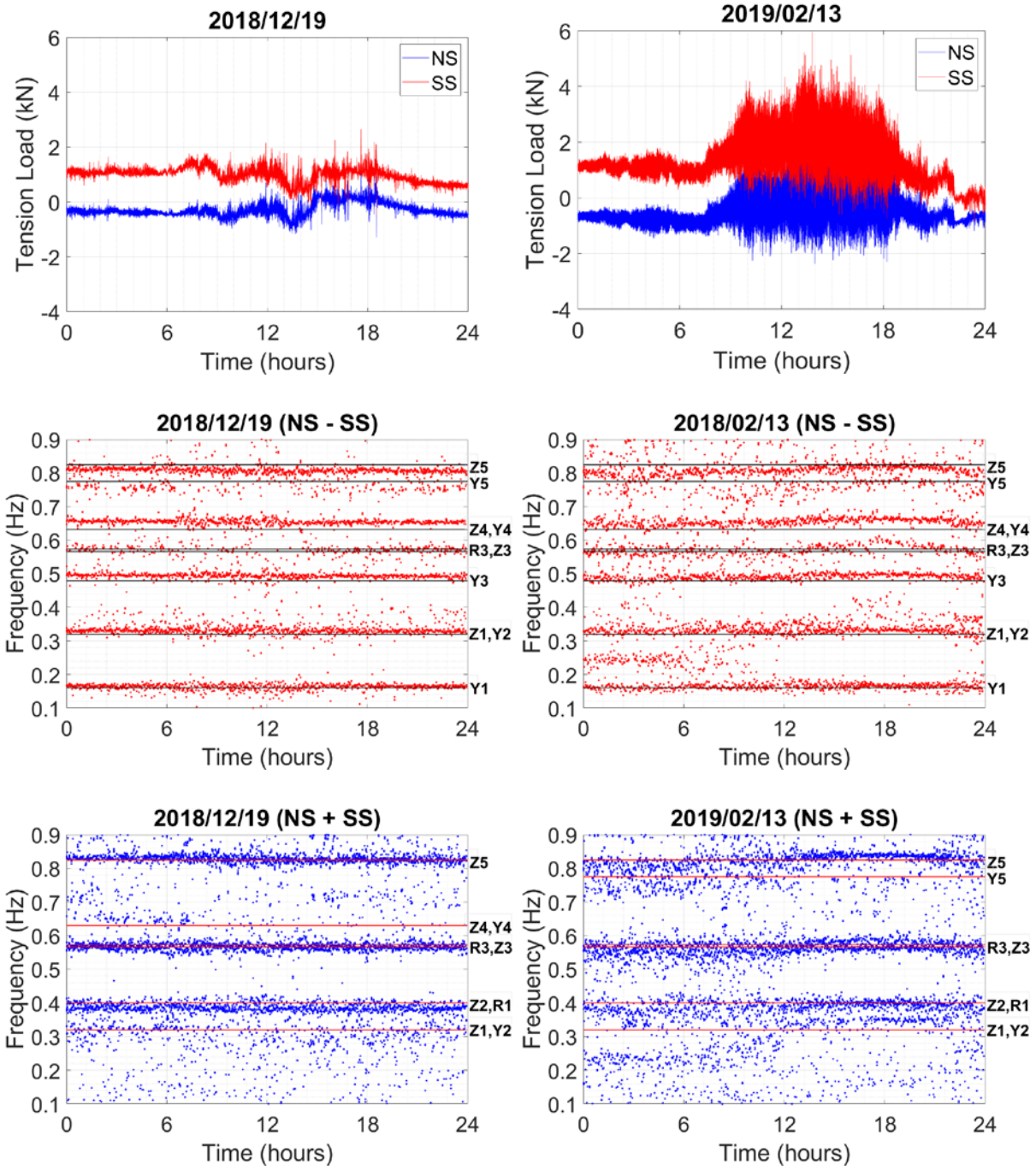

Figure 5.20. Time series of tension load and estimated natural frequencies of standard (left-hand side) and extreme (right-hand side) behaviour of non-galloping records. Predicted modes from the FEM model are superimposed (horizontal lines).

Figure 5.21 shows the accumulated results from the 78 non-galloping daily records illustrated as normalised histograms. It represents the density distribution of the frequency

observations across entire months. Since there is a varying number of non-galloping records for the different months of monitoring, the total number of frequencies has been divided by the number of observations per month to provide a more consistent comparison. This graph provides an overview of the main observed modes of the structure. It is found that despite the apparent scattered results in Figures 5.19 and 5.20, the identified frequencies are concentrated in 8 clusters peaks. Although identified modes from the FEM model are similar to the full-scale measurements, they are generally slightly underestimated in the case of channel subtraction and overestimated in the case of channel addition. The emerging mode around 0.25 Hz has not been identified in the FEM model since it is related to the frequency of one of the tower's modes.

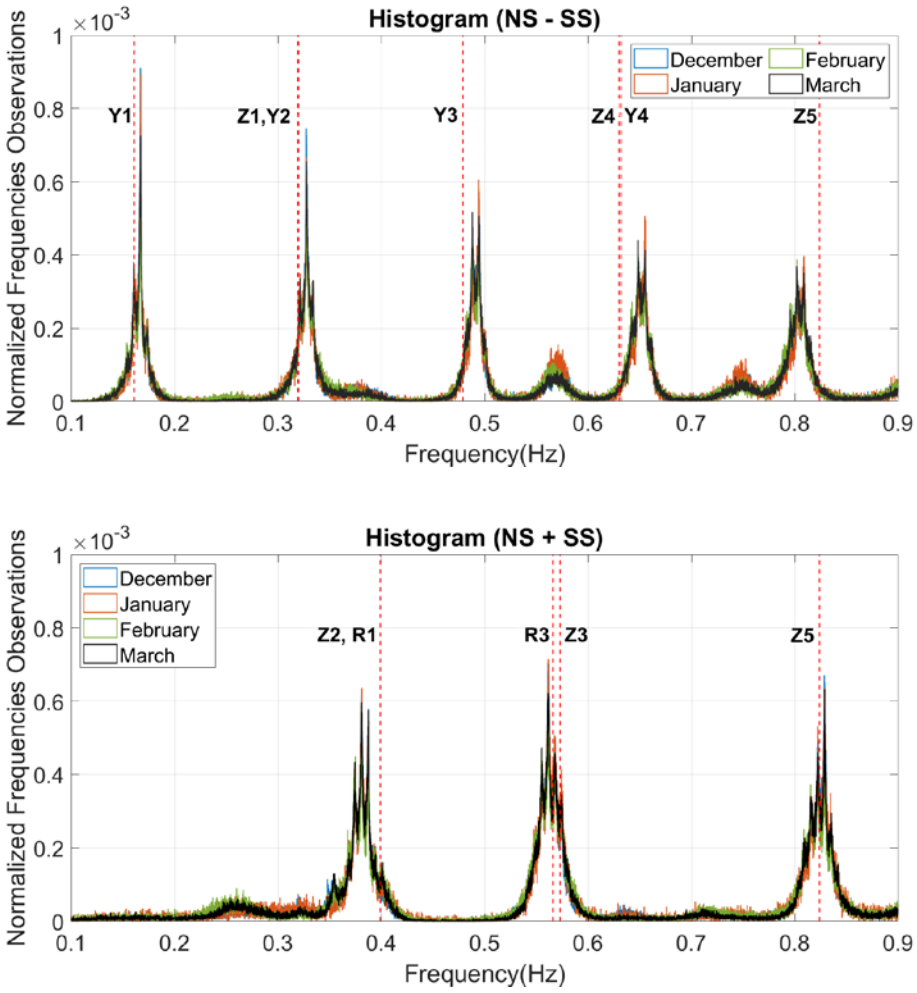

Figure 5.21. Histogram of the normalized frequency observations for each month. The frequencies of the identified modes from the FEM model are superimposed.

The finite element model was not used to create a prefect or high-quality model. However, it is noted that the difference between the predicted frequencies from the FEM model and the

measured ones is probably because the tension load of the SS is higher than in the NS, while the model adopted optimal equally distributed loads for sub-conductors and insulator elements. Detailed analysis of the individual modes shows no clear characteristic differences across different months based on atmospheric conditions, as displayed in Figure 5.22. Considering the frequency ranges around 0.16 Hz, and 0.38 Hz, the frequencies show a trimodal distribution in both cases, where two minor peaks complement a main peak every month.

It would have been expected the differences between different months induced by different atmospheric conditions. Furthermore, it would not have been expected to observe the same multiple peaks within a month for all of the consecutive four monitoring months considered. This might be interpreted as a limitation of the estimation method. Otherwise, for long-term observations, most of the estimated natural frequencies of each mode tend to concentrate around a dominant value, but, probably due to the atmospheric conditions, they change to either a higher or lower value.

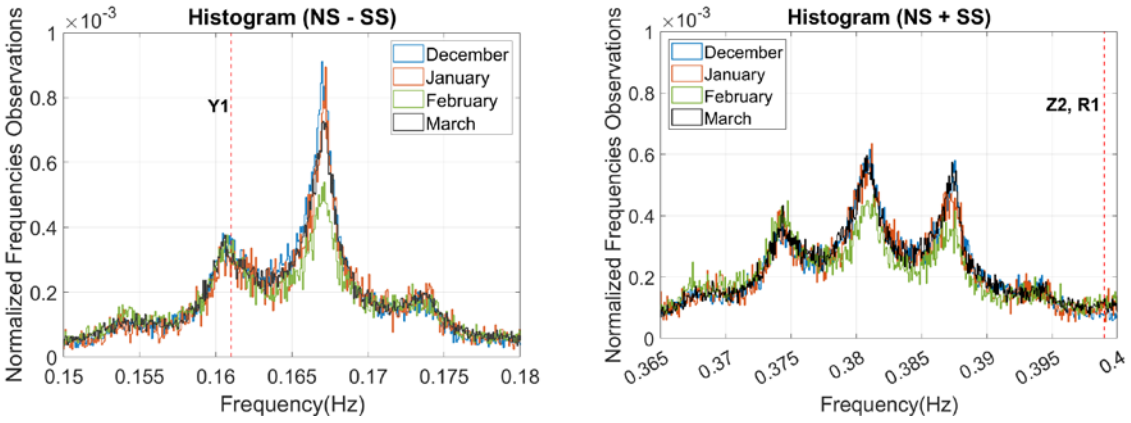

Figure 5.22. Detailed histogram of the normalized frequency observations around the Modes *Y1* and *Z2*, *R1*.

With the aim to provide a more detailed analysis of the data, identified results from whole days within the month are plotted in Figure 5.23 for the 1st identified mode (*Y1*) as an example. The distribution of the frequencies and the corresponding mean wind speed measured on the same time intervals is displayed as violin plots for each day. For most of the records, most of the frequencies are clustered around 0.167 Hz, although some peaks are observed at around 0.161 and 0.174 Hz for several records. Violin plot distributions examine the stationarity or single modality within each day and assess to what extent a global analysis of the present data is suitable.

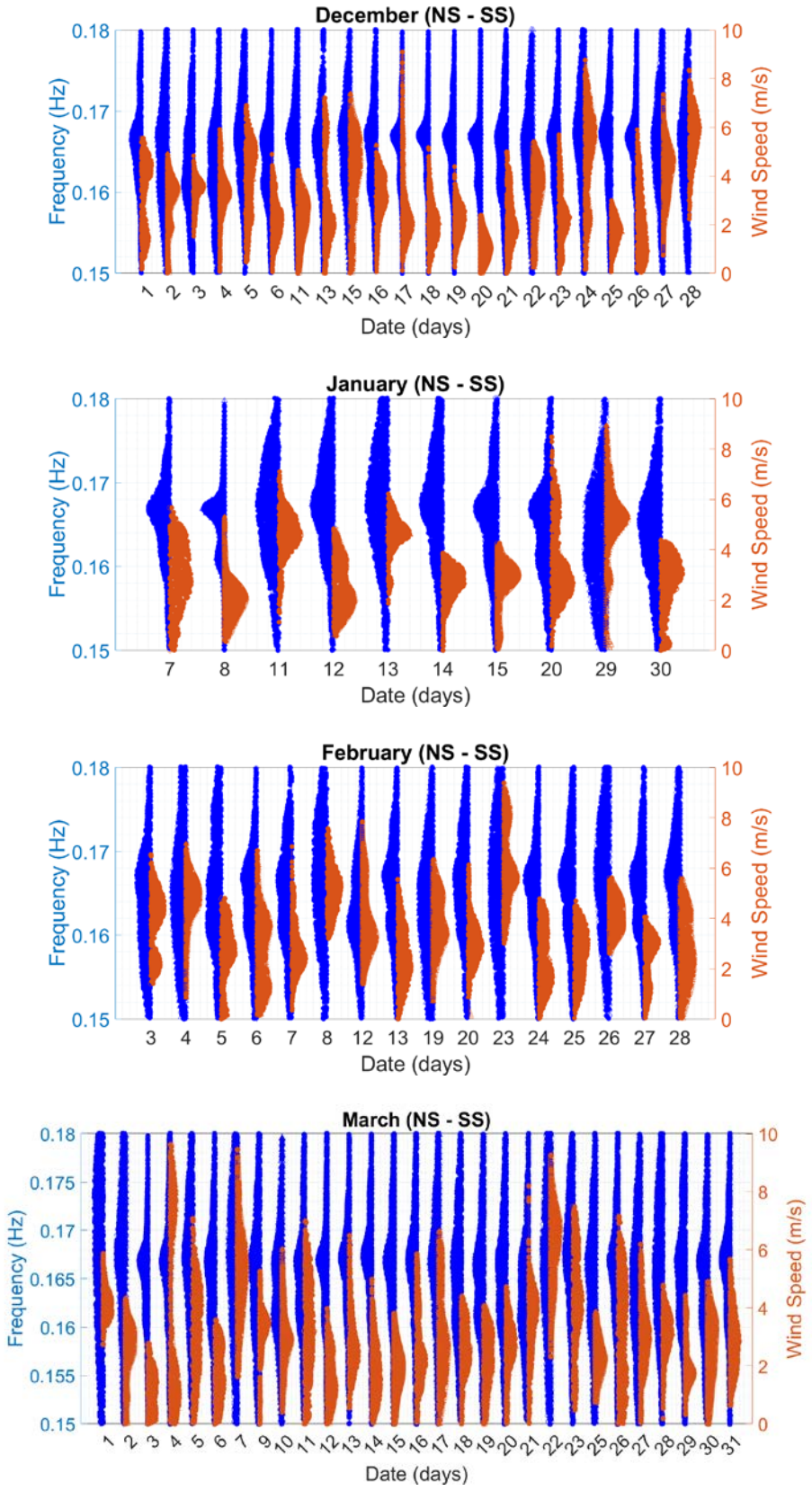

Figure 5.23. Daily distributions of the estimated frequencies around the Mode 1 and the measured wind speeds.

In order to quantify the long-term environmental effects on the structure, the daily tension meter and atmospheric data from non-galloping records were correlated and compared against each other, as shown in Figure 5.24. The natural frequencies have been investigated in relation to a series of parameters, such as the tension in the bundle, temperature and wind speed. Those daily samples of data that did not pass the Anderson-Darling statistical test, as detailed by Stephens (1974), have been neglected on the basis that they are not drawn from the normal distribution.

The frequency change in the vertical axes of subplots in Figure 5.24 is estimated as the change (in %) of each daily mean frequency with respect to the overall mean frequency of each mode. The tension is estimated as the mean of the addition of the two tension channels (NS + SS). The size of the markers is proportional to the daily mean temperature. In order to adjust the scale of the marker size to the minimum and maximum limits of temperatures, their values have been shifted to positive with respect to the lowest negative value. The choice of using the marker colour to represent the daily mean wind speed is based on a preliminary analysis where the variation in the frequency has been observed to be more influenced by the wind speed than by the temperature.

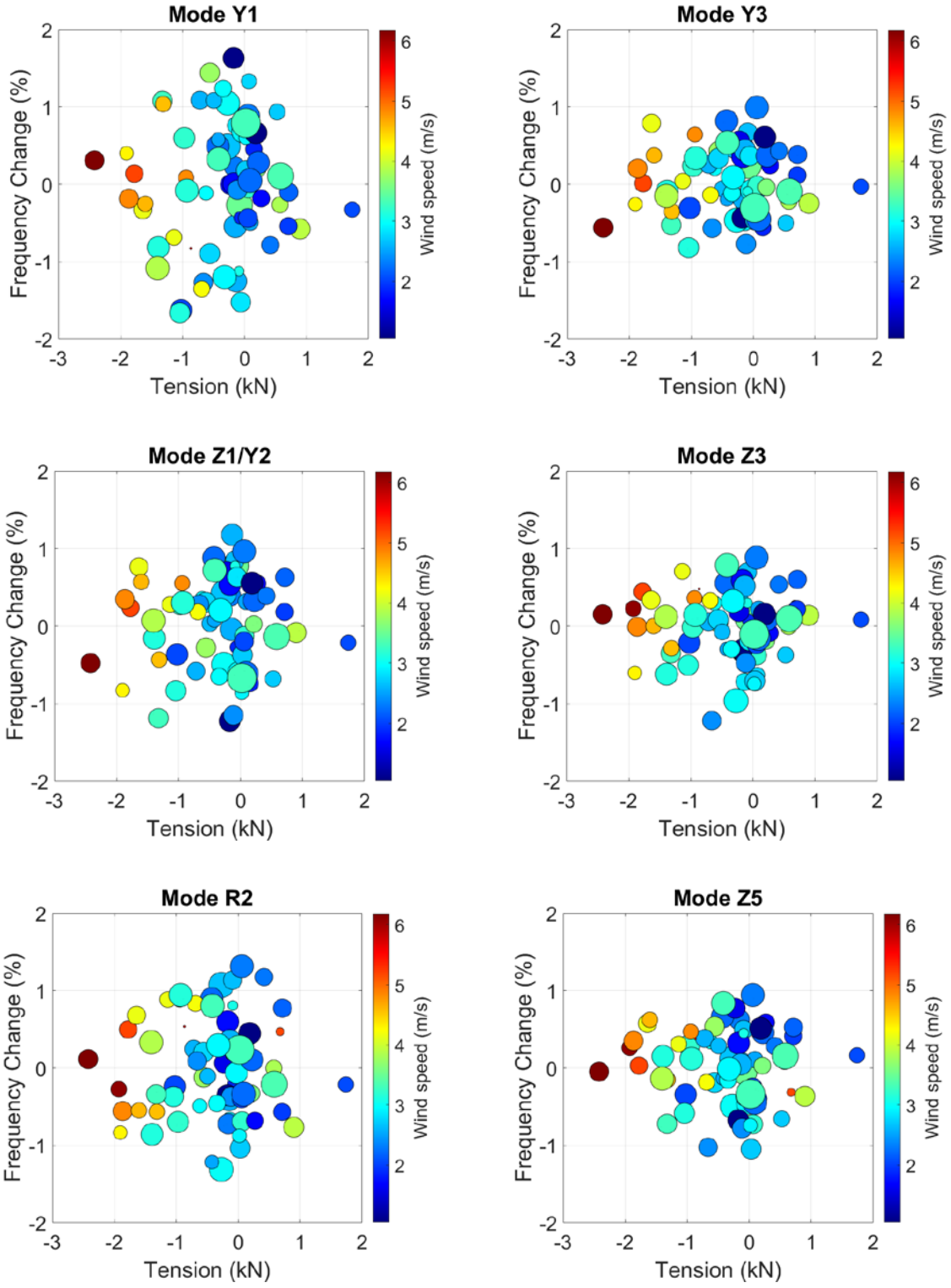

Figure 5.24. Relationship between daily mean frequency change (in %) with respect to the overall mean frequency for each mode and tension loads (NS+SS) in terms of the wind speeds (marker colour) and temperatures (marker size) for selected modes from non-galloping records.

Few clear trends can be observed in the previous relationships. Overall, for mean forces fluctuating between -3 and +2 kN, there is a set of fuzzy distributions of data points where there is a baseline variation in the mean daily natural frequencies ranging between ± 1 % and ± 2 % with respect to the overall mean natural frequency of each mode. From the different modes, the frequencies corresponding to *Y1* show the highest dispersion. Higher values of the daily mean frequency change (in %) are observed with the decrease in the magnitude of the mean daily tension.

The highest dispersion was found around zero mean daily tension for the different modes considered. Since it corresponds to the tension with respect to the initial preload on the bundle, this might indicate that the larger magnitudes of tension values result in a more stable estimation of the frequencies. However, the reasons behind this mechanism are still unknown. For high wind speed, there is an apparent subtle trend of low dispersion in the natural frequencies, although it is difficult to make a clear statement since high wind speed is related to larger tension magnitude.

5.6.2. Galloping events

This section conducts a short-term and detailed analysis of the records where galloping has been observed.

Table 5.5 summarises the 18 galloping events observed through 36 daily records over the 4-month monitoring period given by Matsumiya *et al.* (2022a). They have been identified from the ITV camera image equipment described in Section 5.2. The previous discussion in Figure 5.9 noted that January is the month where the north wind direction is most prevalent (54 % of records). Since winds blowing from north to south usually cause heavy snowfalls on the site of the test line and in most of the observed cases of galloping, ice and snow accretion have been found on the sub-conductors, it is reasonable that most of the galloping events occur in January.

Table 5.5. Observation of the galloping events.

Event number	Start time	End time
1	14/12/2018 02:00:00	14/12/2018 23:00:00
2	29/12/2018 12:30:00	01/01/2019 10:30:00
3	02/01/2019 06:00:00	02/01/2019 14:30:00

4	03/01/2019 03:00:00	04/01/2019 10:00:00
5	05/01/2019 22:00:00	06/01/2019 12:00:00
6	09/01/2019 05:00:00	10/01/2019 06:00:00
7	16/01/2019 09:00:00	17/01/2019 12:00:00
8	18/01/2019 02:00:00	19/01/2019 12:00:00
9	21/01/2019 00:10:00	23/01/2019 00:00:00
10	24/01/2019 00:10:00	25/01/2019 00:00:00
11	25/01/2019 00:10:00	25/01/2019 11:00:00
12	26/01/2019 02:00:00	28/01/2019 02:00:00
13	31/01/2019 15:00:00	02/02/2019 10:00:00
14	09/02/2019 21:00:00	11/02/2019 00:00:00
15	14/02/2019 03:00:00	14/02/2019 16:00:00
16	16/02/2019 14:00:00	18/02/2019 10:00:00
17	08/03/2019 00:10:00	08/03/2019 07:00:00
18	24/03/2019 05:00:00	24/03/2019 12:00:00

Figure 5.25 shows the time series of the overall tension load measured for the 18 galloping events. The presence of abnormally high and low values in the measurement data confirms the occurrence of power outages during some events. Noticeable differences have been found between some files where there are large amplitude signals varying between -20 and +60 kN, while in some other records, tension loads are just between -2 and +3 kN. With the aim to identify trends from different types of galloping events, a series of characteristic events are considered where ice accretion has been confirmed from visual inspection. Thus, it is presented next a detailed analysis of the galloping events 4, 5, 6, 7 and 8, where these events show different shapes of the tension load that are expected to provide distinct features of the structural responses.

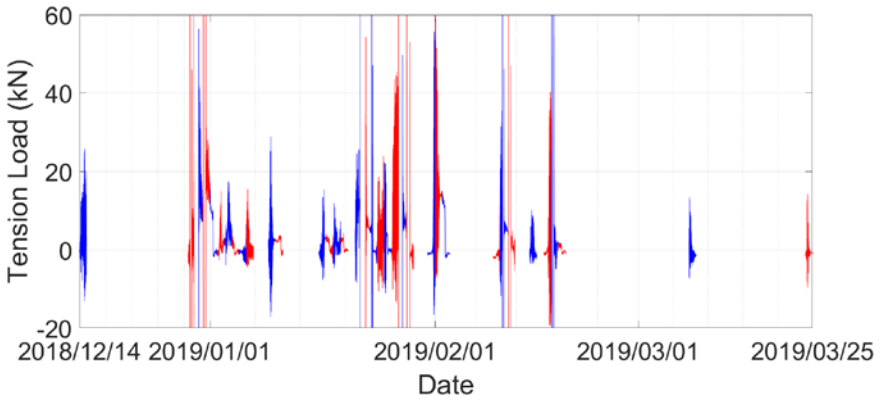

Figure 5.25. Time series of tension force for the 18 galloping events. Alternate colours represent different daily records.

The time series of the tension load and the correlated atmospheric parameters (wind direction and speed), and the natural frequencies are displayed in Figure 5.26 for the galloping events four and five. Galloping event 4 has been considered as an example of a "well-behaving" record. For short periods of time, there are distinct loading regimes with large tension amplitude oscillating between positive and negative values. On the other hand, event 5 seems an "ambiguous" record, which might originate from highly transient conditions where large amplitude signals last for longer periods of time. In order to correlate the visual observations from the ITV and the tension measurements, vertical lines have been superimposed in the plots defining the starting time and the end time of the galloping observations, as displayed in Table 5.5.

The wind conditions and, particularly, the trends in the natural frequencies seem to provide a more comprehensive view of the galloping phenomenon within these periods. As it would be expected, north (between 0 and 45 °) is the prevailing wind direction during galloping. because of the activity of the tower. Although several authors have aimed to establish the critical wind velocity that causes galloping, the critical wind velocity, V_{crit}, according to Post-Tensioning Institute (2006) is used in this analysis as an example. It is given by:

$$V_{crit} = C f_n d \sqrt{\frac{m\zeta}{\rho d^2}} \tag{5.9}$$

Where C is a constant (recommended value of 40 for circular cables)

f_n is the natural frequency (Hz)

d is the cable diameter (m)

m is the cable mass per unit length (kg/m)

ζ is the damping ratio-to-critical

ρ is the air density (kg/m^3)

The critical wind velocity, V_{crit}, given by Equation 5.9, is 5.2 and 7.4 m/s for 0.5 and 1% damping ratio, respectively, as a reference. There is evidence that the occurrence of galloping is induced by an increase in the wind speed above 7 m/s and 10 m/s for event 4 and 5, respectively. However, in event 4, galloping starts when the wind speed is still increasing, and it ends before the wind speed starts to decrease, as it usually occurs in limit cycle oscillations.

Natural frequency estimates show, as observed before, clear concentrated results in the initial small vibrations regime and a strong frequency pattern in the galloping regime. The 1st mode (*Y1*) disappears when galloping starts and remerges when the system stops galloping. Other modes combine together in distinct frequency components that are exact integer multiples of each other (0.32, 0.64…). Overall, it gets scattered because the system is in a violent response region and then moves into galloping. Evidence of classical modes entirely disappears, and all the energy gets distributed across harmonic frequencies. The motion patterns are related to the modes that cause this motion.

On the basis of classical definitions, galloping is usually induced by coupling, which in this case it appears to occur when the predominant torsional frequency *R1* matches the frequency of the vertical mode *Z2* between 0.3 and 0.4 Hz. It might be the case that there are two types of galloping: vertical-dominated galloping and torsional-dominated galloping. Almost all of the galloping phenomena observed by Matsumiya (2022a) in the video images occurred in the pseudo-two-loop/span mode.

However, according to the FEM model results it would correspond to Mode *Z2* (0.399 Hz) and Mode *R1* (0.400 Hz), while from the full-scale measurements, galloping occurs at a slightly lower frequency, around 0.38~0.39. It seems that the finite element results are a useful tool in the interpretation of the data, despite they are slightly higher than the actual ones. Overall, in event 4, the frequencies of the following groups appear to be interacting: *R2*, *Y2* and *Z1* around 0.35~0.4 Hz, *R3*, *Y3* and *Z3* around 0.5~0.6 Hz and *R4*, *Y4* and *Z4* around 0.65~0.7 Hz. There is more obvious presence of results between 0.2 and 0.3 Hz with the increase in excitation probably.

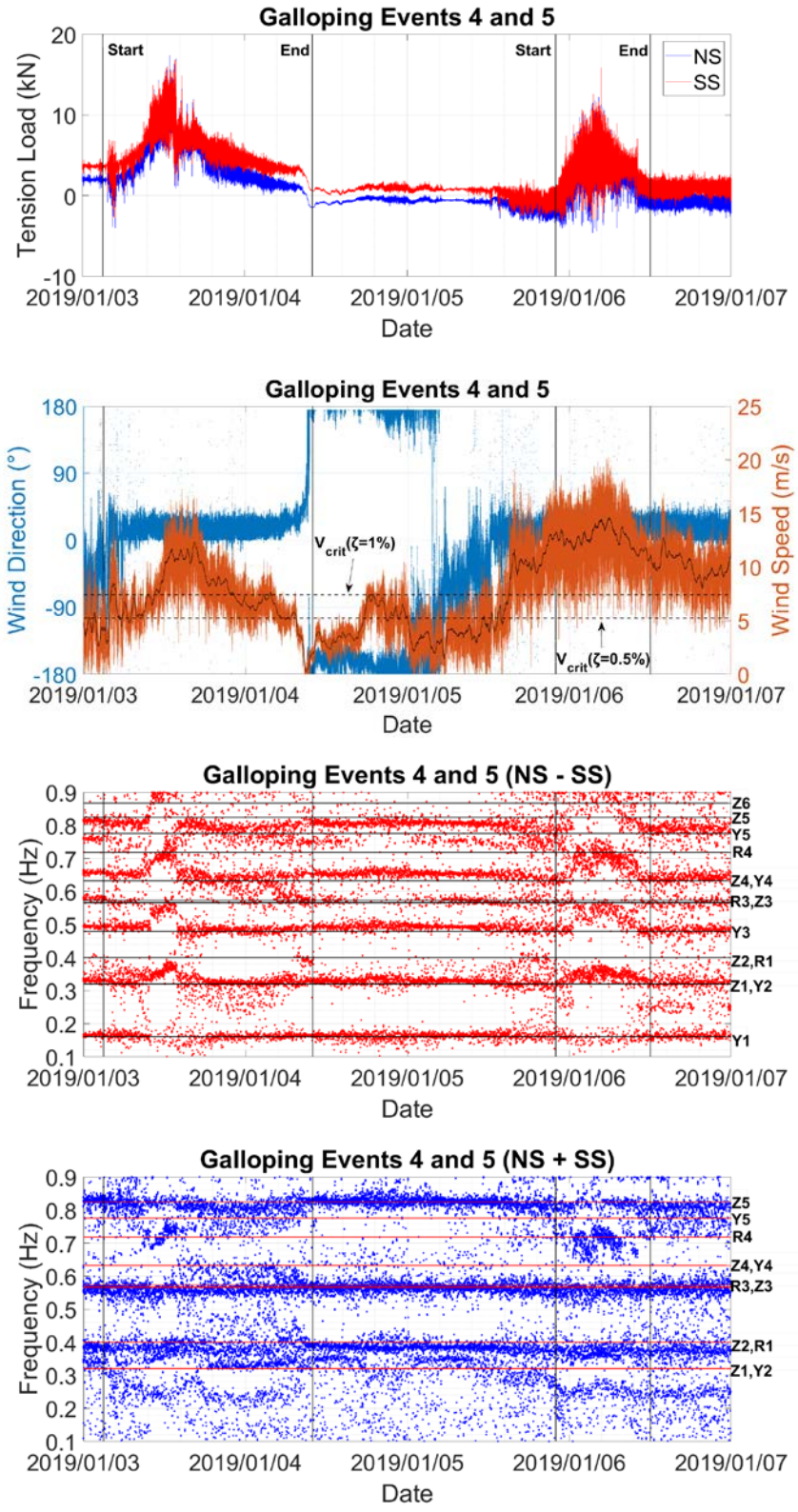

Figure 5.26. Time series of tension force, atmospheric conditions (wind direction and speed including 10-min moving average and critical wind velocity for 0.5 and 1 % damping ratio) and estimated natural frequencies (including predicted values from FEM model) for galloping events 4 and 5.

Galloping event 6, displayed in Figure 5.27, is a good example of what has been classified as an ambiguous galloping record; a mixture of limit cycle oscillation galloping and transient gusts induced by a higher wind speed before the load becomes stable. This results in more scattered frequency estimates compared with "well-behaving" records, such as event 4. Although it is more difficult to make clear statements from this event, there is a clear interaction between the horizontal (Mode *Y2*), vertical (Mode *Z1, Z2*) and torsional frequencies (Mode *R1*) at around 0.33~0.34 Hz for the period of highest excitation load, which presumably corresponds to galloping occurrence. Thus, the apparent galloping frequency in this record is lower than in galloping events 4 and 5, observed around 0.35~0.4 Hz. The north wind direction is also stable during galloping, but based on the behaviour of the frequencies, it starts when the wind speed decreases, although this is still above the critical galloping velocity. The effect of wind direction on the tension response is noted at the end of 2019/01/10, where wind blew north direction, and it changed suddenly towards south inducing a clear drop in the tension load. During galloping events, the emergence of nonlinear response has been observed, which shows strong harmonic participation of a dominant frequency and its higher harmonics. Typically, in limit cycle oscillations in nonlinear systems the frequency of the cycle starts to dominate, and it becomes challenging to continue classical modal analysis due to its association with properties of linear dynamic systems. This seems to be the case for this event, where the primary galloping frequency at 0.32 Hz characterises the limit cycle oscillation. These records show a lower presence of results between 0.2 and 0.3 Hz. Moreover, with the disappearance of the 0.26 Hz mode in the presence of galloping, it seems that the tower is forced to vibrate with the same frequency as the cable does.

These are suitable records to explore the relationship between the mass change and the evolution of the natural frequencies from the FEM parametric analysis and the full-scale measurements. For example, if the mass distribution is changed by 50 % on the bundle, the frequencies of most of the torsional modes change by 5 % (Figure 5.13). However, if 5 % lies within the range of the scattered area, then the change is easily hidden in the noise. Moreover, the lowest wind speed is measured at the end of 2019/01/09 and the start of 2019/01/10, but the regime with the lowest peak-to-peak load is observed at the end of 2019/01/10. There, the frequencies of the modes *R3* and *Z3* (from Figure 5.27 "NS + SS" subplot), which were observed to be some of the most sensitive modes with the increase in mass from the finite element results, are less scattered.

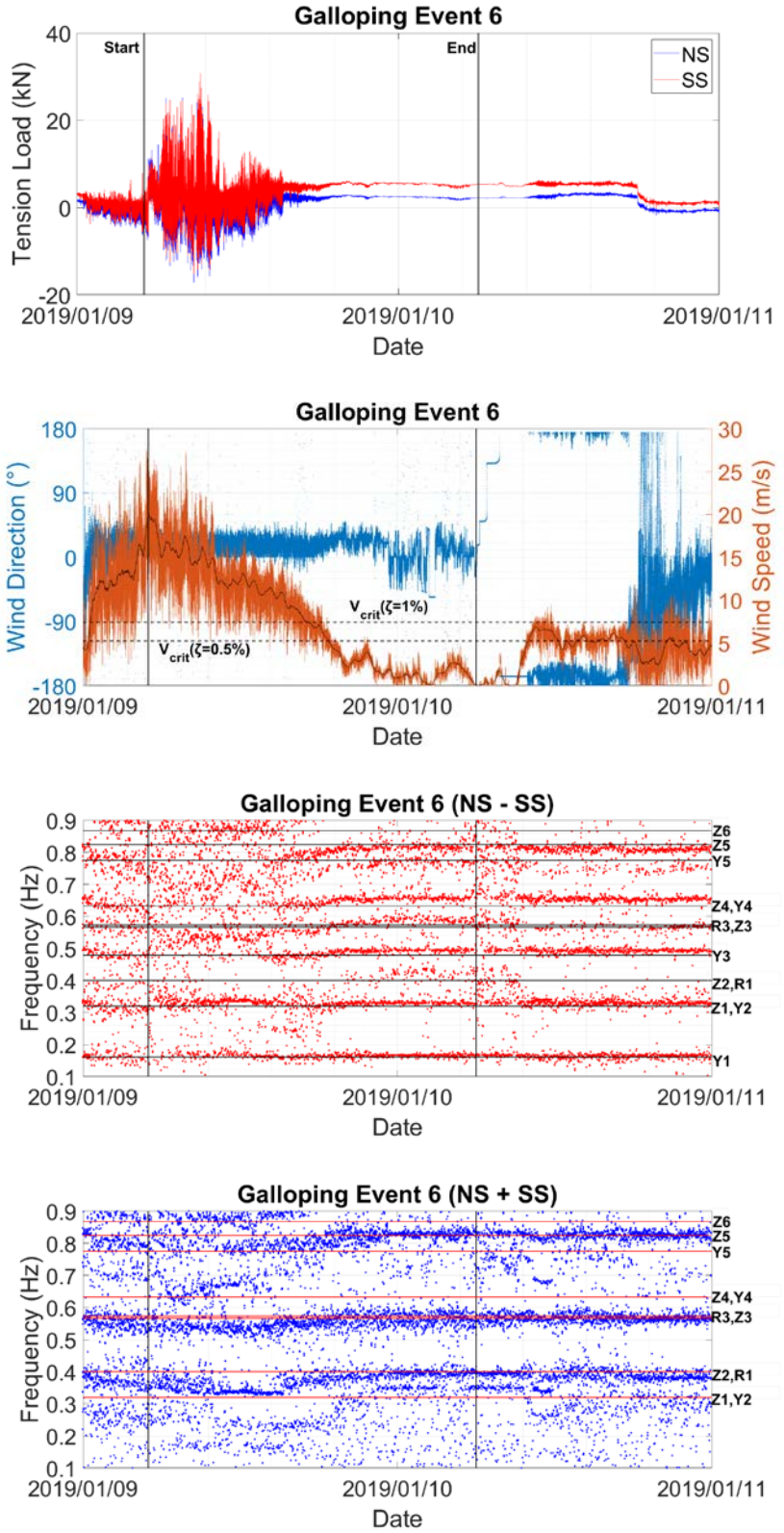

Figure 5.27. Time series of tension force, atmospheric conditions (wind direction and speed including 10-min moving average and critical wind velocity for 0.5 and 1 % damping ratio) and estimated natural frequencies (including predicted values from FEM model) for galloping event 6.

Although it is difficult to quantify the mass of the ice on the bundle and its evolution through the record, it is stated that, aside from the galloping events, the observed dispersion in the natural frequencies is mainly arising from the tension regime rather than the mass or the wind speed.

Galloping events 7 and 8 are also good examples of “well-behaving” records (Figure 5.28). There is an initial regime of small vibrations before transitioning to strong galloping illustrated by the frequency responses. Then, there are a few regimes of approximately steady responses, and the loads finally drop to a level similar to the initial regime. North is also the prevailing wind direction in both events. However, galloping in event 8 occurred at the end of 2019/01/18 for a wind speed lower than 5 m/s, which is less than the critical speed for a 0.5 % damping ratio. The galloping response of event 7 is similar to that of events 4 and 5, where modes combine in the strong frequency components that are exact integer multiples of each other (0.34, 0.52 and 0.66 Hz).

The durations of galloping regimes in event 8 are too short to display clear frequency results, but subtle trends similar to those in event 7 might be inferred from them. These short durations in event 8 are probably related to the low wind speeds. The mode at 0.32 Hz is the one that became unstable, so the limit cycle inherits the motion characteristics of that unstable mode. Although the vertical, horizontal and torsional motions are coupled, the fundamental unstable mode is related to the vertical motion that induces galloping. The mode shapes of vertical and horizontal modes are slightly different.

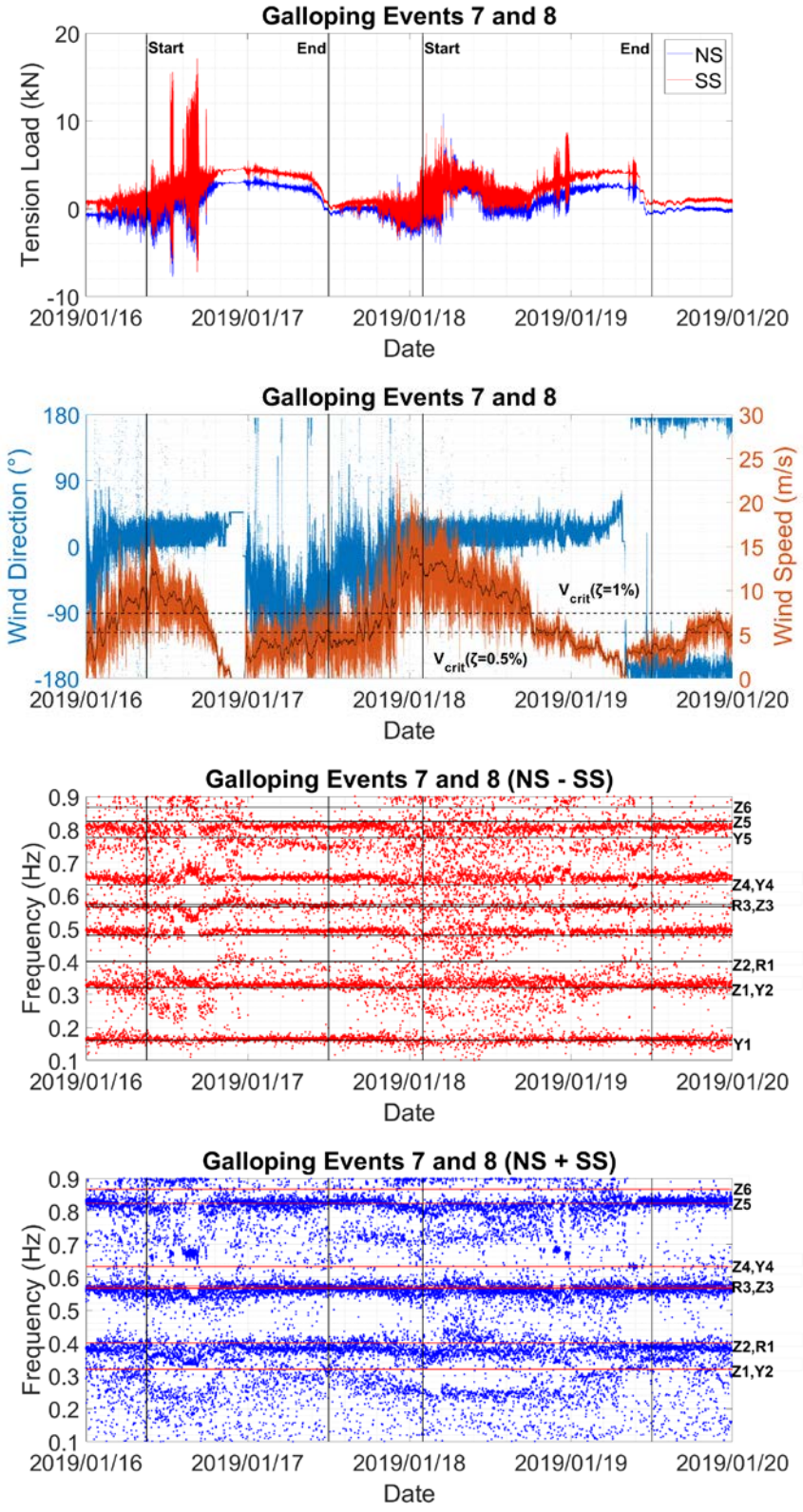

Figure 5.28. Time series of tension force, atmospheric conditions (wind direction and speed including 10-min moving average and critical wind velocity for 0.5 and 1 % damping ratio) and estimated natural frequencies (including predicted values from FEM model) for galloping events 7 and 8.

Based on the detailed analysis of the galloping events 4, 5, 6, 7 and 8, distinct features of the structural responses have been found. The primary galloping frequency that characterises the limit cycle oscillation has been observed at different frequencies for the different galloping events between 0.32 and 0.39 Hz. As is usual for limit cycle oscillations, the frequency estimates switch from one stable branch to the other through the duration of the record. Findings on the observations at the site, with the help of an eigenvalue analysis presented by Matsumiya (2022a), confirmed that galloping sometimes occurs in a pseudo-1-loop/span in-plane mode at 0.426 Hz, which resulted in significant tension variations even for small response displacements. However, it has not been observed in any of the presented galloping events.

5.7. DISCUSSION AND CONCLUDING REMARKS

5.7.1. Discussion

In this analysis, two tension meters and a vane anemometer were used to measure the wind-induced vibrations and associated wind conditions for a four-bundled conductor within a transmission line span over a period of 4 months. The focus of this investigation was to identify trends in the ambient vibrations in a range of atmospheric conditions with the objective to analyse the typical values in operational conditions. Then, the variation of the wind-induced response was analysed in order to identify the most influential parameters in the dynamic response of the system, with a specific focus on the galloping events. The dynamic behaviour of the bundle and the effect of wind direction, and the variation of the tension on the natural frequencies were investigated during both galloping and non-galloping events. From the full dataset of 121 daily records, a global analysis of the long-term trends was conducted in the 78 non-galloping records, while short-term and detailed assessment was made on six galloping events across 10 individual daily records. These findings on the full-scale compared with the results obtained from experimental wind-tunnel data in Chapter 4 based on the same bundle geometry. The novel aspect of this study is that the wind-induced vibrations of the system have been quantified based on the modal parameters obtained from tension readings using only two strain gauges, given the lack of studies found in literature investigating the galloping problem on electricity transmission lines grounded on tension measurements.

A long-term analysis of the non-galloping events resulted in a lack of clear trends. After evaluating the natural frequencies for the main structural modes in relation to a series of parameters, including tension, wind speed and temperature on a basis of the averages of 1-day long records, it was found a baseline variability in the mean daily natural frequencies between ± 1 % and ± 2 % with respect to the overall mean natural frequency of each mode. The frequencies corresponding to the first identified mode (*Y1*) showed the highest dispersion. Moreover, there was an apparent subtle trend of low dispersion in the natural frequencies for higher wind speed. However, a reasonable explanation of the previously observed mechanism could not be provided. It was assumed that the observed frequency change of non-galloping events was the natural variability while the galloping events showed more clear trends, with perceptible differences.

In galloping events, the natural frequencies estimated in the regions with small vibrations were clear and concentrated. When moving to regions with higher excitation, galloping or buffeting, the results became more fuzzy and a much higher frequency variability was measured. In the frequency domain, the modal picture became more complicated after the 1st mode (*Y1*), and the uncertainty in relating the frequency estimates to the different modes identified from the FEM increased. Although many close modes merged during the occurrence of galloping, the apparent coupling occurred in a vertical-horizontal-torsional 3-DOF coupling oscillation in two-loops/span mode. This agrees with the observations from the camera images provided by Matsumiya *et al.* (2022a) and the classical definitions of galloping. From the literature (Post-Tensioning Institute, 2006), the estimated wind speed that induces galloping, which is related to the characteristics of the cable, has been estimated as 5.2 m/s for a typical value of the damping ratio of 0.5 %.

In almost all of the galloping events considered, this velocity has been achieved during the occurrence of galloping, but in two of the events, it started at a slightly lower wind speed. These uncertainties are probably related to the effect of ice accretion and the nonlinearities of this system in particular. These results agreed with the analytical prediction of galloping in Chapter 4, where the emergence of galloping was observed for a given torsional displacement of the bundle when the wind speed was 6.7 m/s. There, it was also observed that for particular test configurations, the wind speed that induces galloping could be as low as 2 m/s for a range of torsional displacements between 20 and 25°.

In line with the full-scale study on tall buildings in Chapter 3 based on minimalistic monitoring approach, it can be concluded that clear information on the natural frequencies of the system could be obtained using only two tension meters. This is particularly relevant in the context of the research on the Tsuruga Test Line because tension meter installation, calibration and maintenance were cheaper and less demanding than more sophisticated equipment (e.g., video cameras or GPS sensors). The arithmetic transformation of the two tension meters effectively uncoupled the modal information into two nearly independent sets, each dominated by either motion in the horizontal, vertical or torsional sense. Relatively accurate estimates of the natural frequencies were obtained in the context of closely spaced modes even during wind-loading events that include coloured noise. Unlike the investigation in tall buildings which were based on the natural frequencies and damping ratios, the estimation of modal damping of the system was left for future research due to the violation of the LTI assumption and additional challenges related to the nonlinearities of the system.

A simple finite element model supported data analysis and provided a relatively close match with the measured natural frequencies. With the aim to simulate the increase in mass due to the attached ice or snow on the bundle, torsional and vertical modes from the finite element results were observed to be the most sensitive with the increase in mass. This was used to help to interpret modal activity with minimal measurements. However, it was difficult to correlate to full-scale measurements, particularly during the galloping events, because it was challenging to quantify the mass of the ice or snow accretion on the bundle and its evolution through the record.

The modal parameter estimation of tall buildings in Chapter 3 was performed using the IWCM as detailed by Macdonald (2000). The added and novel challenges of this study are that the system was not observed to be within stationary conditions, there are several closely spaced modes and the galloping events were dominated by nonlinear behaviour. Thus, conducting modal analysis on the entire daily signal or long subsets was not found to be appropriate. The procedure of using fitting functions, as they were adopted for tall buildings, might have caused the resultant PSD to be influenced by the changes within each time interval, leading to biased damping ratio estimates due to the changing conditions through the test. The application of the ICWM to perform system identification was found to be only suitable for the 1st mode. Instead, the pLSCF method or PolyMAX (Van der Auweraer *et al*., 2001; Guillaume *et al*., 2003; Peeters *et al*., 2004) was adopted despite its limitations since it was not expressly developed to

be used within this context of non-white noise excitation processes where wind plays a major role. A shorter-term analysis was conducted to select more logical and objective subsets, considering the shortest acceptable interval. It partitioned through the daily data files and analysed those small segments to identify more sensible trends. Therefore, alternatively to the investigation in tall buildings, this research has provided a detailed analysis at small scale by conducting as little pre-processing as possible of the data to reduce the influence of subjective assumptions.

In this study, only a few selected galloping events have been shown. They have been used as a baseline to understand the main characteristics of the galloping response observed in the real world full-scale context. Future work might further benefit a more detailed assessment of all the galloping events emphasising the trends in the periods of time where galloping is clearly observed. In addition, future analysis might include a model that match precisely the structural response. A more detailed finite element approach might be conducted in future analysis by assessing the effect of ice eccentricity. Using a similar analysis as an example, Foti and Martineli (2018) studied the effect of the eccentricity of the ice coating on a modelled *U*-shaped corotational beam element under galloping conditions identifying the rotational frequencies in terms of wind speeds. However, the effect of mass variation was not accounted.

The full-scale measurements in this study provided a source to assess the potential variability measured in those circumstances using a refined experimental analysis involving model calibration. A combination of results from galloping or high excitation and small vibrations might be combined to identify the parameters that governs the complex dynamic behaviour of the system. This might be supported by proper modal damping identification, which has not been considered in the present study, with the objective to provide a stability analysis.

A sophisticated model might include all the potential effects that influence the structural response, such as the amount and distribution of ice accretion, the rotation of the bundle due to the wind action on the ice accretion, the temperature and its effect on the thermal expansion of the sub-conductors as well as the effect of the vertical component of the wind load. In addition, since the occurrence of galloping has been identified for wind speed lower than the critical, it seems that existing formulas are not sufficient to predict the galloping wind speed, and they should be adapted to the studied system. It is expected that a comprehensive model can provide

clear results and solutions to the problems and uncertainties arising during the full-scale measurements.

5.7.2. Concluding remarks

To mitigate and control the impact of the aeroelastic phenomena on the critical electric power distribution infrastructure and to explore potential for non-invasive operational monitoring in full-scale conditions, this study uses full-scale data to perform dynamic analysis of the long-term operational conditions and ice galloping events observed on the *Tsuruga test line* in Japan provided by Central Research Institute of Electric Power Industry. Using OMA and supported by finite element model, results from short-term galloping events have been contrasted with the nominal (low vibration) and non-galloping forced response events. The analysis is based on the operational data collected across a 4-month period using a non-invasive monitoring system consisting of a pair of uniaxial strain gauges in the case of a single four-cable bundle. It has been aimed to identify trends in the ambient vibrations in a range of atmospheric conditions with the objective to analyse the typical values in operational conditions with a focus on the galloping events.

The main findings and conclusions of this study are:

- It has been observed that the long-term analysis of the non-galloping events resulted in a lack of clear trends. After evaluating the natural frequencies for the main structural modes in relation to a series of parameters, including tension, wind speed and temperature on a basis of the averages of 1-day long records, it was found a baseline variability in the mean daily natural frequencies between ± 1 % and ± 2 % with respect to the overall mean natural frequency of each mode. The frequencies corresponding to the first identified mode (*Y1*) showed the highest dispersion. Moreover, there was an apparent subtle trend of low dispersion in the natural frequencies for higher wind speed. However, a reasonable explanation of the previously observed mechanism could not be provided.
- It has also been found that the apparent coupling occurred in a vertical-horizontal-torsional 3-DOF coupling oscillation in two-loops/span mode, although many close modes merged during the occurrence of galloping. The primary frequency that characterises the limit cycle oscillation has been observed between 0.32 and 0.39 Hz. Moreover, it has been observed that galloping emerged at a slightly lower wind speed for two short-duration galloping periods, although most of the galloping events occurred under moderate to strong winds in

line with the predicted critical speed rooted in standards (Post-Tensioning Institute, 2006).

- The validity of the finite element model has been established by achieving satisfactory agreement between its first fifteen natural frequencies and the full-scale measurements and via a qualitative agreement between the mode shape indicators implied by the post-processed tension PSDs and the calculated mode shapes. Moreover, it has been also used to emulate the addition of ice to the cables, for which it has been shown that torsional and vertical modes (10.2 and 9.4 % decrease respectively) were the most sensitive when the mass of the cable increases up to 100%.

CHAPTER 6. DISCUSSION AND CONCLUSIONS

6.1. DISCUSSION

This chapter firstly presents a critical appraisal of the work addressing the aim and objectives of the research stated in Section 1.2. The principal conclusions based on the results of this investigation and the recommendation for further work are finally detailed in Sections 6.2 and 6.3 respectively.

6.1.1. Research aim

Full-scale monitoring data has been analysed in this research for two different types of slender structures, two tall buildings in London (i.e., Tower 1 and Tower 2) and a cable bundle within an overhead transmission line in Japan, which has been also studied at wind tunnel scale. In the context of minimal Operational Modal Analysis (OMA), this research has aimed to use measurements from simple monitoring systems to assess the effect of the wind on their responses, within the constraints specific to this study. The purpose of this minimalistic approach was to provide reliable results simply by installing and leaving the monitoring equipment in place for extended periods, and has potential transferability to industrial settings due to its ease of maintenance and low cost. This is particularly relevant for slender structures, which are sensitive to wind-induced vibrations, since occupant comfort and structural damage are of paramount importance in tall buildings and overhead electricity transmission lines respectively. These two systems have been considered to explore the adoption of well-established OMA methodology for bridges and buildings to more complex nonlinear systems, such as cables, in order to gain understanding of wind-induced vibrations, galloping phenomena and the associated characteristics from ambient vibration data.

6.1.2. Minimalistic monitoring

The use of minimalistic monitoring systems has been found to be successful to reveal the main trends of the dynamic characteristics of the two types of studied structures in a wide range of wind conditions.

A set of three accelerometers and an ultrasonic anemometer installed on Tower 1 monitored the effects of the wind on the structure for a period of about a year (although not

continuously), while the same accelerometer equipment was later installed on top of Tower 2, where it provided a set of measurements during a week. Modal parameters have been estimated from general in-plane motion on top of the structures using the three acceleration channels. Despite the spectral analysis of accelerations from a single sensor would have provided the peaks corresponding to all of the modes of the structures, geometric decomposition has been applied to identify separately components of constituting motion acceleration (e.g. swaying and rotation). Due to the proximity of very close modes for Tower 2, signal pre-processing has been conducted using singular value decomposition in order to identify the analogous components of motion for this building.

Two tension meters and a vane anemometer were used to measure the wind-induced vibrations and associated wind conditions on a four-bundled conductor within a transmission line span over a period of 4 months. The preliminary observed emergence of highly coupled behaviour during galloping in the analytical study has provided evidence that manipulation of the channels might lead to discrimination of motion. This has been a great learning transferred to the full-scale investigation, where, indeed, it has been confirmed that subtraction and addition of the two channels highlights clear distinct motions. Differential handling of the channels has revealed more clearly the modes that involve horizontal movement because it creates differential action in the sensors. On the other hand, addition of the two channels provided a better visualization of the vertical and torsional motions. The use of a minimalistic monitoring system has been particularly important in this case, because this research has provided an alternative approach based on tension measurements with respect to recent studies on the target span, which were based on the vertical displacement amplitude obtained from an industrial television (ITV) camera or GPS sensors. Alternatively, two tension meters, which are more practical to install in such a risky location, cheaper to run and easier to maintain, have been considered to be enough to identify the occurrence of galloping and its vibration modes from the estimated natural frequencies.

In the context of minimal OMA, it is concluded that, whilst the presented results are contextual and specific to these two types of structures, the ability of simple monitoring systems to establish the vibration characteristics, to elucidate their root causes and to interpret their variation forms a useful case study evidencing applicability of such tools in the through-life analysis and monitoring of the structural condition and health. Thus, there seems to be potential

transferability to industrial settings due to its ease of maintenance and low cost to assess the performance criterion for serviceability for both type of structures.

6.1.3. Natural frequency monitoring

Since the studied systems have distinctly different characteristics (e.g., overall dimensions, stiffness properties, flat urban vs. mountainous rural environment), this research provides an opportunity to directly quantify and contrast the effect of the wind on their responses. These differences are reflected in varied trends in the estimated modal parameters.

The research on tall buildings has found that reliable estimates of both natural frequencies and damping ratios could be estimated for that type of slender structures subjected to wind loading. However, the modal parameter estimation of the monitored four-bundled conductor, which is a more complex nonlinear system, has been observed to be more sensitive to the loading assumption in the context of wind excitation, particularly in the case of modal damping. Therefore, the analysis of trends of the estimated modal parameters in tall buildings has been based on both natural frequency and modal damping, while in transmission lines, it has been focused on only natural frequency.

In tall buildings, after evaluating the natural frequencies in relation to a series of parameters, including time, acceleration amplitude, wind speed and wind direction, amplitude has been found to be the dominant effect. Natural frequencies showed a decreasing relationship with respect to amplitude and wind speed. Furthermore, given the length of the measurements on Tower 1, a decrease in the frequencies was also observed with the passage of time during the full monitoring period.

The full-scale identification of trends in the cable bundle within electricity transmission lines has been conducted at two separate levels considering both galloping and non-galloping records. Firstly, in the absence of galloping, which corresponds to the majority of the measurement period, a long-term study has been undertaken on the basis of the averages of 1-day long records. The evaluation of the natural frequencies for the main structural modes in relation to tension, wind speed and temperature resulted in a lack of clear trends. A baseline variability in the mean daily natural frequencies between ± 1 % and ± 2 % has been measured with respect to the overall mean natural frequency of each mode. Moreover, there was an apparent subtle trend of low dispersion in the natural frequencies for higher wind speed. However, a reasonable explanation of these mechanism could not be provided.

In galloping events the natural frequencies estimated in the regions with small vibrations are clear and concentrated. When moving to regions with higher excitation, galloping or buffeting, the results become more fuzzy and much higher variability in the frequencies has been measured. However, galloping has been identified to be directly related to a combination of moderate to strong wind (5-15 m/s), according to WMO (1970) classification, and a prevailing wind direction that is associated to ice and snow conditions at the site. In particular, the primary galloping frequency that characterises the limit cycle oscillation has been observed at different frequencies for the different galloping events between 0.32 and 0.39 Hz.

6.1.4. Damping monitoring

Similar analysis of modal damping measured in the two tall buildings in relation to a series of parameters has found that the variation in damping ratio estimates was dominated by vibration amplitude. A trend of the increasing damping ratio with increasing response amplitude and wind speed has been observed for the first three modes in each of the two sway directions and in torsion. Hence, it is noted that the dissipation of energy and consequent mitigation of the oscillations associated with this trend has a positive effect on the integrity of the structures.

A focused study on the amplitude-dependency of damping at high amplitudes has been conducted from measurements in Tower 1, since there is still an open discussion within the community around this phenomenon. A new damping prediction model based on the power-law model from Davenport and Hill-Carroll (1986) has been proposed to fit the amplitude-dependent behaviour of damping obtained. Based on the qualitative evaluation and analysis of the coefficient of determination, R^2, this proposed empirical model has been found more suitable than six previous damping prediction models for the measured data, largely due to the consideration of the structural damping ratio effect. Using the proposed damping model, the amplitude-dependent damping ratio values were shown to range from 0.6% for the near zero amplitudes to 2.1% for the high amplitude conditions.

6.1.5. Coupling and aeroelastic effects

Since coupled motions have been observed in the three full-scale case studies and in the analytical study based on wind tunnel tests data, the occurrence of aeroelastic coupling has been assessed during this research.

In Tower 1, there was evidence of slight coupling of one of the translational directions and torsional motion, and even more closely spaced modes in the two translational directions have been identified in Tower 2. A particular analysis in Tower 1 observed that the structure was barely affected by potential aeroelastic effects. Since the natural frequencies of pairs of modes in the two translational directions have been observed to be close to each other, aeroelastic coupling could occur in the buildings under strong winds. Under the assumption of the aerodynamic damping being responsible for the experimental variations, similar aerodynamic gradient trends have been identified for the damping-wind speed relationships with respect to different wind orientations. Therefore, little evidence was found of an effect of wind direction on the damping ratio to support the aerodynamic damping arguments for the studied structural configuration. Instead, the amplitude-dependent structural effects were identified as the primary source of the observed variations in the identified damping ratios.

Coupled motions of the cable bundle have been also identified from the analytical solutions of the two adopted aeroelastic formulations under two selected moderate wind speeds (6.7 and 10.2 m/s) for a range of angles of attack (0-35°). Full-scale measurements in the target span also confirmed the occurrence of galloping in a vertical-horizontal-torsional three degree of freedom (3-DOF) coupled oscillation under moderate to strong winds in a predominant horizontal wind direction. This agrees with the observations from the camera images obtained by Matsumiya *et al.* (2018) and the classical definitions of galloping. Oppositely to the two monitored tall buildings, the cable structures have been found to be highly sensitive to the aeroelastic effects, mainly due to their lower stiffness. These effects have been also confirmed in the analytical study based on wind tunnel tests under two selected moderate wind speeds for a range of torsional displacements. Moreover, the presence of aeroelastic effects has been clearly illustrated by the shift in the fundamental frequency due to the presence of higher wind speeds, which were directly related to the prevailing wind direction.

6.1.6. Effects of added mass and finite element models

The data records from the different occupation stages of the Tower 1 and from the different atmospheric conditions at the Tsuruga test line has provided great opportunities for further study of all of these areas, since modal parameters can be varied. The adoption of simplified finite element models has been found useful to predict the full-scale results and confirm the variation in the natural frequencies with the change in mass in both types of

structures. They have provided a relatively close match with the measured natural frequencies in Tower 1 and the monitored span. There is evidence that the two types of structures are, on different levels, susceptible to the variation in added mass, even though the dissipation of energy quantified as damping, apparently, has not been significantly influenced by this variation.

In the first case, there was a gradual decrease of the full-scale natural frequency estimates for the first modes in each direction with the observation time over the twelve-month monitoring period. In fact, an asymptotic exponential decay has fitted this relationship. A decrease of approximately 2.0 and 4.3 % was observed at the end of the measurements in the two sway directions and torsion respectively with respect to the start date of monitoring. Also, a simplified finite element model of the tower was used to support the argument that the trends can be attributed to the increasing added mass in the structure during the fitting out and the initial occupation of the building. It has been shown that, based on realistic estimates of the occupancy and loading rooted in standards (Eurocode 1), the model was able to match the observed values under the different fractions of the occupancy loading.

A finite element model of the cable bundle has been used to emulate the addition of ice to the cables by increasing their masses up to 100% the mass of the cable, which is similar to the maximum estimated weight of the ice accretion on the site. It has been observed that torsional and vertical modes (10.2 and 9.4 % decrease respectively) were the most sensitive with the increase in mass. This was used to help to interpret modal activity with minimal measurements. However, it has been difficult to correlate to full-scale frequency estimates to the different modes, particularly during the galloping events, because the modal picture became more complicated after the 1st mode.

The experimental observations in full-scale transmission lines were observed to be under changing conditions associated with mass changes related to the ice accretion on the subconductors, although it has been difficult to quantify its evolution through the record. The mean tension change, which was mainly influenced by the wind force, has been shown to have a greater effect on the changes of natural frequencies than the weight of the ice accretion. In the case that the ice shape develops normal to the wind direction, the force would be large and the mean tension would be mainly influenced by the wind force rather than by the weight of the ice. Thus, it is important to separate the effect of ice amount and wind force influenced by ice shape.

6.1.7. Auxiliary and complementary studies

The preliminary analytical study in transmission lines, based on data from wind tunnel tests presented by Matsumiya *et al.* (2018) on the same full-scale cable bundle geometry of the full-scale line, has been found to be a promising approach to predict the onset of the galloping instability. The eigenvalue analysis has been conducted in this research using the analytically defined aerodynamic damping matrix, taking as a reference two existing quasi-steady aerodynamic force models. It has been highlighted that the galloping instability was mainly driven by the torsional displacement of the bundle, and at a lower extent, by the wind speed. The instability regions found with the help of this approach agreed relatively well with the results obtained from the steady-state time-history response analyses of the first model, which showed good agreement with the full-scale results from the wind tunnel tests. Furthermore, the critical wind speed, which can be defined as the wind speed at which galloping first occurs, has confirmed the classical definitions and formulations, where the condition of galloping instability is governed by the lift force acting on the body section, expressed in the form of lift coefficient. The behaviour estimated using the second model, which assumes the existence of the aerodynamic centre, was also relatively consistent with the results observed in the reference and linearized model. However, it should be noted that only two test cases were considered in this research.

The position of the aerodynamic centre parameter, which was implicitly taken into account by one of the two reference quasi-steady aerodynamic force models, and is commonly used in literature, has not been yet defined theoretically. It has been found in this research in terms of its relative position within the considered bundle geometry and for different angles of attack based on the wind tunnel results. Assuming the wind to be along the principal axis of the system in the horizontal direction, the position of an aerodynamic centre has been found to be approximately at the mid-point of the bundle for those angles of attack for which there is not any sub-conductor directly behind another.

For those angles of attack for which there is at least one sub-conductor directly behind another, its position has been found to be aligned with the wind direction towards the edge of the bundle upwind. It is assumed that the rotational motion causes a relatively large change in the forces, due to the fact that the subconductor sheltered by another will then go into or out of a region with greater local wind velocity.

6.1.8. Limitations of the research

Even though several clear conclusions have been derived from this research, some uncertainties have arisen regarding certain particular topics.

On the one hand, although the monitoring systems remained in place during the full monitoring period, data could not be recorded continuously because it was affected, at different extents in each case study, by technical problems (i.e., power shortages or constraints on the computer memory). However, these constraints are not intrinsic to the proposed minimalistic approach. In particular, despite stationarity tests in Tower 1's wind loading has qualified the data to be considered as stationary, and the use of piecewise approach has reduced the bias in the estimated natural frequencies of the cable bundle, some uncertainties raised in the results in the context of stochastic non-stationary processes.

Moreover, the correlation between damping, wind speed and amplitude made it difficult to disentangle the physical mechanisms behind the aeroelastic effects in the structural responses of tall buildings. Therefore, the simplified analysis based on the assumption of the aerodynamic damping being responsible for the experimental variations, has been found to be constrained by the available data and the irregular distribution of the wind directions measured at the site during the monitoring period. Furthermore, it leads to some uncertainties on the amplitude-dependency behaviour of damping in tall structures and the prediction models.

Although the use of the identified position of an aerodynamic centre has provided relative good agreement with the analytical and full-scale results published by Matsumiya *et al*. (2018) from the wind tunnel tests for one of the two test cases considered, this has been proved to be of limited use because higher discrepancy and evidence of insensitivity to its different positions was observed in the other case. This might have occurred because the range of stable boundaries depends on the static conditions, so the effect of the different positions of an aerodynamic centre based on L_a and γ_r parameters plays a role in the galloping cases whilst in the stable regions it might not be relevant.

Finally, proper modal damping identification from the tension data on full-scale transmission lines has been left for future research due to the violation of the LTI (Linear Time Invariant) assumption and additional challenges related to the nonlinearities of the system. Therefore, the relationship between the dissipation of energy of the system expressed as damping and the mechanical resonance represented by frequency could not be taken into account.

6.2. CONCLUDING REMARKS

Full-scale monitoring data has been analysed in this research for two different types of slender structures, two tall buildings in London (i.e., Tower 1 and Tower 2) and a cable bundle within an overhead transmission line in Japan, which has been also studied at wind tunnel scale. The minimalistic monitoring of the selected slender structures and the subsequent data analysis aimed to give a detailed description of the wind-induced dynamic characteristics of the structures to identify the significance of particular objectives and issues stated in Section 1.2.

The main conclusions of this research are:

- After evaluating the identified natural frequencies in tall buildings in relation to a series of factors, including time, amplitude, wind speed and wind direction, the dominant effect was found to be amplitude. There was also a gradual drop of around 3 % and 5 % in the natural frequency estimates for Tower 1 with the observation time over the monitoring period for the first four modes in each of the two sway directions and torsion respectively. The evaluation of the full-scale natural frequencies for the main structural modes of the cable bundle in relation to tension, wind speed and temperature resulted in a lack of clear trends in the long-term. A baseline variability in the mean daily natural frequencies between ± 1 % and ± 2 % has been measured with respect to the overall mean natural frequency of each mode. However, in the short-term galloping events, the primary frequency that characterises the limit cycle oscillation has been observed between 0.32 Hz and 0.39 Hz. In addition, the mean tension change, which was mainly influenced by the wind force, has been shown to have a greater effect on the changes of natural frequencies than the weight of the ice accretion.
- Similar analysis of modal damping measured in the two tall buildings in relation to a series of parameters has found that the variation in damping ratio estimates was dominated by vibration amplitude. A new damping prediction model has been shown to better represent the amplitude-dependent behaviour of the damping measures obtained from the full-scale measurements in Tower 1 compared to the six selected damping models. Using the proposed damping model, the amplitude-dependent damping ratio values were shown to range from 0.6% for the near-zero amplitudes to 2.1% for the high amplitude conditions.

- Aiming to identify the main source of damping and assess potential aeroelastic coupling effects in tall buildings, a particular analysis investigated the apparent aerodynamic damping gradient in Tower 1 with respect to wind speed under the assumption that aerodynamic damping was responsible for the experimental variations. Since similar aerodynamic gradient trends have been identified for the damping-wind speed relationships with respect to different wind orientations, little evidence was found to support the aerodynamic damping arguments for the studied structural configuration. Instead, the amplitude-dependent structural effects were identified as the primary source of the observed variations in the identified damping ratios. Oppositely to the two monitored tall buildings, the cable structures have been found to be highly sensitive to the aeroelastic effects, mainly due to their lower stiffness. Full-scale measurements in the target cable bundle span confirmed the occurrence of galloping in a vertical-horizontal-torsional three degree of freedom (3-DOF) coupled oscillation under moderate to strong winds. These effects have been also confirmed in the analytical study based on wind tunnel tests under two selected moderate wind speeds for a range of torsional displacements. Moreover, the presence of aeroelastic effects has been clearly illustrated by the shift in the fundamental frequency due to the presence of higher wind speeds, which were directly related to the prevailing wind direction.
- The adoption of simplified finite element models has been found useful to support the full-scale results and confirm the variation that the two types of slender structures are, on different levels, susceptible to the variation in added mass, even though the dissipation of energy quantified as damping, apparently, has not been significantly influenced by this variation. A basic linear model was used to support the argument that the decrease in the natural frequencies with the observation time for Tower 1 can be attributed to the increasing added mass in the structure during the fitting out and the initial occupation of the building. In order to help to interpret modal activity with minimal measurements, a finite element model of the cable bundle has been also used to emulate the addition of ice to the cables by increasing their masses up to 100% the mass of the cable, and it has been observed that torsional and vertical modes (10.2 % and 9.4 % decrease respectively) were the most sensitive.
- The preliminary analytical study in transmission lines, based on data from wind tunnel tests on the same full-scale cable bundle geometry of the full-scale line, has been found to be a promising approach to predict the onset of the galloping instability. The eigenvalue analysis

conducted using the analytically defined aerodynamic damping matrix, taking as a reference two existing quasi-steady aerodynamic force models identified that the galloping instability was mainly driven by the torsional displacement of the bundle, and at a lower extent, by the wind speed. The instability regions found with the help of this approach agreed relatively well with the results obtained from the steady-state time-history response analyses, which showed good agreement with the full-scale results from the wind tunnel tests. The behaviour estimated using the second model, which assumes the existence of the aerodynamic centre, was also relatively consistent with the results observed in the reference and linearized model. The position of the aerodynamic centre parameter, which was implicitly taken into account by one of the two reference quasi-steady aerodynamic force models, and it has not been yet defined theoretically in literature has been found in this research in terms of its relative position within the considered bundle geometry and for different angles of attack based on the wind tunnel results.

In summary, the use of minimalistic monitoring systems for OMA has been found to be successful to reveal the main characteristics of the wind-induced dynamic behaviour of two types of slender structures, tall buildings and electricity transmission lines, in a wide range of wind conditions. Whilst the presented results are contextual and specific to these structures or structural configurations, it is concluded the ability of simple monitoring systems supported by basic finite element models and complementary analytical studies to establish the vibration characteristics, to elucidate their root causes and to interpret their variation. Also, it has demonstrated that this approach can be adopted as a tool in the through-life analysis and monitoring of the structural condition and health to assess the performance criterion for serviceability.

6.3. FUTURE OUTLOOK

Based on the findings of this research, the three main potential areas for further study are the theoretical analyses for comparison with the full-scale site response, deeper analysis of the available full-scale measurements and further site monitoring.

Given the short length of the measurements on Tower 2 and the gaps in time records of Tower 1 due to technical problems, the research in tall buildings could be benefited from a more extensive data recording programme, so higher wind speeds would be measured in a wider

range of wind directions. Moreover, large amplitude response requires very long-term monitoring to capture extreme wind loading. In addition, given the uncertainties on estimating damping accurately, very long continuous records would enhance further estimates of damping.

In the full-scale study on transmission lines presented in Chapter 5, only a few selected galloping events have been shown. Hence, it is recommended further site monitoring be directed towards specific aspects of galloping behaviour not adequately covered. Future work might further benefit from a more detailed assessment of all the galloping events emphasising the trends in the periods of time where galloping is clearly observed. The measured responses could also be compared more thoroughly with the results from the full aeroelastic wind tunnel model tests described in Chapter 4.

It could be complemented by a model able to match precisely the structural response. The full-scale measurements in this study provided a potential source to assess the variability measured in those circumstances using a refined experimental analysis involving model calibration. A combination of results from galloping or high excitation and small vibrations could be combined to identify the parameters that governs the complex dynamic behaviour of the system. This could be supported by proper modal damping identification, with the objective to provide a stability analysis in relation with measured data on the wind tunnel tests. Additionally, more detailed consideration could be given to the comparison of estimated analytical parameters (e.g. natural frequencies, critical wind speed, mass of the bundle) with the equivalent measured responses for validation of analytical techniques.

Also, it would be desirable to include in the model all the potential effects that influence the structural response, such as the amount and distribution of ice accretion, the rotation of the bundle due to the wind action on the ice accretion, the temperature and its effect on the thermal expansion of the subconductors as well as the effect of the vertical component of the wind load. In addition, since the occurrence of galloping has been identified for wind speed lower than the critical, it seems that existing formulas are not sufficient to predict the galloping wind speed, so new formulas should be developed to consider the specific features of the studied system.

REFERENCES

Anderson, T. W., Darling, D. A. (1952), "Asymptotic theory of certain "goodness-of-fit" criteria based on stochastic processes". *Annals of MathematicaL Statistics*, **23**(2), 193-212. https://doi.org/10.1214/aoms/1177729437

Arakawa, T. and Yamamoto, K. (2004), "Frequencies and damping ratios of a high-rise building based on microtremor measurement". *13th World Conf. on Earthquake Engineering*, Vancouver, Canada. https://www.iitk.ac.in/nicee/wcee/article/13_48.pdf

Au, S.K., Zhang, F.L. and To, P. (2012), "Field observations on modal properties of two tall buildings under strong wind". *J. Wind Eng. Ind. Aerodyn.*, **101**, 12–23. https://doi.org/10.1016/j.jweia.2011.12.002

Bashor, R., Kijewski-Correa, T. and Kareem, A. (2005), "On the wind-induced response of tall buildings: the effect of uncertainties in dynamic properties and human comfort thresholds". *Engineering Structures, Proceedings of the 10th Americas Conf. on Wind Engineering*, 1362-1371, Baton Rouge, LA, USA.

Bashor, R., Bobby, S., Kijewski-Correa, T. and Kareem, A. (2012), "Full-scale performance evaluation of tall buildings under wind". *J. Wind Eng. Ind. Aerodyn.*, **104**, 88-97. https://doi.org/10.1016/j.jweia.2012.04.007

Belytschko, T. and Hasieh, B. J. (1973), "Non-linear transient finite element analysis with convected co-ordinates". *Int. J. Numer. Meth. Engin.* **7**(3), 255-271 (1973). https://doi.org/10.1002/nme.1620070304

Bendat, J. and Piersol, A. (2010), *Random Data; Analysis and Measurement Procedures* (Fourth Edition). John Wiley & Sons.

Bernal, D., Dohler, M., Kojidi, K., Kwan, K. and Liu, Y. (2015), "First mode damping ratios for buildings". *J. Earthquake Spectra*, **31**(1), 367-381. https://doi.org/10.1193/101812EQS311M

Bhattacharyya, B. and Dalui, S. K. (2020), "Experimental and numerical study of wind-pressure distribution on irregular-plan-shaped building". *J. Struct. Eng.*, **146**(7), 04020137. https://doi.org/10.1061/(ASCE)ST.1943-541X.0002686

Bishop, R. E. D. and Gladwell, G. M. L. (1963), "An investigation into the theory of resonance testing". *Philosophical Trans. Royal Society of London*, Series A, **255**, 241-280. https://doi.org/10.1098/rsta.1963.0004

Bisplinghoff, R. L. and Ashley, H. (1962), *Principles of Aeroelasticity*. New York, Wiley.

Blevins, R. D. and Iwan, W. D. (1974), "A Model for Vortex Induced Oscillation of Structures". *J. Appl. Mech.*, **41**(3), 581-586. https://doi.org/10.1115/1.3423352

Blevins, R. D. (1990), *Flow Induced Vibration* (Second Edition). Van Nostrand Reinhold, New York.

Blevins, R. D. (1994), *Flow-induced Vibration* (Third Edition). Van Nostrand Reinhold, New York.

BMT Fluid Mechanics (2008), *Newington tall building, London, UK: Wind tunnel testing cladding pressure studies*. Project No. 43837rep2v2.

BMT Fluid Mechanics (2008), *Newington tall building, London, UK: Wind tunnel testing overall engineering structures*. Project No. 43837rep3v2.

BMT Fluid Mechanics (2014), *Newington Butts, London, UK: Wind tunnel testing, wind environment study*. Project No. 431668rep1v4.

Boggs, D.W. (1992), "Validation of the aerodynamic model method". *J. Wind Eng. Ind. Aerodyn.*, **42**, 1011-1022. https://doi.org/10.1016/0167-6105(92)90107-1

Boroschek, R. L. and Bilbao, J. A. (2018), Interpretation of stabilization diagrams using density-based clustering algorithm". *Engineering Structures*, **178**, 245-257. https://doi.org/10.1016/j.engstruct.2018.09.091

Brincker, R., Zhang, L. and Andersen, P. (2000), "Modal identification from ambient responses using Frequency Domain Decomposition". *Proc. 18th Int. Modal Analysis Conf. 1*, San Antonio, Texas, 625-630.

Brincker, R. and Ventura C. E. (2015), *Introduction to Operational Modal Analysis*. John Wiley & Sons, Ltd, Chichester, UK.

Brownjohn, J. M. W. (1988), "Assessment of structural integrity by dynamic measurements". PhD Thesis, Department of Civil Engineering, University of Bristol, UK.

Brownjohn, J. M. W., Pan, T. C. and Deng, X. Y. (2000), "Correlating dynamic characteristics from field measurements and numerical analysis of a high-rise building". *Earthquake Engineering & Structural Dynamics*, **29**(4), 523-543. https://doi.org/10.1002/(SICI)1096-9845(200004)29:4%3C523::AID-EQE920%3E3.0.CO;2-L

BSI (1997), *BS 6399-2:1997 Loading for buildings – Part 2: Code of practice for wind loads*. British Standards Institution, London, UK.

Campbell, R. B. and Vandiver, J. K. (1982), "The determination of modal damping ratios from maximum entropy spectral estimates". *J. Dynamic Systems, Measurement and Control, ASME*, **104**, 78-85. https://doi.org/10.1115/1.3149635

Cauberghe, B. (2004), *Applied frequency-domain system identification in the field of experimental and operational modal analysis*. PhD Thesis, Vrije Universiteit Brussel. Applied frequency-domain … Vrije Universiteit Brussel (vub.be)

Cengel, Y., Cimbala, J. and Turner, R. (2008), *Fundamentals of Thermal-Fluid Sciences (SI units)* (Third Edition). McGraw-Hill, Europe, Middle East & Africa.

Chabart, O. and Lilien, J. L. (1998), "Galloping of electrical lines in wind tunnel facilities". *Journal of Wind Engineering and Industrial Aerodynamics*, **74-76**, 967-976. https://doi.org/10.1016/S0167-6105(98)00088-9

Charisi, S., Thiis, T. and Aurlien, T. (2019), "Full-scale measurements of wind-pressure coefficients in twin medium-rise buildings". *Buildings*, **9**(3), 63–63. https://doi.org/10.3390/buildings9030063

Chen, X. and Wu, Y. (2021), "Explicit close-form solutions of the initiation conditions for 3DOF galloping or flutter". *Journal of Wind Engineering and Industrial Aerodynamics*, **219**, 104787. https://doi.org/10.1016/j.jweia.2021.104787

CIGRE (2001), "Guidelines for field measurement of ice loadings on overhead power line conductors". CIGRE Technical Brochure 179. TF 22.06.01.

CIGRE (2006), "Guidelines for meteorological icing models, statistical methods and topographical effects". CIGRE Technical Brochure 291. WG B2.16.

CIGRE (2007), "State of the art of conductor galloping". CIGRE Technical Brochure 322. TF B2.11.06.

Cole, H. A. (1968), "On-the-line analysis of random vibrations". *Proceedings of the 9th Structural Dynamics snd Materials Conference*, American Institute of Aeronautics and Astronautics, No. 68-288. https://doi.org/10.2514/6.1968-288

Council on Tall Buildings and Urban Habitat (CTBUH) (2017), *Tall Buildings in Numbers: 2017 Year in Review*. CTBUH.

Davenport, A. G. (1961), "The treatment of wind loads on tall towers and long span bridges in turbulent wind". PhD Thesis, Department of Civil Engineering, University of Bristol, UK.

Davenport, A. G. (1962), "Buffeting of a suspension bridge by storm winds". *J. Structural Division*, ASCE 88 (ST3), 233-264. https://ascelibrary.org/doi/10.1061/JSDEAG.0000773

Davenport, A. G. (1962), "The response of slender, line-like structures to a gusty wind". *Proceedings of the Institution of Civil Engineers*, **23**(3), 389-408. https://doi.org/10.1680/iicep.1962.10876

Davenport, A. G. (1965), "The Relationship of Wind Structure to Wind Loading". *National Physical Laboratory, Symposium No. 16, Wind Effects on Buildings and Structures*, pp. 54-102. Her Majesty's Stationery Office, London.

Davenport, A. G. (1967), "The treatment of wind loading on tall buildings". *Tall Buildings*, pp. 3-45. Pergamon. https://doi.org/10.1016/B978-0-08-011692-1.50006-7

Davenport, A., (1977), "The prediction of the response of structures to gusty wind". *Safety of structures under dynamic loading*, **1**, 257-284.

Davenport, A. G. and Hill-Carroll, P. (1986), "Damping in tall buildings: its variability and treatment in design". *Building Motion in Wind ASCE*, Seattle, USA.

Demartino, C., Koss, H. H., Georgakis, C. T. and Ricciardelli, R. (2015), "Effects of ice accretion on the aerodynamics of bridge cables". *Journal of Wind Engineering and Industrial Aerodynamics*, **138**, 98-119. https://doi.org/10.1016/j.jweia.2014.12.010

Den Hartog, J. (1932), "Transmission line vibration due to sleet". *Transactions of the American Institute of Electrical Engineers*, **4**, 1074-1076. https://doi.org/10.1109/t-aiee.1932.5056223

Desai, Y. M., Yu, P., Shah, A. H. and Popplewell, N. (1996), "Perturbation-based finite element analysis of transmission line galloping". *J. Sound and Vibration*, **191**, 469-489. https://doi.org/10.1006/jsvi.1996.0135

De Souza, R. M. (2000), "Force-based finite element for large displacements inelastic analysis of frames". PhD Thesis, Department of Civil and Environmental Engineering, UC Berkeley. De Souza PhD Thesis (sadra.ac.ir)

Dos Santos, F. L. M., Peeters, B., Lau, J., Desmet, W. and Góes, L. C. S. (2014), "An overview of experimental strain-based modal analysis methods". *Proceedings of ISMA 2014 including USD2014*, 2453-24-67. An overview of experimental strain-based modal analysis methods (isma-isaac.be)

Duthinh, D. and Simiu, E. (2011), "The use of wind tunnel measurements in building design". *Wind Tunnels and Experimental Fluid Dynamics Research*, 282-300. https://doi.org/10.5772/18670

Dyke and Laneville (2008), "Galloping of a single conductor covered with a D-section on a high-voltage overhead test line". *Journal of Wind Engineering and Industrial Aerodynamics*, **96**(6-7), 1141-1151. https://doi.org/10.1016/j.jweia.2007.06.036

Edwards, A. T. and A. Madeyski, A. (1956), "Progress Report on the Investigation of Galloping of Transmission Line Conductors". *Transactions of the AIEE Trans, PAS.*, Vol. 75(3), 666-686. https://doi.org/10.1109/AIEEPAS.1956.4499353

Ellis, B. R. (1980), "An assessment of the accuracy of predicting the fundamental natural frequencies of buildings and the implications concerning the dynamic analysis of structures". *Proceedings of the Institution of Civil Engineers*, **69**(3), 763-776. https://doi.org/10.1680/iicep.1980.2376

El-Kafafy, M., Devriendt, C., Weijtjens, W. and De Sitter, G. (2014), "Evaluating Different Automated Operational Modal Analysis Techniques for the Continuous Monitoring of Offshore Wind Turbines", *Dynamics of Civil Structure, Vol. 4. Conference Proceedings of the Society for Experimental Mechanics Series*, 313-329, Springer. https://doi.org/10.1007/978-3-319-04546-7_35

Emes, M.J., Arjomandi, M., Kelso, R.M. and Ghanadi, F. (2016), "Integral length scales in a low-roughness atmospheric boundary layer". *18th Australasian Wind Engineering Society Workshop*, 1-4, McLaren Vale, Australia. https://hdl.handle.net/2440/109454

EPRI (Electric Power Research Institute) (2009), *Transmission line reference book: Wind-induced conductor motion*. Palo Alto. https://hdl.handle.net/2268/102166

ESDU (1983), "Strong winds in the atmospheric boundary layer, Part 2: Discrete gust speeds". Item No. 83045. Engineering Sciences Data Unit, London, UK.

ESDU (1984), “Longitudinal turbulence intensities over terrain with roughness changes”. Item No. 84030. Engineering Sciences Data Unit, London, UK.

ESDU (1985), “Characteristics of atmospheric turbulence near the ground. Part II: single point data for strong winds (neutral atmosphere)”. Item No. 85020. Engineering Sciences Data Unit, London, UK.

ESDU (2006), “Strong winds in the atmospheric boundary layer, Part I: Mean-Hourly Wind Speeds”. Item No. 82026. Engineering Sciences Data Unit, London, UK.

Eurocode 1 (2002), *Actions on Structures-Part 1-1, EN-1991-1-1: General Actions - Densities, Self-Weight, Imposed Loads for Buildings*. The European Union Per Regulation 305/2011, Directive 98/34/EC, Directive 2004/18/EC. EN 1991-1-1: Eurocode 1: Actions on structures - Part 1-1: General actions - Densities, self-weight, imposed loads for buildings (phd.eng.br)

Eurocode 2 (2004), *Design of Concrete Structures EN1992-1-1: General rules and rules for buildings*. The European Union Per Regulation 305/2011, Directive 98/34/EC, Directive 2004/18/EC. EN 1992-1-1: Eurocode 2: Design of concrete structures - Part 1-1: General rules and rules for buildings (phd.eng.br)

fib-International Federation for Structural Concrete (fib) (2012), *Bulletin 55: Model Code 2010, Final draft, Volume 1*. fib Bulletins: Model Code 2010-Final draft, Volume 1 (fib-international.org)

Flay, R. G. J. and Stevenson, D. C. (1988), “Integral length scales in strong winds below 20 m”. *J. Wind Eng. Ind. Aerodyn.*, **28**(1-3), 21-30. https://doi.org/10.1016/0167-6105(88)90098-0

Foti, F. and Martinelli, L. (2018), “Finite element modeling of cable galloping vibrations. Part II: Application to an iced cable in 1:2 multiple internal resonance”. *Journal of Vibration and Control*, **24**(7), 1322-1340. https://doi.org/10.1177/1077546316660017

Frandsen, J. B. (2001), “Simultaneous pressures and accelerations measured full-scale on the Great Belt East suspension bridge”. *J. Wind Eng. Ind. Aerodyn.*, **89**(1), 95-129. https://doi.org/10.1016/S0167-6105(00)00059-3

Fritz, W. P., Jones, N.P. and Igusa, T. (2009), “Predictive models for the median and variability of building period and damping”. *J. Struct. Eng.*, **135**(5), 576-586. https://doi.org/10.1061/(asce)0733-9445(2009)135:5(576)

Fu, J. Y., Wu, J. R., Xu, A., Li, Q. S. and Xiao, Y. Q. (2012), “Full-scale measurements of wind effects on Guangzhou West Tower”. *Eng. Struct.*, **35**, 120-139. https://doi.org/10.1016/j.engstruct.2011.10.022

Gabbai, R. D. and Simiu, E. (2010), “Aerodynamic damping in the along-wind response of tall buildings”. *J. Struct. Eng*, **136**(1), 117-119. https://doi.org/10.1061/(asce)0733-9445(2010)136:1(117)

Gao, M., Chen, Z., Su, J., Su, N. Liu, C., Zhang, J. and Chen. H- (2023), “Experimental study

on the galloping characteristics of single ice-coated transmission lines under oblique flows". *Scientific Reports*, 13, 5172. https://doi.org/10.1038/s41598-023-32393-y

Gasparis, G. (2019) "A Benchmark Study on Operational Modal Analysis System Identification Algorithms for Operating Offshore Wind Turbines". Master of Science Thesis, Technische Universitet Delft.

2019_03_25_Gasparis_G._A_benchmark_study_on_operational_modal_analysis_system_identification_algorithms_Report.pdf

Gersch, W., Nielsen, N. N. and Akaike, H. (1973), "Maximum likelihood estimation of structural parameters from random vibration data". *J. Sound and Vibration*, **31**(3), 295-308. https://doi.org/10.1016/S0022-460X(73)80274-3

Gjelstrup, H. and Georgakis, C. T. (2011), "A quasi-steady 3 degree-of-freedom model for the determination of the onset of bluff body galloping instability". *J. Fluids and Structures*. **27**(7), 1021-1034. https://doi.org/10.1016/j.jfluidstructs.2011.04.006

Gill Instruments (2017), *WindMaster and WindMaster Pro User Manual, 1561-PS-0001*, Issue 11, February 2017. Available from: http://www.gillinstruments.com/data/manuals/1561-PS-0001%20WindMaster%20Windmaster%20Pro%20Manual%20Issue%2011.pdf?iss=1 1.20170306

Gomez, S. S. and Metrikine, A. V. (2019), "The energy flow analysis as tool for identification of damping in tall buildings subjected to wind: contributions of the foundation and the building structure". *J. Vibrations and Acoustics*, **141**(1), 011013. https://doi.org/10.1115/1.4040975

Gonzalez-Fernandez, D., Macdonald, J. H. G., Titurus, B., Margnelli, A., Greco, L., Gkoktsi, K., Leeks, M., Janssen, J. and Zanchetta, M. (2019), "Full-scale identification of aeroelastic effects on a tall building". *15th International Conf. on Wind Engineering*, 521-522, Beijing, China.

Gonzalez-Fernandez, D., Macdonald, J. H. G., Titurus, B. and Margnelli, A. (2020), "Long-term monitoring of wind-induced vibrations of two tall buildings in London". *10th International Conference on Structural Health Monitoring of Intelligent Infrastructure*, 1607-1614, Porto, Portugal.

Guillaume, P., Pintelon, R. and Schoukens, J. (1996), "Parametric identification of multivariable systems in the frequency domain – a survey". *Proceedings of ISMA 21, the International Conference on Noise and Vibration Engineering*, 1069–1082, Leuven, Belgium.

Guillaume, P., Verboven, S., Vanlanduit, H., Van der Auweraer, H. and Peeter, B. (2003), "A poly-reference implementation of the least-squares complex frequency-domain estimator". *Proc. of IMAC21, The International Modal Analysis Conf.*, Kissimmee (FL), USA. (69) A Poly-Reference Implementation of the Least-Squares Complex Frequency-Domain

Estimator | Peter Verboven - Academia.edu

Guillaume, P. (2006), "Multivariable frequency-domain system identification algorithms for modal analysis". *IFAC Symposium Modelling, Identification and Signal Processing (SYSID 2006)*. Multivariable frequency-domain system identification algorithms for modal analysis. Vrije Universiteit Brussel (vub.be)

Gurung, C. B., Yamaguchi, H. and Yukino, T. (2003), "Identification and characterization of galloping of Tsuruga test line based on multi-channel modal analysis of field data". J. Wind Engineering and Industrial Aerodynamics, **91**(7), 903-924. https://doi.org/10.1016/S0167-6105(03)00018-7

Han, P., and De Langre, E. (2022), "There is no critical mass ratio for galloping of a square cylinder under flow". *Journal of Fluid Mechanics*, **931**, A27. https://doi.org/10.1017/jfm.2021.975

Havard, D. G. (1979a), "Detuning Pendulums for Controlling Galloping of Bundle Conductor Transmission Lines". *IEEE Conference Paper*, A 79 501-8, Summer Meeting, Vancouver.

Havard, D.G. (1979b), "Galloping Control by Detuning". EPRI Research Program RP-1095. Progress Report No. 2. Ontario Hydro Research Division Report No. 79-619-K.

Havard, D. G. (1996), "Fifteen years field trials of galloping controls for overhead power Lines". *IWAIS'95, 7th International Workshop on Atmospheric Icing of Structures*, Chicoutimi, Quebec, Canada? "Fifteen Years Field Trials of Galloping Controls for Overhead Power Lines". Research Gate

Havard, D. G. (2003), "Dynamic Loads on Transmission Line Structures During Galloping – Field Data and Elastic Analysis". *Fifth International Symposium on Cable Dynamics*, Santa Margherita, Italy. "Dynamic Loads On Transmission Line Structures During Galloping" Havard (researchgate.net)

Haviland, R. (1976), "A study of the uncertainties in the fundamental translational period and damping values for real buildings". Research Report No. 56, Pub. No. R76-12, Depart. of Civil Eng., MIT, Cambridge, MA, USA.

He, M., and Macdonald, J. H. (2016), "An analytical solution for the galloping stability of a 3 degree-of-freedom system based on quasi-steady theory". *J. Fluids and Structures*, **60**, 23-36. https://doi.org/10.1016/j.jfluidstructs.2015.10.004

He, M., and Macdonald, J. H. (2017), "Aeroelastic stability of a 3DOF system based on quasi-steady theory with reference to inertial coupling". *Journal of Wind Engineering and Industrial Aerodynamics*, **171**, 319-329. https://doi.org/10.1016/j.jweia.2017.10.013

Holmes, J. D. (1996), "Along-wind response of lattice towers: Part II – aerodynamic damping and deflections". *Eng. Struct.*, **18**(2), 483-488. https://doi.org/10.1016/0141-0296(95)00131-x

Holmes, J. D. (2001), *Wind Loading of Structures*. Spon Press, London, UK.

Horiguchi, M. and Mitsuta, Y. (1994), "Wind observation over the mountainous region by

Doppler sodar". *Annuals Disas. Prev. Res. Inst, Kyoto Univ.*, **37**, 23-34. a37b1p03.pdf (kyoto-u.ac.jp)

Huang, Y., Quan, Y. and Gu, M. (2013), "Experimental study of aerodynamic damping of typical tall buildings". *Mathematical Problems in Engineering*, **136**(3-4), 1-9. https://doi.org/10.1155/2013/731572

Huang, X. B., Zhao, L. and Chen G. M. (2016) "Design of a Wireless Sensor Module for Monitoring Conductor Galloping of Transmission Lines. *Sensors*, **16**(10), 1657. https://doi.org/10.3390/s16101657

Huilan, C., Yong, Q., Ming, G. and Di, W. (2012), "Along-wind aerodynamic damping on high-rise buildings". *The 7th International Colloquium on Bluff Body Aerodynamics and Applications (BBAA7)*, 813-824.

Hunt, J. C. R and Richard, D. J. W. (1969), "Overhead Line Oscillations and the Effect of Aerodynamic Dampers". *Proceedings of the IEE IEEE Trans on PAS.*, **116**(11), 1869-1874. https://doi.org/10.1049/piee.1969.0344

IEC (2005) *International Standard IEC 61400-1, "Wind turbines, Part 1: Design requirements"*. Third edition. International Electrotechnical Comission. Wind turbines - Part 1: Design requirements (saiglobal.com)

ISO 8601 (1988) (E). "Data elements and interchange formats - Information interchange - Representation of dates and times". ISO - ISO 8601:1988 - Data elements and interchange formats

Jayatunga, H. G. K. G., Tan, B. T. and Leontini, J. S. (2015), "A study on the energy transfer of a square prism under fluid-elastic galloping". *Journal of Fluids and Structures*, **55**, 384–397. https://doi.org/10.1016/j.jfluidstructs.2015.03.012

Jancauskas, E. D. and Melbourne, W. H. (1986), "The aerodynamic admittance of two-dimensional rectangular section cylinders in smooth flow". *J. Wind Eng. Ind. Aerodyn.*, **23**, 395-408. https://doi.org/10.1016/0167-6105(86)90057-7

Japanese Industrial Standards Committee (1994), *JIS C 3110:1994, Aluminium Conductors Steel Reinforced*. JIS C 3110:1994 Aluminium Conductors Steel Reinforced (saiglobal.com)

Jeary, A. P. (1986), "Damping in tall buildings, a mechanism and a predictor". *Earthquake Eng. Struct. Dyn.*, **14**, 733-750. https://doi.org/10.1002/eqe.4290140505

Jiang, X., Li, B., Mao, X., Peng, Y. And He, S. (2019), "New Approach based on operational strain modal analysis to identify dynamical properties of the high-speed reciprocating operation mechanism". *Journal of Low Frequency, Noise, Vibration and Active Control*, **38** (3-4), 1345-1362. https://doi.org/10.1177/1461348418821203

Joly, A., Etienne, S. and Pelletier, D. (2012), "Galloping of square cylinders in cross-flow at low Reynolds numbers". *Journal of Fluids and Structures*, **28**, 232–243. https://doi.org/10.1016/j.jfluidstructs.2011.12.004

Jones, N. P., Shi, T., Ellis, J. H. and Scanlan, R. H. (1995), "System-identification procedure for system and input parameters in ambient vibration surveys". *Journal of Wind Engineering & Industrial Aerodynamics*, **54**, 91-99. https://doi.org/10.1016/0167-6105(94)00033-a

Kareem, A. (1978), "Wind excited motion of buildings". PhD Thesis, Colorado State University at Fort Collins, Colorado, USA.

Kareem, A. (1982), "Acrosswind response of buildings". *J. Structural Division*, ASCE, **108**(4), 869-887. https://doi.org/10.1061/jsdeag.0005930

Kareem, A. and Gurley, K. (1996), "Damping in structures: its evaluation and treatment of uncertianity". *J. Wind Engineering and Industrial Aerodynamics*, **59**(2-3), 131-157. https://doi.org/10.1016/0167-6105(96)00004-9

Keil, S. (2017). *Technology and Practical Use of Strain Gages With Particular Consideration of Stress Analysis Using Strain Gages*. John Wiley & Sons, Ltd. Technology and Practical Use of Strain Gages | Wiley Online Books

Keutgen, R. (1999), "Galloping Phenomena. A Finite Element Approach". PhD Thesis, Collection des Publications de la Faculté des Sciences Appliquées de l'Université de Liège, No. 191, Belgium.

Kimura, K., Inoue, M., Fujino, Y., Yukino, T., Inoue, H., Morishima, H. (1999), "Unsteady forces on an ice-accreted four-conductor bundle transmission line". *Proceedings 10th Int. Conf. Wind Eng.*, Balkema, Rotterdam, 467-472.

Kijewski, T. and Kareem A. (1999), "Analysis of full-scale data from a tall building in Boston: damping estimates" 10th *Int. Conf. on Wind Eng*., International Association for Wind Engineering (IAWE), Copenhagen, Denmark. 10iwce.PDF (nd.edu)

Kijewski-Correa, T. and Pirnia, J. D. (2007), "Dynamic behavior of tall buildings under wind: Insights from full-scale monitoring". *Struct. Des. Tall Special Build*., **16**(4), 471–486. https://doi.org/10.1002/tal.415

Kim, W., Yoshida, A., Tamura, Y. and Yi, J. (2018), "Experimental study of aerodynamic damping of a twisted supertall building". *Journal of Wind Engineering & Industrial Aerodynamics*, **176**, 1-12. https://doi.org/10.1016/j.jweia.2018.03.005

Kimura, K., Inoue, M., Fujino, Y., Yukino, T., Inoue, H. and Morishima, H. (1999), "Unsteady forces on an ice-accreted four-conductor bundle transmission line". *Proc. 10th Int. Conf. Wind Eng.* Balkema, Rotterdam, 467-472.

Koutselos, L. T. and Tunstall, M. J. (1988), "Further Studies of the Galloping Instability of Natural Ice Accretions on Overhead Line Conductors". Paper A9.1, *Fourth Int. Conf. on Atmospheric Icing of Structures*. Paris, France.

Krajewski, P., Flaga, L. and Flaga, A. (2018), "Aerodynamic calculations of the Sienna towers buildings complex with respect to human vibrations comfort of their users". *AIP Conf. Proceedings*, **1922**(1), 10005. https://doi.org/10.1063/1.5019108

Kubo, Y., Nogami, C., Yamaguchi, E., Kato, K., Niihara, Y. and Hayashida, K. (1999), "Study on Reynolds number effect of a cable-stayed bridge girder". *10th International Conference on Wind Engineering*, 935-940, Copenhagen, Denmark.

Kuznetsov, S. and Pospisil, S. (2019), "Full-scale measurements of local wind loads on a high-rise building using wind tunnel based predictions" *IOP Conference Series: Materials Science and Engineering*, **471**(5), 052053. https://doi.org/10.1088/1757-899X/471/5/052053

Kwiatkowski, D., Phillips, P. C. B., Schmidt, P. and Shin, Y. (1992), "Testing the Null Hypothesis of Stationarity against the Alternative of a Unit Root". *Journal of Econometrics*, **54**(1-3), pp. 159–178. https://doi.org/10.1016/0304-4076(92)90104-Y

Kwok, K. C. S. (2019), "Adverse effects of wind-induced building motion on occupants". *17th International Advanced School on Wind and Structural Engineering*, 213-236, Genova, Italy.

Kwok, K. C. S. and Melbourne, W. H. (1981), "Wind-induced lock-in excitation of tall structures". *J. Struct. Div.*, ASCE 107(ST1), 57-52.

Lagomarsino, S. (1993), "Forecast models for damping and vibration periods of buildings". *J. Wind Eng. Ind. Aerodyn.*, **48**, 221-239. https://doi.org/10.1016/0167-6105(93)90138-E

Li, H. N., Yi, T. H., Yi, X. D. and Wang, G. X. (2007), "Measurement and Analysis of Wind-Induced Response of Tall Building Based on GPS Technology". *J. Advances in Structural Engineering*, **10**(1), 83-93. https://doi.org/10.1260/136943307780150869

Li, Q. S., Yang, K., Zhang, N., Wong, C. K. and Jeary, A. P. (2002), "Field measurements of amplitude-dependent damping in a 79-storey tall building and its effects on the structural dynamic responses". *Struct. Des. Tall Spec. Build.*, **11**(2), 129-153. https://doi.org/10.1002/tal.195

Li, Q.S., Wu, J. R., Liang, S. G., Xiao, Y. Q. and Wong, C. K. (2004), "Full-scale measurements and numerical evaluation of wind induced vibration of a 63-story reinforced concrete tall building". *Eng. Struct.*, **26**(12), 1779–1794. https://doi.org/10.1016/j.engstruct.2004.06.014

Li, Q.S., Xiao, Y. Q. and Wong, C. K. (2005), "Full-scale monitoring of typhoon effects on super tall buildings". *J. Fluids Struct.*, **20**(5), 697–717. https://doi.org/10.1016/j.jfluidstructs.2005.04.003

Li, X. and Li, Q. S. (2018), "Monitoring structural performance of a supertall building during 14 tropical cyclones". *J. Struct. Eng.*, **144**(10), 1-15. https://doi.org/10.1061/(ASCE)ST.1943-541X.0002145

Li, X. and Li, Q. S. (2019), "Damping prediction model for super-tall buildings based on field measurements during tropical cyclone events". *15th International Conf. on Wind Engineering*, 129-130, Beijing, China.

Liepmann, H. W. (1952), "On the application of statistical concepts to the buffeting problem".

J. Aeronaut. Sci., **19**, 793-800. https://doi.org/10.2514/8.2491

Lilien, J. L. and Ponthot, J. P. (1988), "Overhead Lines Galloping-Modelisation". *Conference IMACS. Modelling and Simulation of Electrical Machines and Power Systems*. Elsevier Science Publishers, North-Holland, Imacs, 103-110.

Lilien, J. L. and Dubois, H. (1988), "Overhead Line Vertical Galloping on Bundle Configurations: Stability Criterions and Amplitude Prediction". *IEE Overhead Line Design and Construction: Theory and Practice (up to 150 kV) Proceedings*, 65-69.

Lilien, J. L., Dubois, H. and Dal Maso, F. (1989), "General Mathematical Formulation for Overhead Line Galloping". *AIM study day on galloping*. March 10.

Lilien, J. L. and Chabart, O. (1995), "High Voltage Overhead Lines-Three Mechanisms to Avoid Bundle Galloping". *International Conference on Cable Dynamics*. Liège, Belgium. October 19-21. Report 47.

Long, F. (2004), "Uncertainties in pressure coefficients derived from full and model scale data". PhD Thesis, Texas Tech University, USA.

Macdonald, J. H. G. (2000), "Identification of the dynamic behaviour of a cable-stayed bridge from full-scale testing during and after construction". PhD Thesis, Department of Civil Engineering, University of Bristol, UK.

Macdonald, J. H. G., Irwin, P. A. and Fletcher, M. S. (2002), "Vortex-induced vibrations of the Second Severn Crossing cable-stayed bridge – full-scale and wind tunnel measurements". *Proceedings of the Institutions of Civil Engineers-Structures and Buildings*, **152**(2), 123-134. https://doi.org/10.1680/stbu.2002.152.2.123

Macdonald, J. H. G. (2008), "Pedestrian-induced vibrations of the Clifton Suspension Bridge, UK". *Proceedings ICE: Bridge Engineering*, **161**(2), 69-77. https://doi.org/10.1680/bren.2008.161.2.69

Macdonald, J. H. G. and Daniell, W. E. (2005), "Variation of model parameters of a cable-stayed bridge identified from ambient vibration measurements and FE modeling". *Eng. Struct*., **27**(13), 1916-1930. https://doi.org/10.1016/j.engstruct.2005.06.007

Maia, N. M. M. and Silva, J. M. M. (1997), *Theoretical and experimental modal analysis*. John Wiley & Sons.

Margnelli, A., Greco, L., Gkoktsi, K., Leeks, M., Janssen, J., Macdonald, J. and Zanchetta, M. (2018), "Wind-induced response of tall buildings: case study of a slender tall building in London". *13th UK Conf. on Wind Engineering*, Leeds, UK.

Marple, S.L. (1987), *Digital Spectral Analysis*. Prentice Hall, New Jersey, USA.

Matlab (2022), *MATLAB version: 9.13.0 (R2022b)*, Natick, Massachusetts: The MathWorks Inc.

Matsumiya, H., Nishihara, T. and Shimizu, M. (2011) “Aerodynamic characteristics of ice and snow accreted conductors of overhead transmission lines”. *Proc. 13th Int. Conf. Wind Eng.*, Amsterdam, Netherlands.

Matsumiya, H., Nishihara, T., Shimizu, M. and Yukino, T. (2012), “Observation of galloping of four-bundled conductors on ice-accreted overhead transmission lines”. *Proc. 2012 World Congress on Advances in Civil, Environmental, and Materials Research (ACEM’ 12)*, Seoul, Korea, 1238-1247. http://dx.doi.org/10.5359/jawe.37.27 1189-1290.ACEM’12 PDF (i-asem.org)

Matsumiya, H., Sakaguchi, G., Nishihara, T. and Yukino, T. (2013) “Time-history analysis of galloping of overhead transmission lines based on mode superposition method”. *J. Struct. Eng.*, **59A**, 574-584 (in Japanese).

Matsumiya, H. and Nishihara, T. (2013), “Study on aerodynamic force model of large-amplitude galloping of four-bundled conductors”. *Journal of Wind Engineering*, **38**(4), 87-100. http://dx.doi.org/10.5359/jwe.38.87

Matsumiya, H., Yukino, T., Ichikawa, H., Shimizu, M. and Nishihara, T. (2017), “Field Observation of Galloping Phenomenon of Four-Bundled Conductors under Ice Accretion at Tsuruga Test Lines, Part2 - Galloping Suppression Effect of Diagonally-Arranged Loose Spacers”. CRIEPI Research Report N16006.

Matsumiya, H. Nishihara, T., Yagi, T. (2018), “Aerodynamic modeling for large-amplitude galloping of four-bundled conductors”. *Journal of Fluids and Structures*, 82, 559-576. https://doi.org/10.1016/j.jfluidstructs.2018.08.003

Matsumiya, H., Yagi, T., Macdonald, J. H. G. (2021), “Effects of aerodynamic coupling and non-linear behaviour on galloping of ice-accreted conductors”. *Journal of Fluids and Structures*, **106**, 103366. https://doi.org/10.1016/j.jfluidstructs.2021.103366

Matsumiya, H., Yukino, T., Shimizu, M. and Nishihara, T. (2022a), “Field observation of galloping on four-bundled conductors and verification of countermeasure effect of loose spacers”. *Journal of Wind Engineering and Industrial Aerodynamics*, **220**. https://doi.org/10.1016/j.jweia.2021.104859

Matsumiya, H., Yagi, T, and Macdonald, J. H. G. (2022b), “Unsteady aerodynamic force modelling for 3-DoF-galloping of four-bundled conductors”. *Journal of Fluids and Structures*, **112**, 103581 https://doi.org/10.1016/j.jfluidstructs.2022.103581

Matsumiya, H., Taruishi, S., Shimizu, M., Sakaguchi, G. and Macdonald, J. H. G. (2022c), “Equivalent Static Wind Loads on Snow-accreted Overhead Wires”. *Structural Engineering International*, **32**(1), 78-91. https://doi.org/10.1080/10168664.2021.1967255

McIntosh, A. I. (2016). *The Jackknife Estimation Method*. Prentice Hall. Available from: 1606.00497.pdf (arxiv.org)

Melbourne, W.H. (1982), “Comparison of model and full-scale tests of a bridge and chimney stack”. *Int. Workshop on Wind Tunnel Modelling*, 637-653, Maryland, USA.

Met Office (2019), Met Office MIDAS Open: UK Land Surface Stations Data (1853-current), Centre for Environmental Data Analysis; UK.

Met Office (2020), UK Climate Summaries, London, UK, available at: http://www.metoffice.gov.uk/climate/uk/

Midas Gen. *Integrated Design System for Building and General Structures.* MidasIT Co., Ltd. Midas Structure | Product

Morishita, S., Tsujimoto, K., Yasui, M., Mori, N., Inoue, T., Shimojima, K. and Naito, K. (1984), "Galloping Phenomena of Large Bundle Conductors Experimental Results of the Field Test Lines". CIGRE, 22-04.

Nakamura, Y. (1980), "Galloping of Bundled Power Line Conductors". *J. Sound and Vibration*, **73**(3), 363- 377. https://doi.org/10.1016/0022-460X(80)90521-0

Nakamura, Y. and Mizota, T. (1975), "Torsional flutter of rectangular prisms". *Journal of the Engineering Mechanics Division*, ASCE, **101**(2), 125-142. https://doi.org/10.1061/jmcea3.0002001

Nigol, O. and Clarke, G. J. (1974), "Conductor Galloping and Control Based on Torsional Mechanism". IEEE C-74 116-2. Conference Paper.

Nigol, O. and Buchan, P. G. (1981), "Conductor Galloping, Part 1: Den Hartog Mechanism; Part II: Torsional Mechanism". *IEEE Trans.*, PAS. 100-699.

Noël, J. M., Niquette, C., Lockridge, S. And Gauthier, N. (2008), "Natural configurations and normal frequencies of a vertically suspended, spinning, loaded cable with both extremities pinned". *European Journal of Physics*, **29**(5), 47-53. https://iopscience.iop.org/article/10.1088/0143%2D0807/29/5/N02

Norberg, C. (1993), "Flow around rectangular cylinders-pressure forces and wake frequencies". *Journal of Wind Engineering and Industrial Aerodynamics*, **49**(1-3), 187-196. https://doi.org/10.1016/0167-6105(93)90014-F

Nygaard, B. E. K., Kristjansson, J. E. and Makkonen, L. (2001), "Prediction of In-Cloud Icing Conditions at Ground Level Using the WRF Model". *Journal of Applied Meteorology and Climatology*, **50**(12), 2445-2459. https://doi.org/10.1175/JAMC-D-11-054.1

Ohkuma, T., Kagami, J., Nakauti, H., Kikuchi, T., Takeda, K. and Marukawa, H. (2000), "Numerical analysis of overhead transmission line galloping considering wind turbulence". *Electr. Eng. Japan*, **131**(3), 19-33.

Park, H. S., Sohn, H. G., Kim, I. S. and Park, J. H. (2008), "Application of GPS to Monitoring of Wind-Induced Responses of High- Rise Buildings". *Struct. Des. Tall Special Build.*, **17**(1), 117-132. https://doi.org/10.1002/tal.335

Parkinson, G. V. (1974), "Mathematical models of flow-induced vibrations". in: E. Naudascher (ed.) *Flow Induced Structural Vibrations*, Springer, pp. 81-127.

Pearson, K. (1900), "On the criterion that a given system of deviations from the probable in the case of a correlated system of variables is such that it can be reasonably supposed to have arisen from random sampling". *Philosophical Magazine*, Series 5.50(302), 157-175. https://doi.org/10.1080/14786440009463897

Peeters, B. and De Roeck, G. (2001), "Stochastic System Identification for Operational Modal Analysis: A Review". *Dynamic Systems Measurement and Control*. **123**(4), 659-667. https://doi.org/10.1115/1.1410370

Peeters, B., Van der Auweraer, H., Guillaume, P. and Leuridan, J. (2004), "The PolyMAX frequency-domain method: a new standard for modal parameter estimation?". *Shock and Vibration, Special Issue dedicated to Professor Bruno Piombo*, **11**, 395-409. https://doi.org/10.1155/2004/523692

Peeters, B., Dammekens, F., Magalhães, F., Van der Auweraer, H., Caetano, E. And Cunha, A. (2006), "Multi-run Operational Modal Analysis of the Guadiana cable-stayed bridge". *Conference Proceedings of the Society for Experimental Mechanics Series.* Multi-run_Operational_Modal_Analysis_of_the_Guadia.pdf

Peeters, B., Van der Auweraer, H., Vanhollebeke, F. and Guillaume, P. (2007), "Operational modal analysis for estimating the dynamic properties of a stadium structure during a football game". *Shock and Vibration*, **14**(4): p. 283-303. https://doi.org/10.1155/2007/531739

Peeters, B., Lau, J., Lanslots, J. and Van der Auweraer, H. (2008), "Automatic Modal Analysis – Myth or Reality". *Sound and Vibration*, **42**, 17-21. 0803peet.pdf (sandv.com)

Post-Tensioning Institute (2006), *Post-Tensioning Manual*, 6th Edition. Post-Tensioning Institute, Phoenix, Arizona. (PDF) PTI tab.1-06 Post-Tensioning Manual - 6th Edition.pdf

Propplewell, N. (2005), "Quasi-steady aerodynamic data for moderate transition icing of a single conductor". *11th Int. Workshop Atmospheric Icing Struct.* Montréal, Canada.

Rawlins, C. B. (1979), *Transmission Line Reference Book: Wind-Induced Conductor Motion*, "Chapter 4: Galloping conductors". Electrical Power Research Institute. Palo Alto, California.

Rawlins, C. B. and Pohlman, J. C. (1988), "On the State of Galloping Conductor Technology". *4th International Workshop on Atmospheric Icing of Structures*. Paris. September 5-7.

Reynders, E. (2012), "System Identification Methods for (Operational) Modal Analysis: Review and Comparison". *Archives of Computational Methods in Engineering*, **19**(1), 51-124. 10.1007/s11831-012-9069-x

Richardson, A. S., Martucelli, J. R. and Price, W. S. (1963), "Research Study on Galloping of Electric Power Transmission Lines". *First Symposium on Wind Effects on Buildings and Structures*. Teddington, England; Paper 7, 612.

Rizzo, F. (2021), "Sensitivity Investigation on the Pressure Coefficients Non-Dimensionalization". *Infrastructures*, **6**(4), 53.

https://doi.org/10.3390/infrastructures6040053

Rubio-Gómez, G., Juárez-Pérez, S., Gonzalez-Rodríguez, A., Rodríguez-Rosa, D., Corral-Gómez, L., López-Díaz, A. I., Payo, I., & Castillo-García, F. J. (2021). New Sensor Device to Accurately Measure Cable Tension in Cable-Driven Parallel Robots. *Sensors* (Basel, Switzerland), **21**(11), 3604. https://doi.org/10.3390/s21113604

Ruzzo, C., Failla, G., Collu, M., Nava, V., Fiamma, V. and Arena, F. (2017), "Output-only identification of rigid body motions of floating structures: a case study". *Procedia Engineering*, **199**, 930-935. 188364864.pdf (core.ac.uk)

Rosa, L., Tomasini, G., Zasso, A., & Aly, A. M. (2012), "Wind-induced dynamics and loads in a prismatic slender building: A modal approach based on unsteady pressure measurements". *Journal of Wind Engineering and Industrial Aerodynamics*, **107**, 118-130. https://doi.org/10.1016/j.jweia.2012.03.034

Saunders, J. W. and Melbourne, W. H. (1975), "Tall rectangular building response to cross-wind excitation". *4th Int. Conf. on Wind Effects on Buildings and Structures*, 369-379, Cambridge University, UK.

Schanke, S. A. (2015), "Operational Modal Analysis of Large Bridges". Master Thesis, Norwegian University of Science and Technology. NTNU Open: Operational Modal Analysis of Large Bridges

Sears, W. R., (1941), "Some aspects of non-stationary airfoil theory and its practical application". *J. Aeronautical Sci*. **8**(3) 104–108. https://doi.org/10.2514/8.10655

Sen, S. and Mittal, S. (2015), "Effect of mass ratio on free vibrations of a square cylinder at low Reynolds numbers". *Journal of Fluids and Structures*, **54**, 661–678. https://doi.org/10.1016/j.jfluidstructs.2015.01.006

Sewall, W, (1921), "Correlation and causation". *J. Agricultural Research*, **20**, 557–585.

Shi, W. X., Shan, J. Z. and Lu, X. L. (2012), "Modal identification of Shanghai World Financial Center both from free and ambient vibration response". *Eng. Struct*., **36**, 14–26. https://doi.org/10.1016/j.engstruct.2011.11.025

Shimizu, M., Ishihara, T. and Phuch, P. V. (2004), "A wind tunnel study of aerodynamic characteristics of ice accreted transmission lines". *5th Int. Colloq. Bluff Body Aerodyn. Appl.*, Ottawa, Canada, 369-372.

Shimizu, M. and Sato, J. (2005), "Galloping Simulation and Observation of a 4-Conductor Bundle Transmission Line". *Proceedings of the Fourth European & African Conference on Wind Engineering*, Prague, Czech Republic, 301-302. EACWE-European-African-conference-on-wind-engineering-book-of-extended-abstracts.pdf

Simiu, E. and Miyata, T. (2006), *Design of Buildings and Bridges for Wind: A Practical Guide for ASCE-7 Standard Users and Designers of Special Structures*. Wiley, New Jersey, USA.

Simiu, E. and Scanlan, R. H. (1986), *Wind Effects on Structures: An Introduction to Wind*

Engineering. John Wiley & Sons, New York, USA.

Slater, J. E. (1969), "Aeroelastic Instability of a Structural Angle Section". PhD Thesis, University of British Columbia, USA.

Smith, G. D. (1965), *Numerical Solution of Partial Difference Equations*. London, Oxford University Press.

Smith, M., Smith, R. J. and Merello, R. (2010), "Intrinsic and supplementary damping in tall buildings". *ICE Proceedings Structures and Buildings*, **163**(2), 111-118. https://doi.org/10.1680/stbu.2010.163.2.111

Smith, R. J. and Willford, M. R. (2007), "The damped outrigger concept for tall buildings". *Struct. Des. Tall Special Build.*, **16**(4), 501–517. https://doi.org/10.1002/tal.413

Spence, S. and Kareem, A. (2014), "Tall buildings and damping: a concept-based data-driven model". *J. Struct. Eng*, **140**(5), 04014005. https://doi.org/10.1061/(asce)st.1943-541x.0000890

Sourav, K. and Sen, S. (2020), "Determination of the transition mass ratio for onset of galloping of a square cylinder at the least permissible Reynolds number of 150". *Physics of Fluids*, **32**(6), 063601. https://doi.org/10.1063/5.0007520

Steckley, A. (1989), "Motion induced wind forces on chimneys and tall buildings". PhD Thesis, University of Western Ontario, London, Canada.

Steinhaus, H. (1999), *Mathematical Snapshots*, 3rd ed. New York, Dover.

Stephens, M. A. (1974), "EDF Statistics for Goodness of Fit and Some Comparisons". *Journal of the American Statistical Association*, **69**, 730-737. https://doi.org/10.2307/2286009

Stringer, E. T. (1972), *Foundations of Climatology*. W. H. Freeman and Company, San Francisco.

Tamura, Y. (2005), "Damping in buildings and estimation techniques". *6th Asia-Pacific Conf. on Wind Eng.* (*APCWE-VI*), International Association for Wind Engineering (IAWE), Atsugi, Kanagawa, Japan, 193–213.

Tamura, Y. (2006), "Amplitude dependency of damping in buildings and estimation techniques". *12th Australasian Wind Engineering Society Workshop*, Queenstown, New Zealand.

Tamura, Y., Suda, K. and Sasaki, A. (2000), "Damping in buildings for wind resistant design". *Int. Symp. on Wind and Structures for the 21st Century*, 115-130, Cheju, Korea.

Tamura, Y. and Suganuma, S. (1996), "Evaluation of amplitude-dependent damping and natural freqeuncy of buildings during strong winds". *Journal of Wind Engineering & Industrial Aerodynamics*, **59**, 115-130.

Tamura, Y. and Yoshida, A. (2008), "Amplitude dependency of damping in buildings". *18th Analysis and Comput. Specialty Conf. at Structures Congress*, Structural Engineering

Institute (SEI), Vancouver, Canada. https://doi.org/10.1061/41000(315)39

Tamura, Y. (2013), "Damping in Buildings and Estimation Techniques". In Tamura, Y. and Kareem, A. (eds.), *Advanced Structural Wind Engineering*. Springer, pp. 347-376. https://doczz.net/download/7417893

Tarpo, M., Nabuco, B., Georgakis, C. T. and Brincker, R. (2019), "The Effect of Operational Modal Analysis in Strain Etimation using the Modal Expansion". IOMAC 2019, 8th International Operational Modal Analysis Conference, 699-705. https://www.researchgate.net/publication/333132031_The_Effect_of_Operational_Modal_Analysis_in_Strain_Estimation_using_the_Modal_Expansion

Taruishi, S., Matsumiya, H., Matsushima, H. and Shimizu, M. (2021), "Evaluation of Validity of method for making FEM model of a four-bundled conductor by excitation tests and simulations". *International Symposium on Dynamics and Aerodynamics of Cables (ISDAC 2021)*.

Taurishi, S. and Matsumiya, H. (2022), "Investigation of effect of galloping countermeasure for four-bundled conductor through field observation". *Proceedings Int. Workshop on Atmospheric Icing of Structures. IWAIS 2022*, Montreal, Canada, June 19-23. Taurishi and Matsumiya Paper Template (mcgill.ca)

Tunstall, M. and Koutselos, L. T. (1988), "Further Studies of the Galloping Instability & Natural Ice Accretions on Overhead Line Conductors". *4th Int. Conf. on Atmospheric Icing of Structures*. Paris, France.

United Nations, Department of Economic and Social Affairs (UN DESA), Population Division (2018). *World Urbanization Prospects: The 2018 Revision, Methodology. Working Paper No. ESA/P/WP.252*. New York, United Nations.

Van der Auweraer, H., Guillaume, P., Verboven, P. and Vanlanduit, S. (2001), "Application of a fast-stabilizing frequency domain parameter estimation method". *Journal of Dynamic Systems, Measurement, and Control*, **123**(4), 651-658. https://doi.org/10.1115/1.1410369

Van Dyke, P. and Laneville, A. 2008), "Galloping of a single conductor covered with a D-section on a high-voltage overhead test line". *Journal of Wind Engineering and Industrial Aerodynamics*, **96**(6-7), 1141-1151. https://doi.org/10.1016/j.jweia.2007.06.036

Wang, J. and Lilien, J.L. (1994), "Overhead Transmission Line Galloping. A Comparative Study between 2-DOF and 3- DOF Models". *3ème Congrès National Belge de Mécanique Théorique et Appliquée. Acte du Congrès*, Liège. May. 257-261.

Wang, J. (1996), "Large Vibrations of Overhead Electrical Lines: A Full 3-DOF Model for Galloping Studies". PhD Thesis, Collection des Publications de la Faculté des Sciences Appliquées de l'Université de Liège, No. 151, Belgium.

Wang, J. and Lilien, J. L. (1998), "Overhead Electrical Transmission Line Galloping. A Full Multi-span 3-DOF Model, Some Applications and Design Recommendations". *IEEE Trans. on Power Delivery*, **13**(3), 909-916. https://doi.org/10.1109/61.686992

Wardlaw, R. L. (1991), “Cable supported bridges under wind action”. *Proc. Seminar Cable-stayed Bridges: Recent Developments and their Future*, 10-11 Dec., Yokohama, Japan, 213-234, Elsevier Science.

Watanabe, Y., Isyumov, N. and Davenport, A. G. (1995), “Empirical aerodynamic damping function for tall buildings”. *9th Int. Conf. on Wind Engineering*, 1362-1371, New Delhi, India.

Welch, P. D. (1967), “The use of Fast Fourier Transform for the estimation of Power Spectra: A method based on time averaging over short, modified periodograms”. *IEEE Trans. Audio Electroacoustics*, AU-15, 70-73. https://doi.org/10.1109/tau.1967.1161901

Williams, M. (2016), *Structural Dynamics*. CRC Press.

WMO (1970), *The Beaufort Scale of Wind Force: Technical and Operational Aspects*. Geneva, World Meteorological Organization, Commission for Maritime Meteorology.

Yamaguchi, H. and Jayawardena, L. (1992), “Analytical estimation of structural damping in cable structures”. *Journal of Wind Engineering and Industrial Aerodynamics*, **43**(1-3), 1961-1972. https://doi.org/10.1016/0167-6105(92)90620-P

Yi, J., Zhang, J. W. and Li, Q. S. (2013), “Dynamic characteristics and wind-induced responses of a super-tall building during typhoons”. *J. Wind Eng. Ind. Aerodyn.*, **121**, 116-130. https://doi.org/10.1016/j.jweia.2013.08.006

Yu, P., Desai, Y. M., Shah, A. H. and Popplewell, N. (1993), “Three-degree-of-freedom model for galloping, part 1: Formulation”. *J. Eng. Mech.*, **119**(12), 2404-2425. https://doi.org/10.1061/(asce)0733-9399(1993)119:12(2404)

Yukino, T., Fujii, K. and Hayase, I. (1995), “Galloping phenomena of large bundle conductors observed on the full-scale test line”. *Proc. Int. Symp. Cable Dyn*. Liege, Belgium, 557-563. Yukino-Fujii-Hayase Galloping... - Google Scholar

Yukino, T. and Kuze, T. (2001), “Vibration characteristics in the long span 4 bundled conductors of transmission line”. *Proceedings of the Fifth Asia-Pacific Conference on Wind Engineering*), pp. 193–196. Yukino-Kuze, Vibration ... - Google Scholar

Zanelli, F., Mauri, M., Castelli-Dezza, F., Tarsitano, D., Manenti, A. and Diana, G. (2022) “Analysis of Wind-Induced Vibrations on HVTL Conductors Using Wireless Sensors”. *Sensors*, **22**(21), 8165. https://doi.org/10.3390/s22218165

Zeidler, E. (2013), *Nonlinear functional analysis and its applications: I: Fixed-Point Theorems*. Springer Science & Business Media. Nonlinear Functional Analysis and its Applications: I-III: | SpringerLink

Ziller, C. and Ruscheweyh, H. (1997), “A new approach for determining the onset velocity of galloping instability taking into account the nonlinearity of the aerodynamic damping characteristic”. *Journal of Wind Engineering and Industrial Aerodynamics*, **69-71**, 303-314. https://doi.org/10.1016/S0167-6105(97)00164-5

APPENDIX. FEM MODE SHAPES

The Figures displayed in this Appendix illustrate the mode shapes of the first 15 modes identified from the FEM model of the Phase C four-bundled conductor detailed in Section 5.4.1.

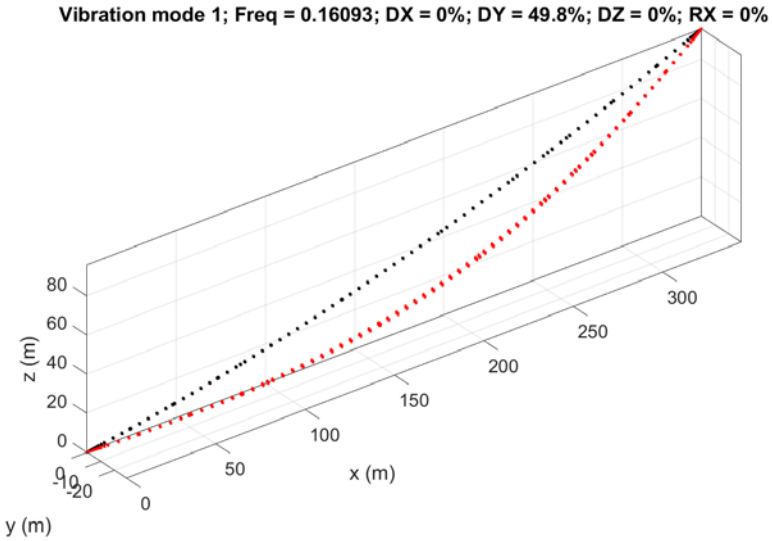

Figure 1. FEM Mode Shape 1.

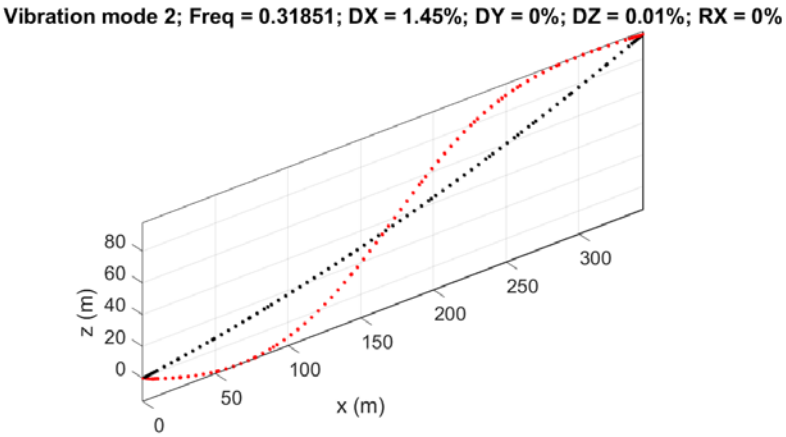

Figure 2. FEM Mode Shape 2.

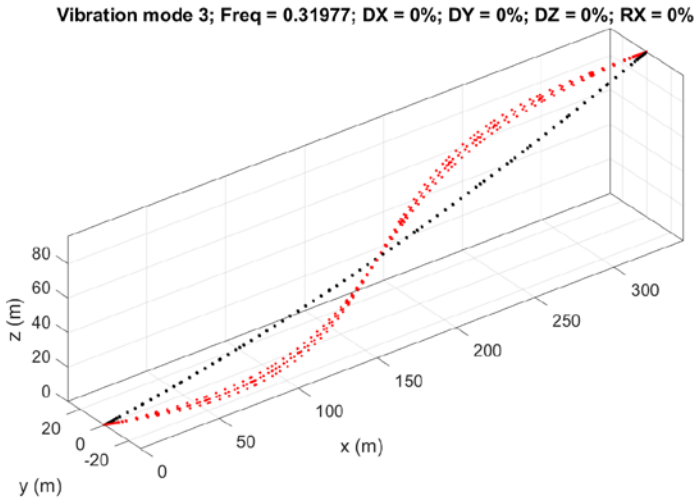

Figure 3. FEM Mode Shape 3.

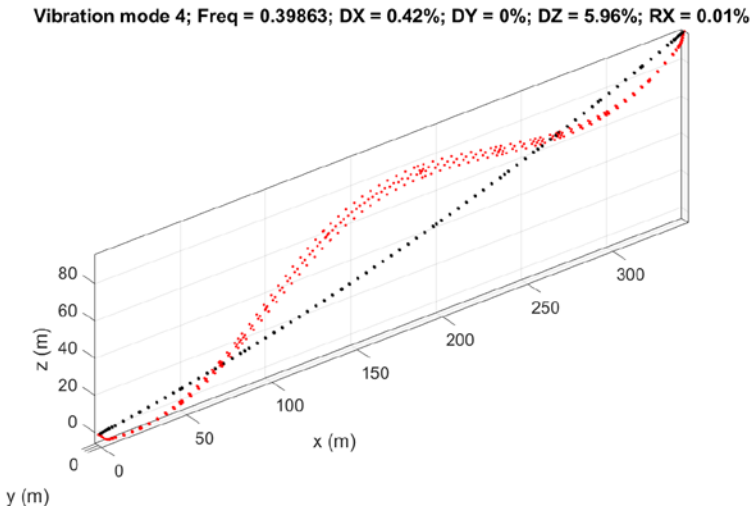

Figure 4. FEM Mode Shape 4.

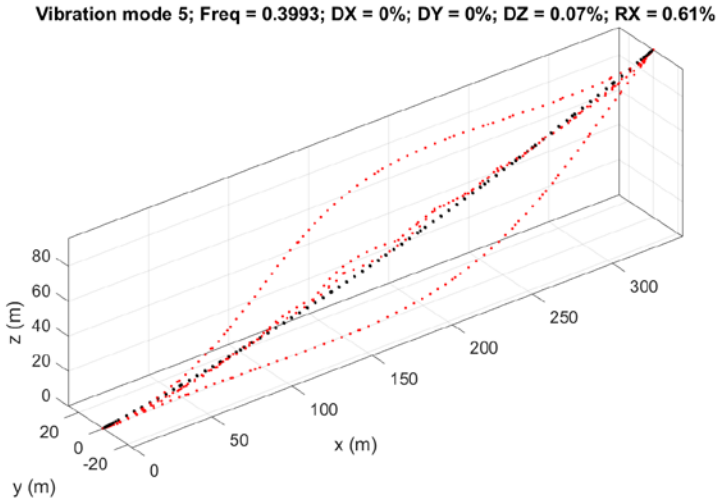

Figure 5. FEM Mode Shape 5.

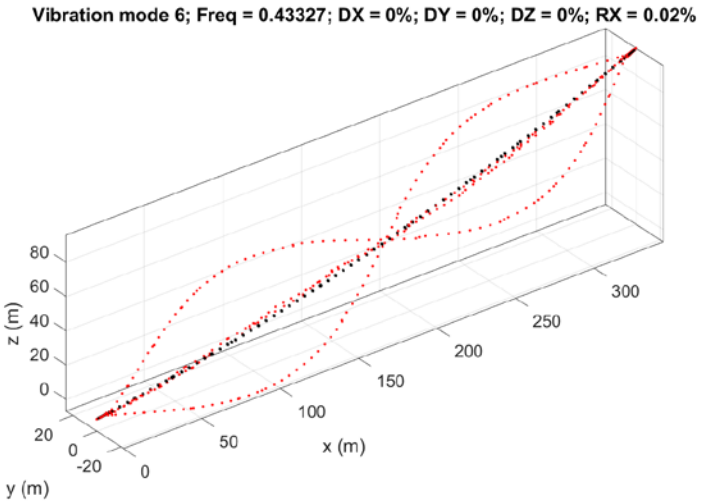

Figure 6. FEM Mode Shape 6.

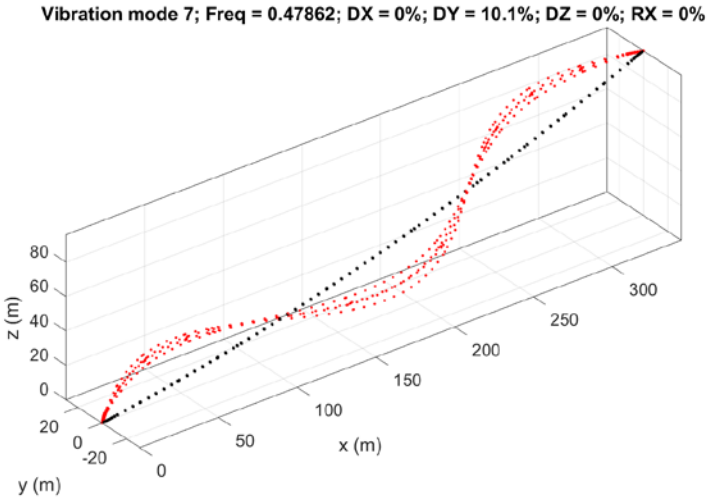

Figure 7. FEM Mode Shape 7.

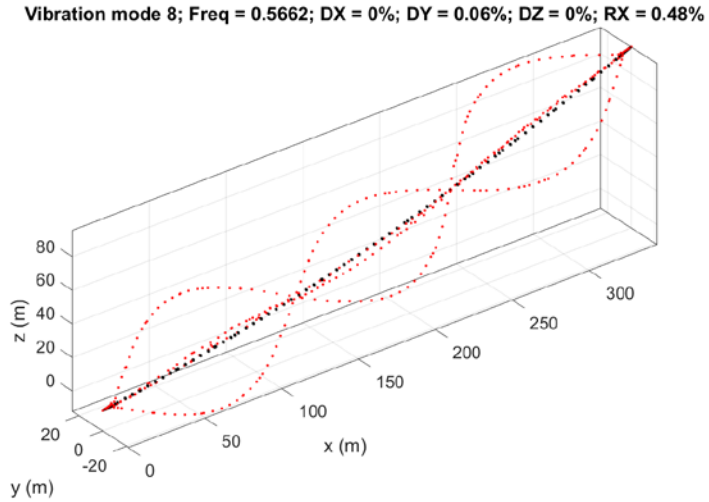

Figure 8. FEM Mode Shape 8.

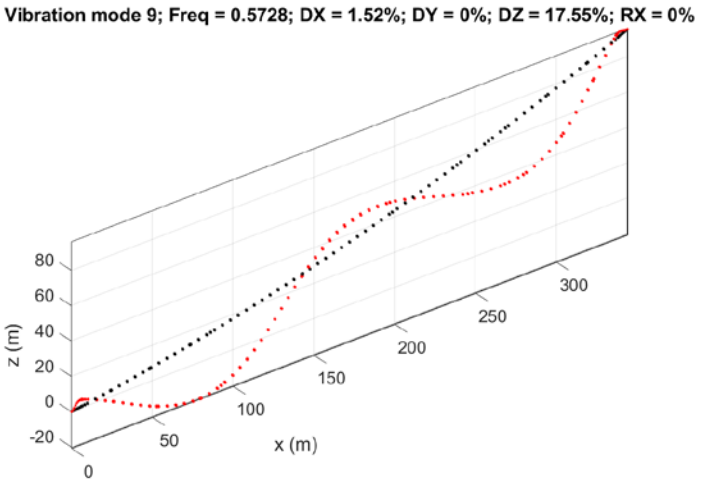

Figure 9. FEM Mode Shape 9.

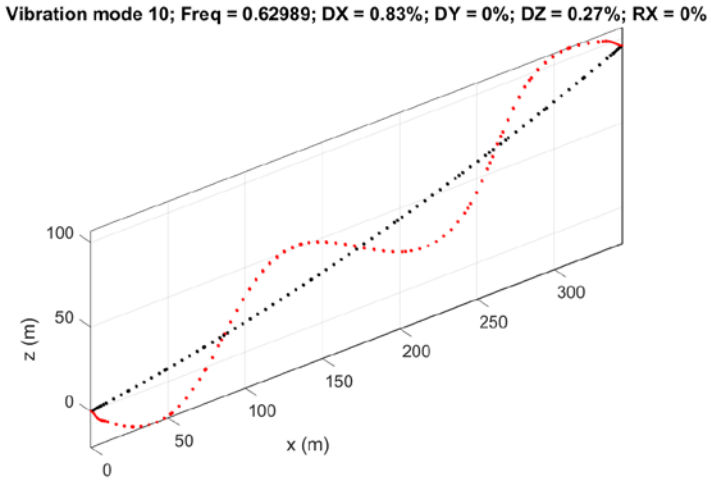

Figure 10. FEM Mode Shape 10.

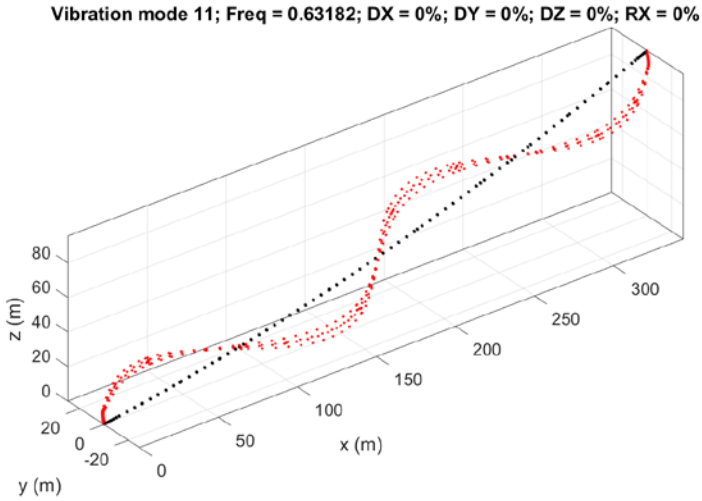

Figure 11. FEM Mode Shape 11.

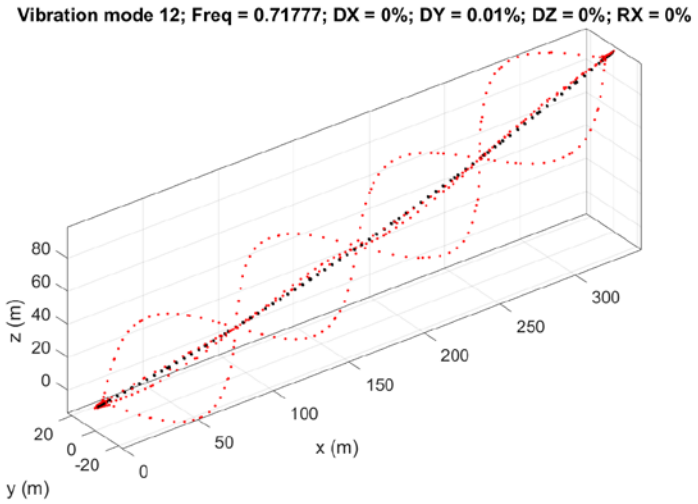

Figure 12. FEM Mode Shape 12.

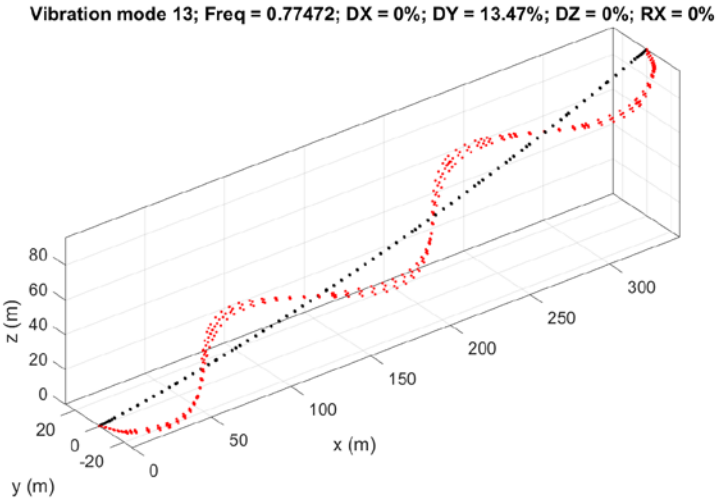

Figure 13. FEM Mode Shape 13.

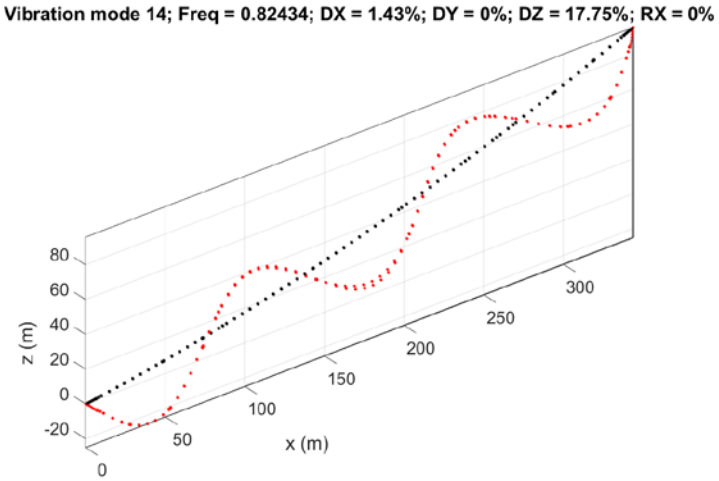

Figure 14. FEM Mode Shape 14.

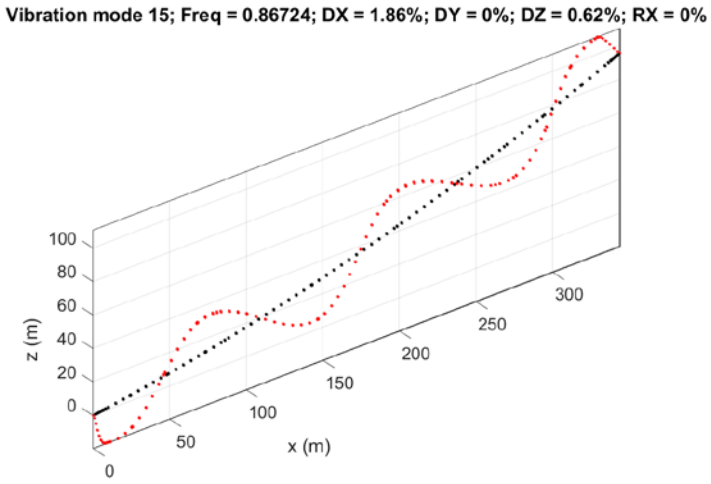

Figure 15. FEM Mode Shape 15.